DOE/DP/40152-22
Distribution Category UC- 712

DOE/DP/40152-22
KMSF-U1871

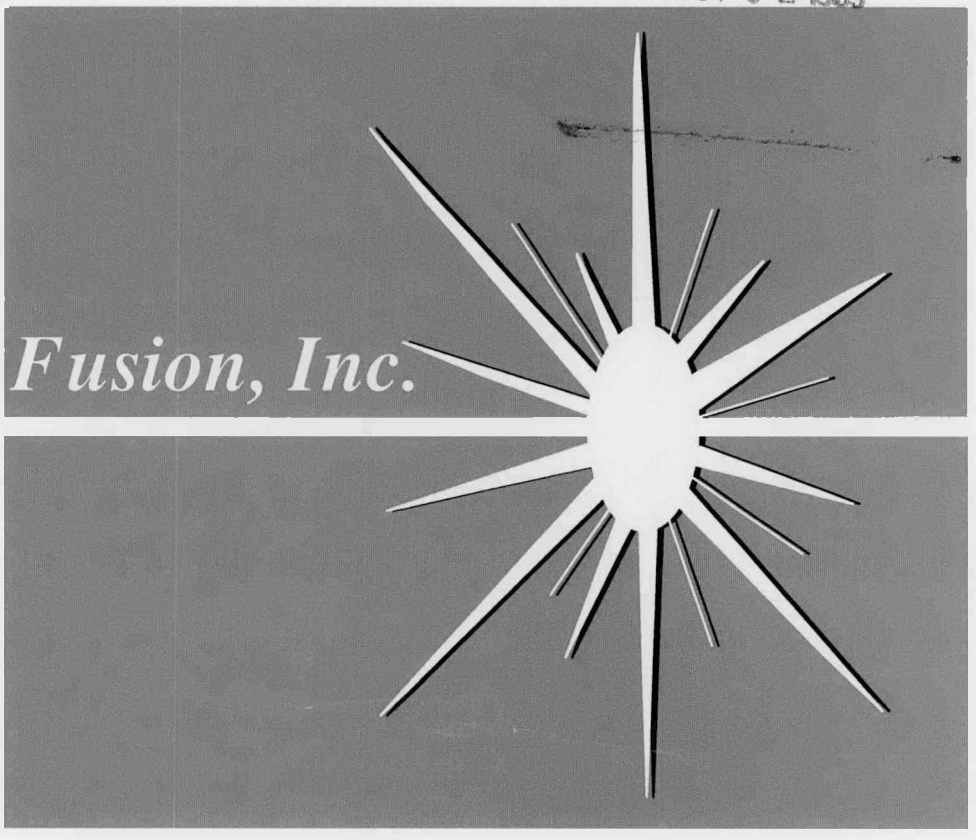

1986 Annual Technical Report

On Inertial Fusion Research

Period Covered: January - December 1986

Work performed under
U.S. Department of Energy Contract DE-AC08-82DP-40152
by KMS Fusion, Inc.
3621 South State Road, Ann Arbor, Michigan 48108
Date: March 1987

31,

DISCLAIMER

Printed in the United States of America

Available from:

National Technical Information Service
U.S. Department of Commerce
5285 Port Royal Road
Springfield, Virginia 22161

DOE/DP/40152-22
Distribution Category: UC-712

DOE/DP/40152-22
KMSF-U1871

DOE/DP/40152--22

DE90 000501

INERTIAL FUSION RESEARCH

1986 ANNUAL TECHNICAL REPORT

KMS Fusion, Inc.
3621 South State Road
Ann Arbor, Michigan 48108

Prepared for the U.S. Department of Energy
Nevada Operations Office
under Contract No. DE-AC08-82DP40152

Executive Editor: Dr. J. T. Larsen
Editor: N. C. Terry
Graphic Artists: W. L. Taylor
D. I. Kern
R. A. Luckhardt
J. S. Thornley
P. D. Trombley

Period Covered: January–December 1986

TABLE OF CONTENTS

FOREWORD

Inertial confinement fusion (ICF) research is dedicated to harnessing the energy source of the sun for man's use here on earth. An almost unlimited supply of fuel exists on the surface of the earth to sustain the same thermonuclear reactions that occur in the sun, and a growing scientific research effort into harnessing this awesome power for peaceful purposes has existed since the development of the thermonuclear bomb in the early 1950s. We at KMS Fusion, Inc. (KMSF), have been a part of that effort for the past 15 years. Our research activities during 1986 have led to significant contributions toward understanding the physics of ICF.

Inertial confinement fusion research is a complex process, requiring years of painstaking effort. To guide us in this effort, we identify milestones, and we meet nearly all of them. One such milestone, initiated nearly a decade ago, was completed in 1986. It is the use of cryogenic (frozen) hydrogen fuel, polymer (plastic) fuel capsules, and temporally shaped, short-wavelength laser light to compress the fusion fuel to a high density. More than 10 years ago, KMSF was the first laboratory in the United States to perform such experiments. Despite the fact that high compression is difficult to achieve with a modest amount of laser energy, our Low Preheat Implosion Campaign of 1986 demonstrated that it can be achieved if the conditions are controlled precisely.

The demonstration of this technology to the ICF research community brings to a close a chapter in KMSF's history; we have completed the last of our implosion experiments. Our laser has insufficient power to meet the next challenge of even higher density. We will support the continuation of these experiments at the other ICF facilities by transferring the technology and working with these facilities in the coming years. (Even though we have completed implosion experiments, our Chroma laser will continue to be used for high-precision experiments vital to the national ICF program.)

As we reach our previously set milestones, we look to the needs of the ICF program for the next few years to develop new ones. Just as, more than 10 years ago, we identified the need to use cryogenic fuel and polymer-shell targets, we have now identified some of the needs for 10 years from now. One of these

needs is the production of high quality, multimillimeter-sized cryogenic fuel targets for the next large ICF facility. We have developed a technique, based on the local deposition of the energy from the nuclear decay of the tritium fuel, for producing the uniform cryogenic fuel layer in these targets. Although the amount of heat is minute, it is sufficient to produce the desired effect. This new technique will take many more years of research to develop to the precision needed for high-gain experiments in the late 1990s.

This next large ICF facility has been dubbed the Laboratory Microfusion Facility (LMF). In 1985, the Department of Energy (DOE) began the process of identifying the requirements of the LMF. As DOE defines the LMF and its needs, KMSF will be following the requirements in the area of target development and production, where we expect to participate, closely. We are also interested in having a major role in the experiments and diagnostic instrumentation activities. If the LMF is to be completed and perform its first experiments before the year 2000, the planning for such a facility must be completed within a year or two, since the construction time will be 10 to 12 years. KMS Fusion expects to play a major role in the deployment and operation of that facility.

As we complete the year 1986, we also complete a five-year contract with DOE. During the past few months, we have prepared and submitted a proposal to continue our research for the next five years. For the first time, DOE has decided to solicit competitive bids for this work, and other proposals were submitted. As we prepare this report, we have learned that KMSF was selected for contract renewal. Indeed, our record of achievements and the capabilities of the strong team formed over the years put us in the winning position.

The end of one chapter and the beginning of another is a propitious time to pause and reflect on the past and on the future. We have come a long way in 15 years. Yet we see a long road ahead of us, and success will not come easily. But we are challenged to continue the pursuit of clean and abundant energy. This challenge necessitates that we now make changes in our direction so as to emphasize those aspects of ICF that we are uniquely suited to pursue. We have identified that the major thrust for KMSF will be in target fabrication technology, and we will see real growth in this area over the next five years. Our experimental activities will continue to support the national program, primarily in performing high-resolution, detailed experiments on the physics of classified targets.

This Annual Technical Report summarizes the unclassified aspects of our ICF research activities for the calendar year 1986. The report is organized into three main sections; the first covers laser-plasma interaction experiments, the second is devoted to our progress in materials development and target fabrication technology, and the third describes our research in laser technology development.

This record of accomplishments is more than that achieved in 1986. It is a culmination of the work of many years. It is a proof that KMSF has assembled a first-class research team. It is a statement of the dedication by many individuals to long hours of research on very difficult problems. It is these qualities that provide the resources needed to meet the challenges of the next decade.

Dr. Jon T. Larsen
Vice-President, Fusion Programs

DO NOT MICROFILM
THIS PAGE

FUSION AND PLASMAS

SECTION ONE

Scientific Editor, Dr. R. R. Johnson

Introduction

The physics of laser-irradiated inertial confinement fusion (ICF) targets was studied extensively in 1986. Experimental campaigns were conducted to explore the important field of high-density implosions, to study ionization physics in high-density plasmas, and to determine the temporal and spatial characteristics of stimulated Raman scattering. In support of these experiments, a calibration facility has evolved that provides accurate absolute calibrations of x-ray spectrographs and other broadband x-ray detectors. The theoretical support of the experiments consisted of modeling interpenetrating plasma streams and developing a fluid code to model stimulated Raman scattering and the two-plasmon decay instability. The target modeling codes have been improved to calculate the hydrodynamic behavior of plasmas more accurately. A viewfactor code has been formulated to determine spatially the laser/plasma interaction region in complex geometries.

The cryogenic implosion experiments performed in 1986 at KMS Fusion (KMSF) were the most complex and sophisticated effort to date to diagnose the conditions of high-density material. The results of these experiments, together with data reduction and interpretation, are given in Section 1.1. The x-ray backlighter diagnostic was the primary tool used to determine the compressed fuel and tamper densities. It has long been a concern to the ICF program that high densities may not be achieved at all because of hydrodynamic instabilities, which can mix the pusher with the fuel. The KMSF experiments showed that mix is an important factor when the target aspect ratio becomes too large. This is the first high-density implosion experiment in which this phenomenon has been observed.

Another important field of ICF physics is the behavior of interpenetrating plasma streams. It is clear that, for high-density, low-temperature plasmas such as imploding targets, collisionality dominates. On the other hand, low-density plasmas can pass through one another with virtually no collisions. The transition region between collisionality and no collisions is discussed in Section 1.2. It is anticipated that experiments will be conducted at KMSF to explore this important transition region.

KMS Fusion has performed experiments on stimulated Raman scattering and the two-plasmon decay instability for a number of years. A fluid code (SATIN) has been developed to model the parametric instabilities in the nonlinear and saturated regions, and this is described in Section 1.3. The two-dimensional feature

of the code provides a framework for studying other nonlinear mechanisms, such as profile modification.

Viewfactor codes have been used to a large extent in problems involving fixed surfaces where the intervening material is vacuum. These applications are typically in astrophysics. However, in ICF targets there are experiments with plasma present, which modifies the results. This is discussed in Section 1.4, where the RAYNA II code is described. This code will be extremely useful in analyzing the results of experiments in complex geometries.

The Delphi code at KMSF has been under development since 1984. It is anticipated that Delphi will eventually replace TRHYD, which has been the workhorse of KMSF target simulations. Progress in the development of Delphi is presented in Section 1.5. The main emphasis of Delphi is to treat nonequilibrium situations that TRHYD cannot handle. It has been apparent for a long time that laser interaction with matter is far from thermal equilibrium because of the temporal and spatial restraints imposed by the ICF experiments.

KMS Fusion began spectroscopic measurements on various types of ICF targets in 1981. X-ray spectroscopy is a powerful tool in determining plasma temperatures and densities. The technique has grown so that spatial and temporal dependencies can be determined. A particular set of spot spectroscopy experiments is described in Section 1.6. These experiments are designed to provide the broadest and most self-consistent set of data possible in order to enhance the capabilities of the atomic physics codes.

The KMSF x-ray calibration facility was put into operation in 1984 and has been used extensively since that time. Improvements have been made and a second calibration facility began operation in 1986. Section 1.7 describes the new facility and the changes that were incorporated.

The integrated reflectivity of Bragg crystal has been measured using the KMSF x-ray calibration facility, and the data are presented in Section 1.8. A number of line sources were used so that the calibration could be extended from 0.18 to 9.6 keV. A full description of possible sources of error is given, together with corrections that were made.

SECTION 1.1

Low Preheat Implosion Experiments

Achievement of ignition in a fusion target is one of the near-term goals of the national inertial confinement fusion (ICF) program.[1] Ignition occurs when sufficient energy is deposited in the fuel by self-generated α-particles to cause a burn to propagate through the remaining fuel. To reach the ignition condition in a fusion target, it is necessary to compress the fuel to the order of a thousand times liquid density so that the range of the α-particles will be small relative to the compressed fuel dimension. The majority of advanced target designs that will be used to explore these conditions require the incorporation of cryogenic fuel layers.[2,3]

To date, all successful laser/target interaction experiments that have used cryogenic fuel layers have been performed by KMS Fusion (KMSF).[4] The experiments performed in 1986 were founded on those of our 1982 series but used advanced target designs and better control of the laser drive parameters. The major improvements over the 1982 campaign were the use of

- laser light at a wavelength of 0.53 μm instead of 1.05 μm,
- laser temporal pulse shaping tailored to the optimal shape, as prescribed by numerical simulations of the target implosions, instead of "square" pulses, and
- spherical poly(vinyl alcohol) (PVA) shells instead of glass shells.

The cryogenic fuel was frozen as a uniform solid layer on the interior of the spherical shell, as was done in 1982.

The goal of the experiment was to control the level of fuel preheat so as to compress the fuel along a nearly Fermi-degenerate adiabat. Here, the achievement of high fuel density results in fuel temperatures so low that a negligible number of neutrons are created within the DT fuel. For this reason, and for ease of handling, the PVA shells were filled only with deuterium.

Numerical simulations predict that, with the laser and target parameters available at KMSF, it should be possible to reach 100 to 200 times liquid density in the compressed fuel. Achievement of an even higher density with the rather modest 250 J of laser energy available from the Chroma laser would necessitate further control of the drive parameters, probably beyond the state of the art.

The experimental campaign began in the fall of 1985, and the preparation for the cryogenic experiments is discussed in the 1985 Annual Technical Report.[5] We present here the data taken in 1986 and discuss the importance of the results.

Theoretical Considerations

It has been known from the beginning of ICF research that preheating the fuel prior to final compression must be avoided in order to achieve high densities using relatively low drive energies.[6] The ultimate limitation is given by the Fermi degeneracy of the fuel. For a given driving pressure (and hence final fuel pressure, as required by an isobaric model), a higher final fuel density may be realized if the temperature of the fuel is kept low. Traditional implosion experiments have used very intense laser beams to create as high a pressure as possible. Unfortunately, use of these rapidly rising pulses results in unacceptable levels of fuel preheat. This occurs for several reasons.

First, high-intensity laser pulses cause high electron temperatures in the target's corona and, if the laser wavelength is longer than $\sim 0.5\ \mu$m, laser/plasma interaction processes can produce very energetic electrons. In either case, there may be an appreciable number of these hot electrons that will penetrate the shell and deposit their energy in the fuel, thus preheating it. The scattering mean-free-path for electron-ion scattering must be sufficiently short that the hot-electron energy is deposited only in the pusher and not in the fuel. This requires the use of targets with a shell density-thickness product that is larger than the scattering mean-free-path of the energetic electrons. This in turn requires more massive targets with smaller aspect ratios for the longer laser wavelengths. However, increased target mass decreases the efficiency of the ICF process.

Second, the high temperature created in the corona of the target by an intense laser beam produces a strong pressure pulse that penetrates the material and shock-heats the fuel by viscous processes. By initially having the laser intensity as low as possible and then increasing the intensity in time, shock heating of the fuel can be kept to a tolerable level while the final pressure can be made high enough to drive the implosion to high density. A pulse-stacking device that allows a prescribed, temporally formed laser pulse shape to be used in the experiments has been in use at KMSF for a number of years.

By carefully controlling the fuel preheat generated by these two mechanisms (radiative preheat does not play a major role in these experiments), a higher final fuel density can be achieved for a given laser energy. In Fig. 1-1, we see the results achieved in the 1982 experimental series and the improvement in the 1985–86 series for the same laser energy. The lower compressions achieved in the earlier series resulted from fuel preheat that was due both to energetic electrons and to shock preheat temperatures of 10 to 13 eV. Preheat in the recent series was inferred to be 2 to 3 eV, resulting in significantly higher fuel densities.

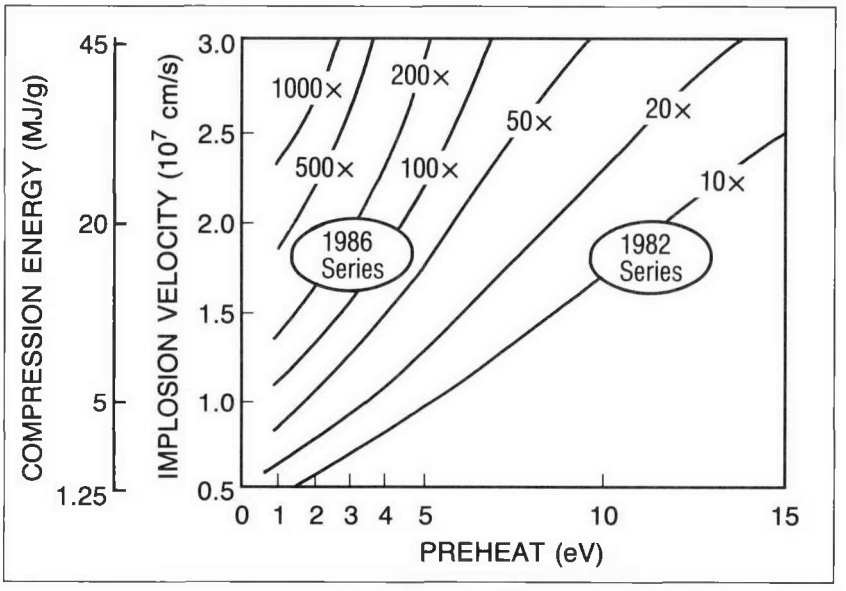

Fig. 1-1. Control of the preheat allows a higher final density to be achieved for a given amount of laser energy. In 1982, we used infrared light and square pulses, which resulted in preheat levels of 10 to 13 eV. By using green light, polymer shells, and shaped pulses in the 1985–86 series, we were able to achieve preheats in the 2 to 3 eV range.

Experimental Approach

The experimental approach was designed to minimize fuel preheat, which can arise from fast electrons, shock heating, or radiative processes. The four factors required to reach high density are listed in their relative order of importance (based on a large number of experimental observations and numerical simulations).

1. *Short wavelength illumination.* The use of 0.53 μm laser light in place of 1.05 μm laser light reduces electron preheat both by producing fewer hot electrons and by lowering the hot electron temperature since, for resonance absorption, $T_H \sim (I \cdot \lambda_L^2)^{0.48}$. As described earlier, this allows the shell wall density-thickness product to be reduced. A reduction of the shell mass is an important consideration, since a smaller amount of mass results in more efficient transfer of laser energy to compressed energy in the fuel by PdV work.
2. *Shaped laser pulses.* Laser pulse shaping is important to minimize shock preheat, since the strength of the shock is roughly proportional to the laser intensity. With pulse shaping, the laser intensity reaches the maximum value at the end of the pulse, when the fuel is approaching its maximum compressed state. Then shock heating plays a different role; namely, it helps initiate the thermonuclear burn.
3. *Low-Z spherical shells.* The use of spherical shells of low atomic number (low-Z) will be important for obtaining the ultimate performance of an ICF target when it becomes necessary to minimize radiative preheat of the fuel. Although

radiative preheat is not of major importance in these experiments, the use of low-Z polymers for the shell material keeps the radiation at a low level, significantly less than shock and electron preheat. This is because the recombination radiation, which is the dominant radiative preheat mechanism, goes as Z^5. The primary advantages of low-Z shells in these experiments are that the diagnosis of the compressed fuel region is made easier and that the targets have less mass for a given aspect ratio and target diameter.

4. *Solid fuel layers.* The solid fuel layer provides the most energy-efficient way to compress the fuel to high density, since the implosion begins with the fuel at a high density in a thin shell at a large radius. Compression of a thin shell to a high-density sphere is more efficient than beginning with a solid sphere. Also, by starting with as high a fuel density as possible, a compression along a near-Fermi degenerate adiabat to a high density is more easily accomplished.

Experimental verification of each of these four factors would require 16 different sets of conditions. Since this was not possible, the parameters were limited to four conditions: shaped pulses with gaseous and cryogenic targets and square pulses with gaseous and cryogenic targets. In addition, the diameters of the PVA shells ranged from 110 to 150 μm, with corresponding initial aspect ratios of 10 to 25. The mass of the targets was held approximately constant so that a nearly equal fraction of energy was transported to the fuel from shot to shot. The fuel mass was approximately 10 ng for the smaller targets.

Altogether, 68 cryogenic target shots were taken throughout the campaign, in addition to 38 room-temperature shots. The laser was configured to give either a square pulse with 500 ps full width at half-maximum (FWHM) or a shaped pulse rising with the square of the time (called a "ramp" pulse), with a base width of 900 ps. Examples of the pulse shapes used in the experiment are shown in Fig. 1-2. The energies for the two different pulse shapes were kept approximately equal.

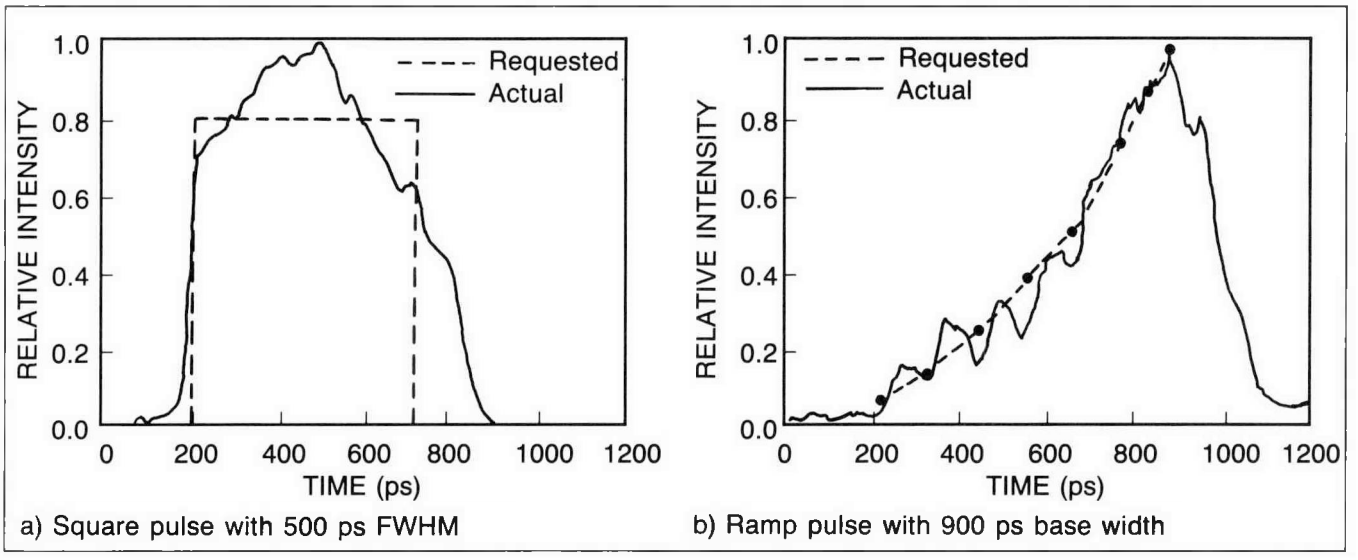

Fig. 1-2. The laser was configured to give either a square pulse with 500 ps full width at half-maximum (FWHM) or a ramp pulse (rising with the square of the time) with a base width of 900 ps. Here, the actual temporal behavior of the laser pulse, measured at the target chamber, is compared to the requested 500 ps square shape (a) and the ramp shape (b).

Diagnosis of High Fuel Densities

The low preheat implosions we performed do not produce measurable thermonuclear reaction particles, nor emit sufficient x-rays from the compressed core to provide a direct measurement of the final state.[7,8] Hence, we rely most heavily on x-ray radiography to infer the conditions achieved in these low preheat implosions.[9–11]

The method is represented schematically in Fig. 1-3. A third beam of Chroma, synchronized to the other two beams, illuminates a metal target to produce x-rays of energy greater than 1 keV; these x-rays are dominated by line emission characteristic of the target. This "backlighter" target is placed close to the low-preheat target. Its x-rays penetrate the imploded target and are recorded through a pinhole by an x-ray streak camera.

For the x-ray backlighter diagnostic to have the optimum sensitivity, it is desirable that the opacity of the shell material, the product of the shell's density and thickness, and the spectral energy of the x-ray backlighter be matched. The opacity of the PVA shell is well known theoretically, and the relative transmission of the x-rays through the target provides a measurement of the density-thickness product. The compressed shell material has a radial density-thickness product of approximately 0.05 g/cm^2, so that opacities in the range of 60 cm^2/g would provide the best information. The opacity of PVA in the regions of temperature and density of interest is shown in Fig. 1-4. It is seen that x-ray photon energies of 4 keV are nearly ideal. Our interpretation of the radiographic data assumes that the fuel/pusher interface is well defined and that the radial density distribution of the PVA shell is known.

The spherical symmetry of the compressed core is an important factor in estimating the compressed fuel densities.

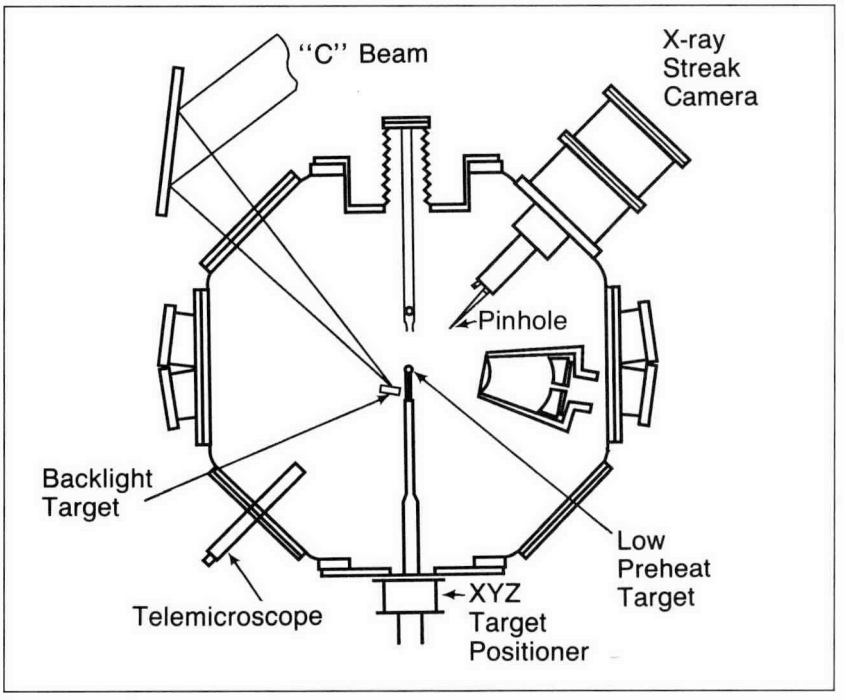

Fig. 1-3. A third beam of Chroma (the "C" beam), synchronized to the other two beams, illuminates a metal backlighter target to produce x-rays that penetrate the imploded target. These x-rays are recorded through a pinhole by an x-ray streak camera. The axis of the main laser beam used to illuminate the target is perpendicular to this view.

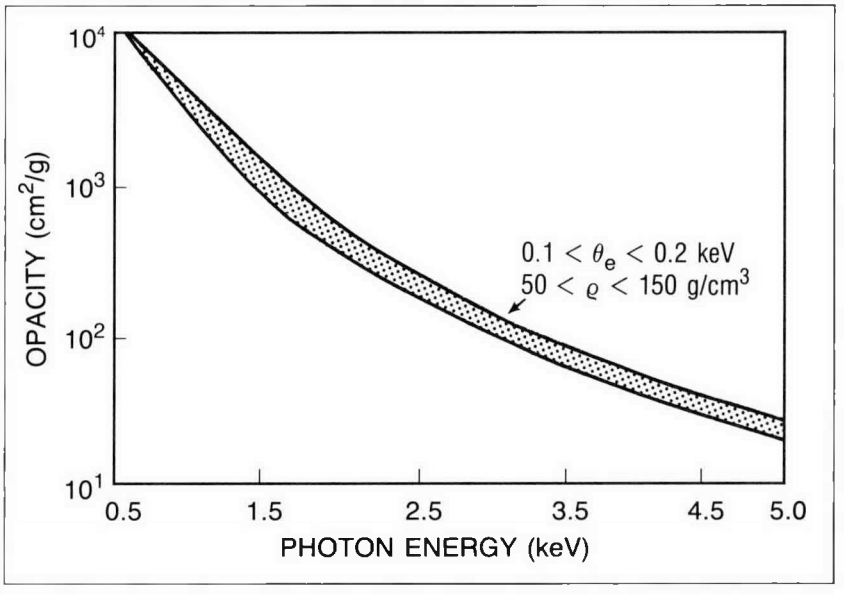

Fig. 1-4. To optimize the sensitivity of the x-ray backlighter diagnostic, we matched the shell material opacity, the shell density-thickness product, and the spectral energy of the x-ray backlighter. Since the compressed shell material has a radial density-thickness product of ~0.05 g/cm², opacities in the range of 60 cm²/g were desired. The opacity of PVA is shown here as a function of x-ray backlighter (photon) energy in the regions of temperature θ_e and density ρ of interest; it is seen that x-ray photon energies of 4 keV are ideal.

Achievement of a spherical compressed state requires that the illumination of the target be as close to spherically uniform as possible. (There will be some thermal smoothing present that will help ameliorate local variations in illumination.) Two-dimensional calculations show that better than 20% uniformity in the illumination pattern is essential to achieving the densities expected in these experiments.

The double-bounce illumination system (DBIS) provides 4π illumination on the target (this apparatus is described in detail in the KMS Fusion 1985 Annual Technical Report[5]). Optical measurements on DBIS, combined with the spatial features of the Chroma laser beams, were used to calculate the optical quality of the illumination system. The quality of the illumination from the DBIS mirrors appears to meet the criterion of 20% uniformity.

One possible contribution to asymmetry in the implosion is the shadowing of the target caused by the fixtures located in the vicinity of the target. These include the mounting post, the cryogenic shroud, the x-ray backlighter target, the pinhole camera, and other diagnostic equipment. The fixtures were made as small as possible to minimize the effects on irradiation uniformity. In addition, the imperfect figure of the DBIS mirror blends these obstructions into a more uniform illumination pattern.

The spherical uniformity of the target must be good if implosion velocities are to be equal from all directions. Shell wall nonuniformity measurements were made for all the targets to determine if the experimental results showed a dependence. In addition, the uniformity of the cryogenic fuel layer must also be reasonably good if implosions are to be centered within the field of view of the streak camera. Measurements of the uniformity of the cryogenic layer were performed in situ moments before each target shot to ensure that the fuel layers were acceptable.

The high-density compressions also require that the imploding shell be hydrodynamically stable. If the shell becomes unstable, there will be mixing of the pusher with the fuel and it will not be possible to make a definitive measurement of the compressed fuel region. The fuel compression results reported here were from target shots in which fuel/shell mixing was believed to be minimal.

The best estimate of the degree of spherical symmetry achieved in these experiments was obtained using holographic interferometry and x-ray pinhole photography. These data are shown in Fig. 1-5 for a cryogenic target shot. The holographic interferometer can measure densities up to 10^{21} electrons/cm^3. As can be seen from the photograph, the spherical symmetry is better than 5% at this density. This implies that any variations in illumination symmetry are not large in the global sense and that small-scale variations are probably diminished by thermal smoothing.

The time-integrated x-ray pinhole photograph provides a measure of the spherical symmetry at higher densities near the ablation surface. The x-ray emission is due to the heating of pusher

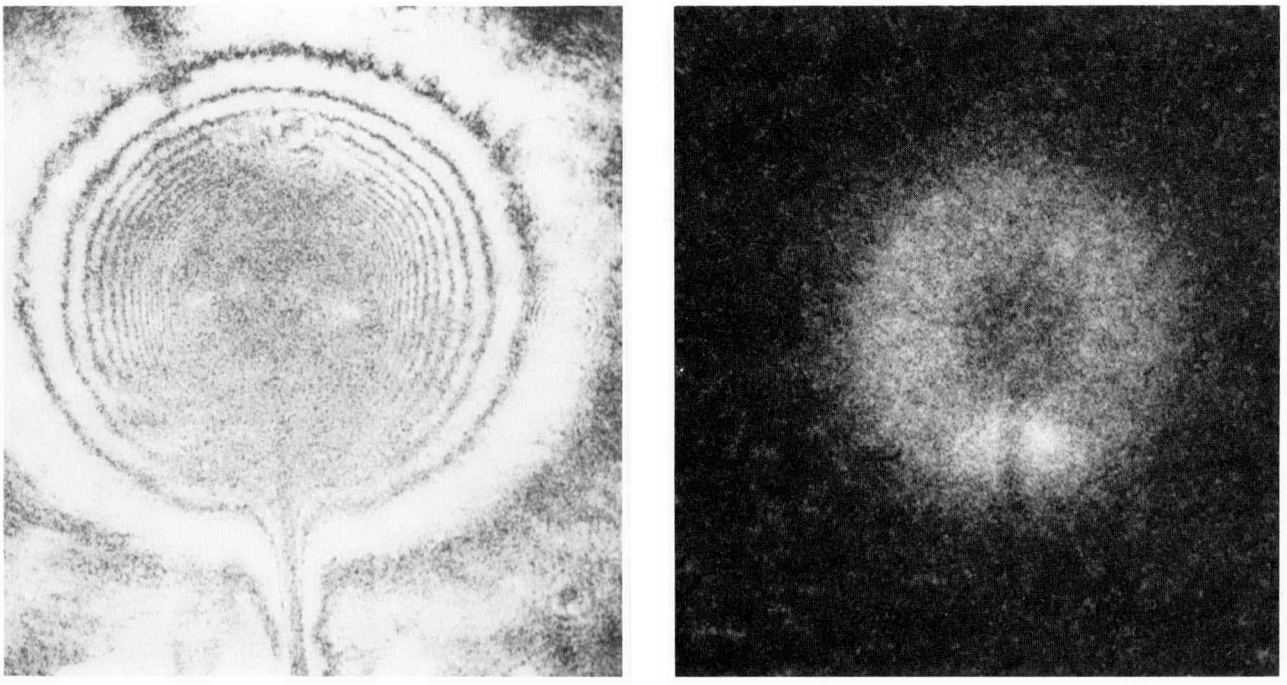

a) Holographic interferogram at 375 ps

b) Time-integrated x-ray pinhole photograph

Fig. 1-5. Several diagnostics are used to provide an indication of the degree of spherical symmetry in an implosion. A holographic interferogram (a) of a cryogenic target shot, measured 375 ps from the leading edge of the laser pulse, provides an indication of symmetry in the plasma region where densities are less than 10^{21} electrons/cm^3. A time-integrated pinhole photograph (b) shows the x-ray emission from the high-density region of the implosion between the critical density surface and the ablation front.

material by thermal conduction from the critical surface to the ablation surface. Since the temperature quickly drops when the laser pulse is turned off, the inner edge of the emission comes from the location of the ablation surface at the end of the pulse. The density of the ablation surface is a few times greater than the original PVA density. The x-ray photograph shows that the symmetry is still good even in this higher-density region, which is located at approximately half the initial target radius. The greatest density in the PVA is located at the fuel/pusher interface, and there is no information on the spherical symmetry at that location. Since the temperature of the compressed fuel and pusher is low, x-ray emission is not strong. The shell density information for the PVA pusher at this interface is given by the x-ray backlighter measurement.

Interpretation of X-ray Backlighter Photographs

The principal diagnostic used to determine density in the vicinity of the compressed fuel region is the x-ray backlighter. The location of the x-ray backlighter source relative to the cryogenic target is shown in Fig. 1-3. The x-ray streak camera was aligned so that the slit of the camera was parallel to the direction of the

main laser beam axis. The resolution of the system was $\lesssim 7$ μm and the vertical positioning relative to the center of the target was accurate to better than 5 μm. The resolution and pointing accuracy were determined by imploding an empty PVA target and simultaneously measuring the size and position of the imploded shell using its x-ray self-emission.

The streak camera photographs of the imploding targets obtained with the x-ray backlighter source are shown in Fig. 1-6 for both a 500 ps square driving pulse and 900 ps ramp driving pulse (refer to Fig. 1-2). The time to peak compression is longer, as expected, for the ramp-pulse case. The target implodes to a higher density when a ramp pulse is used, as is shown by the smaller opaque region in the center of the photograph. A similar streak record for the implosion of a cryogenic target using a ramp pulse is shown in Fig. 1-7. In this case, a densitometer trace through the image at peak compression shows that the x-ray transmission through the core of the target is at the fog level of the film. The diameter of this region is measured to be 21 μm, which is the dimension of the dense PVA shell and the entrapped deuterium fuel. Computer simulations and simple ablation models estimate that 40% of the original mass of the PVA shell is contained in this region; hence, it is possible to estimate the size of the fuel region. The x-ray streak camera records a one-dimensional image, so one must be careful about interpreting the two-dimensional structure of the compressed core.

A detailed analysis of the compressed core requires a calibration of the x-ray backlighter source and information about the x-ray streak camera characteristics. The x-rays needed for the radiograph were produced by irradiating either an aluminum or molybdenum disk, 400 μm in diameter, with intense green laser

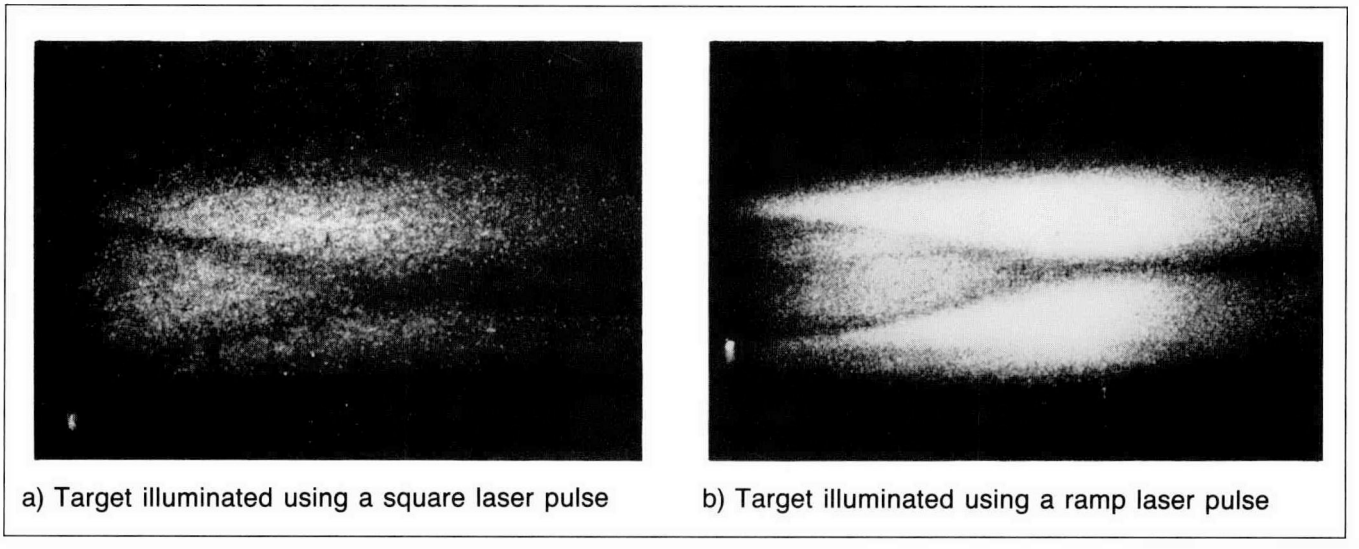

Fig. 1-6. Streak photographs of imploding targets obtained with the x-ray backlighter source are shown for both a 500 ps square driving pulse (a) and a 900 ps ramp driving pulse (b). The backlighter x-rays passing through and around the imploding target were imaged using a 5 μm pinhole. The target implodes to a higher density when a ramp pulse is used, as is shown by the smaller opaque region in the center of (b). Time increases to the right.

light. The x-ray emission at energies above 1 keV consisted of lines characteristic of the target and, in the case of aluminum, a recombination continuum. Examples of aluminum and molybdenum x-ray spectra obtained with a time-integrating crystal spectrograph are shown in Fig. 1-8. Photons at these energies are capable of passing through the PVA shells used to hold the cryogenic fuel. The amount of transmission through the capsule is

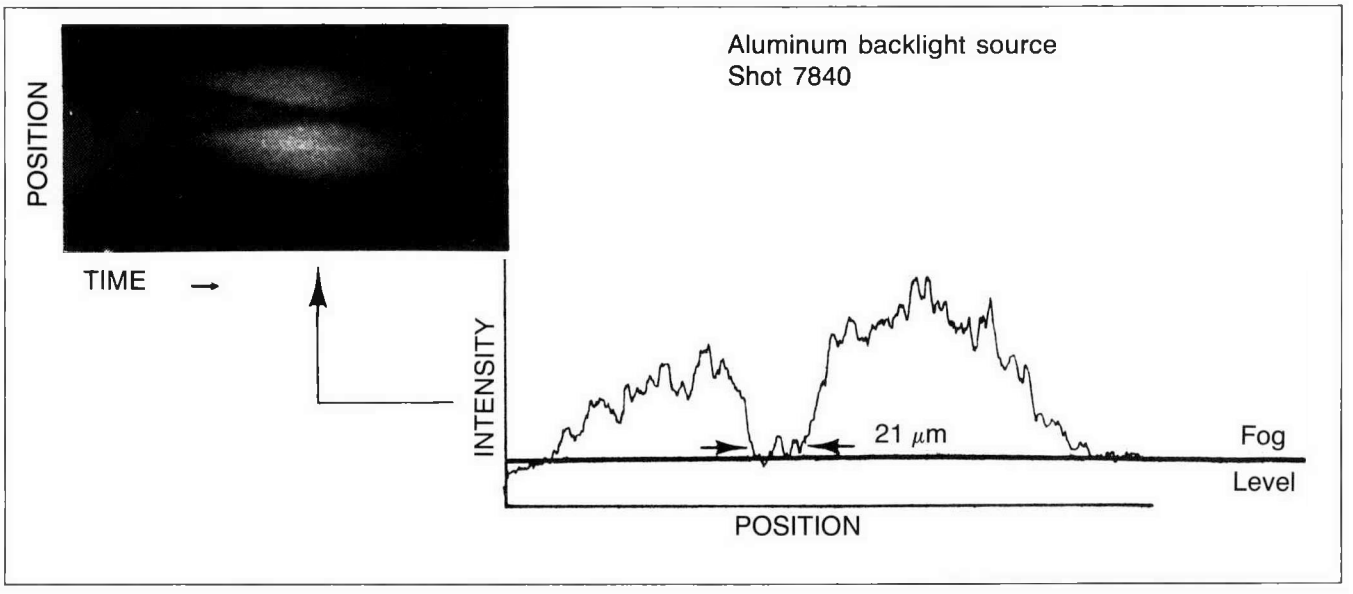

Fig. 1-7. The streak photograph of a cryogenic target illuminated with a ramp laser pulse is shown in the upper left. The densitometer trace taken vertically across the photograph at the position of peak compression (as determined by the minimum extent of the opaque region) is shown in the lower right; the fog level for the film is shown for comparison.

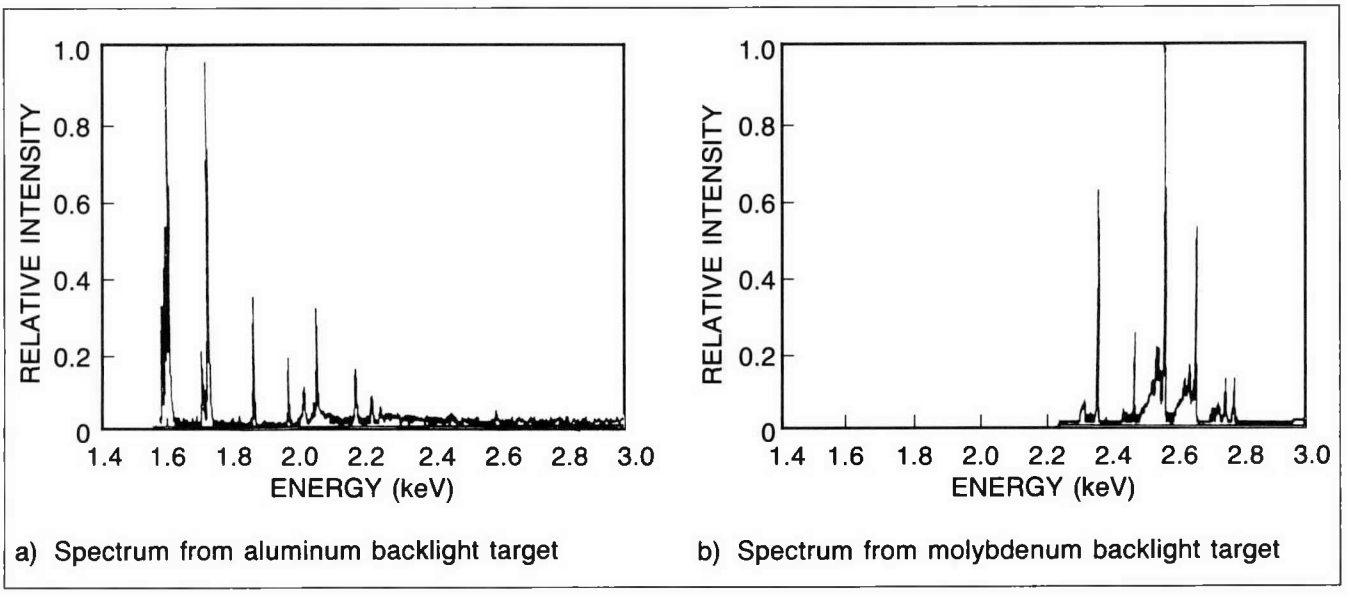

Fig. 1-8. Metal targets illuminated with 0.53 μm laser light emit x-radiation dominated by discrete lines. The spectrum from an aluminum target (a) also has a recombination component above about 2.0 keV. A molybdenum target (b) produces nearly pure line radiation.

also a measure of the degree to which the PVA has been compressed.

A time-resolved radiograph of a chord passing through the center of the target was obtained with a pinhole and an x-ray streak camera. The pinhole consisted of a 5 μm hole in a 5 μm thick gold substrate. In some cases, two pinholes were used, to obtain both the target radiograph and an image of the x-ray source itself. The center of the target radiograph was imaged onto the 400 μm slit of an x-ray streak camera. A low-density CsI photocathode was used to obtain the highest possible x-ray detection sensitivity at these photon energies. The detected signal was then amplified and converted to optical light so that it could be recorded on Royal-X Pan film.

Once recorded, the data were used in a number of ways. Reduction involved scanning the films with a computer-controlled microdensitometer, and then converting the digitized density values to incident intensity. The intensity data, along with the PVA opacity and the x-ray source spectrum, were used to determine the parameters of the imploding shell. The location of the fuel/shell interface at early times can be determined from the transmission minima; an example is shown in Fig. 1-9. Using this method, the trajectory of that interface can be tracked as a function of time.

Examples of measured interface trajectories are shown in Fig. 1-10. The expected variations with incident laser energy and pulse shape were observed. These trajectory measurements have been compared with TRHYD simulations, and reasonably good agreement has been found.

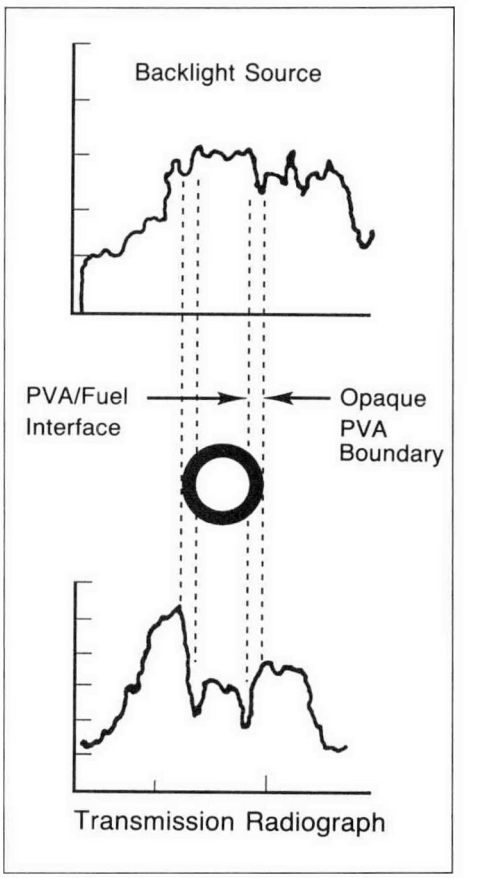

Fig. 1-9. The position of the fuel/pusher interface may be found at early times by comparing the unattenuated x-rays from the backlighter source to those passing through the target, using two pinholes on the streak camera. The minimum transmission will occur at the fuel/pusher interface.

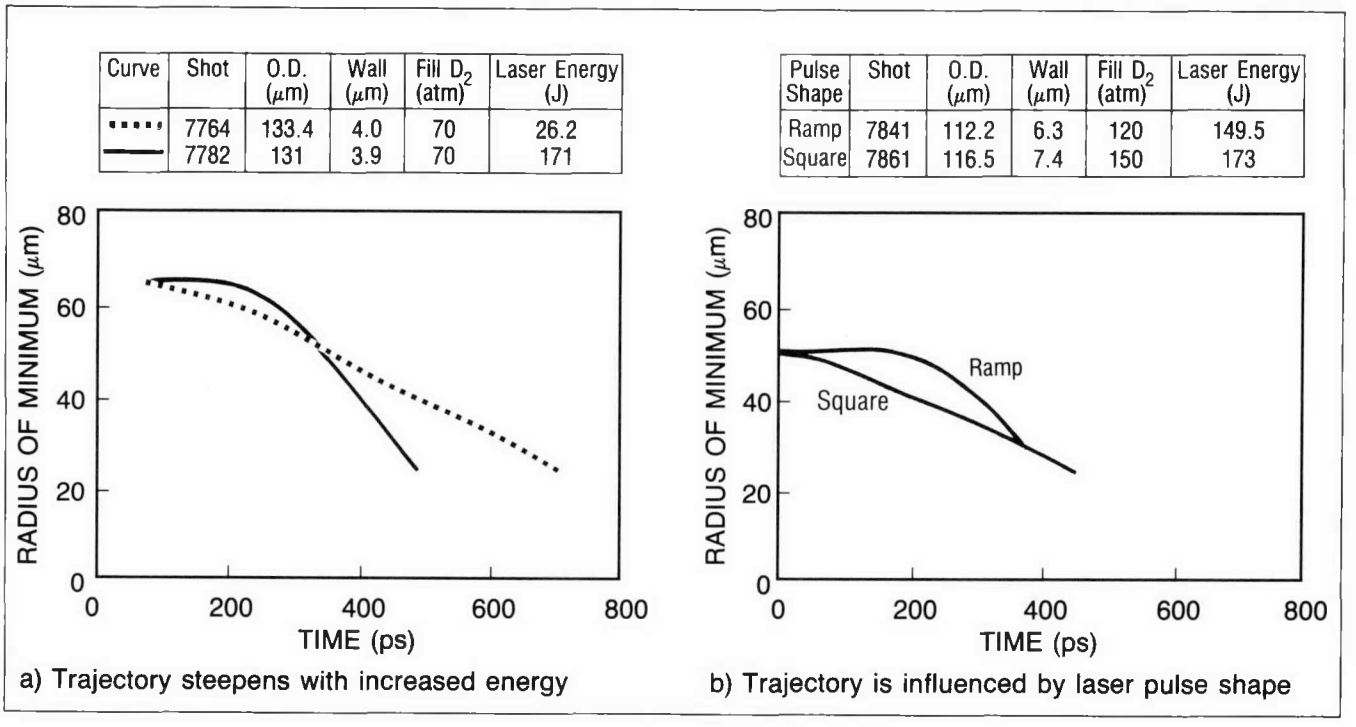

Fig. 1-10. Analysis of the backlighter streak record allows the fuel/pusher interface position to be determined. It can be seen that the implosion proceeds much faster for the higher laser energy (a) and that the trajectory of the interface is affected by the laser pulse shape (b).

Modeling of X-ray Backlighter Data

A simple model for estimating the final compressed target parameters from x-ray radiographs has been developed as a tool to analyze the experiments. The transmission of a specified x-ray spectrum through a model target is calculated to obtain transmission as a function of position at the recording plane. Parameters of the model are adjusted so that the calculated transmission matches the measured values. By repeating this procedure for a series of times, one can deduce the compression history of the target. The model assumes spherical symmetry; any deviations from this will affect the results.

The x-ray source used for the modeling is the measured spectrum shown in Fig. 1-8. This spectrum is corrected for attenuation through various filters in the optical path of the x-rays and for the photocathode sensitivity at the recording plane. The attenuation of the corrected spectrum through a model target is calculated using cold PVA opacities. A geometric correction for the pinhole is then applied to obtain the intensity as a function of position at the film plane.[12]

A crucial element of this model is the assumed form of the density profile of the cold PVA material near the ablation surface. Several different density profiles have been tried; fortunately, the conclusions are not sensitive to the details of the model. The model profile used to compile the results presented here assumes a high-density spike near the fuel/shell interface and an exponential tail outside of the ablation surface. This

model is consistent with profiles from TRHYD simulations. Adjustable parameters in the density model are the inner and outer radii of the cold material and the fraction of the original shell mass remaining. The deduced target parameters are those that provide the best match to the experimental transmission data.

Early in the laser pulse, when the transmission through the target is everywhere nonzero, we have obtained the density profiles from Abel inversion of the transmission data.[13] These experimental plasma densities are consistent with the model profiles, and the mass fractions obtained from the inversions are in reasonable agreement with those inferred from the model at comparable times. However, the Abel inversion technique is not useful later in the implosion because, for many shots, there is no transmission through the target center at peak compression.

Figure 1-11 shows the inferred minimum value of the compressed fuel radius for shots spanning the parameter range of the experiment. The figure shows clearly that ramp pulses produce higher compressions than square pulses. These and other data also indicate that target uniformity and illumination symmetry are important variables. Although previous experiments and simulations have demonstrated an advantage of cryogenic fuel, this is not clearly evident in the data presented here because of the small number of shots with noncryogenic fuel. The highest fuel densities were, however, determined for the cryogenic targets. Typically, we see an improvement in compression of less than a factor of two when using cryogenic fuel configurations.

For most of the shots analyzed, the shell mass fractions F deduced from the model at peak compression are lower than values obtained from TRHYD simulations. This is because using cold opacities to calculate the attenuation through the PVA shell is not a good approximation. However, the features of the calculated transmission traces are more sensitive to the model shell geometry than to the value of F used, so the compressed target dimensions obtained from the model provide reliable quantities for shot-to-shot compression comparisons.

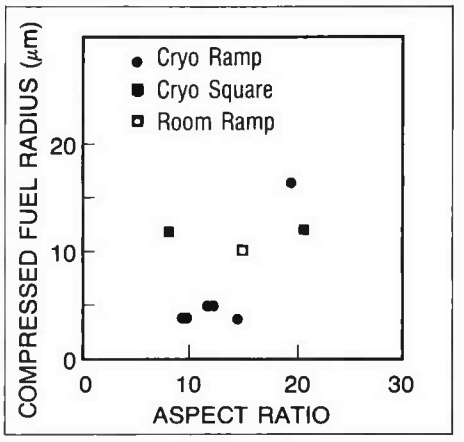

Fig. 1-11. The inferred minimum value of the compressed fuel radius is shown for shots spanning the parameter range of the experiment. It is clear that ramp pulses produce higher compressions than square pulses.

Characterization of the Underdense Plasma

The underdense plasma profiles in these experiments provide the most detailed comparison between theory and experimental data of any of the diagnostic measurements. The measurement of plasma density as a function of time and space allows for a direct comparison to analytic modeling and provides rigid constraint to the numerical simulations. The simulation code has been calibrated to previous data, which provides confidence that target performance can be predicted and optimized.

The underdense plasma density distribution was measured using holographic interferometry.[14] Up to four holographic interferograms were obtained on individual target shots. The time between frames was 67 ps early in the series, but was increased to 125 ps for the later target shots. The interferograms and the plasma profiles derived from them were useful in assessing the

laser irradiation symmetry, and the plasma density data were used to constrain hydrocode calculations by requiring the code-generated plasma expansion to match the plasma profiles in space and time. The coronal temperature can be estimated from a generalized isothermal rarefaction model in conjunction with the plasma profiles. Plasma temperatures of about 1 keV are obtained, which is in agreement with hydrocode calculations.

A typical set of reconstructed interferograms from a single shot (shot 7841) is shown in Fig. 1-12 for four different holographic probe times. The circularity of the interference fringes indicates that the plasma distribution is nearly spherically symmetric. If the plasma is spherically symmetric, then the fringes

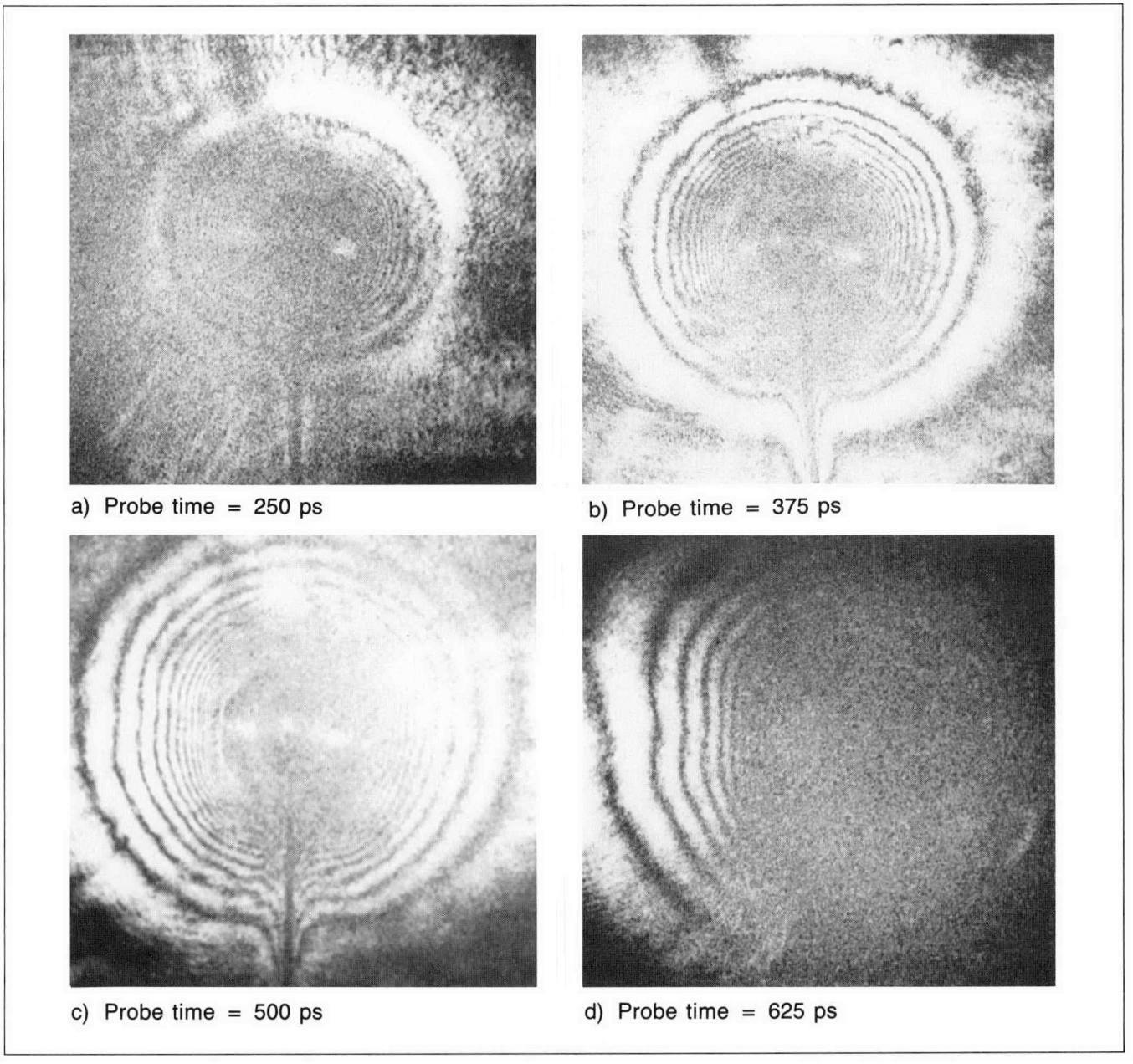

Fig. 1-12. Interferograms of shot 7841 at probe times of 250 ps (a), 375 ps (b), 500 ps (c), and 625 ps (d) show a near-uniform expansion of the corona. This provides a direct estimate of the uniformity of illumination.

represent isodensity contours. The interferogram at 500 ps is shown again in Fig. 1-13a. The fringe data were Abel-inverted along the three radial lines drawn through the fringes to obtain the plasma density distributions along those three lines.[15] All three profiles are plotted together in Fig. 1-13b. The similarity of the curves verifies the assumption that the plasma expansion is spherically symmetric and also allows us to estimate the accuracy of the Abel inversion process. For a given plasma density, these plots show that the uncertainty in the location of that density surface is ± 5 μm. Calculations show that the uncertainty in the illumination uniformity produces density profiles with approximately the variation shown in Fig. 1-13b.

The plasma profiles are most useful in constraining hydrocode calculations. The experimental plasma profile for shot 7841 is plotted along with hydrocode-calculated results in Fig. 1-14. The parameter that most affects the calculated plasma profile is the flux-limit parameter f, which is related to the efficiency with which heat is conducted from the plasma critical surface to the ablation surface. The simulation results agree with the interferometric data if $f = 0.10$, a value that represents essentially classical heat conduction. For $f = 0.03$, heat flow to the ablation surface is reduced, resulting in a lower mass-ablation rate, with the result that the predicted profile shows less mass in the underdense corona. Simple theoretical arguments also show that classical heat flow is expected for these laser intensities and green-light illumination.

Other parameters, such as the absorbed energy fraction and the generation of hot electrons, may also affect the predicted plasma profiles. The expected temperature and fraction of hot electrons generated from resonance absorption is low (about 5 keV) for our experimental conditions. These electrons result from the resonance absorption process. Inclusion of hot electrons in the modeling does not affect the coronal plasma distribution in these experiments. If laser absorption is increased

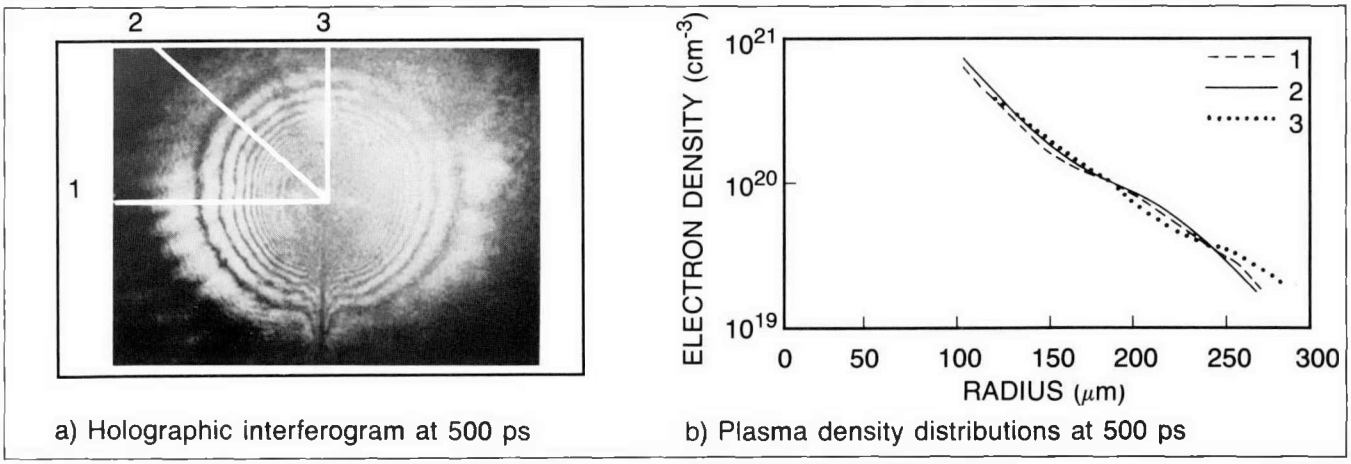

Fig. 1-13. The fringe data of the interferogram of shot 7841 at $t = 500$ ps were Abel-inverted along three radial lines (a) to yield the plasma density distributions along those lines (b). The similarity of the curves verifies the assumption that the plasma expansion is spherically symmetric.

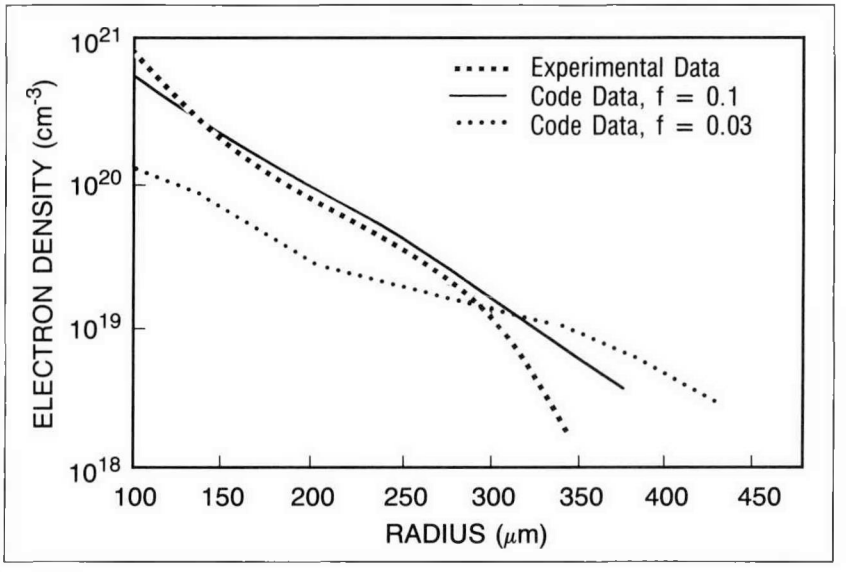

Fig. 1-14. The plasma profile for shot 7841 at $t = 500$ ps is plotted along with simulated (code) profiles for $f = 0.10$ and $f = 0.03$. Simulated curves with $f = 0.10$ agree very closely with the data.

significantly (from 35 to 55%), then the plasma profiles can nearly be matched with $f = 0.03$. However, the code results then disagree with other data, such as the trajectory of the fuel/shell interface. Previous experiments on PVA targets have demonstrated 35 to 40% laser light absorption.

The coronal plasma temperature can be estimated from the plasma profiles and compared to hydrocode predictions. A generalized isothermal rarefaction model to describe the expansion of plasma away from the target surface has recently been developed that is applicable to our conditions.[16] In this model, the plasma density varies as $\exp(-\alpha r/C_s t)$, where α is a geometrical factor, r is the radial coordinate, and the product of the sound speed and expansion time $C_s t$ is the plasma scalelength.

The plasma temperature θ, proportional to C_s^2, can be obtained by plotting the measured plasma scale length as a function of time. In applying this model, we obtain $\theta \sim 0.8$ keV, which compares favorably with the code-predicted temperature of about 1.0 keV. Thus this model seems to allow reasonable estimates of the coronal plasma temperature and thereby determination of variations as a function of different radial directions.

Hydrodynamic Modeling of the Low Preheat Experiments

The fuel/pusher interface trajectories for experiment and simulation were matched for several shots with the legislated absorption and flux limit discussed earlier. Good agreement was attained down to a radius at which the interface could not be experimentally distinguished. This typically occurred for a radius of 20 μm. Simulations were run to peak compression using the flux-limit and absorption values that best match the measured

density and trajectory data. These simulations provide information about the dependence of the final fuel density on laser pulse shape and cryogenic vs. room-temperature fuel. The simulations indicate that the best compression can be attained by using both pulse shaping and cryogenic fuel. The improvement of a ramp pulse over a square pulse, however, is much larger than the improvement attained by using cryogenic fuel compared to room-temperature fuel. As an example, for a target with aspect ratio $R/\Delta R = 9$ and 150 J of energy incident on target, use of a ramp pulse resulted in a 25% reduction in the final compressed radius, whereas cryogenic fuel only gave a 15% improvement. The combination of ramp pulses and cryogenic fuel resulted in a 40% reduction in the final compressed radius compared to a run with room-temperature fuel and a square pulse.

A simple shell model also was used to calculate the interface trajectory. Scaling laws[17] for ablation pressure, ablation density, and ablation velocity were used in a model[18] that assumes a thin shell capsule. The rocket equation was integrated using a fourth-order Runge-Kutta scheme. The computed shell trajectory and experimental interface trajectory are shown for both a ramp-pulse cryogenic shot (Fig. 1-15a) and a square-pulse cryogenic shot (Fig. 1-15b). For the first 400 ps, the measured position of the fuel/shell interface is larger (though within the experimental uncertainty) than the computed trajectory. This was true for both this simple model and the full hydrocode simulation. After the first 400 ps, the slope and position of the interface calculated by the model matched the measured values within experimental uncertainty.

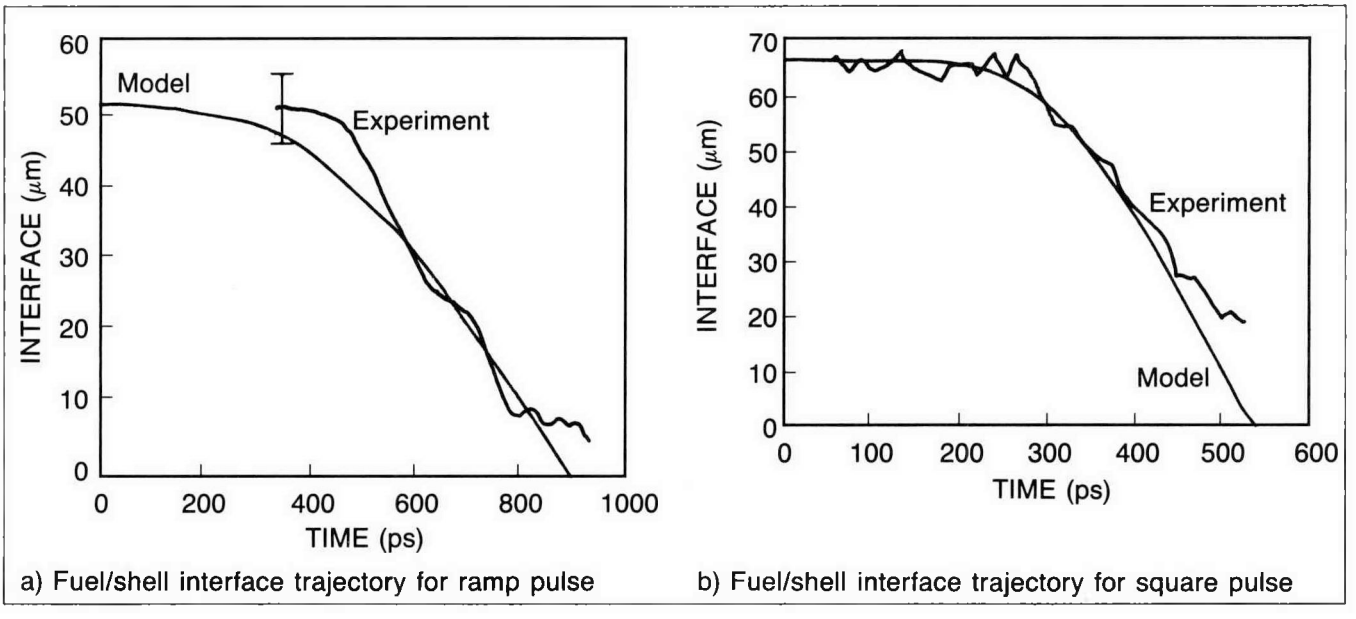

Fig. 1-15. Experimentally determined fuel/shell interface trajectories agree well with those obtained from a simple scaling model for a cryogenic-fuel target for a ramp laser pulse (a) and a square laser pulse (b).

Hydrodynamic Stability and Mix

The success of ICF will depend to a large degree on controlling the fluid stability of the implosion. There are two regions where the Rayleigh Taylor instability may occur. The first region is the accelerating phase, where low-density fluid of the corona pushes on a higher-density fluid so that there are opposing pressure and density gradients. The classical expression for the growth rate is $\gamma = \epsilon(AK\alpha)^{1/2}$, where A is acceleration, K is the wavenumber of the perturbation, α is the Attwood number, and $\epsilon < 1$ is the reduction constant that results from density gradient effects at the ablation surface. This accelerating phase has been examined at length and the number of e-foldings is given as $n \sim \epsilon(2\pi R/\Delta R)^{1/2}$. It has been suggested that ϵ is approximately 1/2 for green laser light, so that shells with initial aspect ratios of $R/\Delta R < 30$ will survive compression to high densities. Thus, large aspect ratio targets are expected to be unstable and the uncertainty is in knowing how large a value can be tolerated. The small aspect ratio targets are more stable but the larger mass will require a larger laser to reach breakeven.

The other region of concern is the deceleration phase, where high-density fluid pushes against the lower-density fluid. This region has not received as much attention, and it is not clear how serious this instability will be. For instance, a small amount of mixing of the pusher with the fuel may be tolerable.

In our experiments, we have observed the possibility that part of the PVA shell is mixed with fuel. Figure 1-16 shows two time-integrated pinhole photographs; a central x-ray emission feature is seen in one case but not the other. These emission features are believed to arise from the collision of portions of the PVA shell in the interior of the target. Deuterium gas does not radiate efficiently and, in normal compressions, acts as a cushion to reduce

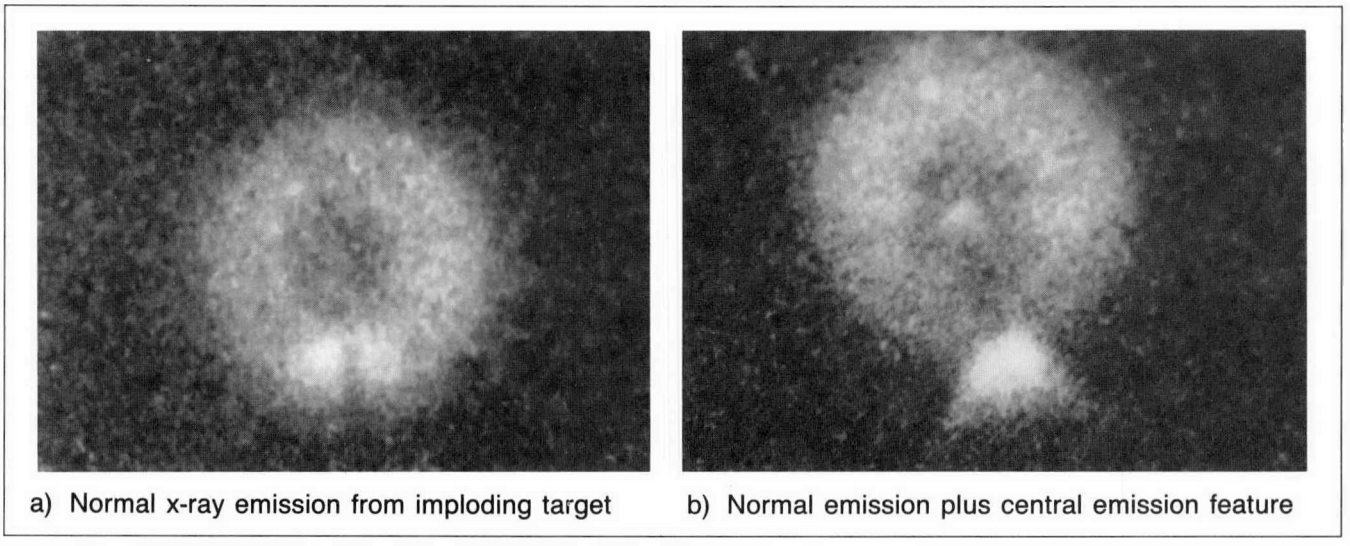

Fig. 1-16. Time-integrated x-ray photographs of self-emission from imploding PVA targets suggest that, in some cases, part of the PVA shell is mixed with the fuel. Normal emission for an imploding target is shown in (a); the presence of a central emission feature along with the normal emission (b) provides evidence of shell breakup.

the velocity of the imploding PVA shell. As a result, the PVA temperature at stagnation is much lower and no x-rays are expected. The central x-ray emission observed in some shots was unexpected. It was found that there was a correlation between the intensity of this x-ray radiation and the aspect ratio of the original PVA shells. This correlation is shown in Fig. 1-17, where the intensity of the central emission relative to the emission from the rest of the target is plotted as a function of the aspect ratio of the target. It was found that, for targets with aspect ratios greater than 15, nearly all target shots with ramp pulses showed this "shell breakup" effect. For targets with aspect ratios less than 15, nearly all target implosions produced normal emissions, as shown in Fig. 1-16a. The breakup was observed with approximately the same frequency in both room-temperature and cryogenic targets. On the other hand, there was a noticeable difference between experiments using ramp pulses and those

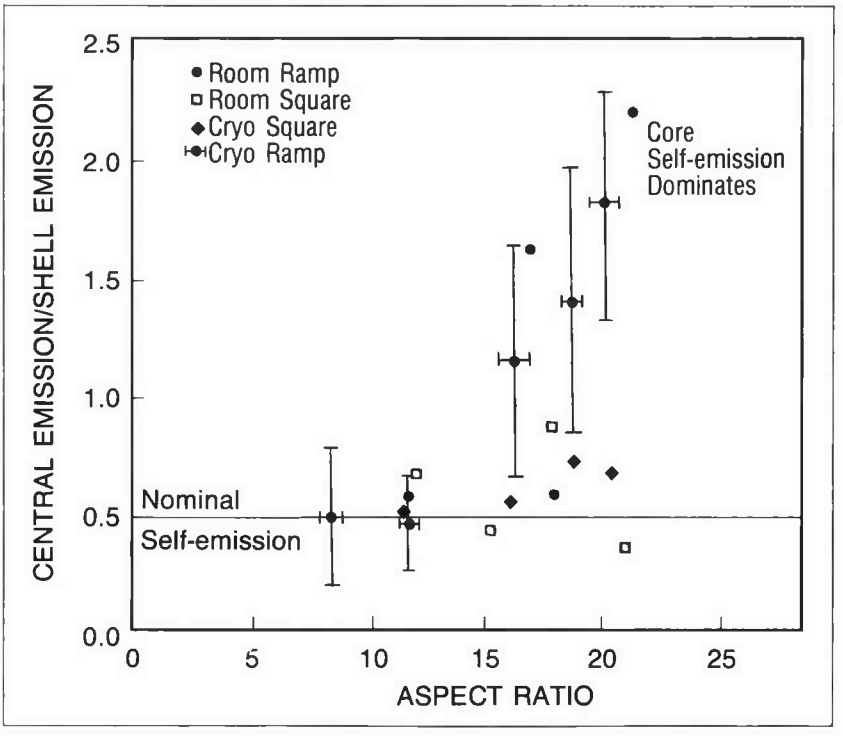

Fig. 1-17. The x-ray emission from the center of the target, relative to the rest of the target, is shown as a function of the initial aspect ratio of the target. The data are derived from experiments using both square and ramp pulses, with both room-temperature and cryogenic targets. No central emission is seen for targets with initial aspect ratios ≤ 15, which suggests that these implosions are stable.

with square pulses. From Fig. 1-6, it is observed that the experiment with a square laser pulse has a shorter implosion time and that it does not reach as high a compression as the experiment using a ramp laser pulse. Both of these effects would probably result in a more hydrodynamically stable implosion for the case of the square laser pulse. This observation of shell breakup provides the first evidence of hydrodynamic instability in spherical implosions.

For additional information, please contact Dr. R. R. Johnson

SECTION 1.2

Counterstreaming Plasmas

In a number of experiments, plasma moving at high velocity collides with other plasma, which may be moving or at rest. A particular example is the plasma produced from the double-foil targets used in x-ray laser experiments[19] and in stimulated Raman scattering experiments.[20] In both of these laser-plasma experiments, the motivation is to create large regions of very uniform, low-density plasma by filling the region between the foils with plasma blown off from each foil.

An issue arises in the modeling of the colliding plasma in these experiments by fluid simulations. The standard treatment of colliding plasmas, for example in TRHYD or LASNEX, implicitly assumes that the mean-free-path for slowing down the plasma streams is small compared to hydrodynamic scalelengths. However, calculation of the ion-ion mean-free-path reveals that, in a number of cases, the stopping length is comparable to or larger than the hydrodynamic scalesize. Other model calculations have been done in which collisions are ignored, and two fluids are followed and are allowed to interpenetrate. Neither calculation provides a complete picture, since, as the density increases in the region where the streams interpenetrate, the mean-free-path can encompass both limits.

Below, we improve the previous two-fluid calculations of interpenetrating plasmas by including the effects of ion-ion collisions in the momentum and energy equations. We find for thin, low-atomic-number (low-Z) foils that the interaction is very nearly collisionless insofar as the gross behavior of the density and flow velocity are concerned. However, significant ion heating occurs that can be deleterious in the case of x-ray laser applications. For thick, high-Z foils, we find that the interaction, which is initially collisionless, evolves eventually to a strongly collisional one for which the standard single-fluid picture used in the simulation codes is adequate. However, significant differences occur in the intermediate times that have implications for laser absorption and x-ray production.

Before presenting the results of the collisional interaction of interpenetrating plasma, we study two plasma instabilities that have the potential to slow the streams, even if weak Coulomb collisions do not. We find that the importance of these instabilities cannot be dismissed entirely because they do result in noticeable ion heating and may provide an effective mean-free-path comparable to the ion-ion collisional mean-free-path. However, only long-wavelength modes ($\lesssim 10\ c/\omega_{pi}$, where c is the speed of light and ω_{pi} is the ion plasma frequency) are not stabilized by moderate ion heating (a natural result of the instability itself); these modes may be weakened further if the effects of inhomogeneity or collisions are included.

Instabilities of Counterstreaming Plasma

At the midpoint between the two foils, two equidensity streams of ions with equal and opposite flow velocities $\pm U$ interpenetrate. The electrons form a hot neutralizing background and the electron thermal velocity $v_e = (T_e/m_e)^{1/2}$, where m_e is the electron mass, greatly exceeds both the ion flow velocity U and the ion thermal velocity $v_i = (T_i/m_i)^{1/2}$. Two instabilities can be supported by such a distribution of particles: an electrostatic ion two-stream instability and an electromagnetic Weibel instability. We limit our discussion to spatially uniform plasma with supersonic flow $U > C_s$, where the isothermal sound speed $C_s = (Z\,T_e/m_i)^{1/2}$, and Z is the charge state of the ion.

Electrostatic Two-Stream Instability. The electrostatic two-stream instability has been studied extensively both with and without a uniform external magnetic field. Without a magnetic field, purely growing sound waves are driven unstable, provided the wavevector $\vec{k}$ satisfies $|\vec{k}\cdot\vec{U}| < kC_s$ and the ion temperature $T_i < T_{ic} = 0.27\,Z\,T_e$. It is easy to understand why purely growing modes are favored because a mode with a real frequency has a phase velocity closer to the velocity of one of the streams, and its behavior is thus dominated by that velocity distribution. Moreover, the dominant contribution to the imaginary part of the dispersion relation must damp a mode with a real frequency (since, without the other stream, the mode is certainly stable).

When the streams interpenetrate, the ion temperature of each stream is very small due to expansion cooling, and the conditions for instability are certainly met in a collisionless plasma. Initially, energy is acquired by the unstable modes and is lost by the kinetic energy of the flow at the maximum rate $\gamma \sim \omega_{pi}$. However, it has been shown by formulating a quasi-linear theory and by particle-in-cell simulations[21] that the wave energy is transferred to ion thermal energy until the plasma satisfies the marginal stability condition $T_i = T_{ic} = 0.27\,Z\,T_e$. Because we are interested in supersonic flow, the available ion kinetic energy greatly exceeds the amount of energy transferred to the waves and thus to the ion thermal energy; viz.,

$$\frac{1}{2}\,m_i U^2 = \frac{1}{2}\,M^2 Z T_e \gg T_{ic} \sim Z\,\frac{T_e}{4}\ , \qquad (1)$$

where, by assumption, the Mach number $M \gg 1$. We conclude that this instability is unlikely to impede the interpenetration.

Electromagnetic Ion Weibel Instability. The transversely polarized electromagnetic ion Weibel instability[20] is driven by the anisotropic nature of the total ion velocity distribution for interpenetrating plasma streams: The total energy in the direction of the flow velocity vector for each stream is

$$\frac{n_i}{2}\,(m_i U^2 + T_{xi})\ ,$$

where n_i is the ion density, whereas the energy in each orthogonal direction is $n_i T_{yi}/2$. Here, the purely growing Weibel mode

propagates in the y-z plane with its electric field vector in the direction of the flow.

The ion dynamics of this instability are easy to follow in planar geometry. Consider the case where the perturbed magnetic field points in the z-direction and the wavevector is in the y-direction. The magnetic force deflects the oppositely propagating ion beams in opposite directions along the y-axis. There is therefore a charge bunching or beam pinching for each beam but no net charge density perturbation and thus no electrostatic field. There is, however, a net current perturbation since the opposite signs of the density perturbation are multiplied by the opposite signs of the stream velocities. As the ion temperature increases, the ion pressure will oppose bunching and reduce the strength of the instability by moving to eliminate the electric field. In the cold plasma limit $|\omega| \gg kv_e$, the electrons are very effective in preventing the development of an electric field. However, the limit $|\omega| \ll kv_e$ is the case of interest, and a kinetic treatment is necessary. If $|\omega/kv_e| \to 0$, the electrons make no contribution to the current and, if $T_i = 0$, the growth rate is

$$\gamma = \omega_{pi} \frac{U}{c} \left(1 + \frac{\omega_{pi}^2}{c^3 k^2}\right)^{-1/2} . \tag{2}$$

A complete description of this mode requires a kinetic description for the ions and electrons. The Vlasov equation for the component of the distribution function $\delta f_{k\alpha}$ that responds to the Weibel mode electric and magnetic field perturbation is

$$(-i\omega + i\vec{k}\cdot\vec{v})\,\delta f_{k\alpha} = -\frac{eZ_\alpha}{m_\alpha}\left(\vec{E}_k + \frac{\vec{v}}{c} \times \vec{B}_k\right) \cdot \frac{\partial}{\partial \vec{v}} f_{0\alpha} \tag{3}$$

where the electric field vector $\vec{E}_k$ points in the direction of the flow, and the magnetic field vector $\vec{B}_k$ and wavevector $\vec{k}$ are in the plane orthogonal to the flow velocity vector. The set of equations is completed by Ampere's and Faraday's laws,

$$i\vec{k} \times \vec{B}_k = -\frac{i\omega}{c} \vec{E}_k + \frac{4\pi}{c} \bar{Z}_\alpha e_\alpha \int d^3v\, \vec{v}\, \delta f_{k\alpha} \tag{4}$$

and

$$i\vec{k} \times \vec{E}_x = \frac{i\omega}{c} \vec{B}_k , \tag{5}$$

where $e_\alpha = Z_\alpha e$ for ions and $e_\alpha = -e$ for electrons. Combining these equations, we arrive at the dispersion equation,

$$0 = k^2 \vec{E}_k + \sum_\alpha \frac{4\pi i\omega Z_\alpha^2 e^2}{m_\alpha c^2} \int d^3v \frac{\vec{v}}{(-i\omega + i\vec{k}\cdot\vec{v})} \times \left[\vec{E}_k\left(1 - \frac{\vec{k}\cdot\vec{v}}{\omega}\right) + \frac{k}{\omega}\, \vec{v}\cdot\vec{E}\right] \cdot \frac{\partial}{\partial v} f_{0\alpha} , \tag{6}$$

provided we neglect the small displacement-current contribution. For an isotropic distribution, the contributions from the second and third terms in square brackets (i.e., those arising from the magnetic field forces) cancel. The ion distribution is taken to be the sum of Maxwell-Boltzmann distributions centered at velocities $\pm U$; i.e., $f_i = f_B(\vec{v} - \vec{u}) + f_B(\vec{v} + \vec{u})$, where

$$f_B(v) = n_i\left(\frac{m_i}{2\pi T_i}\right)^{3/2} \exp\left(\frac{-m_i v^2}{2T_i}\right) .$$

The electrons form a hot neutralizing background with the isotropic Maxwell-Boltzmann distribution,

$$f_e(v) = n_e\left(\frac{m_e}{2\pi T_e}\right)^{3/2} \exp\left(\frac{-m_e v^2}{2T_e}\right) ,$$

such that $n_e = 2Zn_i$. Using these distribution functions in the dispersion equation [Eq.(6)], we obtain the dispersion relation given by

$$c^2k^2 + i\,\frac{\sqrt{\pi}}{2}\,\frac{\omega}{kv_e}\,\omega_{pe}^2 + \omega_{pi}^2\left\{1 - \frac{T_{xi} + m_i U^2}{T_{yi}}\,[1 + \xi_i Z(\xi_i)]\right\} = 0 , \tag{7}$$

where $\xi_i = \omega/\sqrt{2}\,kv_i$ and $Z(\xi)$ is the plasma dispersion function. The second term in Eq. (7) is electron damping and is important for long wavelengths. At short wavelengths, where electron damping is small, and further for cold beams,

$$1 + \xi_i Z(\xi_i) \cong -k^2 v_i^2/\omega^2 ,$$

and the growth rate is given by Eq. (2). The maximum rate $\gamma_{max} = \omega_{pi}\,U/C$ is obtained for $kc \gg \omega_{pi}$. Ion thermal terms set a maximum value of k for instability that approaches zero as T_i increases, as shown in Fig. 1-18. Because the electrostatic instability growth rate is much larger than the present one (ω_{pi} versus $\omega_{pi}\,U/C$), we shall assume that the ions have been heated by the electrostatic mode to roughly its marginal stability temperature ($ZT_e/4$). At this temperature, the Weibel growth rate is about $1/10\ \gamma_{max}$, and unstable wavenumbers are less than $6\ \omega_{pi}/c$ or wavelengths $\lambda > 7\ (A/Z)^{1/2}\ (10^{21}/n_e)^{1/2}\ \mu$m, where A is the atomic mass. The dependence of the peak growth rate on the ion temperature is shown in Fig. 1-19 for $U/C_s = 2$. As a practical example, the peak growth rate at $T_i = ZT_e/4$, $n_e = 10^{21}$, and $Z/A = 1/4$ is $\sim 3 \times 10^{10}$ sec^{-1}, and the effective mean-free-path $\lambda_{eff} = U/\gamma = 10\ c/\omega_{pi} \simeq 150\ \mu$m.

For the range of velocities of interest, the ion-ion collisional mean-free-path for one stream slowing down with respect to the other is estimated, by using the formulae in the next section, to be comparable to this effective mean-free-path for the parameters used above. Thus, although we cannot rule out a role for

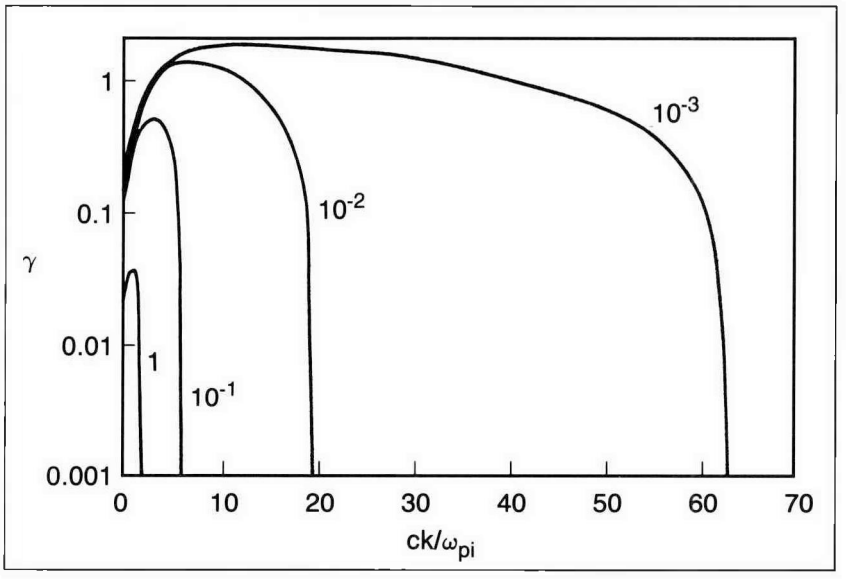

Fig. 1-18. The ion Weibel instability growth rate γ for counterstreaming flow (in units of $\omega_{pi} C_s/c$) is shown as a function of ck/ω_{pi}. The curves are labeled by the value of T_i/ZT_e ($\equiv\tau$).

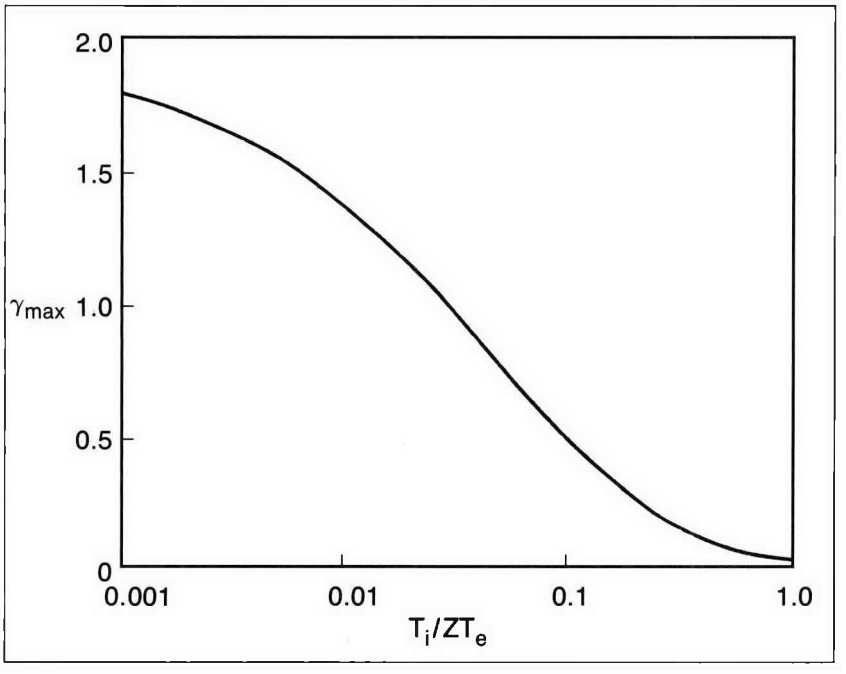

Fig. 1-19. The ion Weibel growth rate (maximized as a function of k and in units of $\omega_{pi} C_s/c$) is shown as a function of T_i/ZT_e.

the Weibel mode in the slowing down of interpenetrating streams, we conclude on the basis of our estimates that neglecting its effect will not produce a serious error in the results we now obtain with only ion-ion Coulomb collisions.

Effect of Ion-Ion Collisions on Interpenetrating Plasma Streams

We derive a set of equations that describe two ion fluids in a background of neutralizing electrons. Each ion fluid will be distinguished by its flow velocity U_α and temperature $T_{i\alpha}$. Interaction between the fluids is taken to be ion-ion collisions; in the regime of interest, these collisions dominate ion-electron collisions. We start with the Fokker Planck equation, written in the frame moving with an ion fluid element velocity U_α,

$$\frac{df_\alpha}{dt} + v_j \frac{\partial}{\partial x_j} f_\alpha - \left(\frac{Z_\alpha e}{m_\alpha} \frac{\partial}{\partial x_j} \phi + \frac{d}{dt} U_{\alpha j}\right) \frac{\partial}{\partial v_j} f_\alpha$$

$$- \left(\frac{\partial}{\partial x_k} U_{\alpha j}\right) v_k \frac{\partial}{\partial v_j} f\alpha = C_{ii}(f_\alpha, f_\alpha) + C_{ii}(f_\alpha, f_\beta) \ . \tag{8}$$

We shall obtain fluid equations for each plasma stream by taking the usual velocity moments of Eq. (8). First, we estimate the size of the two terms on the right side of Eq. (8), the self-collision term and counterstreaming collision term,

$$C_{ii}(f_\alpha, f_\alpha) = \frac{v}{\lambda_{\alpha\alpha}} \quad \text{and} \quad C_{ii}(f_\alpha, f_\beta) = |\vec{U}_\alpha - \vec{U}_\beta| \lambda_{\alpha\beta}^{-1} \ ,$$

respectively. If we estimate

$$v = \left(\frac{T_i}{m_i}\right)^{1/2} \quad \text{and} \quad |\vec{U}_\alpha - \vec{U}_\beta| = 2U_\alpha \sim 2MC_s \ ,$$

then we obtain $\lambda_{\alpha\beta}/\lambda_{\alpha\alpha} = 16M^4(ZT_e/T_i)^2 \gg 1$. The self-collision mean-free-path is typically small compared with hydrodynamical length,

$$\lambda_{\alpha\alpha} = \frac{T_i^2}{4\pi N_i Z^4 e^4 \ln \Lambda} \cong 1.5 \times 10^{-6} \text{cm} \ , \tag{9}$$

for typical plasma parameters $T_i = 1$ keV, $ZN_i = 10^{21}$, $\ln \Lambda = 10$, and $Z = 20$, whereas the interpenetrating fluid mean-free-path is much larger,

$$\lambda_{\alpha\beta} = 10^5 \lambda_{\alpha\alpha} = 0.15 \text{ cm} \ , \tag{10}$$

if $T_e = 1$ keV and $M = 2$. Because λ_{ii} is much smaller than typical gradient scalelengths ($\sim C_s t$), we assume that f_α is a local Maxwell-Boltzmann distribution [thus, $C_{ii}(f_\alpha, f_\alpha) = 0$] in evaluating the momentum and heat exchange from the first and second moments of the right side of Eq. (8). This collision term makes no contribution to the zeroth moment, the continuity equation. The moment equations are

$$\frac{\partial}{\partial t} n_\alpha + \frac{1}{r^{n-1}} \frac{\partial}{\partial r} (r^{n-1} n_\alpha U_\alpha) = 0 \ , \tag{11}$$

$$n_\alpha m_\alpha \frac{d}{dt} U_\alpha = -Z_\alpha e n_\alpha \frac{\partial}{\partial r} \phi - \frac{\partial}{\partial r} P_\alpha + R_{\alpha\beta} \ , \tag{12}$$

and

$$\frac{3}{2} n_\alpha \frac{d}{dt} T_\alpha + P_\alpha \frac{1}{r^{n-1}} \frac{\partial}{\partial r} (r^{n-1} U_\alpha) = Q_{\alpha\beta} \ , \tag{13}$$

where $d/dt \equiv \partial/\partial t + U\,\partial/\partial r$ and $P_\alpha = n_\alpha T_\alpha$. Because of the small value of $\lambda_{\alpha\alpha}$, the pressure is a scalar; the heat flow is small,

$$q_\alpha \approx n \lambda_{\alpha\alpha} \frac{\partial T}{\partial r} \ ,$$

and is neglected. This latter assumption allows a great deal of simplification in the numerical solution because no second-order derivatives appear. The terms $R_{\alpha\beta}$ and $Q_{\alpha\beta}$ were evaluated in the limit

$$m_i |\vec{U}_\alpha - \vec{U}_\beta|^2 \gg T_{i\alpha}, T_{i\beta}$$

and corrected to be valid in the opposite limit of a single fluid. The final expressions are

$$R_{\alpha\beta} = -\nu_{\alpha\beta} n_\alpha m_\alpha (U_\alpha - U_\beta) \tag{14}$$

and

$$Q_{\alpha\beta} = -\frac{1}{2} (U_\alpha - U_\beta) R_{\alpha\beta} - \nu_{\alpha\beta} n_\alpha (T_\alpha - T_\beta) \ , \tag{15}$$

where

$$\nu_{\alpha\beta} = \frac{4\pi n_\beta Z_\alpha^2 Z_\beta^2 e^4 \ln \Lambda_{\alpha\beta}}{m_i \left(|U_\alpha - U_\beta|^2 + \dfrac{T_{i\alpha} + T_{i\beta}}{m_i} \right)^{3/2}} \ . \tag{16}$$

The equations obviously conserve momentum ($R_{\alpha\beta} = -R_{\alpha\beta}$) and total ion energy:

$$\sum_\alpha \left[n_\alpha \frac{d}{dt} \left(\frac{1}{2} m_i U_\alpha^2 + \frac{3}{2} T_\alpha \right) \right] = 0 \ . \tag{17}$$

The potential ϕ is obtained self-consistently from Poisson's equations,

$$\frac{1}{r^{n-1}} \frac{d}{dr} \left(r^{n-1} \frac{d\phi}{dr} \right) = -4\pi e \left(n_e - \sum_\alpha Z_\alpha n_\alpha \right) \ , \tag{18}$$

and the steady-state electron fluid equations. If we neglect electron inertia ($m_e \to 4$) and assume rapid electron heat conduction ($\partial T_e/\partial_r = 0$), the electrons have a Boltzmann distribution,

$$n_e = n_0 \exp\left(\frac{-e\phi(x)}{T_e}\right) . \tag{19}$$

For convenience in modeling thick foils (i.e., the laser burns through after the plasma density between the foils has reached the density of interest), we allow two groups of electrons, at different but uniform temperature, each of which obeys Eq. (19).

Before we describe the behavior of interpenetrating plasma streams, we review solutions of Eqs. (11) through (13) for single foils. These solutions provide a basis for understanding the plasma formed by interpenetrating streams when collisions and plasma instabilities are weak.

For thick foils, such that the laser does not burn through the initial solid in the time interval of interest and such that $C_s t$ is less than the laser spot diameter, the hot underdense plasma density $n(x)$ and fluid velocity $U(x)$ are well represented by a planar, isothermal, exponential, self-similar rarefaction given by

$$n(x) = n_0 \exp\left[-\frac{(x - x_0)}{C_s t}\right] \tag{20}$$

and

$$U(x) = C_s\left[1 + \left(\frac{x - x_0}{C_s t}\right)\right] , \tag{21}$$

for $x > x_0$ where n_0 is an arbitrary reference value. For thin foils such that the laser does burn through, the plasma density takes a Gaussian self-similar form[22] given by

$$n = n_0 \exp\left[-\frac{(x - x_0)^2}{2L^2}(t)\right] , \tag{22}$$

with an associated velocity profile given by

$$u = \frac{(x - x_0)\dot{L}}{L} , \tag{23}$$

where $\dot{L} = \partial L/\partial t$, and

$$L(t) = \sqrt{2}C_s t\left[\ln\left(\frac{\sqrt{2}C_s t}{L_0}\right)\right]^{1/2} . \tag{24}$$

In Eqs. (22) through (24), x_0 is the midpoint of the foil, L_0 is a length of order of the initial foil thickness, and n_0 is an arbitrary reference density that, together with L_0, can be chosen to conserve mass.

Properties of Interpenetrating Solutions

At times before burnthrough, we use Eqs. (20) and (21) as a model of the underdense plasma from each foil, with the origin at $x = 0$ and a foil at $x_0 = \pm x_w$. For weakly collisional plasma, the density at $x = 0$ is nearly the simple sum of each component. The velocity of stream α, U_α, and total density at $x = 0$ are related by

$$|U(x=0)| = C_s\{1 + \ln[2n_0/n(x=0)]\} \ . \tag{25}$$

As a consequence, the mean-free-path of the interaction cannot be enhanced or weakened by varying the distance between the foils (only the time at which the interaction becomes collisional and the total hydrodynamic scalelength at that time changes). Substituting Eqs. (20) and (21) in Eqs. (14) through (16), we note that $R_{\alpha\beta}$ and $Q_{\alpha\beta}$ are independent of space and $R_{\alpha\beta}$ is given by

$$R_{\alpha\beta} = \frac{Zn_e^2(x=0)e^4 \ln \Lambda_{\alpha\beta}}{8m_i T_e\left\{1 + \ln\left[2n_0 Z/n_e(x=0)\right]\right\}^2} \ , \tag{26}$$

if $T_i \ll ZT_e$ as expected. Thus, when a low-density stream interacts with a high-density stream, the velocity and temperature of the low-density stream will change more rapidly. Since the head of the stream has the lowest density, the stream will not break up (as it might if the interaction were collisional at $x = 0$ and collisionless at either side) and the solution is well behaved. From Eq. (26), we note that "collisionality" increases for higher $Z \ln \Lambda_{\alpha\beta}/m_i$ and lower electron temperature. Obviously, the second parameter is easier to vary in an experiment.

Numerical Solution of Interpenetrating Plasmas

The hydrodynamic equations [Eqs. (11) through (13)] are solved for each stream in a standard conservative Lagrangian framework. The terms $R_{\alpha\beta}$ and $Q_{\alpha\beta}$ (not standard) are treated explicitly, and thus are not time-centered. This can be a source of error when $R_{\alpha\beta}$ is not small, so a small time step is required in that case. Conservation of energy [Eq. (17)] is used rather than the explicit form of $Q_{\alpha\beta}$ to evaluate the first term in Eq. (15). The charge state and $\ln \Lambda_{\alpha\beta}$ used in Eq. (16) are determined in a simple manner that is similar in spirit to the work reported by Albritton.[22] In this model, we have Z_* free electrons forming a shell at r_0, and $Z_n - Z_*$ bound electrons forming a shell at the atomic radius, r_a. The nuclear charge is Z_n, and r_0 is the ion sphere radius defined by

$$\frac{4\pi r_0^3 n}{3} = 1 \ .$$

If two ions collide, their repulsive Coulomb force is proportional to Z_*^2 if they are a distance $r > r_a$ apart; however, if $r < r_a$, we assume the repulsive force is proportional to Z_n^2. Because

the relative velocity for counterstreaming plasma is quite large, the classical distance of closest approach can be smaller than the atomic radius. The distance of closest approach is

$$b_{\min} = \frac{m_i Z^2 e^2}{2\epsilon i} \ ,$$

with $Z = Z_n$ if $b_{\min} < r_a$ and $Z = Z_*$ if $b_{\min} > r_a$, where the ion kinetic energy is

$$\epsilon_i = \frac{m_i}{2} | U_\alpha - U_\beta |^2 \gg Z T_e \ .$$

If $b_{\min} < r_a$, then the scattering strength will be greater in fact than the expression given in Eq. (16) with $Z = Z_*$. Over most of the orbit, the repulsion will be proportional to Z_*^2; however, over the last part the repulsion is proportional to Z_n^2. The outer limit to the calculation of scattering strength is the effective screening distance, λ_s. For hot, low density plasma, λ_s is the ion Debye length, but often r_0 is larger (there are fewer than one ion per Debye volume and screening is neutral cell), so that we take $\lambda_s = \max(\lambda_i, r_0)$, where λ_i is the Debye length of the majority species. Our expression for the scattering strength is given by

$$Z_\alpha^2 Z_\beta^2 \ln \Lambda_{\alpha\beta} = Z_*^4 \ln\left(\frac{\lambda_s}{r_a}\right) + Z_n^4 \ln\left(\frac{r_a}{b_{\min}}\right) \text{ if } b_{\min} = (Z_n) \ ; \quad (27)$$

otherwise,

$$= Z_*^4 \ln\left(\frac{\lambda_s}{b_{\min}}\right) \ . \quad (28)$$

This choice of Eq. (27) rather than Eq. (28) when $b_{\min} < r_a$ increases the scattering rate by a factor of 2 to 3 in simulations of gold foils at an electron temperature of 2 keV. The behavior of the solutions of Eqs. (11) through (19) will be compared to a standard solution valid in the limit of small mean-free-path. In this limit, the fluids are brought to a stop in a short distance after meeting. This model in a Lagrangian formulation sets the velocity of the zone boundary where the fluids meet to zero and converts the lost kinetic energy to ion internal energy. Such a solution is equivalent to the solution that results from treating the collision of plasma streams with a single fluid.

An example of the single-fluid solution to colliding plasma streams is shown in Fig. 1-20. Initially, two 15-μm-thick solid foils, of uniform ion density, are located 0.16 cm apart. The atomic weight $A = 200$, the charge state $Z = 50$, and the nuclear charge $Z_n = 79$. Two groups of isothermal electrons are used: a "hot" group with temperature $T_e = 2.5$ keV and initially uniform density $n_e = 10^{22}$ cm^{-3} and a "cold" group with temperature $T_{ew} = 100$ eV and initially uniform density $n_{ew} = 2.5 \times 10^{24}$ cm^{-3}. Before the collision, the expansion from each foil

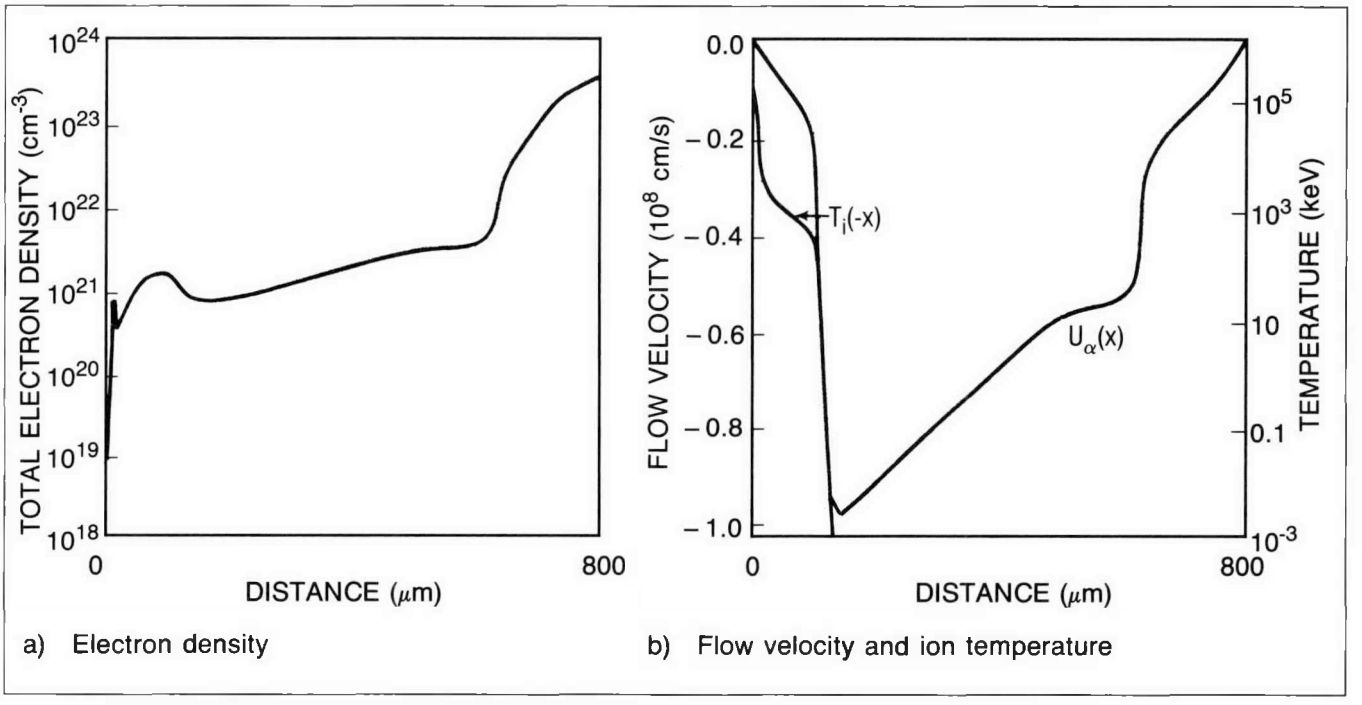

Fig. 1-20. The results of a single-fluid simulation of counterstreaming plasma originating from foils at ±800 μm are shown at 950 ps. Initial conditions and other parameters are given in the text. The electron density is shown in (a); the ion temperature (right scale) and flow velocity (left scale) are shown in (b). Because of symmetry about $x = 0$, only values for $0 < x < 800$ μm are shown.

driven by the hot electrons agrees with Eqs. (20) and (21), an isothermal planar rarefaction. After colliding, a shock is set up across which the velocity decreases and the ion temperature and electron (ion) density increase. Because of the high velocity of the flow, the ion temperature jumps to large values (≥1 MeV). We note that, in the unshocked low-density region that is dominantly populated by 2.5 keV electrons ($150 < x < 600$), the flow velocity depends linearly on x and the density exponentially on x, in agreement with the planar rarefaction model of Eqs. (20) and (21). In Fig. 1-21, the results of a two-fluid simulation with the same initial conditions as in Fig. 1-20 are shown for the time at which the average density near the midpoint ($x = 0$) is the same as in Fig. 1-20. The total density monotonically increases away from a minimum at $x = 0$ (the midpoint between the foils), in contrast to the result in Fig. 1-20. The flow velocity increases in magnitude with distance from the foil until the electron pressure changes sign at $x = 0$. Thereafter, the friction is the dominant force and the velocity decreases in magnitude until it merges with the counterstreaming plasma flow. The ion temperature of each stream increases and reaches values close to 1 MeV near the head of the stream. We note, however, that the zone-averaged ion temperature is much less than 1 MeV because the higher-density plasma has a much lower ion temperature. Also, the ion temperature at $x = 0$ is several hundred kilovolts in Fig. 1-21 rather than several megavolts as in Fig. 1-20. Near the head of the stream, the mean-free-path is very small (~1 μm).

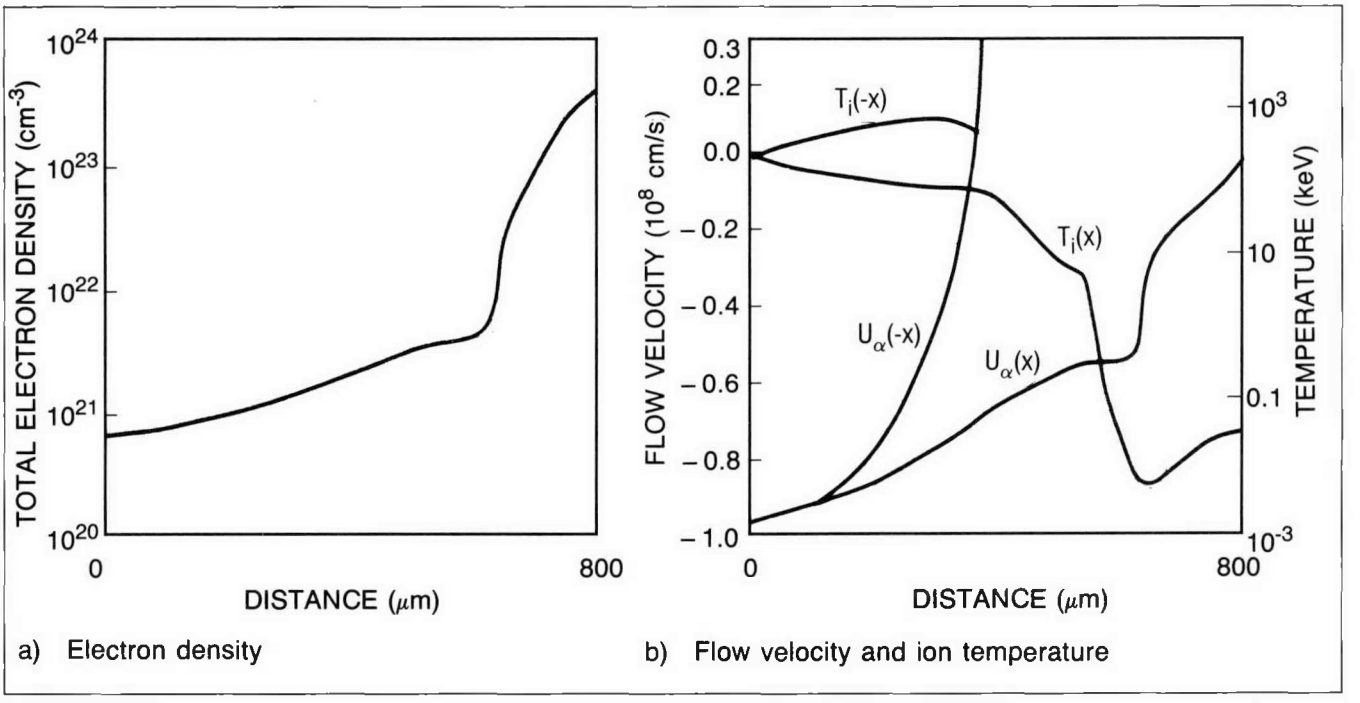

Fig. 1-21. The two-fluid simulation results are shown for the same parameters and initial conditions as in Fig. 1-20. The electron density is shown in (a); the flow velocities $U_\alpha(x)$ and $U_\alpha(-x)$ and ion temperatures $T_i(x)$ and $T_i(-x)$ are shown in (b) for $0 < x < 800$ μm.

Thus, in a few micrometers (about the resolution of the numerical grid) beyond the last velocity and temperature value plotted, the velocity and temperature of the lower-density stream will merge with the incoming stream. A short time later ($t = 1.1$ ns), the electron density at $x = 0$ is 2×10^{21} cm^{-3}, the mean-free-path there is 10 μm, and the plasma streams stagnate. The plasma density, velocity, and temperature distribution near the midpoint evolve from then on in accordance with the single-fluid picture.

As mentioned previously, the electron temperature is the parameter with the most influence on collision strength. Increasing the electron temperature to 5 keV changes the time at which the density at $x = 0$ reaches the value in Fig. 1-21 from 870 to 630 ps. At this time, the low-density stream stops much closer to the foil, deposits significant energy there, and causes a mild modification to the density profile. Even for this weakly collisional case, the ion temperature at $x = 0$ reaches several hundred kilovolts.

Reducing the electron temperature to 500 eV increases the time to achieve the same density at $x = 0$ to 1.5 ns, at which time the simulation resembles the single-fluid picture shown in Fig. 1-20.

Simulations also were done of thin selenium double-foils ($Z = 26$, $Z_n = 34$, $A = 79$) with a single electron group at $T_e = 2.0$ keV. The foils, initially 0.2 μm thick, are separated by 200 μm. Each foil quickly rarefies and approaches the solution defined by Eqs. (22) through (24). The mean-free-path remained large

(~1 mm) during the simulation that was run until $t = 100$ ps, when electron density is uniform between the foils at a value of $\sim 10^{21}$ cm^{-3}. Nonetheless, the ion temperature of each stream increases to ~30 keV at $x = 0$, which may result in significant Doppler broadening of the atomic lines. That broadening may be deleterious for x-ray laser gain.

Summary

A two-fluid model has been constructed and used to study the collisional interaction between counterstreaming ions. For thick foils, the plasma streams begin to slow down only when they encounter the high-density plasma of the unrarified foil. As the density builds up on-axis (the midpoint between the foils), the streams slow significantly and heat up, eventually merging when their velocities and temperatures equilibrate. For "hot" plasmas ($T_e > 2$ keV), the kinetic energy of the streams is shared with a large fraction of the underdense plasma and, thus, average ion temperatures are much less than the temperature (2 MeV) that a single-fluid model would predict. At lower electron temperatures ($T_e \leq 500$ eV), the single-fluid picture is valid because the mean-free-path for interpenetration is less than a hydrodynamic scale-length ($\sim C_s t$). These simulations neglect the influence of plasma velocity-space instabilities in which collective modes grow by tapping the free energy in the counterstreaming flow. Two such unstable modes were studied and shown to be weakened or stabilized once the streams are heated to the point that $T_i/ZT_e \geq 0.27$. Such heating can result from the collisional processes just discussed and from the natural evolution of the instability itself.

For additional information, please contact Dr. R. L. Berger

SECTION 1.3

SATIN: A Fluid Code for the Study of Two-Plasmon Decay and Stimulated Raman Scattering

The saturation and nonlinear coupling of plasma instabilities is a topic of much interest in inertial confinement fusion (ICF). Saturation of instabilities has been observed experimentally in plasmas illuminated with long-wavelength lasers (10.6 μm; Refs. 23 and 24), and studied analytically for a small number of decay modes.[25] The most complete understanding of saturation phenomena to date has come from particle simulations.[26,27] Some of the nonlinear processes (e.g., profile modification and secondary wave coupling) believed to be important to saturation are not, however, kinetic in nature and hence can be addressed in a fluid simulation. A fluid code approach, in addition to reducing computational requirements, could provide a testbed for isolating different mechanisms for study. We have developed such a fluid code (SATIN) to study the two-plasmon decay (TPD) and stimulated Raman scattering (SRS) instabilities. Currently, the saturation occurs by pump depletion, but the structure allows for including other mechanisms, such as profile modification and Langmuir wave interactions with ion waves.

The Code

The SATIN code solves the two-dimensional coupled wave equations for SRS and TPD in the plane of polarization of the pump wave. The model plasma has an arbitrary density profile in the x-direction (propagation direction) but is uniform in the y-direction. The wave equations can consequently be represented as a set of coupled second-order differential equations in the x variable, where each equation represents a distinct wavenumber component in the y-direction. The equations are solved on the time scale of the instability growth rates; i.e., the fast frequency dependence of the waves is assumed to be $\exp(i\omega_j t)$ and the frequency shifts small so that only first-order derivatives in time are retained. For convenience, the variables are normalized as follows: x is in units of k_0^{-1}, the normalized time variable t is $\omega_0 t$, the frequencies Ω_j are in units of ω_0, K_j is the y-component of the wavenumber in units of k_0, N is the electron density normalized to critical density, V_e is the electron thermal velocity normalized to the speed of light, and the normalized electric field of the jth component E_j is eE/mk_0c^2. The resulting equations are

$$\left[\frac{\partial^2}{\partial x^2} + \Omega_j - N - K_j^2 + 2i\Omega_j \frac{\partial}{\partial \tau}\right]\vec{E}_j - (1 - 3V_0^2)\nabla(\nabla\cdot\vec{E}_j)$$
$$= \sum\left[-\frac{N}{2\Omega_k\Omega_1}\nabla(\vec{E}_k\cdot\vec{E}_1) - \frac{\Omega_j}{\Omega_1}(\nabla\cdot\vec{E}_k)\vec{E}_1\right],$$

where the sum on the right side includes all pairs k,l such that $\Omega_j = \Omega_k + \Omega_1$ and $K_j = K_k + K_1$. The equations are solved by an implicit finite difference scheme for the uncoupled wave equations, but with the coupling terms calculated explicitly. Langmuir wave damping is included in the electron thermal velocity V_e, and collisional damping is included in the density N in the manner prescribed by Forslund et al.[28]

The time step $\delta\tau$ is chosen to limit the growth predicted by the theoretical homogeneous plasma growth rate to less than 10% in one time step. The density profile is arbitrary, but generally is chosen to be linear or exponential with scale length $L \equiv (\partial N/\partial x)^{-1}$ in the coupling region, which corresponds to realistic ICF plasma profiles. The density profile is smoothed to have zero gradient both at the high-density ($N = N_{max}$) and low-density ($N = 0$) boundaries. Spatially resolving the Langmuir waves sets the number of zones required to $N_{max}K_0L/V_e$.

The boundary conditions assume that each mode E_j is purely transverse and far from its turning point density at the boundary. The light waves (except the pump) satisfy outgoing-wave boundary conditions. The Langmuir wave contribution is forced to zero by enhanced damping near the boundaries. The noise sources and coupling are also zero near the boundaries.

For this scheme, the frequency band represented by a single component Ω_j is limited by numerical damping to $\sim 1/\delta\tau$. In practice, the width of an SRS mode is set by the light-wave boundary conditions, which are satisfied only for the single mode with wavenumber $(\Omega_j^2 - N)^{1/2}$. For TPD, the frequency range is limited by the spectral width of the instability, which is in practice smaller than $1/\delta\tau$.

Stimulated Raman Scattering Results

Thresholds and growth rates for SRS below quarter-critical density have been calculated using the SATIN code and compared to theoretical values as a test of the code. Although the observed thresholds and growth rates agree well with theoretical predictions, convective saturation of the instability does not occur when $N_{max} > .25$, presumably due to reflections of light at the quarter-critical surface. In all unstable cases with $N_{max} > .25$, the growth continues until the decay amplitudes become comparable to the pump amplitude and saturation by pump depletion occurs. For cases run with no quarter-critical surface ($N_{max} < .25$), convective saturation is observed near threshold, but again growth appears absolute for strong coupling.
Figure 1-22 shows the evolution of SRS for parameters corresponding to strong growth. At early times, the decay modes are dominated by the initial noise (Fig. 1-22a), but after a few growth times for the instability, the coherent mode structure of the decay waves becomes apparent (Fig. 1-22b). After many e-foldings, the energy in the decay waves becomes significant and the pump is strongly depleted in the coupling region (Fig. 1-22c). Because the SRS growth rate is large for these parameters, the Raman light is still localized in the coupling region at the onset

of pump depletion. As shown in Fig. 1-23, the SRS thresholds and growth rates observed in the SATIN runs agree well with theoretical predictions.

Simulations that include collisional damping show strong suppression of SRS when the parameter of interest, $\mu \equiv 2\pi ZL/\lambda_0^2$

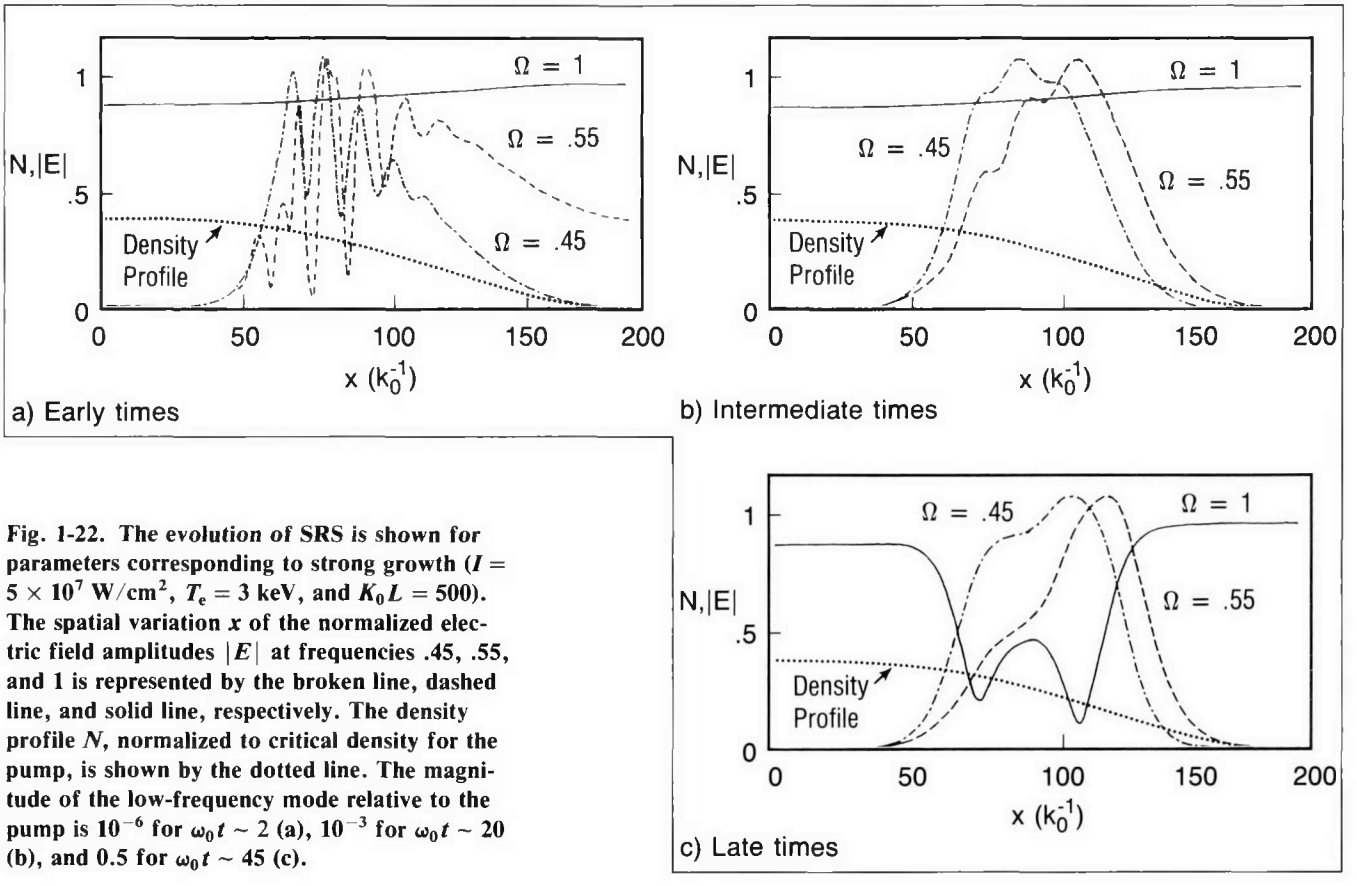

Fig. 1-22. The evolution of SRS is shown for parameters corresponding to strong growth ($I = 5 \times 10^7$ W/cm^2, $T_e = 3$ keV, and $K_0L = 500$). The spatial variation x of the normalized electric field amplitudes $|E|$ at frequencies .45, .55, and 1 is represented by the broken line, dashed line, and solid line, respectively. The density profile N, normalized to critical density for the pump, is shown by the dotted line. The magnitude of the low-frequency mode relative to the pump is 10^{-6} for $\omega_0 t \sim 2$ (a), 10^{-3} for $\omega_0 t \sim 20$ (b), and 0.5 for $\omega_0 t \sim 45$ (c).

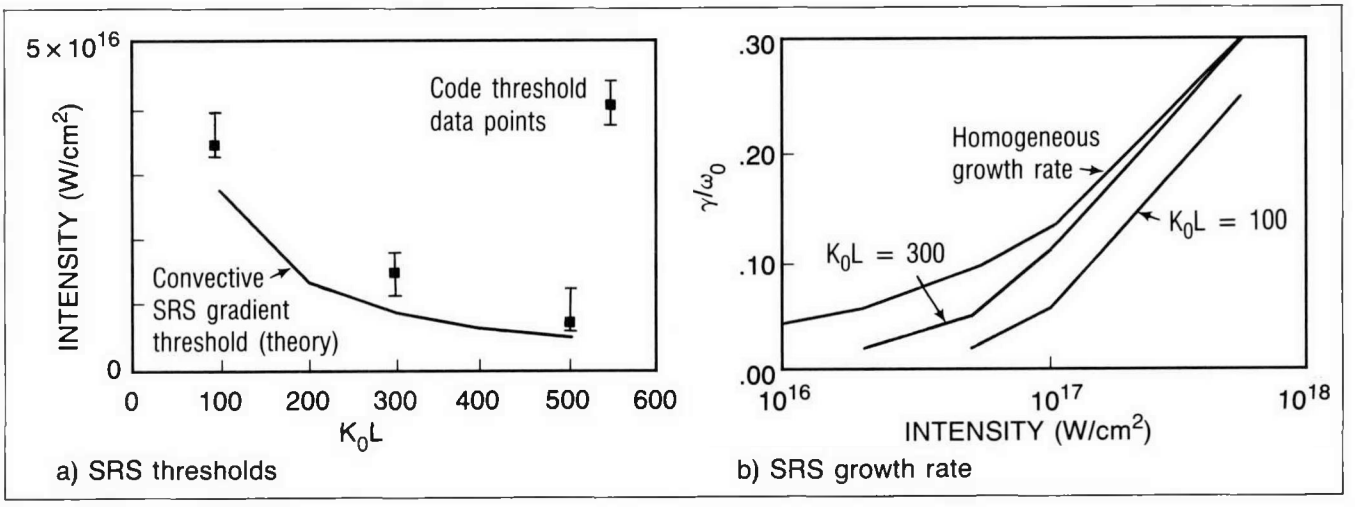

Fig. 1-23. SATIN calculations of SRS thresholds (a) and growth rates (b) are shown for $T_e = 3$ keV and normalized frequencies of .45 for the Langmuir wave frequency, .55 for the scattered light frequency, and 1 for the pump frequency. The results agree well with theoretical predictions.

(which is approximately proportional to the collision rate times the plasma density scale length), is large. For the same conditions as in Fig. 1-22, SRS growth is significantly affected by collisional damping for $\mu > 10^6$, and SRS is suppressed completely for $\mu > 10^7$. Experiments performed at Lawrence Livermore National Laboratory (LLNL)[29] showed strong suppression of SRS in long-scalelength plasmas ($L/\lambda_0 \sim 1000$) produced by illuminating gold targets with 0.26 μm laser light ($\mu \simeq 2 \times 10^6$), but strong SRS for 0.53 μm illumination ($\mu \simeq 10^6$).

Two-Plasmon Decay Results

SATIN simulations of linear TPD have also been compared to linear theory. The intensity and dependence on K_j of the linear growth rates show the expected behavior. Because the frequency spectrum of unstable modes is relatively narrow for TPD, all the modes can be adequately represented by a single frequency component $\Omega_j = .5$. This is fortunate for code efficiency but complicates interpretation of the frequency spectrum. The frequency spectrum for TPD near threshold is obtained by fast-Fourier transform (FFT) decomposition and agrees with linear theory. In the case of strong coupling, the frequency spectrum cannot be resolved adequately because the FFT frequency resolution is proportional to the growth rate.

Simultaneous SRS and TPD

When SRS and TPD occur simultaneously, the levels of fluctuations may be affected by interactions among the various decay modes. Ultimately the SATIN code can be a useful tool for studying the effect of such nonlinear interactions on the decay spectra and saturation. We have made a preliminary study of the effects of two of these nonlinear interaction mechanisms—pump depletion and profile steepening—on the saturated Langmuir wave spectrum.

Pump depletion can significantly affect the Langmuir wave spectrum if a significant amount of pump energy is converted to Langmuir wave energy. Then the pump energy available to drive unstable modes near quarter-critical density will be reduced by SRS at lower densities, so that the growth of TPD and SRS near quarter-critical density will be reduced. We have calculated the energy partitioning in frequency and wavenumber space when the decay modes are saturated by pump depletion. Since the SRS boundary conditions severely limit the mode width, scattering in the underdense plasma is best approximated by including a large number of frequency modes. In the linear growth phase of the instabilities, the energy fraction in a decay mode scales as $1/n$, where n is the total number of modes. For parameters corresponding to strong SRS below quarter-critical density, the energy partitioning in frequency space changes significantly for modes saturated by pump depletion as n increases. For the same parameters as in Fig. 1-22, absorption due to SRS at low densities completely turns off SRS backscatter at quarter-critical density

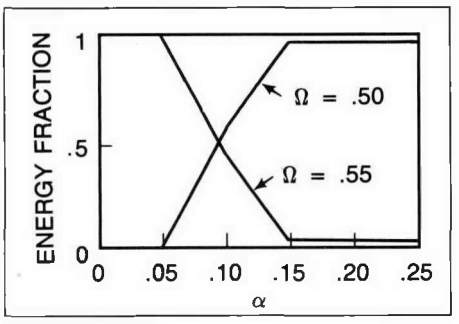

Fig. 1-24. Saturated energy levels for scattered light frequencies Ω = .5 and .55 are shown as a function of the steepening parameter α. The input parameters were L = 250, T_e = 1.3 keV, and $I\lambda_0^2 = 8 \times 10^{15}$ W/cm^2. Steepening of approximately a factor of 10 is necessary to affect the energy partitioning for these conditions significantly.

when more than 10 equally spaced decay modes are present. Two-plasmon decay modes ($K_j > 0$) also are suppressed due to the faster SRS growth.

As a preliminary test of the effect of profile steepening, we have calculated the decay spectrum for a piece-wise-linear, fixed profile with scalelength L at low densities ($N < .22$) and a scalelength αL in the region near quarter-critical density. Figure 1-24 shows the fraction of energy in each mode as a function of the steepening parameter α. The input parameters were $L = 250$, $T_e = 1.3$ keV, and $I\lambda_0^2 = 8 \times 10^{15}$ W/cm^2; only two scattered light frequencies, $\Omega = .5$ and $\Omega = .55$, were included in order to reach saturation in a reasonable amount of computer time. Steepening of approximately a factor of 10 is necessary to affect the energy partitioning for these conditions significantly. A consistent treatment of the effect of profile modification on the spectrum of unstable modes will require solving the hydrodynamic equation for the ion motion, including the ponderomotive force exerted by the decay modes.

In particle simulations, interactions between Langmuir waves and ion waves play an important role in limiting the levels of SRS and TPD. If the Langmuir waves remain at a low level due to these secondary wave-coupling processes, pump depletion and profile steepening at quarter-critical density may in reality be unimportant in determining the saturated spectra, since both of these processes are operative only when a substantial amount of the pump energy is transferred to the decay modes. The coupling between Langmuir waves and ion waves must be included in SATIN to provide a more complete picture of the competition among various nonlinear processes.

Summary

A fluid code, SATIN, has been developed to study the nonlinear evolution of coupled TPD and SRS in two dimensions. In addition, the code can provide complete information about the linear phases of the instabilities, including sidescatter, absolute modes, and reflections. Preliminary calculations of the energy partitioning of modes saturated by pump depletion have been done for both linear and steepened profiles. Work is underway to include ion motion via Eulerian hydrodynamics to provide a self-consistent model of profile modification. The code provides a framework for studying other nonlinear mechanisms such as the coupling between Langmuir waves and ion waves.

For additional information, please contact Dr. L. V. Powers

SECTION 1.4

Viewfactor Code Treatment of Time-Dependent Radiation Transport Problems Involving Participating Media

Viewfactor computer codes have been used successfully at KMS Fusion (KMSF) and other facilities to solve radiation transport problems involving fixed surfaces with intervening vacuum.[30] Recently, viewfactor codes have been applied successfully to time-dependent, multi-dimensional radiation transport problems in hohlraums.[31,32] However, when the effects of an intervening medium such as a gas or a plasma must be considered, use of such codes has been limited by available computer speed and memory to steady-state problems. We are currently developing a new algorithm for dealing with time-dependent problems with simple geometries that involve participating media.

In general, viewfactor codes involve the subdivision of given surfaces into small surface elements, either manually or with the aid of a computer algorithm; the specification of the surface elements so generated; and the modeling of the radiative transfer between the surfaces with the aid of viewfactors. They can be applied where complex radiation source dependence on time and space make application of competing methods, such as Monte Carlo, extremely costly in terms of computer time and memory. Unfortunately, to date the use of viewfactor codes has been limited mainly to situations in which there is no participating medium such as a gas or plasma.

It is not difficult to understand why. For vacuum problems, the fraction of radiation emitted by one surface that eventually strikes another surface is merely a function of the source strength at the emitting surface and the areas and orientations of the two surfaces. If some intervening medium is included, however, it is necessary to know not only the emissive and absorptive characteristics of the medium and how it varies over some large number of time steps, but how these characteristics are affected by the radiation field. Furthermore, some techniques must be developed for determining the contribution of the medium to beams of radiation as they pass from one surface to another. If the realistic assumption is made that the medium is nonhomogeneous, and its characteristics can vary more or less drastically throughout the given volume, the complexity of the problem is evident.

At KMSF, considerable progress has been made recently toward the goal of including the effects of participating media in viewfactor calculations. In the process, techniques have been developed that can be applied to "traditional" vacuum transport problems, allowing order-of-magnitude improvements in time and space resolution where axial symmetry exists.

RAYNA II, the code used at KMSF, can handle problems involving disks, cylinders, cones, spheres, rectangles, and various

derivatives of these surfaces. Except for rectangles, all of the surfaces are handled in the same way: First, the code automatically divides the surfaces that make up the problem into a number of rings, which are subdivided further into a number of elements of approximately equal area. The actual number of elements generated is specified by the user, limited by machine speed and memory constraints. This procedure is illustrated in Fig. 1-25 for the case of a disk.

It is evident that all of the rings generated by the code have a common axis of symmetry. As all of the surfaces specified are subdivided in turn, the code stores the axes of symmetry, and compares them once the calculation is completed. If all of the surfaces are found to share a common axis, certain simplifications are possible, as mentioned above.

The use of axial symmetry is illustrated by Fig. 1-26, which depicts the problem of coaxial disks. It can be seen that ring A of disk II makes the same contribution to each of the elements in ring B of disk I. Consequently, if the radiative contribution from each element in ring A to one element in ring B is calculated for a given time step, the total contribution can be found

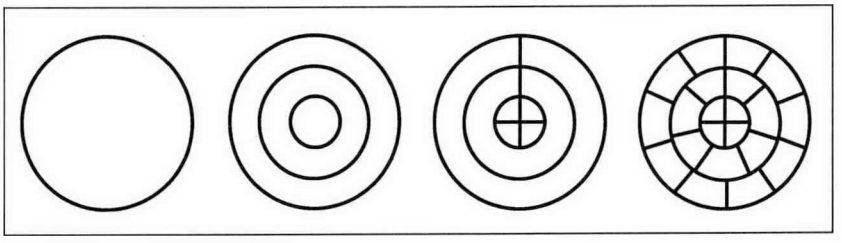

Fig. 1-25. RAYNA II subdivides a surface into areas of approximately equal size. For a disk, the division algorithm first forms concentric rings, and then further divides them into azimuthal segments.

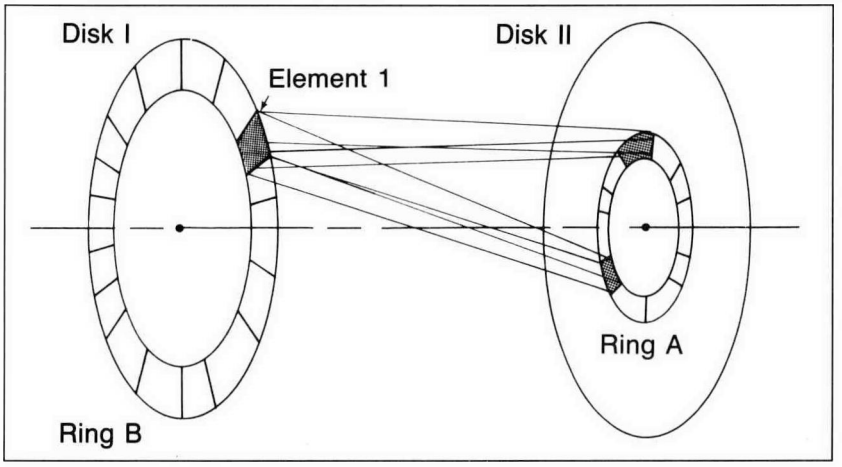

Fig. 1-26. Problems that have certain symmetries can be reduced to a simpler case. For example, two coaxial disks can be represented in part as a source element on ring A radiating to each element on ring B.

by summing. The other elements in ring B, and all of the other rings in the problem, can be handled in the same way.

The resolution in time and space made possible by this approach is better by an order of magnitude than was possible previously. We have been able to take advantage of these improvements to successfully model test problems that have been pathological for viewfactor codes in the past, such as those involving delta-function sources.[33] The savings in computer resources realized by taking advantage of problem symmetry also come in very handy in problems involving intervening media, to which we now turn.

If participating media are included, one must not only determine what fraction of radiation from one surface element is emitted in the direction of another surface element, but what happens to the radiation as it passes through the intervening material. As a minimum, one must set up a volume mesh and specify the emissive and absorptive characteristics of the material at each mesh point. Some volume must be associated with each mesh point, and an algorithm must be provided to update the physical characteristics of the medium at each point as it emits and absorbs radiation. Finally, one must calculate what volume elements are passed through by a beam that was emitted by one surface element in the direction of another surface element, and the proportion of the total path length between the two surface elements that is traveled in each of these volume elements.

Let us turn to the first of the tasks mentioned above: that of generating a volume mesh. RAYNA II does this by finding a two-dimensional (2-d) outline or cross-section of the problem. A 2-d mesh is set up on this outline by stepping along the axis of symmetry of the problem in increments of appropriate length and then sending out perpendicular rays from the points found in this manner. Mesh points are spaced along all segments of these rays that are found to be inside the space of the problem. When the entire 2-d mesh has been generated, each point is rotated about the axis of symmetry to generate a three-dimensional mesh. Obviously, each of the volume mesh points generated by one of the points in the 2-d outline in this manner belongs to a single volume ring, a circumstance that once again allows the code to take advantage of the symmetry of the problem.

Next, the code must identify the volume elements that are traversed by the radiation traveling between any two given surface elements and determine the fraction of the total distance between the surface elements that is spent in each volume element. This is accomplished by stepping in very small increments along the path between the two surface elements, and by calculating which volume mesh point is closest at each of these increments. It is assumed that the characteristics of the medium are determined at any point by those of the closest volume mesh point.

It is assumed that the problem space is completely enclosed. This does not greatly limit the usefulness of the code, since any desired openings for energy injection, diagnostic ports, etc., can be simulated by declaring black, nonemissive surface patches.

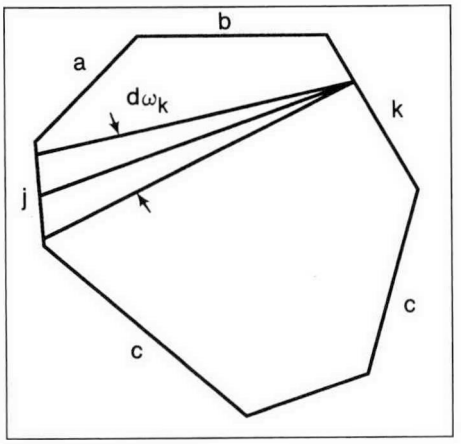

Fig. 1-27. In any enclosure, if the enclosing surface is divided into infinitesimal surface elements, the sum of all paths between any two of the elements will sweep the entire enclosed volume. A typical path between elements *j* and *k* is shown.

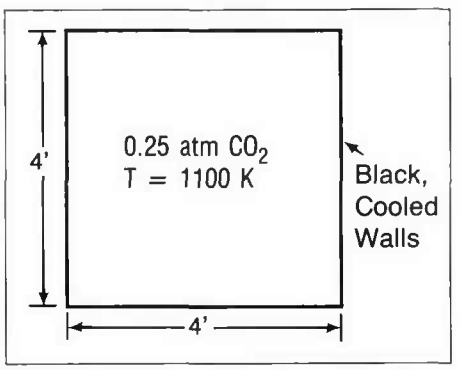

Fig. 1-28. In this sample problem involving participating media, the tank is a right-cylinder with a black interior and contains 0.25 atm of CO_2 at a temperature of 1100K. The problem is to determine the amount of energy that must be removed from the surface of the tank to keep it cool. (Note: Only emission from the gas is significant.) The semiempirical result is 7.94×10^4 J/s; the code result is 8.24×10^4 J/s.

The problem of how to deal with emission from intervening gases or plasmas is greatly simplified by assuming that the problem space is completely enclosed. For example, consider an enclosure composed of some chosen number of discrete surface elements, as shown in Fig. 1-27. The incoming radiation at surface *k* is equal to the sum of the contributions from all the other surfaces after allowing for absorption in the intervening medium, plus the contribution due to emission from the gas. In the figure, the radiation path between *k* and another surface *j* within the incident solid angle $d\omega_k$ is shown. If the contributions from all of the other surfaces, including that from surface *k* itself if it is concave, are determined by following the paths between the surfaces, the solid angles swept out will encompass all of the gas or plasma that can radiate to surface *k*. Thus, if the contribution of gas emission at all points along the path between two surfaces is taken into account for all surfaces, the gas emission for the entire volume will be accounted for automatically. This obviates the necessity for complicated schemes that attempt to handle volumetric emission and absorption independently. In other words, there is no need to use large amounts of computer memory to store information regarding the destination of radiation originating at every volume cell within the medium. The fraction of radiation originating in a given cell that should be contributed to a beam between two surface elements can be calculated based on the areas, positions, and orientations of those elements.

Because of memory constraints, application of RAYNA II is currently limited to simple geometries such as closed cylinders or concentric spheres. These constraints should be alleviated considerably by the larger memories available with machines now being introduced. The problem shown in Fig. 1-28 was modeled as a CO_2 gas-filled cylinder with the ends closed by disks of appropriate size, or a total of three regions. All three regions were subdivided in 30 surface elements of approximately equal size. Even with this relatively coarse resolution, the code solution given in the figure was within 4% of the "analytic" solution. The code could solve this problem equally well for an arbitrary temperature distribution on the walls and in the gas.

For additional information, please contact Dr. D. J. Drake

SECTION 1.5

Development of a New One-Dimensional Hydrocode

The basic one-dimensional (1-d) simulation code at KMS Fusion, TRHYD, was developed between 1972 and 1982.[34] In recent years, it has grown out-of-date and cumbersome to modify. As a result, it was decided to develop a new 1-d capability using more modern numerical techniques and incorporating new physics packages. The result of this program is Delphi.

Delphi is a fully conservative, 1-d Lagrangian hydrocode with the plasma represented by a three-temperature model for ions, thermal electrons, and suprathermal electrons. Radiation transport is computed by the variable Eddington (VE) method with coupling terms relativistically correct to $0(v/c)$. Heat conduction and collisional interactions include electron degeneracy with laser absorption through inverse bremsstrahlung and resonant processes. Equation-of-state options include SESAME tables, mean-ion local-thermodynamic-equilibrium (LTE) and mean-ion non-LTE. Nuclear burn of DT and D_2, with tracking and deposition of the mass and energy of reaction products, is available.

In the following sections, the basic physics included in the code is described, together with the corresponding differential equations. A brief discussion of some of the numerical techniques is also given.

Lagrangian Hydrodynamics—Conservative Work Terms

The fundamental equations solved by the code are the conservation laws for mass, momentum, and energy. These equations are supplemented by constitutive relations that describe the atomic state of the material, various scattering processes, and the emission and absorption of radiation. Because the fundamental differential equations are conservation laws, it is an important feature of Delphi that the difference analogs also guarantee conservation.[35] In most cases, this is fairly straightforward to achieve, but for the hydrodynamic work terms, some restructuring of the differential equations is required to obtain conservative difference forms.

The equations of mass, momentum, and energy for 1-d Lagrangian hydrodynamics are

$$dm = \frac{1}{\alpha}\,\rho\, dr^{\alpha} \ , \tag{29}$$

$$\frac{dv}{dt} = -\frac{1}{\rho}\frac{\partial P}{\partial r} \ , \tag{30}$$

and

$$\frac{d\epsilon}{dt} = P\,\frac{\partial}{\partial m}\,(r^{\alpha-1}v) \ , \tag{31}$$

where r and t are the position and time variables, v is the velocity, ρ is mass density, P is the pressure, ϵ is the internal energy, and $\alpha = 1,2,3$ corresponds to plane, cylindrical, and spherical geometry. The mass variable dm is mass per unit area in plane geometry and mass per steradian in spherical geometry.

By working in a Lagrangian system, the mass elements are constant by definition, and the difference analog of Eq. (29) is used to calculate zone density from the zone boundary positions. It is clear that linear momentum is conserved in cylindrical and spherical geometry because of the symmetry. It is also easy to show that the usual difference forms of Eq. (30) conserve momentum in planar geometry.

However, the obvious difference forms of Eqs. (29) to (31) do not conserve energy. To construct conservative difference equations, it is first necessary to rewrite Eq. (31) as

$$\frac{d\epsilon}{dt} + \frac{\partial}{\partial m}\left(r^{\alpha-1}vP\right) - \frac{v}{\rho}\frac{\partial P}{\partial r} = 0 \ . \tag{32}$$

The last term in Eq. (32) becomes $d/dt\ (v^2/2)$ by means of Eq. (30), which leads naturally to a globally conservative difference form.

Since the pressures and internal energies are composed of ion, thermal electron, and hot electron components, Eq. (32) must be split into three equations, each with a separate work term corresponding to the three partial pressures that make up the total pressure appearing in the momentum equation [Eq. (30)],

$$\frac{d\epsilon_i}{dt} + \frac{\partial}{\partial m}\left(r^{\alpha-1}vP_i\right) - \frac{v}{\rho}\frac{\partial P_i}{\partial r} = 0 \ ,$$

$$\frac{d\epsilon_e}{dt} + \frac{\partial}{\partial m}\left(r^{\alpha-1}vP_e\right) - \frac{v}{\rho}\frac{\partial P_e}{\partial r} = \Delta\phi_e \ ,$$

and

$$\frac{d\epsilon_h}{dt} + \frac{\partial}{\partial m}\left(r^{\alpha-1}vP_h\right) - \frac{v}{\rho}\frac{\partial P_h}{\partial r} = \Delta\phi_h \ .$$

In these basic energy equations, the source terms for laser absorption also have been added.

Heat Conduction and Collisional Exchange

Heat conduction and collisional energy exchange between the plasma constituents also must be included in the basic energy equations, with the result,

$$\frac{d\epsilon_i}{dt} + \left(P_i \frac{dV}{dt}\right) - \frac{C_v^i}{k\tau_e}(\theta_e - \theta_i) + \frac{\partial}{\partial m}(r^{\alpha-1} q^i) = 0 \ , \qquad (33)$$

$$\frac{d\epsilon_e}{dt} + \left(P_e \frac{dV}{dt}\right) + \frac{C_v^i}{k\tau_e}(\theta_e - \theta_i) - \frac{C_v^i}{k\tau_h}(\theta_h - \theta_e) + \frac{\partial}{\partial m}(r^{\alpha-1} q^e) = \Delta\phi_e \ ,$$

and

$$\frac{d\epsilon_h}{dt} + \left(P_h \frac{dV}{dt}\right) + \frac{C_v^i}{k\tau_h}(\theta_h - \theta_e) + \frac{\partial}{\partial m}(r^{\alpha-1} q^h) = \Delta\phi_h \ .$$

In these equations, $\theta = kT$, C_v^i is the ion specific heat, q is the heat flux, and τ is the relaxation time for collisional exchange. For convenience, the work terms discussed above are written here in the shorter form $P\,dV/dt$, where $V = \rho^{-1}$ is the specific volume.

Since the hot electrons couple poorly to the ions, $\tau \gg \tau_e$, this exchange term has been dropped. The relaxation times for coupling between the hot and cold electrons and the cold electrons and ions are those given by Spitzer.[36] The thermal electron-ion time has been modified for electron degeneracy as shown by Brysk.[37]

In the absence of hot electrons, the cold electron and ion heat fluxes are given by the expression,

$$q - K' \frac{\partial T}{\partial r} \ , \qquad (34)$$

where K' is a flux-limited conductivity. For electrons,

$$K_e' = \frac{K_e}{1 + (\epsilon\delta)' \dfrac{40}{f_c}\left(\dfrac{2}{\pi}\right)^{1/2} \dfrac{\lambda_s}{|L|}} \ , \qquad (35)$$

where K_e is the Spitzer conductivity, λ_s is the scattering length, $|L|$ is the magnitude of the temperature gradient scale length, f_c is the flux-limit parameter, and $(\epsilon\delta)'$ is given by

$$(\epsilon\delta)' = \epsilon\delta\left[1 + \frac{(0.268\, G_\Gamma \ln\Lambda)^2 (T_F/T_e)^3}{(\epsilon\delta)^2}\right]^{1/2} \ .$$

This form of $\epsilon\delta$ contains the Fermi temperature T_F and a function G_Γ obtained by Hubbard that corrects the usual Spitzer conductivity for electron degeneracy.[38] The ion conductivity is handled as in Eqs. (34) through (35) except for the degeneracy correction.

When hot electrons are present, the expressions for heat flux are more complex than Eq. (34). The currents induced by the temperature and density gradients in both electron components interact through the quasineutral electric field. This interaction leads to heat flux expressions that contain both temperature and density gradients. These expressions will be considered in more detail below.

The conservative differencing of Eq. (33) is straightforward. The exchange terms simply cancel when the internal energy equations are added together. The heat flux terms cancel zone by zone when the zone energies are summed, leading directly to the global conservation equation.

Since the relaxation times and conductivities depend on temperature, the centering of these terms in an implicit difference scheme presents problems. The standard approach is to iterate, but this is impractical in a large code with multifrequency radiation and non-LTE rate equations. The Delphi code uses a predictor-corrector scheme to handle the nonlinear transport coefficients.[38] At each time step t^n, an explicit difference form is used to get temperatures at t^{n+1}. These are the predicted temperatures; the nonlinear terms at the advanced time are evaluated in terms of the predicted temperatures, which allows the coupled set of difference equations to be solved by the tridiagonal algorithm.

Radiation

Radiation transport is handled by the VE method.[39] In this method, the radiation field is represented by its first three angular moments, energy density E, flux F, and radiation pressure P. In general, an infinite sequence of moments is required, but in the VE method the sequence is truncated by $P = fE$, where $f(r,t,v)$ is called the Eddington factor.

If the Eddington factor were known exactly, no approximation would be involved. In practice, f can be calculated by a discrete ordinate or S_n snapshot routine or by a number of different analytical prescriptions (see, for example, Pomraning[40]). Even very simple Eddington factors give good results in 1-d because of the high degree of symmetry.

The great advantage of the VE method is that the equations automatically reduce to diffusion in optically thick regions and to wave propagation in optically thin regions, so that zoning and accuracy of the difference equations are essentially independent of the large variations in opacity.

The derivation of the radiation equations must include relativistically correct coupling to the material. The proper derivation of these coupling terms has a long history in the astrophysical literature. A derivation[41] for the VE equations to $0(v/c)$ leads to the following extension of Eq. (32):

$$\frac{d\epsilon_i}{dt} + \left(P_i \frac{dV}{dt}\right) - \frac{C_v^i}{k\tau_e}(\theta_e - \theta_i) + \frac{\partial}{\partial m}(r^{\alpha-1}q^i) = 0 ,$$

$$\frac{d\epsilon_e}{dt} + \left(P_e \frac{dV}{dt}\right) + \frac{C_v^i}{k\tau_e}(\theta_e - \theta_i) - \frac{C_v^i}{k\tau_h}(\theta_h - \theta_e) + \frac{\partial}{\partial m}(r^{\alpha-1}q^e)$$

$$- \frac{1}{\rho}[c\bar{\sigma}_E E - 4\pi J] = \Delta\phi_e ,$$

$$\frac{d\epsilon_h}{dt} + \left(P_h \frac{dV}{dt}\right) + \frac{C_v^i}{k\tau_h}(\theta_h - \theta_e) + \frac{1}{\rho}(4\pi J_{ff}^h) + \frac{\partial}{\partial m}(r^{\alpha-1}q^h) = \Delta\phi_h \ , \qquad (36)$$

$$\frac{d}{dt}\left(\frac{E}{\rho}\right) = \frac{1}{\rho r^{\alpha-1}}\frac{\partial}{\partial r}(r^{\alpha-1}F) + \frac{1}{\rho}[c\bar{\sigma}E - 4\pi J - 4\pi J_{ff}^h] = 0 \ ,$$

$$\frac{1}{c}\frac{d}{dt}\left(\frac{F}{\rho}\right) + \frac{c}{\rho}\left[\frac{\partial}{\partial r}(fE) + \frac{\alpha-1}{2r}(3f-1)E\right] + \bar{\sigma}_F\left(\frac{F}{\rho}\right) = 0 \ .$$

A further result of the relativistic derivation is an additional radiation pressure term in the momentum equation [Eq. (30)].

The set of Eqs. (36) are differenced implicitly and solved as a coupled set of matrix equations. The radiation equations in Eqs. (36) are frequency-integrated, and contain two frequency-averaged cross-sections. These energy-and flux-weighted mean cross-sections are obtained by a separate multifrequency snapshot calculation each time step.[39] This approach is designed to get the overall energy flows correct in the main implicit hydro routine. More detailed properties of the radiation field can then be obtained by postprocessor calculations based on time-dependent temperature and densities given by the main code.[42]

The multifrequency absorption cross-sections and emission functions for free-free, free-bound, and bound-bound processes are obtained from standard opacity references.[42] These functions depend on the occupation numbers for the mean ions in each hydro zone. Since the code is designed for non-LTE calculations, these radiation properties must be calculated from the basic formulae each time step. The use of tabular opacities as a function of temperature and density is only possible in LTE.

Radiative interaction with the hot electrons is limited to bremsstrahlung emission. The resulting hard x-rays are assumed to leave the target with negligible absorption.

Hot Electrons

In the approach to hot electron transport taken in Delphi, the electron distribution function is decomposed into cold and hot components $f = f_e + f_h$. The Boltzmann equation then becomes[43]

$$\frac{\partial f_e}{\partial t} + v\mu\frac{\partial f_e}{\partial r} - \frac{eE}{mv}\left[v\mu\frac{\partial f_e}{\partial v} + (1-\mu^2)\frac{\partial f_e}{\partial \mu}\right] = -K(f_e, f_z) - K(f_e, f_e) - K(f_e, f_h) \ , \qquad (37)$$

$$\frac{\partial f_h}{\partial t} + v\mu\frac{\partial f_h}{\partial r} - \frac{eE}{mv}\left[v\mu\frac{\partial f_h}{\partial v} + (1-\mu^2)\frac{\partial f_h}{\partial \mu}\right] = -K(f_h, f_z) - (f_h, f_h) - K(f_h, f_e) \ .$$

The interaction between the two groups occurs through the quasi-neutral field E and the collision terms $K(f_e, f_h)$ and $K(f_h, f_e)$. If we restrict our consideration to the case of a

Lorentz plasma where each electron component only interacts with the ions that are considered fixed, the scattering terms can be written[44]

$$K(f_i,f_z) = \frac{v}{\lambda_i}\ (f_i = f_i^0)\ , \tag{38}$$

where f_i^0 is the Maxwell-Boltzman distribution at the local temperature kT_i, λ_i is the scattering length for momentum-exchanging collisions, and the index i = e,h labels the electron components.

Based on two assumptions, a solution to the equations in (37) with collision term [Eq. (38)] can be obtained that is valid for both small and large gradients. Equation (38) is correct in the short mean-free-path limit (small gradient) and also correct in the long mean-free-path limit, where it approaches zero. The assumption is made that the relaxation form of the collision term holds approximately in between these two limits. The second assumption is that the angular dependence of the distribution functions is weak, and these functions can be represented in the separable form $f_i = I_i(t,r,v)\psi_i(t,r,v,\mu)$, where ψ is slowly varying.

With these assumptions, Eq. (37) can be solved[43] to yield distribution functions of the form

$$f_i = \frac{I_i}{4\pi}\ \frac{1}{R_i(\coth R_i - \mu)}\ , \tag{39}$$

where I is expressed in terms of the equilibrium distribution by $I_i = \omega_i I_i^0$, and the parameter R_i is given by

$$R_i = -w_i \lambda_{s_i} x_i^4 \left[\frac{eE}{kT_i} + \frac{1}{P_i}\frac{\partial P_i}{\partial r} + (x_i^2 - 2.5)\ \frac{1}{T_i}\frac{\partial T_i}{\partial r} \right] . \tag{40}$$

In these expressions, the scattering length is $\lambda_{s_i} x_i^4$, where

$$\lambda_{s_i} = \frac{(kT_i)^2}{\pi N_z Z^2 e^4 \ln \Lambda} \text{ and } x_i^2 = \frac{mv^2}{2kT_i}\ .$$

With this solution, one can obtain the electric current and heat flux from

$$j_i = -e\int_0^\infty J_i v^2\, dv \quad \text{and} \quad q_i = \frac{m}{2}\int_0^\infty J_i v^4\, dv\ , \tag{41}$$

where $J = vI\Gamma R$ with $\Gamma = (R \coth R - 1)R^{-2}$. When the functions R_i are expressed by Eq. (40), the current and heat flux take the forms

$$j_i = \sigma^i \frac{N_i}{N_e} E\phi_E^i + \frac{\sigma^i}{eN_e}\frac{\partial P_i}{\partial r}\phi_E^i + \alpha^i \frac{N_i}{N_e}\frac{\partial T_i}{\partial r}\phi_T^i$$

and (42)

$$q_i = -\beta^i \frac{N_i}{N_e} E\psi_E^i - \frac{\beta^i}{eN_e} \frac{\partial P_i}{\partial r} \psi_E^i - K^i \frac{N_i}{N_e} \frac{\partial T_i}{\partial r} \psi_T^i ,$$

where

$$\sigma^i = 2\left(\frac{2}{\pi}\right)^{3/2} \frac{(kT_i)^{3/2}}{Zm^{1/2}e^2 \ln \Lambda} , \quad \alpha^i = \frac{3}{2} \frac{k}{e} \sigma^i ,$$

$$K^i = 20\left(\frac{2}{\pi}\right)^{3/2} \frac{k(kT_i)^{5/2}}{Zm^{1/2}e^4 \ln \Lambda} , \quad \text{and} \quad \beta^i = \frac{2}{5} \frac{e}{k} K^i \tag{43}$$

are the familiar Lorentz gas transport coefficients.[36] The gradient correction factors,

$$\phi_E^i = \frac{1}{2} \int_0^\infty \omega_i^2 \Gamma_i y^3 e^{-y} dy ,$$

$$\phi_T^i = \frac{1}{3} \int_0^\infty \omega_i^2 \Gamma_i (y - 2.5) y^3 e^{-y} dy ,$$

$$\psi_E^i = \frac{1}{8} \int_0^\infty \omega_i^2 \Gamma_i y^4 e^{-y} dy , \tag{44}$$

and

$$\psi_T^i = \frac{1}{20} \int_0^\infty \omega_i^2 \Gamma_i (y - 2.5) y^4 e^{-y} dy ,$$

reduce to unity for small gradients, giving the classical result. For large gradients, these factors correct the diffusion expressions for the effects of long mean-free-path electrons in the distribution, so that the current and heat flux expressions [Eq. (42)] are inherently flux-limited.[44]

The quasineutral field can be obtained from Eq. (42) by setting the total electric current $j = j_e + j_h$ equal to zero. We further assume that the number density of hot electrons is everywhere much less than the number density of cold electrons, so that $N_c \simeq N_e \gg N_h$. Under this assumption, $\rho_N \rho_T^{3/2} \ll 1$, where $\rho_N \equiv N_h/N_e \equiv T_h/T_e$, and the cold and hot electron heat fluxes reduce to

$$q_e = -\left(0.4\rho_N \rho_T^{3/2} \phi_E^h \frac{\psi_E^c}{\phi_E^c}\right) \frac{K_e T_e}{N_e} \frac{\partial N_e}{\partial r} - \left(\psi_T^c - 0.6\phi_T^c \frac{\psi_E^c}{\phi_E^c}\right) K_e \frac{\partial T_e}{\partial r}$$
$$+ \left(0.4\rho_N \rho_T^{3/2} \phi_E^h \frac{\psi_E^c}{\phi_E^c}\right) \frac{K_e T_h}{N_h} \frac{\partial N_h}{\partial r} + \left(0.4\rho_N \rho_T^{3/2} \phi_T'^h \frac{\psi_E^c}{\phi_E^c}\right) K_e \frac{\partial T_h}{\partial r} , \tag{45}$$

$$q_h = (0.4\rho_N \psi_E^h) \frac{K_h T_e}{N_e} \frac{\partial N_e}{\partial r} + \left(0.4\rho_N \phi_r'^c \frac{\psi_E^h}{\phi_E^c}\right) K_h \frac{\partial T_e}{\partial r}$$
$$- (0.4\rho_N \psi_E^h) \frac{k_h T_h}{N_h} \frac{\partial N_h}{\partial r} - (0.4\rho_N \psi_T^h) K_h \frac{\partial T_h}{\partial r} . \tag{46}$$

Since $N_h \ll N_e$, we assume that everywhere $N_e = ZN_i$ and calculate N_h from the continuity equation,

$$\frac{dN_h}{dt} + \alpha \frac{\partial}{\partial r^\alpha} (r^{\alpha-1} J_h) = S_h \ , \tag{47}$$

where the particle current density follows from Eq. (42) and $j_h = -eJ_h$,

$$J_h = \left(\frac{3}{2} \rho_N \phi_E^h\right) \frac{\alpha_h}{e} \frac{T_e}{N_e} \frac{\partial N_e}{\partial r} + \left(\frac{2}{3} \rho_N \phi_T'^c \frac{\phi_E^h}{\phi_E^c}\right) \frac{\alpha_h}{e} \frac{\partial T_e}{\partial r}$$
$$- \left(\frac{2}{3} \rho_N \phi_E^h\right) \frac{\alpha_h}{e} \frac{T_h}{N_h} \frac{\partial N_h}{\partial r} - \left(\frac{2}{3} \rho_N \phi_T'^h\right) \frac{\alpha_h}{e} \frac{\partial T_h}{\partial r} \ . \tag{48}$$

The continuity equation [Eq. (47)] with the particle current [Eq. (48)] must be added to the set of energy equations [Eqs. (36)]. In this set of equations, the heat flux terms [Eqs. (45) and (46)] must be included specifically. When the radiation flux equation is solved for F and substituted into the radiation energy equation, the total number of equations is reduced to five. The coupled set of five equations, when differenced, assumes the matrix form, which is solved by the tridiagonal algorithm with the transport coefficients determined by the predictor-corrector technique.

$$\begin{vmatrix} D_1 \\ D_2 \\ D_3 \\ D_4 \\ D_5 \end{vmatrix} = - \begin{vmatrix} A^{11} & A^{12} & A^{13} & 0 & 0 \\ A^{21} & A^{22} & A^{23} & 0 & 0 \\ A^{31} & A^{32} & A^{33} & 0 & 0 \\ 0 & 0 & 0 & A^{44} & \\ 0 & 0 & 0 & & A^{55} \end{vmatrix} \begin{vmatrix} N_H \\ \theta_H \\ \theta_e \\ \theta_i \\ E \end{vmatrix}_{j+3/2}$$

$$+ \begin{vmatrix} B^{11} & B^{12} & B^{13} & 0 & 0 \\ B^{21} & B^{22} & B^{23} & B^{24} & 0 \\ B^{31} & B^{32} & B^{33} & B^{34} & B^{35} \\ 0 & B^{42} & B^{43} & B^{44} & 0 \\ 0 & 0 & B^{53} & 0 & B^{55} \end{vmatrix} \begin{vmatrix} N_H \\ \theta_H \\ \theta_e \\ \theta_i \\ E \end{vmatrix}_{j+1/2}$$

$$+ \begin{vmatrix} C^{11} & C^{12} & C^{13} & 0 & 0 \\ C^{21} & C^{22} & C^{23} & 0 & 0 \\ C^{31} & C^{32} & C^{33} & 0 & 0 \\ 0 & 0 & 0 & C^{44} & 0 \\ 0 & 0 & 0 & 0 & C^{55} \end{vmatrix} \begin{vmatrix} N_H \\ \theta_H \\ \theta_e \\ \theta_i \\ E \end{vmatrix}_{j+1/2}$$

Equation of State

Three equation-of-state options are available, SESAME tables, a mean-ion LTE model, and a mean-ion non-LTE model. The LTE equation-of-state follows the original work of Mayer[45] and the later improvements of More and Zimmerman.[46] Pressure ionization is taken from the Thomas-Fermi model of Zink.[47]

In the non-LTE model the set of rate equations for the level populations P_n are solved over each hydro time step using a stiff ordinary differential equation (ODE) solver. These equations are of the form,

$$\frac{dP_1}{dt} = Q_1 \sum_{m=2}^{10} P_m R_{m1}^{D} + Q_1 R_{c1}^{D} - P_1 \sum_{m=2}^{10} Q_m R_{1m}^{U} - P_1 R_{1c}^{U} ,$$

$$\frac{dP_2}{dt} = Q_2 P_1 (R_{12}^{U} + R_{12}^{DE}) + Q_2 \sum_{m=3}^{10} P_m R_{m2}^{D} - P_2 Q_1 R_{21}^{D}$$

$$- P_2 \sum_{m=3}^{10} Q_m R_{2m}^{U} - P_2 R_{2c}^{U} + Q_2 R_{c2}^{D} ,$$

$$\frac{dP_n}{dt} = Q_n \sum_{m=1}^{n-1} P_m (R_{mn}^{U} + R_{mn}^{DE}) + Q_n \sum_{m=n+1}^{10} P_m R_{mn}^{D}$$

$$+ Q_n R_{cn}^{D} - P_n \sum_{m=1}^{n-1} Q_m R_{nm}^{D} - P_n \sum_{m=n+1}^{10} Q_m R_{nm}^{U} - P_n R_{nc}^{U} ,$$

where $Q_n = 1 - P_n/2n^2$ is the availability of state n. The rates included in this model are collisional excitation and deexcitation ($R_{mn}^{C,U}$, $R_{nm}^{C,D}$), collisional ionization and three-body recombination ($R_{nc}^{C,U}$, $R_{cn}^{C,D}$), radiative excitation and deexcitation ($R_{mn}^{R,U}$, $R_{nm}^{R,D}$), photoelectric ionization and radiative recombination ($R_{nc}^{R,U}$, $R_{cn}^{R,D}$), and dielectronic recombination (R_{nm}^{DE}).

The collisional rates including three-body recombination are taken from Post et al.[48] Radiative rates follow from the radiation emission and absorption functions by an analysis similar to Lokke and Grasberger,[49] although a different procedure is used for the coupling of induced rates to the radiation field. Dielectronic recombination rates are adapted from Zhdanov.[50]

In the present version of Delphi, the user chooses either the LTE or non-LTE model. In future versions, the code will decide whether non-LTE is required in each zone. If not, the much faster LTE subroutine will be used. The use of non-LTE makes a large difference in many problems of current interest.

Nuclear Burn

In the current version of Delphi, only D_2 and DT reactions are considered:

$$D + T \rightarrow H_e^4(3.52\ \text{meV}) + n(14.07\ \text{meV})$$

$$D + D \begin{cases} \rightarrow T(1.01\ \text{meV}) + p(3.02\ \text{meV}) \\ \rightarrow H_e^3(0.82\ \text{meV}) + n(2.45\ \text{meV}) \end{cases} .$$

The rate equations for these reactions are[51]

$$-\frac{dN_D}{dt} = -\frac{dN_T}{dt} = \frac{dN_\alpha}{dt} = \frac{dN_n}{dt} = N_D N_T (\overline{\sigma v})_{DT} ,$$

$$-\frac{dN_D}{dt} = N_D^2 (\overline{\sigma v})_{DD} + N_D N_T (\overline{\sigma v})_{DT} ,$$

$$-\frac{dN_T}{dt} = N_D N_T (\overline{\sigma v})_{DT} - \frac{1}{4} N_D^2 (\overline{\sigma v})_{DD} .$$

The reaction rates from Post[52] give

$$(\overline{\sigma v})_{DD} = 2.6 \times 10^{-14} T_i^{-2/3} \exp(-18.76\, T_i^{-1/3}) \text{cm}^3/\text{s}$$

for the D_2 rate. From Arnold et al.,[53] we obtain

$$(\overline{\sigma v})_{DT} = 3.8 \times 10^{-12} T_i^{-2/3} \exp(-19.02\, T_i^{-1/3}) , \quad T_i < 10\ \text{keV}$$
$$= 3.41 \times 10^{-14} T_i^{-2/3} \exp(-27.22\, T_i^{-2/3} + 3.64\, T_i^{-1/2}) , \quad T_i > 10\ \text{keV}$$

for the DT rate. The charged particles created by the nuclear reactions in each fuel zone are tracked, and their energy and mass deposited nonlocally using conventional stopping-power formulae to partition the energy between electrons and ions.[54] When the energy of a charged particle is reduced to the thermal energy of a zone, it is considered stopped and its mass added to that zone. Neutrons are considered to escape without attenuation.

Summary and Conclusions

Delphi is a laser/plasma interaction code designed for the study of plasmas that are, in general, far from thermal equilibrium. The code is based on a three-temperature model in which the ions, thermal electrons, and suprathermal electrons are described by separate temperatures. Both the hot and cold electrons are assumed to be in quasi-Maxwellian distributions warped by the gradients and quasineutral field. Inverse bremsstrahlung heats the thermal electrons, and resonant processes, mostly legislated, produce the suprathermal population.

The atomic properties of the plasma are described by a non-equilibrium mean-ion model in which rate equations are solved to obtain the time-dependent populations of the atomic levels. These populations reflect the balance of competing ionization, recombination, excitation and deexcitation mechanisms and can

be very different from equilibrium values. Local thermodynamic equilibrium options also are available.

Radiation transport is by a multifrequency VE method. Transport coefficients for the thermal electrons are corrected for degeneracy, and conduction is inherently flux-limited. Nuclear burn of D_2 and DT is included with the nonlocal deposition of charged-particle mass and energy.

The code is designed to guarantee the conservation of mass, momentum, and energy identically independent of zoning. This has the advantage that even small numerical problems usually show up as a failure of conservation.

Delphi has been used to calculate a wide variety of different laser/plasma problems, including microballoon implosion experiments, cryogenic experiments, breakeven target experiments, x-ray laser experiments, x-ray laser double-foil target design, and dot spectroscopy experiments. A number of classified experiments have also been simulated successfully.

For additional information, please contact Dr. P. M. Campbell

SECTION 1.6

Spectroscopic Technique Development

The use of x-ray line ratios with simulation codes is of interest in determining certain physical characteristics of laser-irradiated targets. Of particular interest is the high-power irradiation of disk targets by laser light of very short pulse duration. The resulting emission and recording of x-ray lines yields line ratios that could be applied to simulation codes to determine temperature and density. However, this approach is hampered by a lack of confidence in the accuracy of the non-local thermodynamic equilibrium (non-LTE) atomic-level-population codes used in the simulations.

Results obtained with such codes have been shown to differ by a factor of two or more, depending on the plasma conditions and the particular code used.[55] Among themselves, code differences depend sensitively on the number of Rydberg states included and on variations among computer collision rates. Consequently, hot-plasma temperature and density measurements made using spectral line-ratio methods based on these codes would not be expected to be reliable. Moreover, transient quasi-equilibrium conditions that exist in certain plasmas may not be adequately addressed in the codes.

If, however, the x-ray emission from simple disks can be modeled correctly, then spectroscopic line-ratio measurements of temperature and density of more complicated shapes can be applied with greater confidence. An experimental series was begun to measure the temperature and density of laser-irradiated dot targets, independent of line-ratio methods, and compare them to the line-ratio results provided by one or more simulation codes.

Technical Scope

The present effort is concerned with the application of a spectroscopic method known as "spot spectroscopy"[56] to generate a confined plasma whose properties vary essentially only in one dimension. The plasma is probed normal to this dimension by various diagnostic techniques to determine its temperature, density, and x-ray emission profiles.

The plasma temperature is determined by recording the hydrogen-like and helium-like free/bound continua of a metal, such as magnesium or aluminum. The plasma temperature is derived from the slope of the free/bound continuum. In contrast to the line-ratio method, this method is rather simple and is not subject to questions of interpretation. This temperature method is not ordinarily used, since free/bound continua are not as radiant as nearby spectral hydrogen-like and helium-like lines. Whenever it has been used, it is with time-integrating spectrographs.[57] To

our knowledge, the present program is the first to employ time-resolving spectrographs to measure these highly transient disk plasmas using spot-spectroscopy techniques.

The plasma density is determined by a four-frame, UV holographic probe interferometer capable of providing fringe patterns that can be processed, using Abel inversion techniques, to yield axial and three-dimensional density profiles. Each frame is recorded in a 10 ps exposure. The intervals between frames can be adjusted in a range from 40 to 400 ps (Ref. 15).

The Experiments

Diagnostic Instruments and Methods. In spot spectroscopy, a small metal dot of interest is deposited on, or embedded in, a thick substrate. Upon laser irradiation of a larger spot surrounding the dot, the blow-off plasma will contain the plasma from the dot in a slowly diverging column, as shown in Fig. 1-29. Since the diameter of the metal dot column is small compared to the irradiated spot, its plasma conditions are expected to be constant throughout a cross-section of the column. Viewing the narrow dot plasma column with a spectrograph set up with a slit to resolve intensity variations spatially along the length of the column, a spectrum as shown in Fig. 1-30 is obtained. Two such time-integrating, spatially resolving spectrographs were used in these experiments.

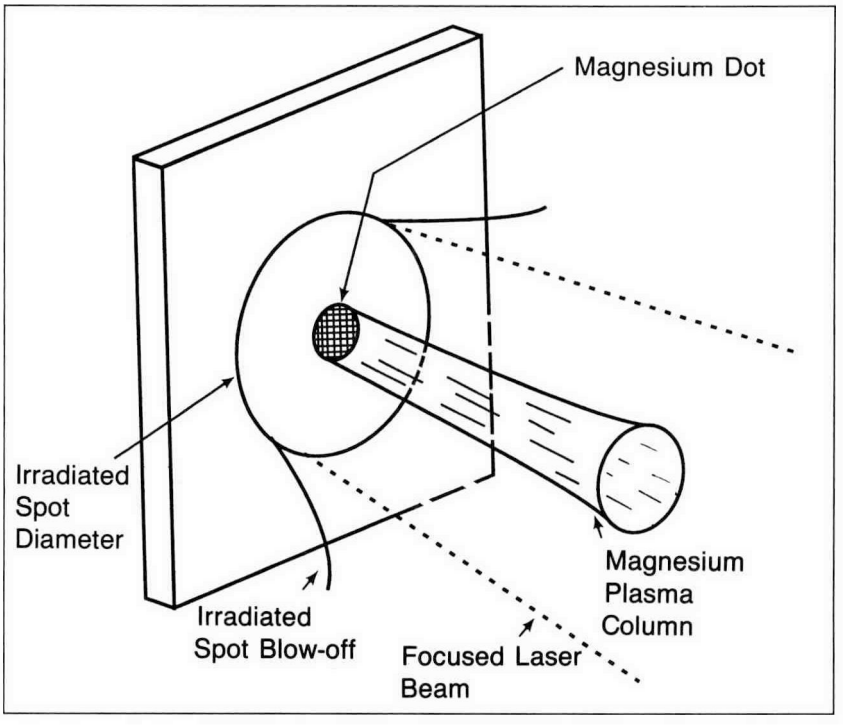

Fig. 1-29. Plasmas of interest are created by focusing the laser beam on a flat target that consists of a metal dot on a thick substrate of a material of lower atomic number. The laser irradiates a spot that contains (but is larger than) the dot. Thus, the plasma column from the dot is contained by the irradiated spot blow-off plasma of the substrate material. The target in this case is a magnesium dot.

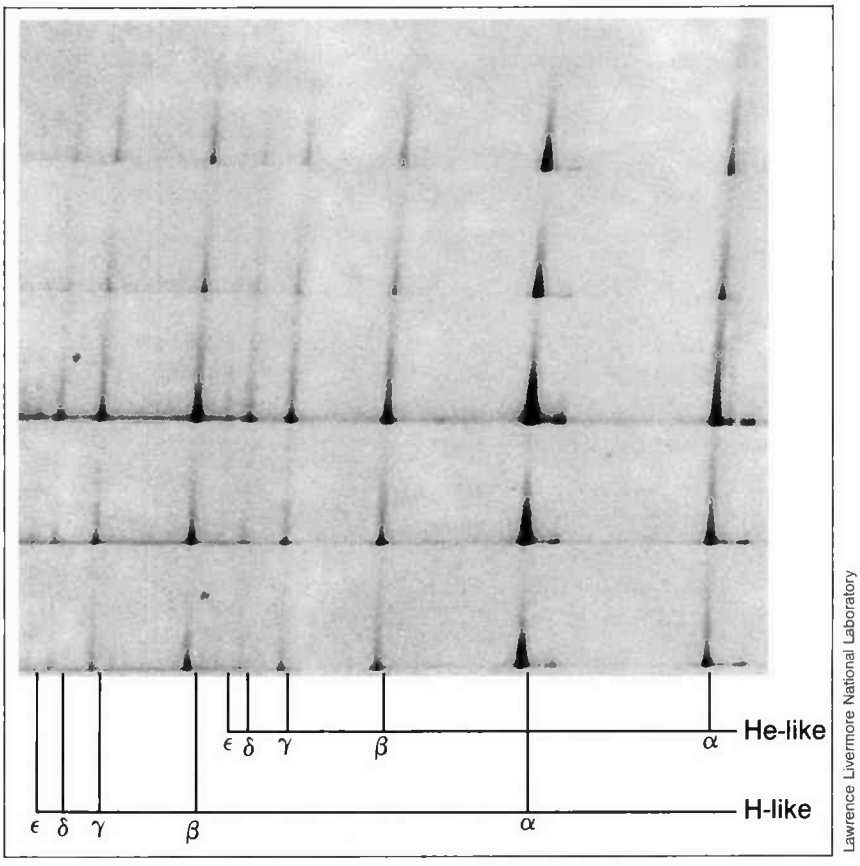

Lawrence Livermore National Laboratory

Fig. 1-30. The narrow plasma column from a target consisting of a 100 μm diameter magnesium dot on polystyrene, viewed by a spectrograph set up to spatially resolve intensity variations along the length of the column, yielded this time-integrated helium-like and hydrogen-like magnesium spectrum. Spatial resolution was provided by five slits of widths (from top to bottom) of 10, 5, 25, 10, and 5 μm.

The technique offers four special features that we wish to exploit:

1. The containment of the dot plasma column by the substrate blow-off.
2. The uniformity of the column's brightness over any cross-section normal to its flow.
3. The spatial resolution.
4. The spectral line emission along the length of the plasma column.

By adding a streak crystal spectrograph camera (SCSC) constrained to view the emitting plasma from only a small length of the plasma column (Fig. 1-31), spectral lines and continua can be recorded. All of the spectral lines and continua arise from ions with very similar plasma conditions. Ratios of these lines can then be used in determinations of temperature via the simulation codes, while the free/bound continua provide independent measurements of the temperature.

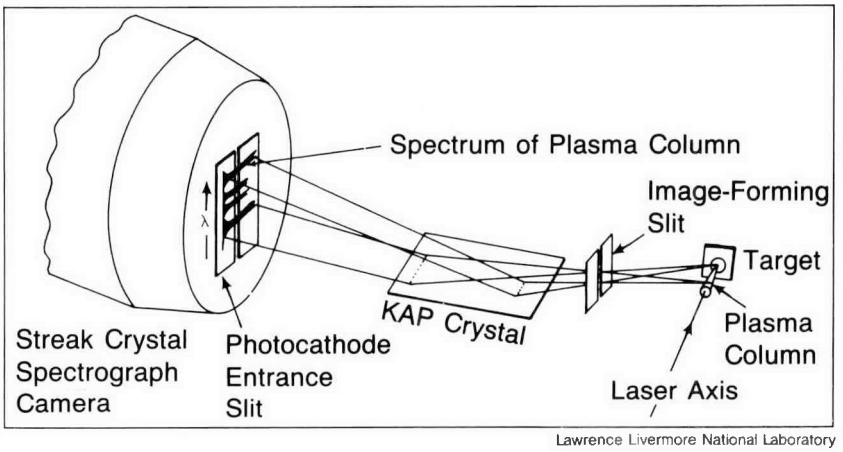

Fig. 1-31. One of the most important diagnostic instruments is the streak crystal spectrograph camera (SCSC). It records spectra emitted from a spatially selected region of the plasma column, with a time resolution of 60 ps over a time interval of 2.4 ns. The SCSC provides high spatial, temporal, and energy resolution.

The SCSC records spectra emitted from a spatially selected region of the plasma column, with a time resolution of 60 ps over a time interval of 2.4 ns. A framing crystal x-ray spectrometer (FCXS),[58] which provides spatially resolved spectra of the entire plasma column over a time interval of 100 to 250 ps, is used to complement the SCSC measurements.

As the spectral measurements are made, four-frame holographic interferograms are obtained that "bracket" the time during which the spectra are recorded. Thus, we have both temperature and density information with which to "calibrate" temperature- and density-sensitive line ratios directly and line-ratio simulation codes indirectly.

Two x-ray pinhole cameras are used. One, at 45° to the laser axis, provides a measure of the irradiated spot size; the other, at 90° to the laser axis, yields information on the position and spatial extent of the blow-off plasma.

The target diagnostic instruments are shown in Fig. 1-32. The instruments are viewed end-on in a plane that is normal to the laser axis and contains the target.

Types of Targets. Targets for the series consisted of four types:

1. Thick magnesium slabs.
2. Magnesium dots (100, 75, and 50 μm in diameter, and 3 to 5 μm thick) on thick polystyrene substrates.
3. Magnesium dots (100, 75, and 50 μm in diameter, and 3 to 5 μm thick) on thick silicon substrates.
4. Salts of sodium (100 μm in diameter) on polystyrene substrates.

The magnesium slabs were used to align the four spectrographs (i.e., the SCSC, the FCXS, and the two time-integrating,

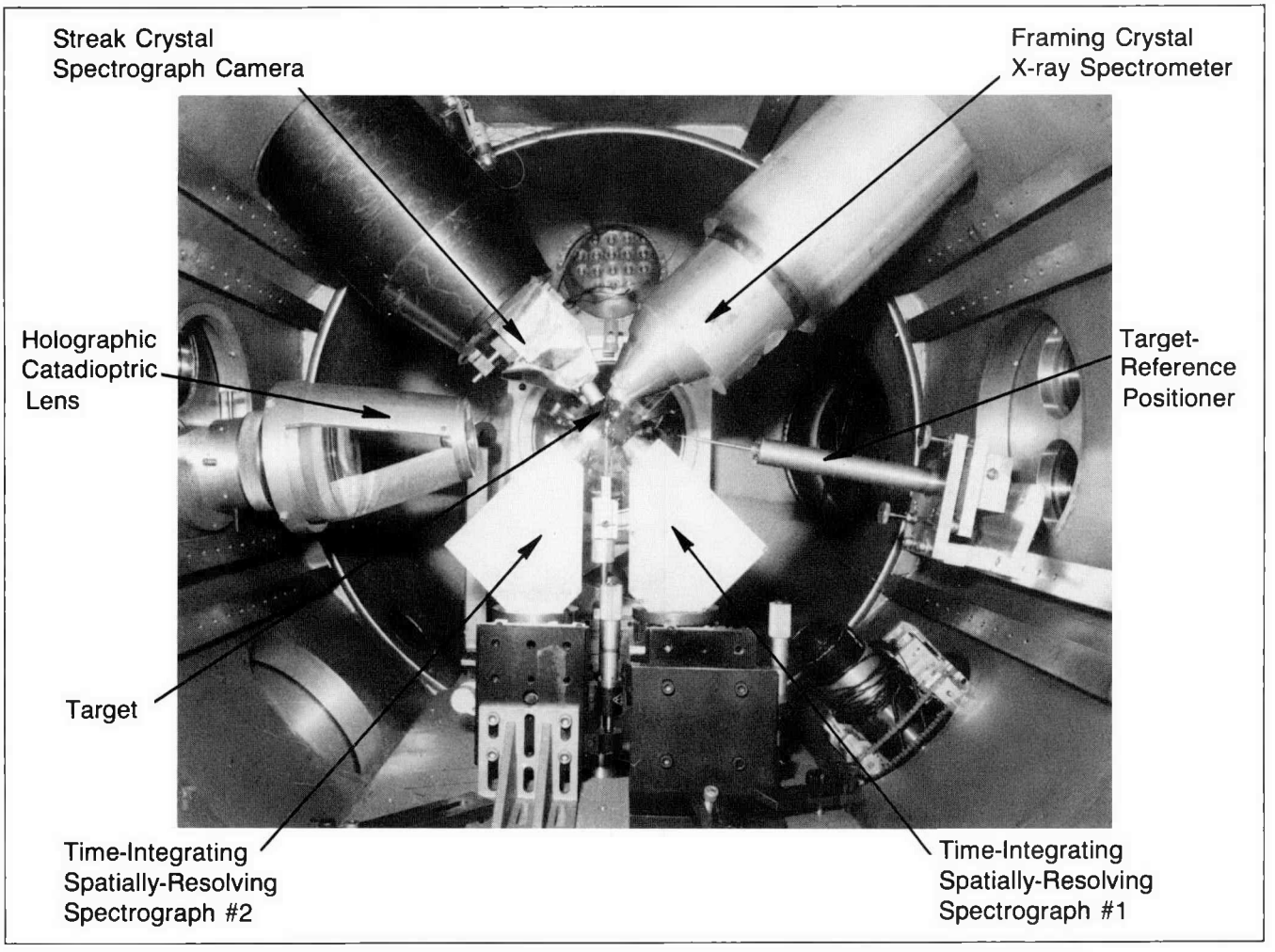

Fig. 1-32. Characterization of the plasma in these experiments requires many diagnostic instruments looking at the plasma. The time-resolved, spatially resolved streak crystal spectrograph camera views the emitting plasma from a small length of the plasma column, allowing spectral lines and continua to be recorded; the framing crystal x-ray spectrometer provides spatially resolved spectra of the entire plasma column over a time interval of 100 to 250 ps; the time-integrating, spatially resolving spectrographs resolve intensity variations along the length of the plasma column; and the holographic interferometer provides independent density measurements at four different times. Two x-ray pinhole cameras (not shown) yield information on the irradiated spot size and the position and spatial extent of the blow-off plasma.

spatially resolving spectrographs) and to establish the magnesium dot diameters and irradiance conditions necessary for the spot spectroscopy. The magnesium dots on silicon were used in target shots designed to establish the electron density distribution of the magnesium plasma column within a confining blow-off plasma of a substrate whose atomic number was similar to that of the metal dot. Shots with magnesium dots on polystyrene were designed to examine the electron density profile of the magnesium plasma column within a confining plasma substrate material of substantially different (average) atomic number than that of the dot. Finally, sodium salts, such as $NaNO_3$, were used to provide hydrogen-like free/bound continua in nearly the same spectral range used by the spectrographs in recording spectra of magnesium.

Preliminary Results

Within constraints imposed by the allowed distances of the four spectrographs, we found that the 50 μm diameter dot targets did not yield sufficient x-ray flux to be useful, even though they would have provided spectra with higher resolution than the 75 or 100 μm diameter dot targets. Sufficient spectral resolution for clear resolution of the ^{3}P line from the ^{1}P line of magnesium He_α was possible for the 75 and 100 μm diameter dots. The laser and diagnostic parameter ranges that were used in the present series are listed in Table 1-1.

Figure 1-33 represents a typical spectrum obtained with a time-resolving, spatially resolving spectrograph. It is a spectral streak record for a shot in which the SCSC was configured to view the magnesium plasma column region near the surface of a 100 μm diameter magnesium dot on a polystyrene target. The K-shell lines of helium-like and hydrogen-like magnesium are easily identifiable, as is the helium-like free/bound continuum. Not all of the hydrogen-like continuum is recorded because the spectral dispersion was too large for it to be contained within the allotted spectral range at the streak camera photocathode.

Table 1-1. Laser, Target, and Diagnostic Instrument Parameters

Laser and Target Parameters

Laser Wavelength: 0.53 μm
Laser Pulse Length: 1080 ps (nominal)
Irradiated Spot Diameter: 100 to 300 μm
Energy on Target: 10 to 70 J
Target Irradiance: 2×10^{13} to 8×10^{14} W/cm^2

Holographic Interferometer

Wavelength: 0.26 μm
Number of Frames: 4
Exposure Time/Frame: 20 ps
Holographic Probe Frame Times: 40 to 1940 ps
Holographic Probe Frame Intervals: 100 and 200 ps

Streak Crystal Spectrograph Camera

Photocathode: CsI
Target-to-Photocathode Distance: 14 cm
Crystal: KAP
Spectral Range: 4 to 9 Å
Spatially Resolving Slit: 70 μm
Target Magnification at Film: 7×
Recording Film: Kodak Royal X-Pan
Sweep Speed: 60 ps/mm on film
Time Resolution: 60 ps

Framing Crystal X-ray Spectrometer

Photocathode: CsI
Target-to-Photocathode Distance: 12.5 cm
Crystal: KAP
Spectral Range: 4 to 9 Å
Recording Film: Kodak Royal X-Pan and 2484
Number of Striplines: 3
Stripline Triggering: Auston Switch
Exposure Interval: 100 to 250 ps
Spatial Resolution: 50 μm at Target
Target Magnification at Film: 6.5×

Time-Integrating Spatially Resolving Spectrographs (2)

Crystal: TlAP
Recording Film: Kodak Direct Exposure Film
Target-to-Crystal-to-Film Distance: 14 cm
Spatially Resolving Slits: 5, 10, and 25 μm
Target Magnification at Film: 6×

Pinhole Cameras

	At 90°	At 45°
Magnification:	10	10
Film Distance:	18.2 cm	17.9 cm
Recording Film:	Kodak DEF	Kodak DEF

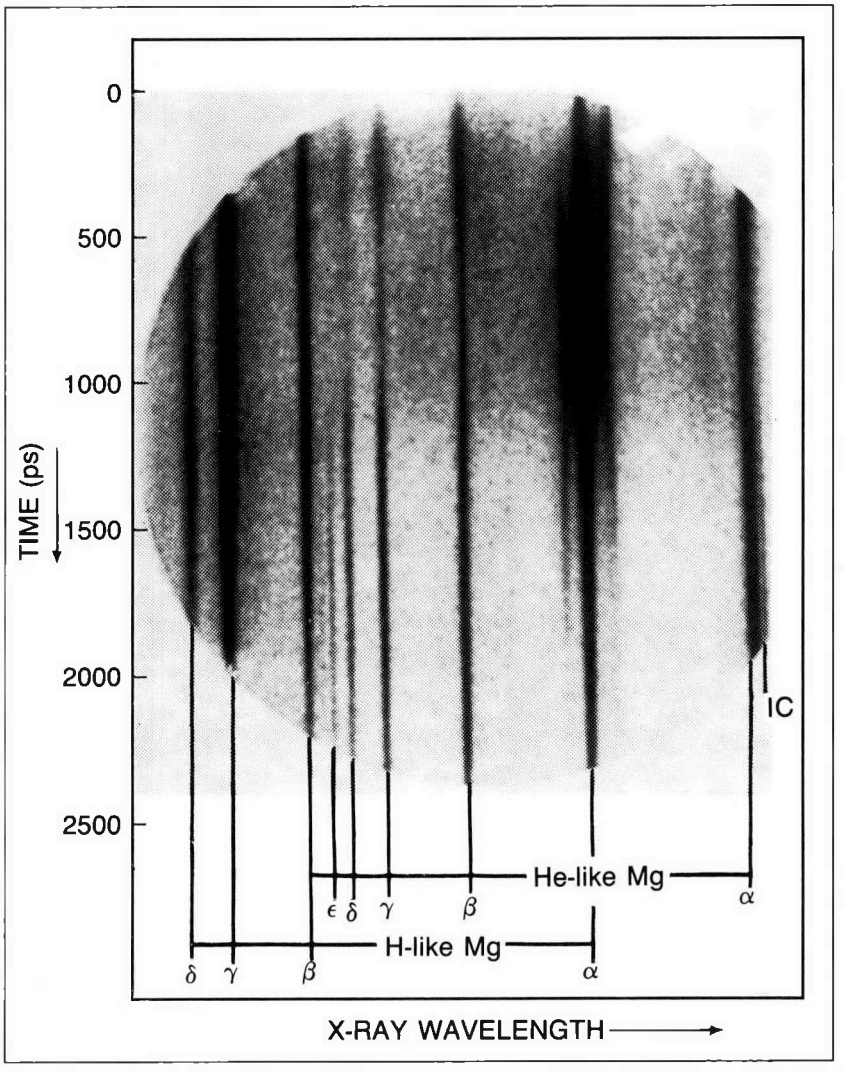

Fig. 1-33. This typical time-resolved magnesium spectrum was recorded by the streak crystal spectrograph camera, viewing the plasma column ~100 μm from the target surface. The target was a 100 μm magnesium dot on a polystyrene substrate. "IC" is the intercombination line.

Shifting the spectrum toward shorter wavelengths exposes the hydrogen-like continuum at the expense of the He_α lines.

Figure 1-34 shows three stripline spectra, each corresponding to a 150 ps exposure beginning, respectively, at 850, 1200, and 1600 ps for a FCXS film record for a typical shot. Scattering, associated with the cladding of the fiber-optic coupling to the film, produced discernible "halos" for the strong lines; these halos must be removed in processing the data for this diagnostic instrument. A later series of experiments will correct this shortcoming by replacing the fiber-optic with another having less observable scattering.

Our simultaneous time- and space-resolved spectra show the relative abundance of hydrogen-like and helium-like lines changing dramatically as a function of both space and time. We also see that the ^3P (2p−1s) intercombination line has a definite spatial dependence. Further, lithium-like dielectronic satellite lines

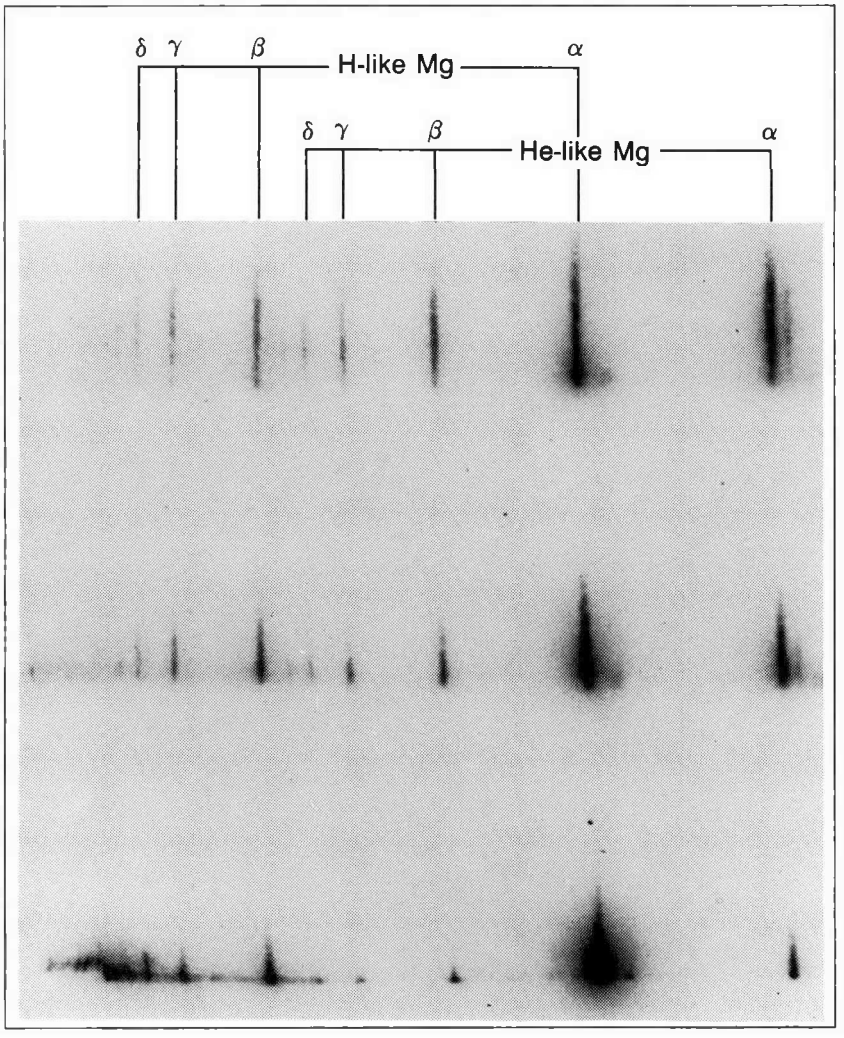

Fig. 1-34. These typical spatially resolved magnesium spectra of the entire plasma column were recorded by the framing crystal x-ray spectrometer. The duration of exposure at any wavelength was ~150 ps. Exposures were begun at (bottom to top) 850, 1200, and 1600 ps, respectively, for the three spectra.

appear only near the critical surface. We do not see satellites in the plume (beyond 100 μm) even though our measurements indicate a temperature (100 to 200 eV) at which they should appear.

Electron density profiles for both $NaNO_3$ and magnesium dot targets have been determined from interferometry. The density for the $NaNO_3$ target at 100 μm from the critical surface is 5 to $10 \times 10^{20}/cm^3$, decreasing exponentially to $2 \times 10^{19}/cm^3$ at distances of 500 to 900 μm farther out in the plume. Magnesium dot targets, irradiated similarly, yield almost identical results. Densities determined from the ratio of $He_\beta/^3P$ (2p–1s) spectral lines using SPECTRA,[59] as seen in Fig. 1-35, are approximately a half-decade lower than the interferometry measurements.

Electron temperature profiles for $NaNO_3$ slab targets were obtained using the slope of the hydrogen-like free/bound continuum. As shown in Fig. 1-36, the electron temperature for times after the laser is off is 300 eV near the critical surface,

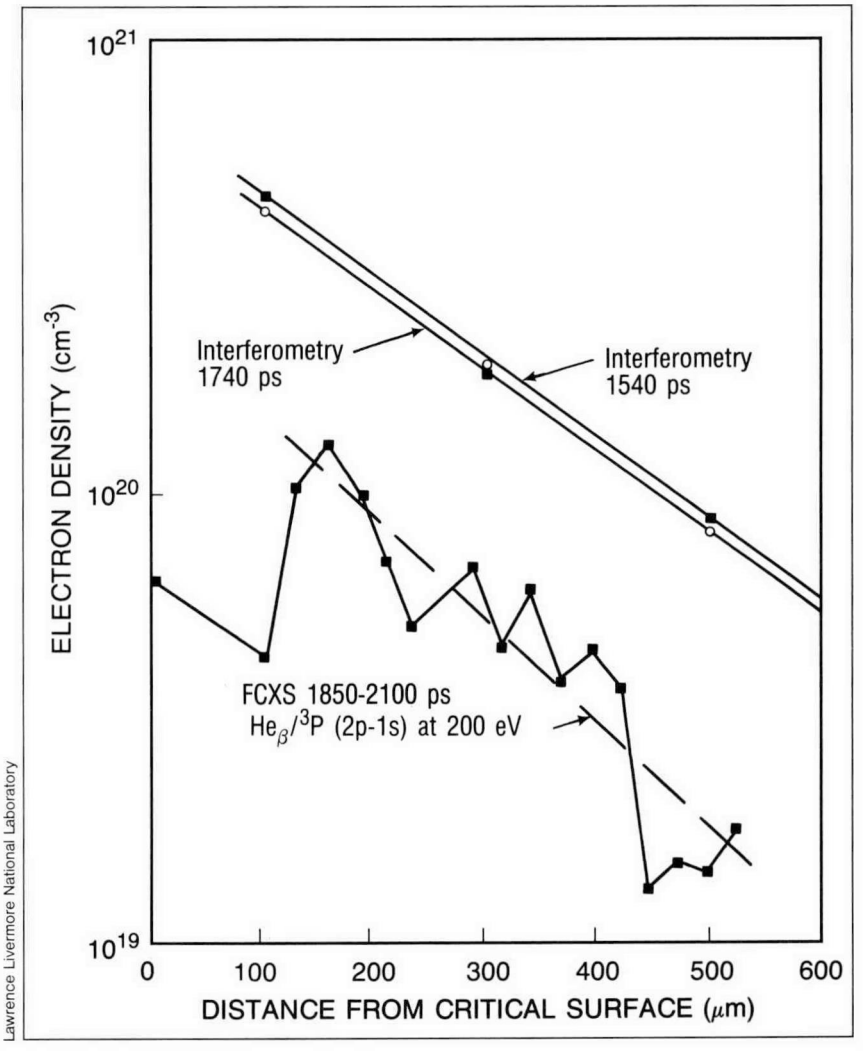

Fig. 1-35. Axial electron density profiles for shot 8087-3 as measured by holographic interferometry and the framing crystal x-ray spectrometer (FCXS) are compared. The target was a 100 μm diameter magnesium dot on a $(CH)_n$ substrate that was irradiated at an intensity of 6.8×10^{13} W/cm^2.

decreasing to 100 to 290 eV at distances of 200 to 500 μm out in the plume. In comparison, the line-ratio measurements, using He_β/Ly_β and He_γ/Ly_γ ratios of magnesium, follow the general profile shape of the free/bound continuum measurements but yield temperatures, via SPECTRA, 200 to 300 eV higher at comparable distances from the critical surface.

The discrepancies between the code-dependent line-ratio measurements and independent determinations of both density and temperature may be due to the transient nature of the laser-produced plasmas used in the present experiments; the steady-state atomic physics are not strictly applicable for these plasmas. It is also possible that quasi-equilibria do indeed exist in our laser-produced plasmas but that the atomic physics code we are using is not adequately configured.

In a later series of experiments, the density and temperature measurements obtained via K-shell spectroscopy will be repeated

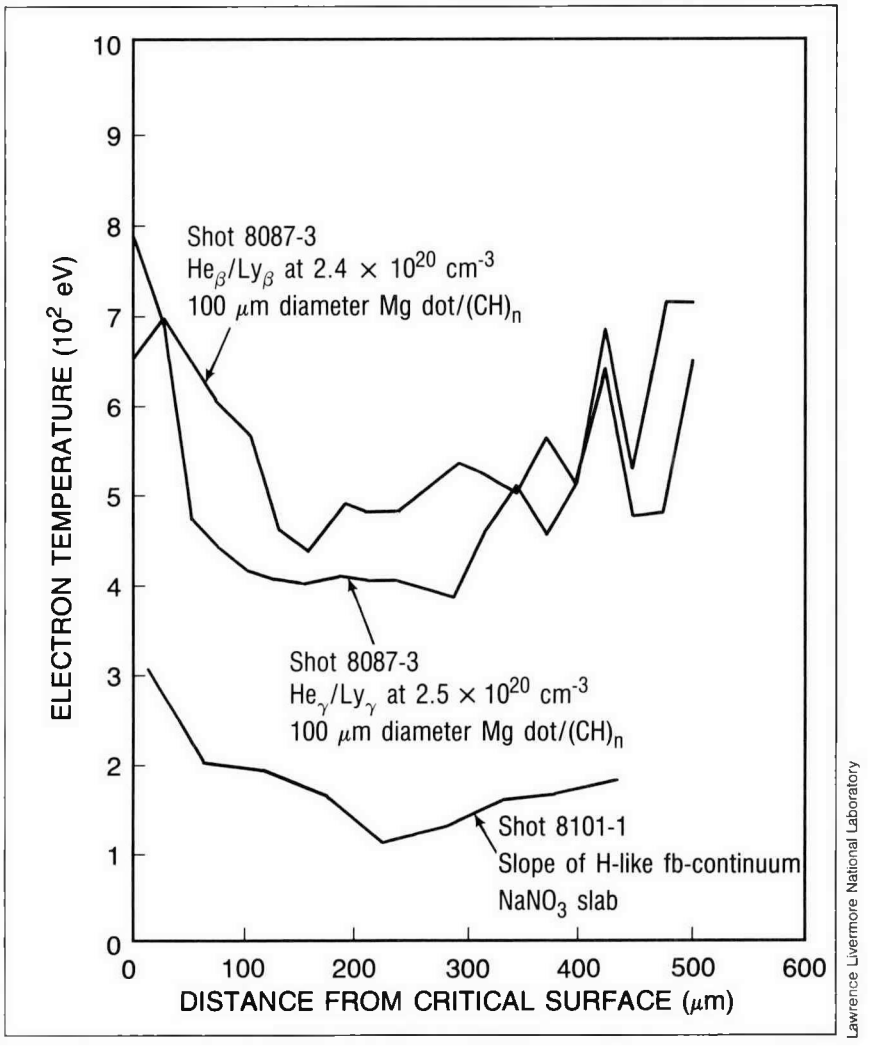

Fig. 1-36. The electron temperature profile as measured by the spectral line ratio method (using He_β/Ly_β and He_γ/Ly_γ ratios of magnesium) is compared with the slope of the hydrogen-like fb-continuum of sodium. Data are from the framing crystal x-ray spectrometer at 1850 to 2100 ps; the intensity was 6.8 to 7.1 × 10^{13} W/cm^2.

as a means of characterizing L-shell lines of yttrium, for example, or other elements with L-shell lines in the 4 to 9 Å wavelength range. In addition, attempts will be made to obtain temperatures and densities of exploding foil plasmas using the K-shell techniques learned in the present series.

For additional information, please contact Dr. G. Charatis

SECTION 1.7

The Automation of X-Ray Calibration: XCALIBR II

KMS Fusion (KMSF) now has a fully automatic x-ray diagnostic calibration facility, XCALIBR II. This facility covers the energy range of 0.184 to 9.75 keV and adds significantly to the abilities provided by XCALIBR I, our earlier manually operated calibration system.

While both systems can measure film sensitivity, crystal integrated reflectivities, and detector sensitivities, XCALIBR II allows the calibration of crystal rocking curves and microchannel plate angular quantum efficiencies, which could not be performed on XCALIBR I. Further, its automation relieves the need for continuous operator observation and enhances the efficiency of our facility.

All operations of XCALIBR II are monitored and controlled by an IBM® PC-XT (see Fig. 1-37). The test instruments are placed in a 50 cm diameter vacuum chamber. A separate chamber, which has two 6 in. ports at right angles in the same plane, contains a point x-ray source. One of the ports connects it to the test chamber (the other links it to diagnostic instruments). The x-ray source vacuum and the chamber vacuum are controlled independently. The system also includes an EG&G Ortec Multiplexer and MCA emulation software. Pumping is performed with sorption pumps, a cryo pump, and an ion pump, ensuring

Fig. 1-37. XCALIBR II is a fully automated x-ray calibration facility that covers the energy range from 0.184 to 9.75 keV. All XCALIBR II operations are monitored and controlled by an IBM® PC-XT. The facility includes a vacuum chamber for test instruments, a point x-ray source, and a variety of pumps.

a clean, oil-free environment. Optical interfaces connect the PC and the electromechanical system to prevent spurious commands caused by electromagnetic interference.

Software controls are written in Assembler and Basic and consist of a "monitor" and a "control" program. The monitor program has eight checking routines, which continuously operate in the background, noting nearly 20 separate system conditions. These include such items as gate valve positions, water flow, chamber pressure, and cryo pump temperature. Based upon these conditions, the program will prevent an operator from damaging equipment in an attempt to open valves at the wrong time or to turn on source high voltage at too high a pressure. The control program operates in the foreground and permits the toggling of 10 separate controls on XCALIBR II. Thus, a pump-down procedure can be initiated automatically, gate valves can be opened, the x-ray source filament and high voltage can be turned on, and the entire system shut down—all from the PC terminal. These controls have been conveniently identified with the 10 function keys on the keyboard.

The display shown in Fig. 1-38 represents the system condition in real time and reflects the working of the monitor program. The function keys may be used whenever this diagram is being

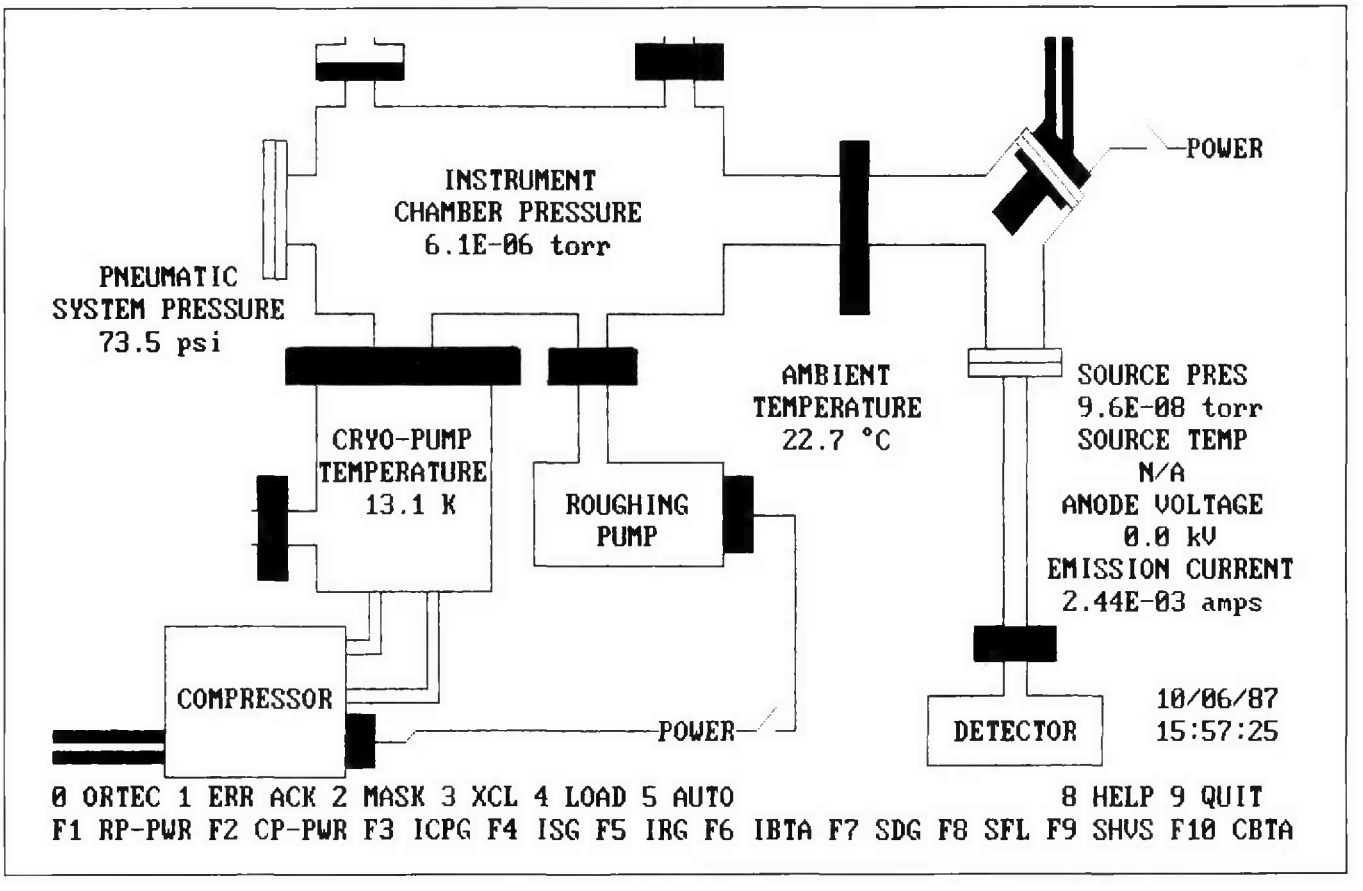

Fig. 1-38. This display represents the system condition in real time and reflects the working of the monitor program. The second-to-last line on the screen lists the mnemonics that represent various control options.

displayed. However, if pressing a function key will directly result in creating a dangerous system condition, then a message telling the operator that the request has been denied will be displayed across the screen, along with the reason for the denial. The second-to-last line on the display screen lists the mnemonics that represent various control options. These options perform such functions as initiating the Ortec MCA program, cheating interlocks in the control program, disabling checking routines in the monitor program, and defining automatic control sequences to perform specific tasks.

The x-ray source in XCALIBR II is a 100 W thermoelectrically cooled, rotatable anode soft x-ray tube of KMSF design (patent #46 851 198 487). Two 75 W coolers rapidly conduct the heat away from the electrostatically focused electron beam on the surface of the cylindrical anode. As shown in Fig. 1-39, the heat is ultimately conducted away by a water manifold, but the thermoelectric coolers permit anode rotation without any rotating water-vacuum seals. Different anode materials can be placed upon the anode to enable the production of many different x-ray energies without breaking vacuum.

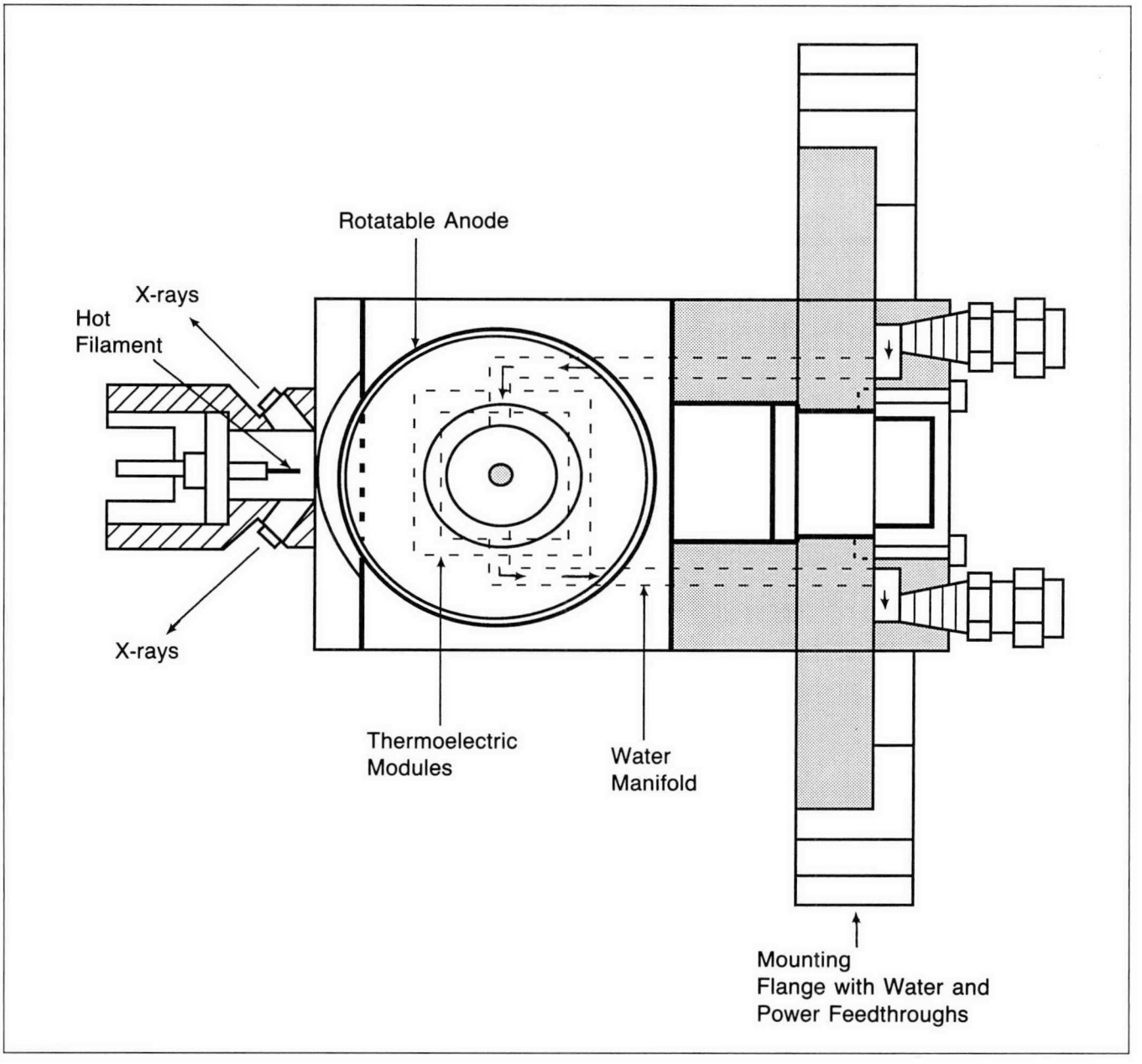

Fig. 1-39. The x-ray source in XCALIBR II is a 100 W thermoelectrically cooled, rotatable anode soft x-ray tube of KMSF design. Two 75 W coolers rapidly conduct the heat away from the electrostatically focused electron beam on the surface of the cylindrical anode. The heat is ultimately conducted away by a water manifold, but the thermoelectric coolers permit anode rotation without any water-vacuum seals.

For additional information, please contact Dr. P. D. Rockett

SECTION 1.8

Crystal R_c Calibrations with an Uncollimated, Point X-Ray Source

The practical application of Bragg crystals in x-ray spectroscopy frequently involves the deduction of incident energy in specific x-ray lines. This has been particularly characteristic of recent x-ray laser studies,[60–63] but the need for such absolute measurements reaches into many other scientific fields.[10,64] The original "rocking curve" technique for measuring reflectivity from a Bragg crystal is not suitable for x-ray spectroscopy measurements because x-ray sources frequently have an angular extent that is greater than the crystal rocking curve. Thus, the use of crystal integrated reflectivity R_c to infer incident flux becomes mandatory.

The common technique for measuring Bragg crystal R_c requires a well-collimated input beam and a collimated detector[65–67] to measure a detailed rocking curve, and then integrating under that curve. Such measurements require an expensive apparatus and accuracies of seconds of arc. We have developed a method to measure R_c readily with an uncollimated, filtered, point x-ray source. Using this technique, integrated reflectivities can be performed with arc minutes of resolution. In fact, only 10 to 20 arc minutes of resolution is required to characterize the single crystal R_c fully.

Theoretical Analysis of Flat Crystal Reflection

The concept of "integrated reflectivity" derives explicitly from the Prins function $P(\theta)$, a measure of the crystal rocking curve.[66] As a result, many researchers use the techniques of rocking curve measurements to determine R_c. Ideally, rocking widths are measured with a monochromatic, perfectly collimated x-ray beam incident on a crystal. The crystal is rotated (or rocked) through angles near the Bragg angle θ_0, producing a diffracted beam that varies as $P(\theta)$. Since rocking widths can be in the 10 to 60 arc second range, much care goes into building highly accurate θ-2θ tables and expensive grid collimators. Simpler systems attempt to measure only R_c, but still retain collimation at the arc minute level using Soller slits. With a finely adjusted rotation, one obtains a curve that convolves $P(\theta)$ with the collimation function. Upon integration, this curve should yield R_c since area will be conserved.

Simply expressed, the integrated reflectivity can be written as

$$R_c = \int_0^{\pi/2} P(\theta)\, d\theta \tag{49}$$

where the full width at half maximum (FWHM) of $P(\theta)$ is the crystal diffraction width or the rocking curve. The limits are pedantic since the integrand rapidly tends to zero away from the Bragg angle. With finite divergence of the incident beam, Eq. (49) becomes

$$R_c = \int_0^{\pi/2} \int_{\phi_1}^{\phi/2} G(\phi) P(\phi) d\phi d\theta \ , \tag{50}$$

where $G(\phi)$ represents the collimation function. $G(\phi)$ can frequently be described as a Gaussian function, while $P(\theta)$ behaves as a Lorentzian distribution.[63] Their convolution yields a profile characterized by a Voigt function. In cases where ϕ is much greater than the rocking width, the Gaussian collimation function will dominate.

In some applications (laser plasmas, synchrotron radiation) the x-ray source is virtually a point source. Its reflection from a crystal is described in Fig. 1-40 as the diffraction of a wide beam of width W and angular divergence $d\phi$ at the surface of the crystal. The source of intensity I_0 (photons/sec-srad) sits a mean distance p from the crystal, and the detection plane follows at a distance q. Length along the plane of dispersion is measured in differential units as ds.

Since most applications of R_c occur in this geometry, we may use the same geometry for calibration of R_c. The differential number of photons dN in a differential element wavelength $d\lambda$ intercepted and diffracted by the crystal of Fig. 1-40 is

$$\begin{aligned} dN &- S(\lambda,\Omega) d\lambda P(\theta,\lambda)(pW\, d\theta/p^2) \\ &= S(\lambda,\Omega) d\lambda P(\theta,\lambda) W\, d\theta/p \ , \end{aligned} \tag{51}$$

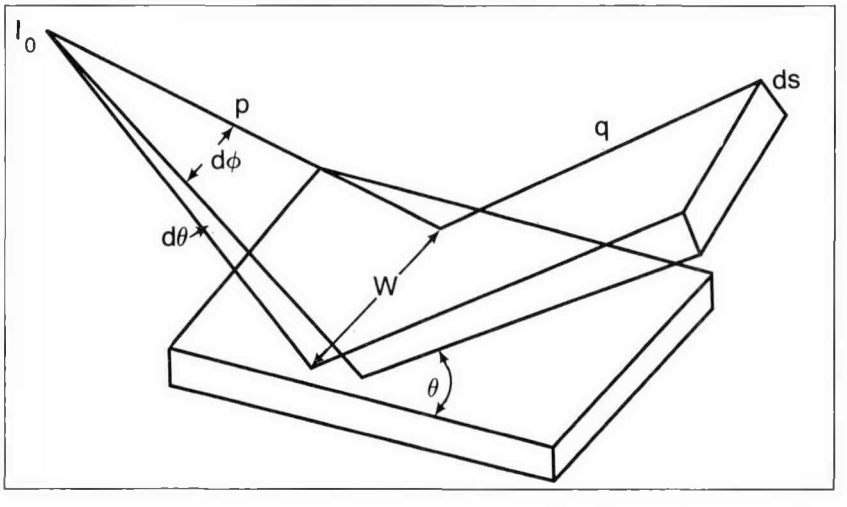

Fig. 1-40. In some applications the x-ray source is virtually a point source. Its reflection from a flat crystal is depicted here as the diffraction of a wide beam of width W and angular divergence $d\phi$ at the surface of the crystal. The source of intensity I_0 (photons/sec-srad) sits a mean distance p from the crystal, and the detection plane follows at a distance q. Length along the plane of dispersion is measured in differential units as ds.

where $S(\lambda,\Omega)$ is the number of photons/srad-dλ and $W\,d\theta/p$ is the diffracted solid angle. The left side of Eq. (51) can be written as

$$I(s)dA = dN \ , \tag{52}$$

where $I(s)$ is the number of photons/cm^2 striking the detector along the direction of dispersion. In Fig. 1-40, the exposed area in the detector plane is $dA = ds\,W(p+q)/p$, which, upon substitution in Eq. (51), yields

$$P(\theta,\lambda)d\theta = \frac{LI(s)ds}{S(\lambda,\Omega)d\lambda} \ , \tag{53}$$

where $L = p + q$ has been used.

If our photon counting detector has a width of s, then upon integration of Eq. (53), we have

$$\int P(\theta)d\theta = R = \frac{L\int_{s_1}^{s_2} I(s)ds}{\int_{\lambda_1}^{\lambda_2} S(\lambda,\Omega)d\lambda} \ , \tag{54}$$

where it is assumed that the Prins function varies only slightly over the wavelength range of interest. The limits of integration on the right side are, of course, intimately linked. In particular, the differentials are related through the Bragg relation, so that

$$ds = \frac{Ld\lambda}{2d\cos\theta} \ . \tag{55}$$

Thus the choice of the range of s determines the choice of limits of λ. In practice, this means that one must be careful to measure the source function $S(\lambda,\Omega)$ with as much energy resolution as possible.

Multiplying and dividing the numerator of Eq. (54) by the height of the detector, H, results in the final working equation,

$$\int P(\theta,\lambda)d\theta = R(rd) = \frac{(L/H)\int I(s)dA}{\int S(\lambda,\Omega)d\lambda} \ , \tag{56}$$

from which a measurement of integrated reflectivity can be made. The integral in the numerator represents the total number of photons diffracted from the crystal, while the integral in the denominator represents the incident photons/srad in the wavelength band of interest. As noted in the preceding paragraph, a measurement of a given detected band after the crystal must be correlated with a measurement of the incident x-ray flux in the same band.

Experimental Measurements of Crystal Reflectivity

Equation (56) fully describes the measurement of R_c. A high-resolution ultra-thin window Si(Li) detector can measure the incident flux per unit bandwidth per unit solid angle, and a proportional counter can measure the reflected flux from the crystal at a given angle. The size of the proportional counter window determines the detected wavelength band, which then is used to establish regions of interest in the incident spectrum.

Our x-ray source consists of a directly excited tube followed by K- or L-edge filters. The tube is extremely low power, consuming at most 1 W, and was built by J. E. Manson, Inc. Anodes are formed primarily by pressing rods of the characteristic material of interest into a copper support. Filters are either evaporated or self-supporting foils, designed to transmit roughly 40% of the desired x-ray line.

Bremsstrahlung continuum is the primary source of error with this measurement technique. Even the Si(Li) detector cannot remove all the continuum from beneath the observed line used for calibration. Thus one must infer the proper continuum contribution from looking at the complete spectrum. Subtraction of the bremsstrahlung removes a source of error, which varies from 10 to 70% depending on the x-ray tube's accelerating voltage. Evans and Leigh[66] show that one can even use the crystal itself to find the strength of the background relative to the desired line. This depends simply on the fact that R_c does not vary strongly over small wavelength excursions.

Our calibration facility, named XCALIBR (see Section 1.7), consists of the Manson source, a Kevex ultra-thin window Si(Li) detector, a θ-2θ table, a subatmospheric proportional counter, and a Nuclear Data 62 multi-channel analyzer. We have used anodes of boron, silicon carbide, nickel, cobalt, copper, magnesium, aluminum, silicon, scandium, titanium, and zinc. The resulting lines span the range from 0.184 to 9.57 keV, including oxygen K_α at 0.523 keV.

The reduction of absolute fluxes from the Si(Li) detector required a careful characterization of detector sensitivity and area. Side-by-side comparisons were made with the subatmospheric proportional counter at a variety of photon energies. The results are depicted in Fig. 1-41 along with a computed sensitivity curve fit to the experimental data.

Examples of measured flat crystal integrated reflectivities appear in Table 1-2.

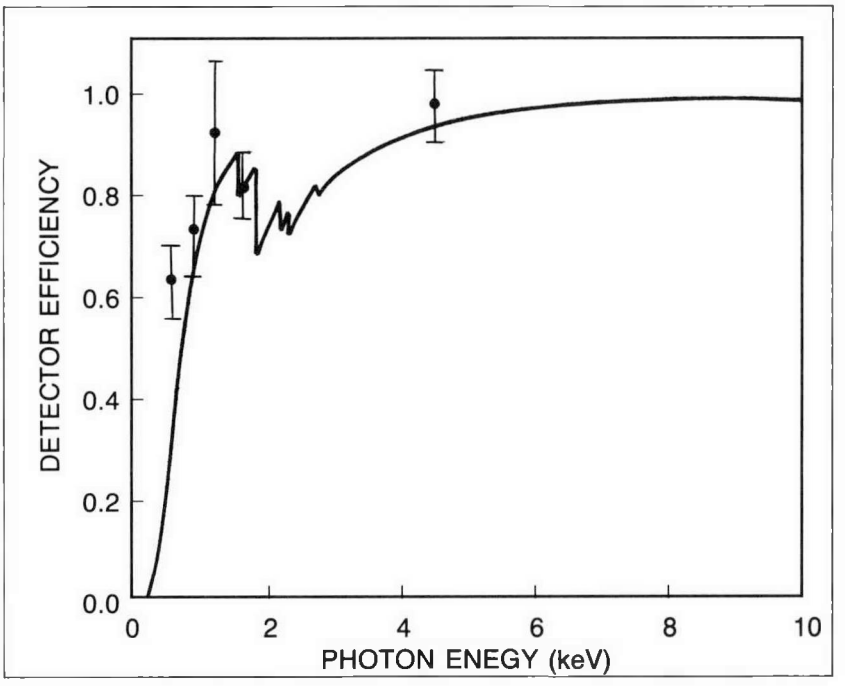

Fig. 1-41. Our calibration facility incorporates a Kevex ultra-thin window Si(Li) detector to measure the incident flux per unit bandwidth per unit solid angle. The reduction of absolute fluxes from the Si(Li) detector required a careful characterization of detector sensitivity and area. Side-by-side comparisons were made with the subatmospheric proportional counter at a variety of photon energies. The results are shown here along with a computed sensitivity curve fit to the experimental data. The solid curve is a calculation that assumed 100 nm parylene N, 100 nm aluminum, 0.02 nm gold, 300 nm SiO, and 500 μm of silicon.

Table 1-2. Measured Flat Crystal R_c (rad)

Crystal	at Wavelength (Å)				
	13.3	8.33	7.13	2.75	2.51
Beryl 1010 #1	1.75×10^{-5}	3.60×10^{-5}	–	–	–
Beryl 1010 #2	1.96×10^{-5}	3.50×10^{-5}	–	–	–
Beryl 1010 #3	2.20×10^{-5}	3.44×10^{-5}	–	–	–
Beryl 1010 #4	2.13×10^{-5}	3.60×10^{-5}	–	–	–
LiF 200 #1	–	–	–	1.42×10^{-4}	1.83×10^{-4}
LiF 200 #2	–	–	–	1.56×10^{-4}	1.30×10^{-4}
Si 111 #1	–	–	–	5.70×10^{-5}	–
Si 111 #2	–	–	–	5.90×10^{-5}	–
PET 002	–	–	1.90×10^{-6}	–	–

For additional information, please contact Dr. P. D. Rockett

REFERENCES

1. S. E. Bodner, *Journal of Fusion Energy* **1** (1981), p. 221.
2. K. A. Brueckner and S. Jorna, *Rev. Mod. Phys.* **46** (1974), p. 325.
3. R. J. Mason and R. L. Morse, *Phys. Fluids* **18** (1975), p. 814.
4. *KMS Fusion 1982 Annual Technical Report on Inertial Fusion Research*, Report KMSF-U1317, KMS Fusion, Inc., Ann Arbor, MI, p. 20.
5. *KMS Fusion 1985 Annual Technical Report on Inertial Fusion Research*, Report KMSF-U1728, KMS Fusion, Inc., Ann Arbor, MI, p. 13.
6. Ibid, p. 18.
7. D. T. Attwood, N. M. Ceglio, E. M. Campbell, J. T. Larsen, D. L. Matthews, and S. L. Lane, *Laser Interaction and Related Plasma Phenomena*, Vol. 5, edited by H. Schwarz, H. Hora, M. Lubin, and B. Yaakobi (Plenum Press, New York, 1981), p. 423.
8. M. C. Richardson, P. W. McKenty, R. L. Keck, F. J. Marshall, D. M. Robak, C. P. Verdon, R. L. McCrory, and J. M. Soures, *Phys. Rev. Lett.* **56** (12 May 1986), p. 2048.
9. D. L. Matthews et al., J. *Appl. Phys.* **54** (1981), p. 4260.
10. B. Yaakobi et al., "High x-ray conversion efficiency with target irradiation by a frequency-tripled Nd:glass laser," *Opt. Commun.* **38** (1981), pp. 196–200.
11. J. D. Kilkenny, B. J. MacGowan, and P. T. Rumsby, *Appl. Phys. Lett.* **43** (1983), p. 233.
12. *Annual Report to the Laser Facility Committee 1984*, Report RAL-84-049, Laser Division, Rutherford Appleton Laboratory, Chilton, Didcot, Oxon, 1984, p. a2.22.
13. *Annual Report to the Laser Facility Committee 1983*, Report RAL-83-057, Laser Division, Rutherford Appleton Laboratory, Chilton, Didcot, Oxon, 1983, p. 6.3.
14. Gar. E. Busch, C. L. Shepard, L. D. Siebert, and J. A. Tarvin, "Four-Frame Holographic Probing System for Plasma Density Measurements," *Rev. Sci. Instrum.* **56** (1985), p. 879.
15. W. B. Fechner, C. L. Shepard, Gar. E. Busch, R. J. Schroeder, and J. A. Tarvin, *Phys. Fluids* **27**, (1984), p. 1552.
16. R. F. Schmalatz, "New Self-Similar Solutions for the Unsteady One-Dimensional Expansion of a Gas into a Vacuum," *Phys. Fluids* **28** (1985), p. 2923.
17. B. Ahlborn and M. H. Key, Laboratory Report #73, Department of Physics, University of British Columbia, Vancouver, BC, February 1980.
18. F. J. Mayer, J. T. Larsen, and J. W. Steele, *Phys. Fluids* **26** (1983), p. 830.
19. D. W. Forslund and C. R. Shonk, *Phys. Rev. Lett.* **25** (1970), p. 281; E. A. Foote and R. M. Kulsrud, *Phys. Fluids* **24** (1981), p. 1532.
20. N. A. Krall and A. W. Trivelpiece, *Principles of Plasma Physics* (McGraw Hill, New York, 1973), pp. 482–494.
21. R. London and M. D. Rosen, "Hydrodynamics of Exploding Foil X-ray Lasers," Report UCRL-9405, Lawrence Livermore National Laboratory, Livermore, CA, February 1986.
22. J. R. Albritton, "Electron-Ion Collisions in Partially Ionized High-Z Plasmas," *Laser Program Annual Report—84*, Report UCRL-50021-84, Lawrence Livermore National Laboratory, Livermore, CA, 1985, pp. 3–50 through 3–54.
23. H. A. Baldis and C. J. Walsh, *Phys. Fluids* **26** (1983), p. 1364.
24. J. Meyer and H. Houtmann, *Phys. Rev. Lett.* **53** (1984), p. 1344.
25. S. J. Karttunen, *Phys. Rev. A* **23** (1981), p. 2006.

26. A. B. Langdon, B. F. Lasinski, and W. L. Kruer, *Phys. Rev. Lett.* **43** (1979), p. 133.

27. J. M. Kindel, D. W. Forslund, W. B. Mori, C. Joshi, and J. M. Dawson, "Computer Simulations on Two-Plasmon Decay," *15th Annual Anomalous Absorption Conference*, Banff, AB, June 23–28, 1985.

28. D. W. Forslund, J. Kindel, K. Lee, E. L. Lindman, and R. L. Morse, *Phys. Rev. Lett. A* **11** (1974), p. 579.

29. R. E. Turner, K. G. Estabrook, R. L. Kauffman, D. R. Bach, R. P. Drake, D. W. Phillion, and B. F. Lasinski, *Bull. Am. Phys. Soc.* **29** (1984), p. 1298.

30. D. J. Drake, "A Viewfactor Code for Solving Time-Dependent Radiation Transport Problems Involving Fluid Surfaces with Intervening Participating Media," Report KMSF-U1925, KMS Fusion, Inc., Ann Arbor, MI, December 1987.

31. D. J. Drake, "Comparison of Viewfactor Code Results with Analytic Solutions to a Time-Dependent Vacuum-Transport Problem," Report KMSF-U1668, KMS Fusion, Inc., Ann Arbor, MI, August 1985.

32. N. A. Hoffman, "New Analytic Solutions to a Time-Dependent Vacuum Transport Problem and their Comparison to Viewfactor and Monte Carlo Code Results," Report LA-CP-84-242, November 1984.

33. R. Siegel and J. R. Howell, *Thermal Radiation Heat Transfer* (McGraw Hill, New York, 1982), p. 551.

34. K. Brueckner et al., "TRHYD-1 Physics Second Edition," Report KMSF-U54, KMS Fusion, Inc., Ann Arbor, MI, 1972; P. M. Campbell, "Energy and Momentum Transfer in Dense Thermonuclear Plasmas," Report KMSF-U105, KMS Fusion, Inc., Ann Arbor, MI, 1973.

35. P. M. Campbell, "A Conservative Difference Method for Hydrodynamics and Heat Transport in Two-Temperature Plasmas," Report KMSF-U1698, KMS Fusion, Inc., Ann Arbor, MI, 1986.

36. L. Spitzer, *Physics of Fully Ionized Gases* (Interscience, New York, 1956).

37. H. Brysk, "Electron-Ion Equilibration in a Partially Degenerate Plasma," *Plasma Phys.* **16** (1974), p. 927.

38. H. Brysk, P. M. Campbell, and P. Hammerling, "Thermal Conduction in Laser Fusion," *Plasma Phys.* **17** (1975), p. 473.

39. P. M. Campbell, "A Variable Eddington Method for Radiation Transport in Dense Fusion Plasmas," Report KMSF-U458, KMS Fusion, Inc., Ann Arbor, MI, 1976.

40. G. Pomraning, "A Comparison of Various Flux Limiters and Eddington Factors," Report UCID-19220, Lawrence Livermore National Laboratory, Livermore, CA, 1981.

41. P. M. Campbell, "Relativistic Velocity Terms in Lagrangian Fluid Dynamics," Report KMSF-U1283, KMS Fusion, Inc., Ann Arbor, MI, 1982.

42. P. M. Campbell, "SNAPSHOT Calculations of Radiative Emission from Laser Heated Plasmas and Diagnostic Instrument Response," Report KMSF-U1130, KMS Fusion, Inc., Ann Arbor, MI, 1981.

43. P. M. Campbell, "Transport Effects of Interacting Hot and Cold Electrons in Laser-Heated Plasmas," *Fusion Technology* **9** (1986), p. 391.

44. P. M. Campbell, "Transport Phenomena in a Completely Ionized Gas with Large Temperature Gradients," *Phys. Rev. A* **30** (1984), p. 365.

45. H. Mayer, "Methods of Opacity Calculations," Report LA-647, Los Alamos National Laboratory, Los Alamos, NM, 1947.

46. R. More, "Electronic Energy Levels in Dense Plasmas," Report UCRL-85911, Lawrence Livermore National Laboratory, Livermore, CA, 1981; G. Zimmerman and R. More, "Pressure Ionization in Laser-Fusion Target Simulation," Report UCRL-81336, Lawrence Livermore National Laboratory, Livermore, CA, 1978.

47. J. W. Zink, "Shell Structure and the Thomas-Fermi Equation of State," *Phys. Rev.* **176** (1968), p. 279.

48. D. Post, "Radiative Cooling of Low-Density, High-Temperature Plasmas," *Atomic Data and Nuclear Data Tables* **20** (1977), p. 434.

49. W. Lokke and W. Grasberger, "XSNQ-U, a Non-LTE Emission and Absorption Coefficient Subroutine," Report UCRL-52276, Lawrence Livermore National Laboratory, Livermore, CA, 1988.

50. V. Zhdanov, "The Effect of the Electron Density on Dielectronic Recombination," *Sov. J. Plasma Phys.* **5** (1979), p. 320.

51. S. Glasstone and R. Lovberg, *Controlled Thermonuclear Reactions* (Van Nostrand Reinhold Company, New York, 1960).

52. R. Post, *Rev. Mod. Phys.* **28** (1956), p. 338.

53. W. R. Arnold et al., "Cross-Sections for the Reactions D(d,p)T, D(d,n)He^3, T(d,n)He^4, and He^3(d,p)He^4 below 120 keV," *Phys. Rev.* **93**(3) (1954), pp. 483–497.

54. E. Nardi, E. Peleg, and Z. Zinamon, "Energy Deposition by Fast Protons in Pellet Fusion Targets," *Phys. Fluids* **21** (1978), p. 21. See also the references therein.

55. S. R. Stone and J. C. Weisheit, "A Comparison of Various Codes in Computing the Charge-State Population of an Argon Plasma," Report UCID-20262, Lawrence Livermore National Laboratory, Livermore, CA, 1984.

56. M. J. Herbst et al., *Rev. Sci. Instrum.* **55** (1982), p. 1418.

57. P. G. Burkhalter et al., *Phys. Fluids* **26** (1983), p. 3650.

58. F. K. Young, R. E. Stewart, J. G. Woodworth, and J. Bailey, Report UCRL-94052, Lawrence Livermore National Laboratory, Livermore, CA, 1986.

59. R. W. Lee et al., "SPECTRA—A Model for K-Shell Spectroscopy," *J. Quant Spectrosc Radiat. Transf.* **32**(1) (1984), pp. 91–101.

60. P. G. Burkhalter, G. Charatis, and P. D. Rockett, "X-ray spectral line coincidences between fluorine K- and transition-metal L-series lines," *J. Appl. Phys.* **54**(11) (1983), pp. 6138–49.

61. D. L. Matthews et al., *Phys. Rev. Lett.* **54** (1985), p. 110.

62. P. G. Burkhalter, D. A. Newman, C. J. Hailey, P. D. Rockett, G. Charatis, B. J. MacGowan, and D. L. Matthews, "Spectroscopy of L-series transitions for x-ray laser photopumping," *J. Opt. Soc. Amer.-B* **2** (1985), p. 1894.

63. V. A. Bhagavatula, "Soft X-ray Population Inversion in Laser Plasmas by Resonant Photoexcitation and Photon-Assisted Processes," *IEEE J. Quantum Electron.* **QE-16** (June 1980), pp. 603–618.

64. M. Key, P. Rumsby, R. Evans, C. Lewis, J. Ward, and R. Cooke, *Phys. Rev. Lett.* **45** (1980), p. 1801.

65. A. Burek, "Crystals for Astronomical X-ray Spectroscopy," *Space Science Instrumentation* **2**(1-3) (1976), pp. 53–104.

66. K. D. Evans and B. Leigh, "The Absolute Calibration of the Reflection Integral of Bragg X-ray Analyser Crystals—Single Reflection Methods," *Space Science Instrumentation* **2**(1-3) (1976), pp. 105–123.

67. B. L. Henke, R. C. C. Perera, E. M. Gullikson, and M. L. Schattenburn, "High-efficiency low-energy x-ray spectroscopy in the 100–500 eV region," *J. Appl. Phys.* **49** (1978), pp. 480–494.

TARGET FABRICATION TECHNOLOGY

SECTION TWO

Scientific Editor, Dr. R. L. Downs

Introduction

Progress in target technology is critical to the advancement of the national inertial confinement fusion (ICF) program. This progress is sought on many fronts, including cryogenics, target fabrication, coating deposition, and characterization. We made significant accomplishments in each of these areas in 1986. In parallel with this research and development work, we produced and delivered the equipment needed for cryogenic experiments on the Omega laser, as well as a variety of targets for specific ICF experiments on the Nova, Omega, and Chroma lasers.

An important contribution in the area of cryogenics was the further development of the mathematical model for β-heating, which is discussed in Section 2.1. The focus of this year's β-heating modeling study was determination of the DT ice thickness uniformity that can be attained within a cryogenic target under experimentally achievable environmental conditions. This value depends on the physical characteristics of the target, the method(s) of mounting the target within an enclosure, and the thermal coupling of the target to the enclosure. These parameters have consequently been incorporated into our model. Early modeling results are encouraging: It appears that a practical target-mounting material and design should have almost negligible effect on the DT ice uniformity.

Most of this year's polymer shell development efforts were devoted to the production of the larger poly(vinyl alcohol) (PVA) shells that will be needed for future low preheat implosion experiments. Because we encountered difficulties producing target-quality PVA shells in the size range of interest, we conducted a systematic analysis of PVA shell production and developed a physical model of PVA shell formation. The model simulates the evaporation of methanol and water from a hollow drop of dissolved PVA. In general, the simulated results from the model were consistent with experimental results.

As the need for polymer shells with more fuel increases, identification of means to increase shell strength becomes even more important. We have known for some time that heating PVA shells increases their strength; several different heat treatments were compared this year to identify the conditions that produce the greatest increase in compressive strength. Of the treatment conditions examined, heating between 170 and 180°C in air for 15 min was most effective. A modest radiation-induced decrease in compressive strength was found for PVA shells filled with DT.

The ideal polymer shell would combine the best attributes of both PVA and polystyrene (PS). Consequently, work on hybrid shells is also underway. Using hybrid shells produced at Lawrence Livermore National Laboratory, we have found that the fuel retention of PVA-coated PS shells approaches that predicted for pure PVA shells of comparable dimensions. The temperature-dependent permeabililty of PVA to neon, a potential diagnostic gas, was also determined. Our work with polymer shells is the subject of Section 2.2.

Glass shells, which are discussed in Section 2.3, continue to be important to the ICF program. Currently, most of our glass shell fabrication efforts are focused on the production of hollow macrospheres that range from 2 to 10 mm in diameter. It is these larger shells that will be required for commercial energy production. However, we are also continuing to expand our basic knowledge of glass shell characteristics. This year, we evaluated the factors that affect the tensile strength of large (450 to 750 μm in diameter) glass shells. The extensive measurements taken in this study were used to produce a predictive model that can be used to set limits on the aspect ratio of shells that can be filled to any given fuel pressure.

The national program requires fuel shells with CH coatings that have ultrasmooth surface finishes; consequently, we concentrated on improving our understanding of glow discharge polymerization (GDP) and completing construction of a new parylene coating system that incorporates a plasma-assist capability.

We have encountered three areas of persistent difficulty in the application of GDP-CH coatings to glass shells: (1) reproducibility of the coating rate, (2) achievement of target-quality surface finish, and (3) adhesion of the coating to the target. Replacement of faulty equipment seems to have solved the reproducibility problem. While we have not yet eliminated surface roughness, we have identified several possible causes and are exploring solutions. While efforts to improve adhesion are continuing, results to date have been very satisfactory. This work has also led to a promising study of stress in films.

The coatings produced by GDP are hard, strong, and tough. For applications requiring a soft, elastic coating, parylene is used. In 1986, we constructed a new parylene coating system that is more efficient, easier to operate, and capable of coating larger substrates than our old system. We subsequently determined the operating conditions required for the production of smooth, pinhole-free films. This new system also incorporates a plasma-assist capability. This work is reported in Section 2.4.

The ability to characterize shells, coatings, and fuel layers accurately is vitally important. During 1986 we extended the capabilities of our three-dimensional ray-trace computer code for the analysis and prediction of classical interferometric fringe patterns for shells. As reported in Section 2.5, we can now simulate both single- and double-pass interferograms with this code. The code handles transparent hollow spherical fuel containers, either empty or filled with gaseous DT. The ability to model filled

shells is important, since interferometric images can change dramatically when fuel is present in a shell. The code can also generate fringe patterns corresponding to single-pass interferograms of shells containing condensed DT layers that are contiguous with the inner surface of the shell.

To determine the sphericity of cavities produced in glass samples, the first step in making the hollow macrospheres described in Section 2.3, we developed a white-light photographic technique and image-analysis procedure.

Evaluation of the cryogenic fuel layer (liquid or solid) in large or thick-walled targets will require a diagnostic technique that is less sensitive to the effects of the fuel container than is classical interferometry. Holographic interferometry is both more accurate and more sensitive than classical interferometry. Development work is underway at KMS Fusion (KMSF) to produce a holographic interferometry system for fuel layer characterization.

In 1984 KMSF agreed to assist the University of Rochester Laboratory for Laser Energetics (LLE) in preparing for a series of cryogenic target implosion experiments on their Omega laser by building a simulation chamber, cryogenic equipment, and ancillary hardware. This apparatus is described in Section 2.6. This year we finished the project, delivering the system in September. Acceptance tests conducted both at KMSF and at LLE verified that the system functioned as intended.

During 1986 we delivered ICF targets and target components to Lawrence Livermore National Laboratory (LLNL), to Los Alamos National Laboratory (LANL), and to LLE. While most requests were for spherical glass shells filled with D_2 or DT at pressures of 5 to 100 atm, other materials, geometries, and fill gases were also requested.

We also supplied a variety of targets for KMSF experiments. These included D_2-filled PVA shells and aluminum disks (for x-ray backlighting) for the Low Preheat Implosion Campaign, "spot" and "slab" targets of materials such as magnesium, silicon, aluminum, CaF, etc., for the x-ray spectroscopy series, and targets for five different classified experiments. The targets for each of these programs required us to develop new procedures and designs. This resulted in the overall extension of our target-support capabilities, and is detailed in Section 2.7.

SECTION 2.1

Inclusion of a Realistic Target Environment in the β-Heating Model

The formation of uniform solid or liquid layers of DT in inertial confinement fusion (ICF) targets is very important to successful cryogenic experiments. For targets with diameters up to a millimeter and fuel layers of a few micrometers, the fast-refreeze method[1] produces excellent results. For shells with multimillimeter diameters, however, this technique is not successful. Alternative methods must be developed.[2]

Modeling studies performed in 1985 encouraged us to pursue the application of β-heating (from tritium decay) to this problem. We investigated the effectiveness with which β-heating could drive the DT ice layer in a cryogenic target toward uniform thickness. This target was postulated to be suspended within an isothermal enclosure, and coupled thermally to this enclosure only by helium gas as a coolant. Under conditions that were clearly idealized, we determined that DT ice nonuniformity would decrease by approximately a factor of 10 every hour.[2] This result encouraged us to pursue this concept.

We continued to develop our β-heating model during 1986. Two questions required further clarification and definition: (1) What is the practical expectation for DT ice thickness uniformity under experimentally achievable environmental conditions within a cryogenic target? (2) What is the rate at which the DT ice can be redistributed to achieve this degree of uniformity? The answers to these questions depend upon the details of the target, the method(s) of mounting the target within an enclosure, and the thermal coupling of the target to the enclosure. Our 1986 studies were devoted to answering the first of these questions.

The equilibrium DT ice distribution is considered to have been attained when the temperature of the DT solid/vapor interface is the same at all points on the interface (i.e., when the interface is isothermal). In the nonideal world where the target must be physically supported, the DT solid/vapor interface will become isothermal, but the ice thickness will not necessarily be uniform. However, the degree of nonuniformity may be sufficiently small that the target can still be used for ICF experiments.

Target Mount

Several possible methods of mounting the targets within the cryogenic enclosure have been considered. These include a stalk support and a tent design that uses a membrane to encapsulate the target. The latter concept was selected as the more realistic

approach. Figure 2-1 shows a generic tented target. The thickness of the tent material, the perforation fraction of the membrane (the membrane is perforated to remove excess material), and the degree of tenting (i.e., the fraction of the target surface that is not in contact with the membrane) are design parameters. The tent membrane extends radially many diameters from the target at the equator, forming a plane of symmetry for the heat-transfer computations.

The Heat Transfer Problem

The transfer of the β-energy from the target to the isothermal enclosure is treated as conductive both for the membrane and for the gaseous helium. Because the thermal conductivity of the membrane is different (higher) than that of helium, the equilibrium DT ice distribution that gives an isothermal DT solid/vapor interface will be nonuniform. We have developed an algorithm to determine the equilibrium DT ice layer distribution.

For the initial set of computations, specific target and tent designs were selected, with membrane thickness as a parameter. (Because it can be a major influence on the distribution of the DT ice layer, the membrane was the initial focus of our study.) Figure 2-2 shows the details of the target at the beginning of the computation and the parameters that are involved in the heat-transfer computations. For the most general cases, a three-dimensional heat transfer code is needed. However, because of the symmetry of target design, the method of target mounting, and the isothermal enclosure, a two-dimensional axisymmetric heat transfer code is appropriate for this case. The two geometric coordinates are radius r and angle ϕ.

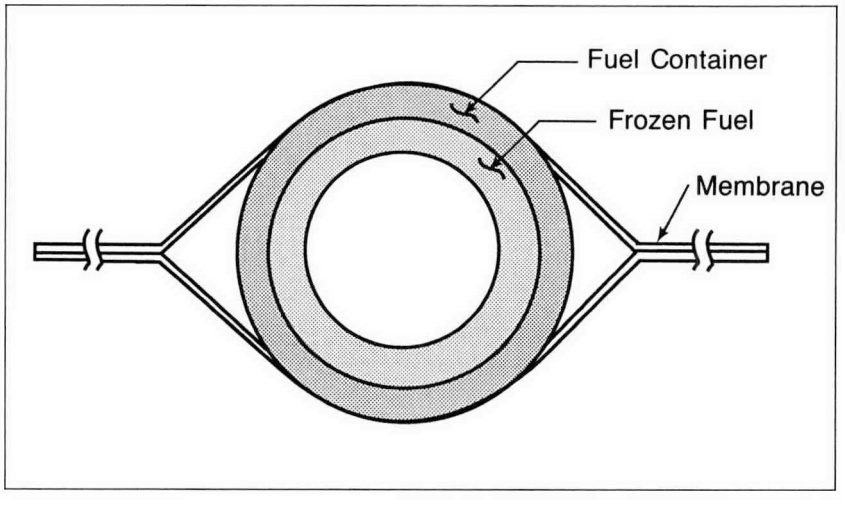

Fig. 2-1. Several different methods were evaluated for mounting the targets within the cryogenic enclosure. We ultimately decided to encapsulate the target within a thin membrane "tent." The tenting results in incomplete contact between the membrane and the fuel container (zero tenting means that the membrane is in complete contact with the external target surface).

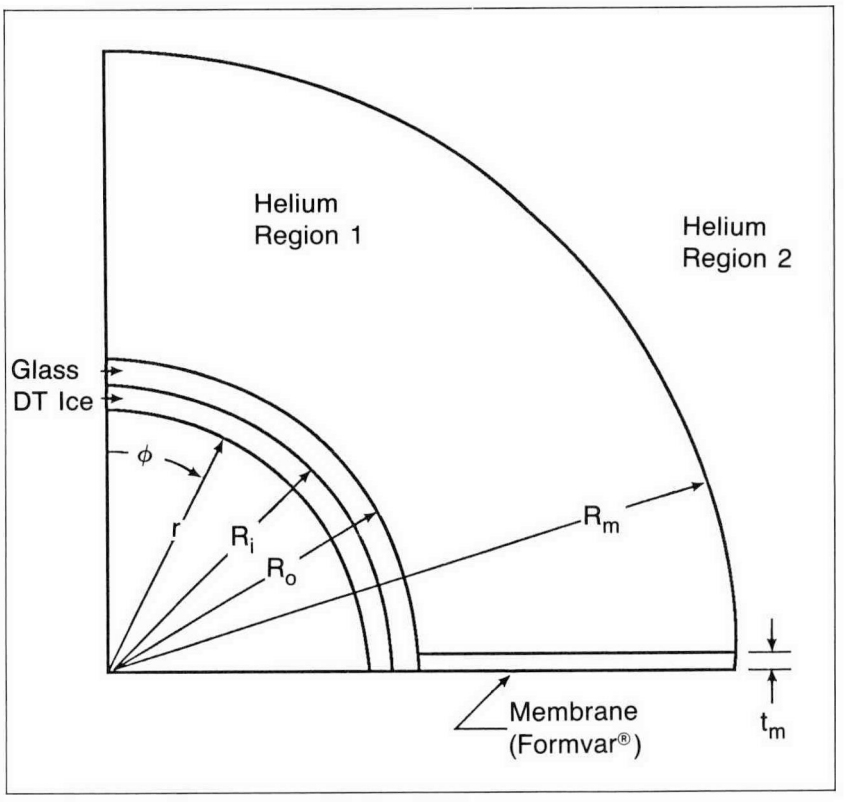

Fig. 2-2. A section of the membrane-supported target used in the heat-transfer computations discussed in the text is shown at the beginning of the computation. The inner radius of the target R_i is 0.48 cm. The outer radius of the target is represented by R_o, the membrane thickness by t_m, and the membrane radius by R_m; r and ϕ are defined in the text. The figure is out of proportion to enhance the details in the model.

Again referring to Fig. 2-2, the membrane extends away from the target at the equator. Any variation of the DT ice thickness can be expressed as a function of the angle ϕ, where ϕ varies from 0 at the pole (which is the axis of symmetry) to $\pi/2$ at the equator (which is the plane of symmetry).

Because of the computational demands, we chose to determine the value of a membrane radius R_m for which there is acceptable accuracy of results at a reasonable calculational effort. The value of R_m is such that increasing it further has little effect on the temperature at the base of the membrane at R_o. Within the limit of R_m, the heat transfer is two-dimensional. Beyond R_m, the heat transfer is treated as radial only, with the conduction limit of the Nusselt analogy applied at R_m.

Computations

As a brief review, the conduction limit is the dimensionless Nusselt number, Nu, equal to 2, where

$$Nu = 2 = \frac{hD}{k} ,$$

$$D = 2\,R_m$$

is the diameter of a sphere, h is the overall heat-transfer coefficient, k is the thermal conductivity of the medium (helium or the membrane), and all terms are in consistent units.

For the numerical computations, an initial DT ice distribution is set. The DT solid/vapor interface is defined by several radial nodes equally spaced between the pole and the equator. The ice/container interface is defined by R_i. The refrigerant, helium, is divided radially into two regions. Helium in region 1 is in contact with the outer surface of the fuel container at $R = R_o$ and with the fin-like surface of the membrane. The outer radius of region 1 is equal to the outer radius of the membrane R_m. Region 2 comprises the rest of the helium refrigerant and is an infinite heat sink. The DT ice has internal power generation by β-heating. Heat transfer within the ice, glass, and membrane occurs by conduction. Heat transfer across the DT solid/vapor boundary is prohibited. (The objective of this first computation is to determine the DT ice distribution that results in an isothermal solid/vapor interface within the cryogenic target; for an isothermal DT solid/vapor interface, there is no net sublimation anywhere in the target.)

At the outer edge of region 1, the overall heat transfer gradient is related to the Nusselt number. For that portion of the surface area corresponding to helium, the thermal conductivity of helium is used in the Nusselt number; for that portion of the surface area corresponding to the membrane, the thermal conductivity of the membrane is used in the Nusselt number. The model incorporates temperature-dependent properties. In the Nusselt number, then, the thermal conductivity is an average of that at the outer boundary of region 1 and that of the bulk material.

The Computer Code for Solving the Problem

To solve this heat equation, we have acquired a two-dimensional finite-element code called PLTMG. It uses an optimal speed multigrid method[3] to solve a class of nonlinear two-dimensional equations that includes our heat equation model. The code contains an automatic triangulation subroutine that divides the region of interest into triangular elements. It then solves the equation using a finite-element method that approximates the temperature distribution by piece-wise linear functions on the triangles.

To increase accuracy without increasing computer time any more than necessary, the code automatically refines the triangulation in areas where the solution changes abruptly. The code has several refinement levels; higher levels increase both computational requirements and the accuracy of the results.

Solving the Problem

As stated above, Fig. 2-2 shows the target at the beginning of the computation. The target was coated on the inner surface

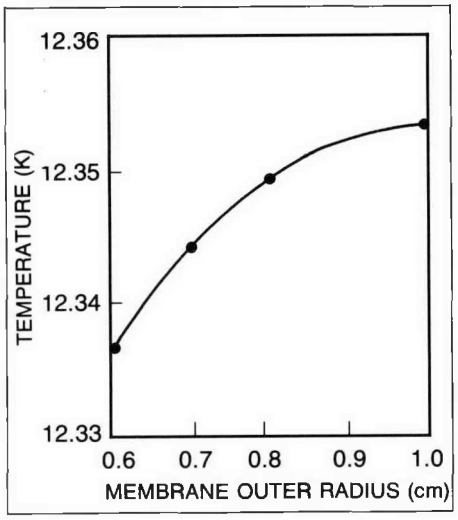

Fig. 2-3. For the heat-transfer computations, a value was needed for membrane radius R_m that would yield accurate results without requiring excessive computer time. A fairly thick (t_m = 50 μm) membrane was chosen in this initial calculation so that it would have a discernible effect on temperature and DT ice distribution. The value of R_m was varied from 0.6 to 1.0 cm. The resulting temperatures at the base of the fin are shown here. From these results, a value of 1.0 cm for R_m was selected. (Target dimensions are as in Fig. 2-2, and the Nusselt number is 2.0.)

with an initially uniform layer of DT ice, and the helium sink temperature was 10K.

Our first objective was to find a value for the outer radius R_m that would satisfy our accuracy requirements and, at the same time, not be so large that we would use excessive computer time. Our second goal was to investigate the effect of varying the thickness of the membrane t_m.

We chose a fairly thick membrane (t_m = 50 μm) for the membrane outer radius study; 50 μm was selected as a worst-case value, which would have a discernible effect on temperature and DT ice distribution. We varied the outer radius from 0.6 to 1.0 cm. The resulting temperatures at the base of the fin are shown in Fig. 2-3. From the results, we selected a radius of 1.0 cm for R_m for this portion of our studies.

Using an R_m value of 1.0 cm, we then varied the thickness of the membrane from 1.8 to 50 μm. The resulting temperature profiles along the solid/vapor interface of the uniform ice layer are shown in Fig. 2-4. The temperature profile is not affected by the presence of the 1.8 μm thick membrane. The 5 μm thick membrane, however, does have a slight effect on the temperature profile. As the thickness of the membrane is increased, the overall temperature of the target decreases and the temperature profile along the solid/vapor interface becomes more and more nonuniform. The most significant point is that, for an actual tent membrane of 1.8 μm, a minimal effect on DT ice distribution occurs for our standard target.

However, anticipating that some target-diameter/membrane-thickness scenarios may be less favorable, we developed a procedure to determine the DT ice distribution that corresponds to a solid/vapor interface isotherm. For this procedure, an initially uniform DT ice thickness is assumed, and the temperature distribution at the solid/vapor interface is determined. A logic has been developed to modify this ice distribution iteratively, based upon deviations of the actual temperature profile from average temperature (sine weighted).

For this analysis, we chose the target described above but with the 50 μm thick membrane because of the significant departure from a uniform temperature profile along the solid/vapor boundary. This was done to give us confidence in both the code and procedure; that is, that the process will converge to an ice-layer shape that results in a uniform temperature (within some small error) along the solid/vapor interface. The results of the analyses to date are shown in Figs. 2-5 and 2-6. Although we are close to converging to a uniform temperature profile, we have not yet done so: The bulge in Fig. 2-6 corresponds to a nonuniformity of the ice layer, $(W_{max} - W_{min})/W_{avg}$, of about 18%.

We are encouraged by the modeling results obtained thus far. For the first target-mounting system evaluated, which is the worst case for a membrane support (Fig. 2-2), it appears that the mounting system can be made to have almost negligible effect on the DT ice uniformity (Fig. 2-4). A 1.8 μm thick membrane of Formvar® should be usable for large-diameter targets.

For the target in this model, the calculated temperature nonuniformity induced by this thickness is not perceptible within 1 mK.

We plan to continue these modeling studies and will investigate the effects of a target material other than glass. Low atomic number materials under consideration include polystyrene and beryllium. Beryllium is the lowest atomic number metal that is usable for this purpose; it has a much higher thermal conductivity than glass and should allow a more uniform ice layer to be achieved, independent of the mounting method. It will also affect the rate of DT ice redistribution.

During 1987 we will investigate the effect of the thermal conductivity of the shell material on the rate of DT ice redistribution in the shell.

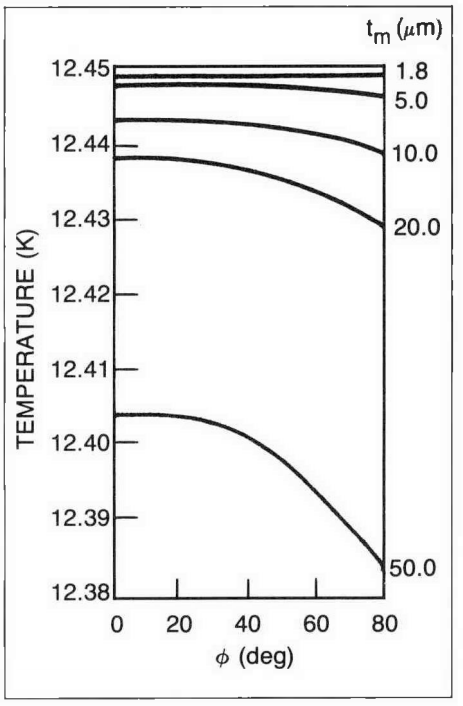

Fig. 2-4. Using the value of 1.0 cm for membrane radius R_m we varied the thickness of the membrane t_m from 1.8 to 50 μm. The resulting temperature profiles along the solid/vapor interface of the uniform layer are shown. As the thickness of the membrane is increased, the overall temperature of the target decreases and the temperature profile along the solid/vapor interface becomes more and more nonuniform. (Target dimensions and Nusselt number are as in Fig. 2-3.)

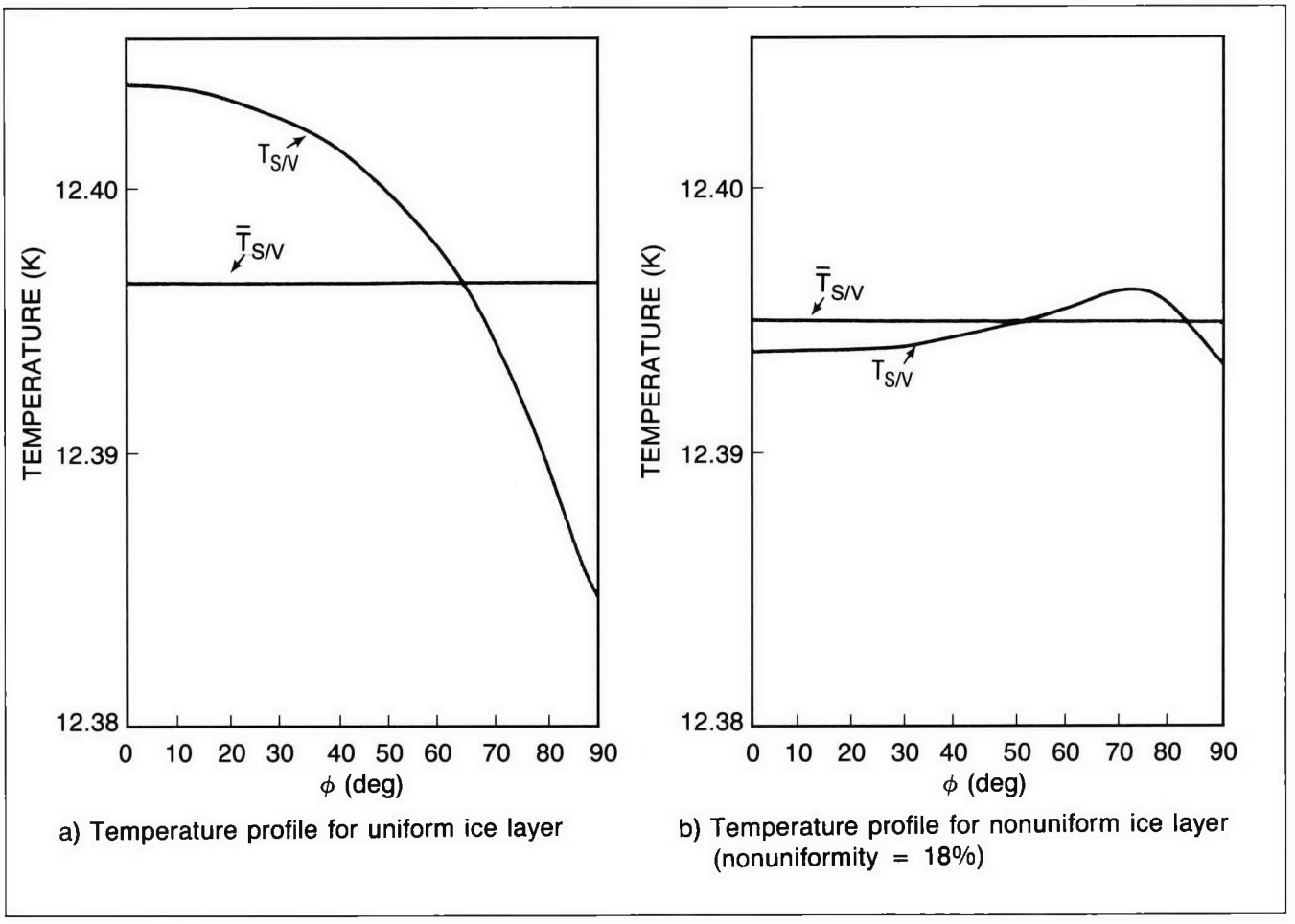

Fig. 2-5. A procedure was developed to determine the DT ice distribution that corresponds to an isothermal solid/vapor (S/V) interface. An initially uniform DT ice thickness is assumed (a), and the temperature distribution at the solid/vapor interface is determined. The ice distribution is then modified iteratively, based upon deviations of the actual temperature profile from average temperature (sine weighted), yielding the intermediate temperature profile for a nonuniform layer (b). Target dimensions and Nusselt number are as in Fig. 2-3, and t_m = 50 μm.

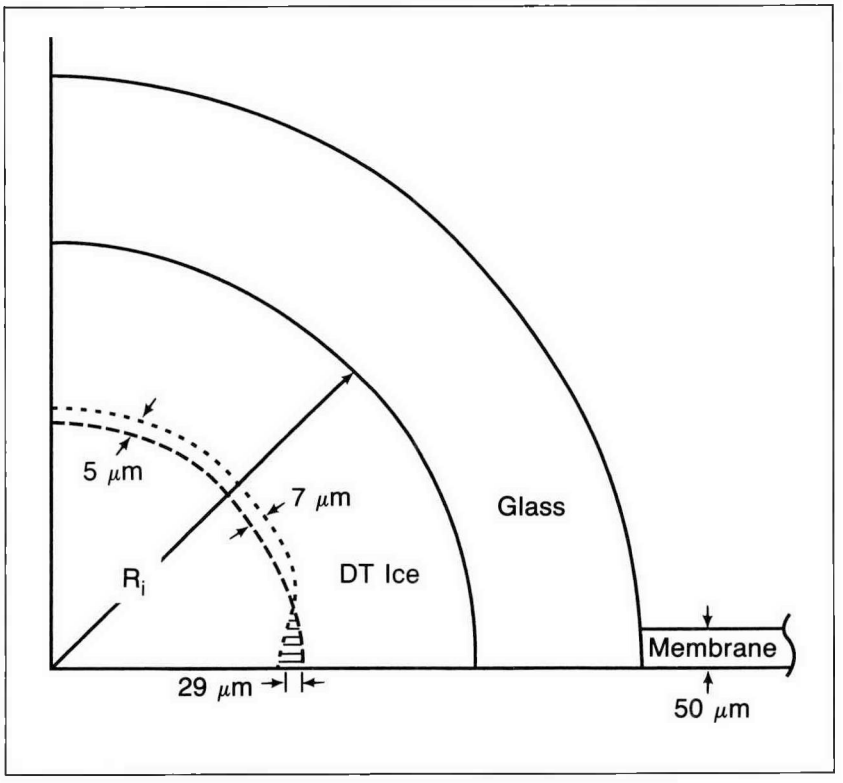

Fig. 2-6. The ice layer shapes shown here (broken and dotted lines) correspond to the DT solid/vapor interface temperature distributions shown in Fig. 2-5. The initial conditions (Fig. 2-5a) are represented by the broken line; intermediate conditions (Fig. 2-5b) are represented by the dotted line. The figure is out of proportion so that the distortion of the DT solid/vapor boundary (corresponding to an ice layer nonuniformity of about 18%) caused by the presence of the membrane support is more apparent.

For additional information, please contact Mr. A. J. Martin

SECTION 2.2

Fabrication and Analysis of Polymer Shells

Poly(vinyl alcohol) (PVA) and polystyrene (PS) are the leading candidates for use as low atomic number (low-Z) inertial confinement fusion (ICF) targets. If the choice were made on the basis of plasma physics and fusion diagnostic considerations, PS would be the preferred material because carbon ($Z = 6$) is its highest-Z element, whereas oxygen ($Z = 8$) is the highest-Z element in PVA. Although the atomic numbers of these two materials differ by only two, the effect on radiative processes is large, since, for free/bound interactions, the emission rate is proportional to the fourth power of the atomic number.

Certain engineering or material-property considerations also figure importantly in the choice of polymer, however. These include how easily the polymer can be formed into shells, how readily a desired size or wall thickness can be achieved, how well the shells retain hydrogen, and how resistant they are to damage from β-particles produced by radioactive decay of the tritium in the fuel. Poly(vinyl alcohol) is preferred on all but the last of these grounds.

Exposure to tritium degrades the permeation barrier properties of PVA but not PS.[4] However, even irradiated PVA is a better permeation barrier than is PS. Further, the conditions under which PVA shells are exposed to tritium can be made sufficiently mild that fuel gas retention by PVA is acceptable (i.e., retention times should be long enough to conduct a fusion experiment).

On balance, then, engineering considerations favor the use of PVA shells.[5] Poly(vinyl alcohol) shells were consequently chosen for our 1986 Low Preheat Implosion Campaign. (This campaign is discussed in Section 1.1 of this report; most of the development work on these shells was done last year and is discussed in the 1985 Annual Technical Report.[5]) In accordance with size specifications determined by code simulations, the shells supplied for these experiments ranged in diameter from ~110 to ~140 μm; their walls ranged from 3.0 to 6.5 μm thick. The wall nonuniformity of shells delivered for this campaign was generally less than 20%, with a small fraction of the shells less than 10% nonuniform.

Most of this year's development efforts were devoted to the production of larger PVA shells, which will be needed for future low-preheat implosion experiments. Because of difficulties producing target-quality PVA shells in the size range of interest, we conducted a systematic analysis of PVA shell production and developed a physical model of PVA shell formation. The model, which simulates the evaporation of methanol and water from a hollow drop of dissolved PVA, will provide insight into the temperature profiles that are required for the production of PVA

shells. In general, the simulated results from the model were consistent with experimental results.

As shell diameters become larger, identification of means to increase shell strength becomes even more important. We have known for some time that heating PVA shells increases their strength; several different heat treatments were compared this year to identify the conditions that produce the greatest increase in compressive strength. Of the treatment conditions examined, heating between 170 and 180°C in air for 15 min was most effective. Shells exposed to radiation suffered an 18% decrease in compressive strength.

The ideal polymer shell would combine the best attributes of both PVA and PS. Consequently, work on hybrid shells is also underway. This year we conducted investigations of the fuel permeation behavior of PVA/PS composite films and PVA-coated PS shells fabricated at Lawrence Livermore National Laboratory (LLNL). We found that the fuel retention of the shells approached that predicted for pure PVA shells of comparable dimensions.

An Analysis of the Production of PVA Shells

Most of our efforts were focused on the production of PVA shells with dimensions of 400 × 5 μm (diameter × wall thickness). Such shells will be required for future low preheat implosion experiments at the University of Rochester's Laboratory for Laser Energetics (LLE). Initial attempts to produce target-quality shells (i.e., shells with walls less than 10% nonuniform) were unsuccessful; consequently, we undertook a systematic analysis of the operation of our shell-production process. This system is based on a hollow droplet generator and droplet-drying column.

Hollow Droplet Generator. The hollow-droplet generator (HDG) incorporates a concentric-orifice nozzle that allows us to produce hollow drops of a specified size. It has been reported that the primary operating parameters for an HDG are the gas pressure and flow rate used to generate the bubble in the droplet, the liquid pressure and flow rate, and the vibrational amplitude and frequency of the acoustical excitations that are used to break up the liquid jet.[6] Our experiments confirmed this. Although there were simple relationships between most of the parameters and the hollow drop that was produced, the effect of the acoustical excitation (provided by a ceramic piezoelectric plate for our work) was very complicated.

Three control regimes were identified in experiments where the vibrational amplitude (piezoelectric voltage) and frequency (function generator) were independently varied. At low applied voltages (less than 10 V), the drop-formation frequency did not follow the frequency produced by the function generator. There appeared to be a natural frequency that governed the formation of hollow drops. This phenomenon is analogous to the capillary jet instability that was first mathematically described by Rayleigh.[7] The natural drop-formation frequency was controlled

only by the positions and sizes of the inner and outer orifices (for a given set of gas and solution parameters).

When the applied voltage exceeded ~40 V, the drop formation was synchronous with the frequency produced by the function generator. We were apparently able to override the natural frequency and (within limits) produce any drop-formation frequency we desired. There was an intermediate range (~10 to 40 V) in which the controlling parameters were not as obvious. There does not appear to be a relationship between applied voltage and wall uniformity.

The size of the outer orifice was found to be an important parameter. Using a variety of outer orifices (125, 275, and 320 μm), we observed that collapsed shells or "pancakes" resulted when the size of the bubble that was produced exceeded the outer orifice diameter. Evidently, the shear stress present in squeezing a large bubble out of a small outer orifice caused some drops eventually to burst. Current practice is to limit the bubble to ~1.2 times the diameter of the outer orifice. Nevertheless, we were unable to improve shell quality significantly by varying the operating conditions of the HDG.

Droplet-Drying Column. Primary process parameters for the drying column (a 15 cm o.d. tube with ten 61-cm heating zones) were the temperature profile and gas flow rate. For our experimental conditions, the temperature profile of the drying column had a slight effect on the uniformity of the shells. Temperature profiles that peaked in the second or third zone and then gradually decreased appeared to produce the best shells. However, these shells did not satisfy the uniformity criteria for target-quality shells.

Gas-flow patterns were established by either a spiral inlet ring near the entrance of the column (laminar plug flow) or a gas jet tumbler that could be positioned along the axis of the column (turbulent mixing flow). Although these produced significantly different gas dynamic environments, there were no significant improvements in shell wall uniformity using either device.

Effect of Varying Precursor Solution. We observed a significant difference in the nature of the PVA shells when we varied the properties of the PVA shell precursor solutions. For historical reasons, ordinary tap water has been used to make PVA solutions. We repeated some experiments using distilled water instead of tap water as the solvent. Large droplets ($\gtrsim$300 μm o.d.) of the solution made from distilled water were much more difficult to dry than those made from tap water. Smaller shells made from solutions containing distilled water were, on average, more uniform in wall thickness. These differences were due either to rheological or chemical effects. Since solution viscosities were almost identical, we did not think that rheological differences between the solutions were significant. On the other hand, our tap water contained significant concentrations of alkali (sodium and potassium) and alkali earth (manganese and calcium) metals, which may have affected the formation of PVA shells.

There are two possible explanations for the observed drying

behavior. First, dissolved ions or particulate matter may have catalyzed or facilitated PVA polymer crosslinking reactions. Crosslinking could occur during preparation of the solutions, where the reaction temperatures approach 100°C. Because crosslinked polymers would be easier to dehydrate (less soluble), we expect the tap water solution to be easier to dry. Crosslinking should affect the solution viscosity, but this was not observed. Second, dissolved ions have a tendency to inhibit hydrogen bonding of PVA molecules with water.[8] Since hydrogen bonding with water helps make the PVA more soluble, we expect dissolved ions to decrease the solubility of PVA. During the evaporation of a drop of PVA in tap water, the degree of hydrogen bonding should decrease significantly as more solvent evaporates (and the concentration of ions increases). At some point, PVA might be "salted out" of a tap water solution. If spatial (alkali) concentration gradients exist within the drop, "salting out" may occur earlier in some portions of the drop, leading to the formation of a nonuniform shell. We expect this phenomenon to be more significant for large shells. Future experiments will address in greater detail the effect of solution chemistry on the production of uniform PVA shells.

Shell Formation Model. In parallel with our experiments on PVA shell formation, we have developed a model of the major physical processes involved in the drying of hollow drops. To gain a better insight into the temperature profiles that are required for the production of PVA shells, we attempted to simulate the evaporation of methanol and water from a hollow drop of dissolved PVA. Because we were only interested in an estimate, a simple physical model was employed. We completely neglected the skin-over phenomenon that has been postulated for the production of PVA shells.[9]

Three balance equations describe the evaporation of a falling drop. Mass transport from the drop is accomplished primarily by convective motion of material from the drop surface, S, to the bulk gas, B. The balance equation governing the evaporation of methanol, MeOH, and water, W, is

$$\frac{dM}{dt} = A(N_{\mathrm{MeOH}} + N_{\mathrm{W}}) \ ,$$

where M is the mass of the drop, A is the surface area of the drop, and N is the mass flux. These mass fluxes may be approximated using mass transport coefficients, k_i. The symbols $y_{i,\mathrm{B}}$ and $y_{i,\mathrm{S}}$ denote the mass fractions of the i^{th} components in the bulk gas and at the surface of the drop, respectively,

$$N_i = k_i(y_{i,\mathrm{B}} - y_{i,\mathrm{S}}) \ .$$

A generally accepted correlation[10] for convection from a single sphere is

$$k_i = 2.0 \frac{P_T D_i}{R_{\mathrm{G}} T D_p} (2.0 + 0.347 \ \mathrm{Sc}^{0.31} \mathrm{Re}^{0.62}) \ ,$$

where D_i is the molecular diffusion coefficient of the i^{th} component, R_G is the gas constant, P_T is the bulk gas pressure, D_p is the drop diameter, T is temperature, Sc is the Schmidt number, and Re is the Reynolds number. An equilibrium constant was used to relate the concentrations of methanol and water at the drop surface.

The energy balance is coupled to the material balance,

$$MC_p \frac{dT}{dt} = \frac{-\lambda\, dM}{2} + hA(T_B - T_S) \ ,$$

where C_p is the heat capacity, λ is the heat of vaporization, and h is the heat transfer coefficient. The bulk gas temperature T_B could be predicted with the following equation,[11]

$$\frac{T_B - T_w}{T_0 - T_w} = \sum_{n=1}^{\infty} \frac{2}{a_n J_1(a_n)} J_0\left[a_n \frac{r}{R}\right] \exp\left[\frac{-2a_n^2 x}{\mathrm{Pe}\, R}\right] \ ,$$

where T_0 and T_w are the gas inlet and wall temperatures, r and x are the radial and axial coordinates, R is the heating zone radius, Pe is the Peclet number, and a_n satisfies $J_0(a_n) = 0$. J_i is the Bessel function of the first kind of order i.

Finally, we need to satisfy the momentum balance so that the drop position can be determined,

$$-\frac{d(Mv)}{dt} = -Mg + \frac{\pi\rho D_p^3 g}{6} + \frac{\pi\rho v^2}{8} D_p^2 C_d + \frac{\pi\rho D_p^3}{12} \frac{dv}{dt} \ ,$$

where v is the drop velocity (relative to the gas), g is the acceleration due to gravity, and C_d is the drag coefficient. The coupled equations were solved numerically. We should note that the model allowed for the expansion and contraction of the drop while the PVA was still dissolved. The derivation of the following cubic equation was based on the Young-Laplace and the ideal gas equations,

$$R_o^3 + \frac{2\gamma}{P_T} R_o^2 - \frac{2M_G R_G T}{4\pi M_{w_G} P_T} = 0,$$

where R_o is the radius of the bubble, γ is the surface tension, M_G is the mass of the bubble, and M_{w_G} is the molecular weight of the bubble's contents.

Given the wall temperature profile and the initial conditions of the drop, the model estimated the drop position, velocity, diameter, mass, temperature, and composition as well as the diameter of the bubble.

In general, the simulated results from the model were consistent with the results of experiments. Both the final shell diameter and the approximate thermal history were similar to those determined from experiments. For example, if the model predicted that the shell would experience excessively high temperatures, we observed collapsed shells and raisin-like shells in the

product. On the other hand, if the model suggested that the drop would not dry, we noticed wet product in our experiments. Figure 2-7 illustrates the results of a typical simulation. The shape of the wall temperature profile was determined experimentally. We noticed that the best quality shells were produced when the temperature of the second zone was greater than that of the first zone. The drop temperature was fairly constant at the wet-bulb temperature until the shell dried completely. Subsequently, the temperature of the shell approached the temperature of the carrier gas.

In conclusion, we have gained a better understanding of the production of PVA shells using the HDG system. Incremental improvements in shell wall uniformity were demonstrated by varying the drying column temperature profile. While we still do not produce a significant quantity of target-quality shells, investigations into the effects of solution properties on the formation of shells hold promise in significantly improving shell wall uniformity. Finally, the development of a numerical model of the drying of an aqueous PVA drop will be valuable not only in predicting the results of a particular experiment, but also in evaluating the limitations of our drying column.

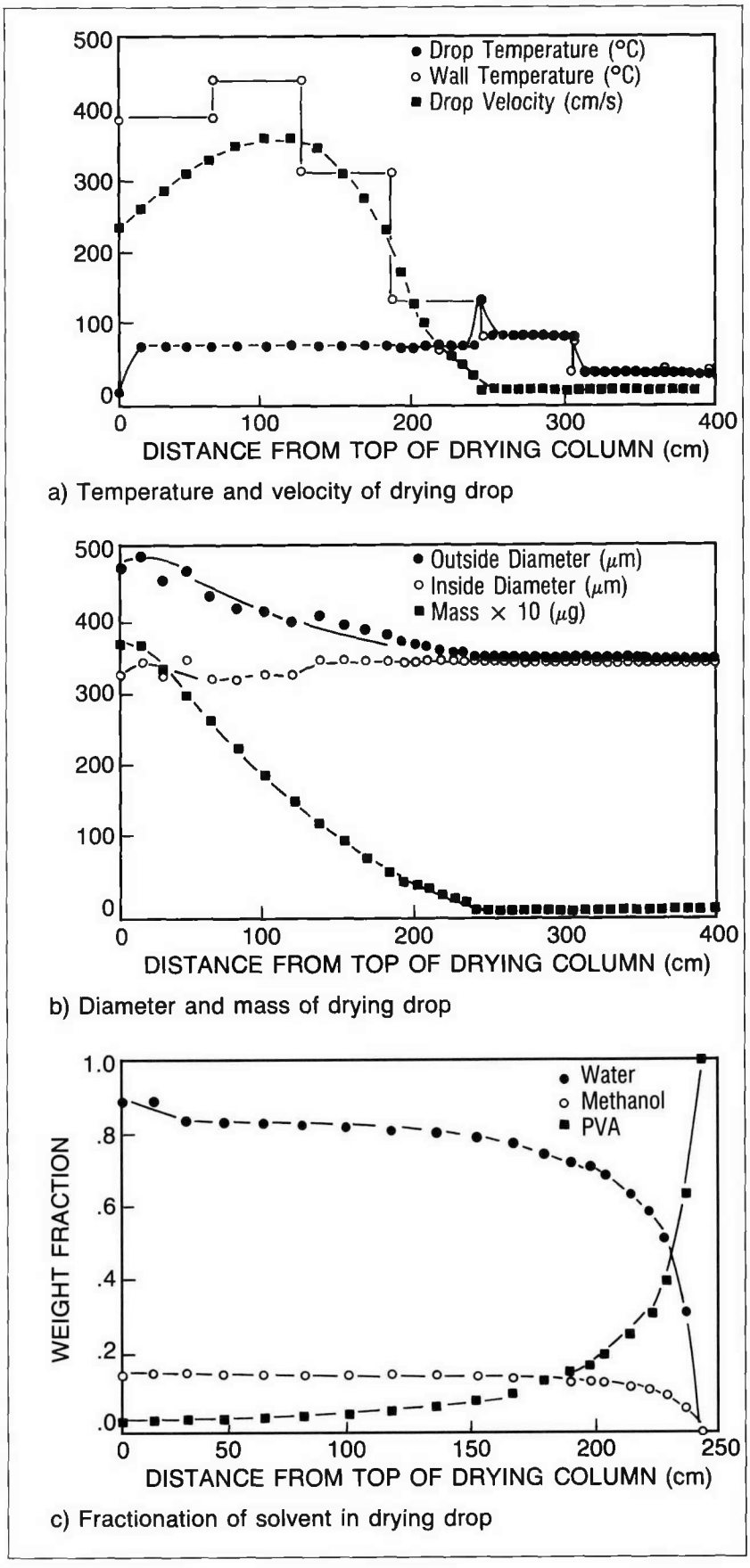

Fig. 2-7. We have developed a simple physical model of a hollow drop as it passes through a drying column. The parameters used in this simulation are typical of our experiments. Initial conditions are: composition 14.7 wt.% methanol, 2 wt.% PVA, 83.3 wt.% water; drop temperature 25°C; drop velocity ~260 cm/s; carrier gas (nitrogen) velocity 20 cm^3/min. The model predicts the temperature and velocity changes of the drop as it passes through the column (a), the change in drop diameter and mass when the drop is heated to its saturation temperature (b), and the fractionation of the solvent in the drying drop (c). The drop should be completely dry 250 cm from the top of the column.

For additional information, please contact Dr. L. T. Thompson

Shell Strength Tests

Effect of Heat Treatment on Compressive Strength. We have known for some time that heat-treating PVA shells increases their strength, probably by increasing the number of crystallites in the polymer matrix. Using a procedure described previously,[12] we investigated various heat treatments to identify the conditions that produce the greatest increase in the compressive strength of PVA shells.

Poly(vinyl alcohol) shells were heated in air at various temperatures for varying amounts of time and then their diameters and wall thicknesses were measured (diameters ranged from 145 to 170 μm, wall thicknesses from 3.0 to 4.0 μm). These shells were then exposed to increasing pressures of nitrogen gas at 50°C until the shells collapsed (as verified with a microscope). Using these data and the following formula, the Young's modulus for PVA was calculated for each treatment temperature,

$$P = 8E[3(1 - \nu^2)]^{-1/2}\left(\frac{w}{o.d.}\right)^2$$

where P is the external pressure when the shell collapses, E is Young's modulus, ν is Poisson's ratio, w is wall thickness, and *o.d.* is outside diameter. The results are depicted graphically in Fig. 2-8. Maximum strength is observed when shells are heated between 170 and 180°C for approximately 15 min.

The data for shells heated above 180°C for longer than 20 min were very scattered and were not reproducible (unlike data obtained below this temperature), suggesting that the polymer was degraded. Shells heated for these longer times at higher temperatures developed a distinctive brown color; this also indicates degradation.

We subjected a second batch of PVA shells to the conditions identified above as producing the greatest increase in compressive strength (175°C for 15 min). These shells were then exposed to increasing pressures of nitrogen gas at different temperatures until they collapsed; the results are depicted graphically in Fig. 2-9. As was done for the first batch of shells, the Young's modulus was calculated from the collapse pressure and physical (geometrical) measurements of each shell. Each point in the graph in Fig. 2-9 is an average modulus value for approximately 30 shells.

It can be seen that the strength of PVA shells falls rapidly with increasing temperature. This temperature dependence must be taken into account in developing any protocol for filling PVA shells with the hydrogen isotopes used as fuel. High-pressure fills above room temperature must be staged in fairly small steps to avoid shell collapse; data from the graph allow a reasonably accurate calculation of optimal pressure step sizes for a given fill temperature.

For comparison, some data for PS shells are also displayed in Fig. 2-9. These shells were tested with water rather than nitrogen gas because they are permeable to nitrogen. Higher temperatures were not investigated because the polymer softens.

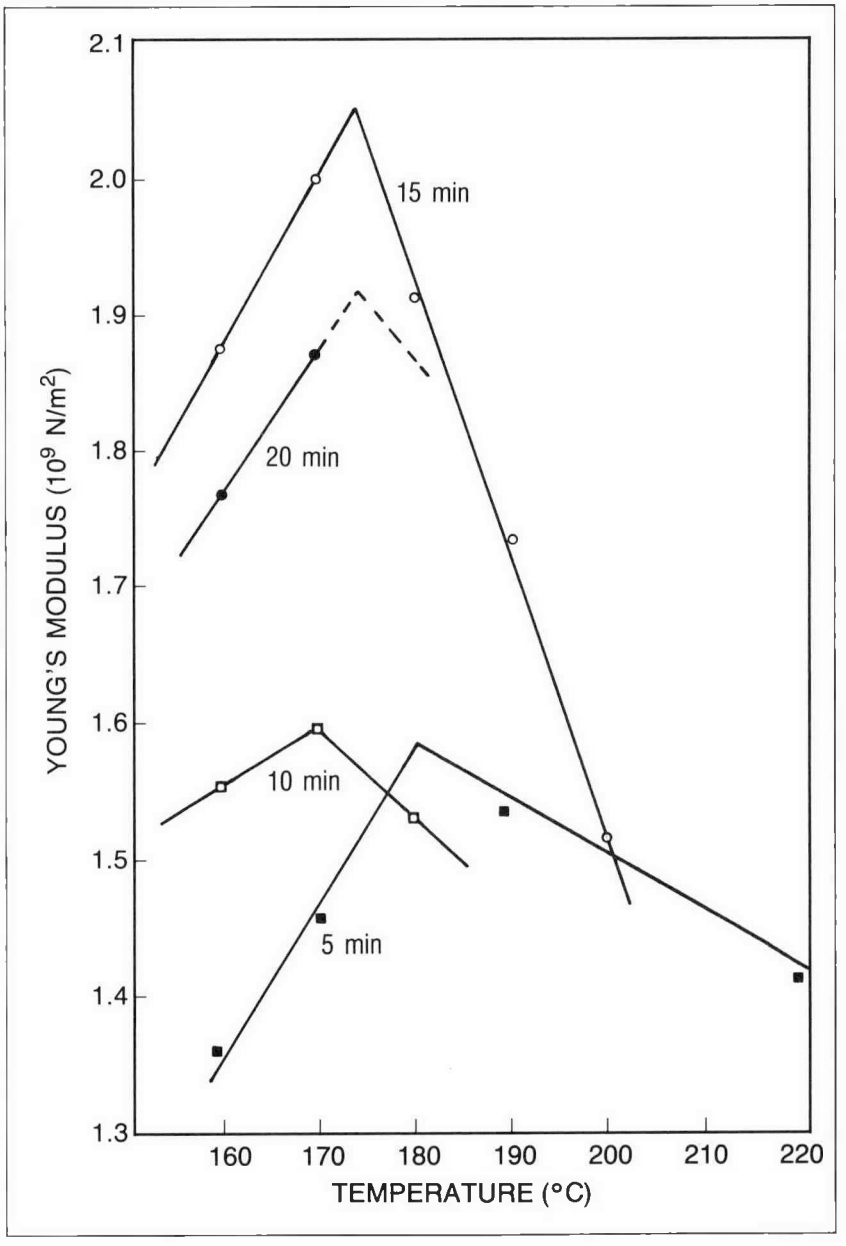

Fig. 2-8. Several heat treatments were investigated to identify the conditions that produce the greatest increase in the compressive strength of PVA shells. The shells represented in this figure were exposed to the temperatures indicated for 5, 10, 15, or 20 min. The Young's modulus was then measured at 50°C; it is shown to be highly dependent upon previous heat treatment of the shells. Shells heated between 170 and 180°C for 15 min showed the greatest increase in strength.

Effect of Radiation Exposure on Compressive Strength. Radiation damage is known to reduce the strength of polymer shells. To measure the effects of exposure to radiation on PVA shells, we divided a batch of unirradiated shells into three groups. One group was filled to 50 atm DT at 110°C for 7.5 h, then emptied. A second group was filled to 50 atm H_2 under the same conditions and then emptied. The third group was subjected to 100 h

of high humidity at 50°C, then heated at 175°C for 15 min. After these treatments, the compressive strength of all three groups of shells was tested. All samples were maintained at 50°C during the test.

Results from this test are listed in Table 2-1. There is a moderate loss of strength (about 18%) from radiation damage that cannot be attributed to filling conditions nor to a possible reduction in strength by absorption of water vapor into the PVA. The calculated radiation dose from this experiment was 2.5×10^8 rads.

Tests of Tensile Strength. We also tested the tensile strength of a sample of PVA shells that had been heated at 175°C for 15 min. The results of these tests were less quantitative than our tests of compressive strength, as we were unable to identify the exact pressure at failure in the tests of tensile strength. In our procedure, we filled shells with hydrogen, then slowly reduced the pressure outside the shells, thereby producing a pressure differential that should have caused the shells to burst. However, rather than bursting at the failure pressure, many shells merely stretched, forming oblong shapes. Furthermore, some shells fractured hours after the test was finished. Under ambient conditions (1 atm external pressure, ~25°C), most shells in a test batch with nominal dimensions of 160 × 3.3 μm (o.d. × wall thickness) withstood 20 atm internal pressure. They began to yield at 30 to 40 atm and all shells burst open at 50 atm internal pressure.

Conclusions. Identification of the treatment conditions that produce the greatest increase in PVA shell strength will enable us to bring all of our PVA shells reproducibly to a condition of maximum strength. Unfortunately, filling shells with fuel will remain a slow, cumbersome process since the shells are so much weaker at filling temperatures than at room temperature and below. This may be compounded for fills that involve tritium, which further reduces shell compressive strength. Future work will focus on strength measurements on coated PVA shells, and measurement of radiation damage to such shells.

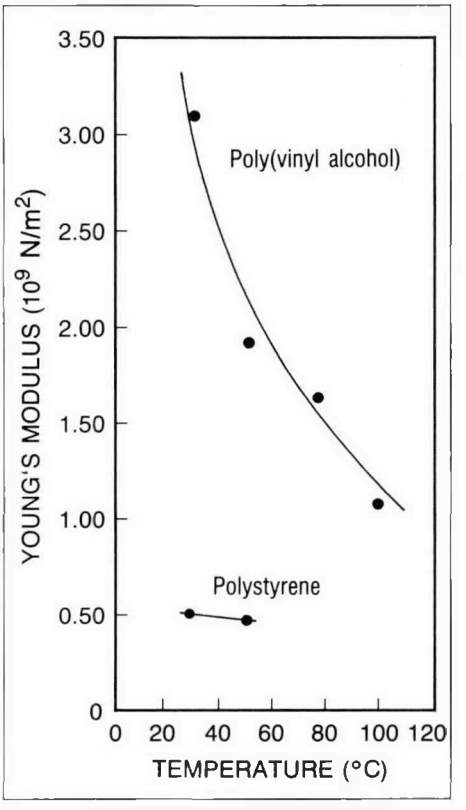

Fig. 2-9. The Young's modulus for PVA drops rapidly with temperature, but is much higher than that for PS even at 100°C. These shells were treated at 175°C for 15 min, then their compressive strength was tested by exposing them to gaseous nitrogen at the temperatures indicated. Each data point is an average value from approximately 30 shells.

Table 2-1. Compressive Strength of PVA Shells After Various Treatments

Shell Treatment	Mean Value of Young's Modulus (10^9 N/m^2)
H_2 fill	1.941 ± 0.026
DT fill	1.582 ± 0.032
Humidity	1.874 ± 0.050

For additional information,
please contact Dr. R. G. Schneggenburger

Measurement of Gas Permeation Coefficients for PVA and PVA/PS Composites

Permeability is a very important characteristic of any material that is to be considered as an ICF fuel container. The material must be sufficiently permeable at elevated temperatures to be filled with fuel and/or diagnostic gases in a reasonable time, but must become sufficiently impermeable at reduced (room) temperatures to retain the fill gases long enough to be used in experiments. It is known that the room-temperature permeation rate of PVA is reduced by heat treatment. This year we tried to find the best treatment temperature for PVA/PS composite films and shells. We also conducted a separate effort to measure the permeability of untreated PVA to neon.

Three techniques are routinely used at KMS Fusion (KMSF) to measure permeability. These are (1) the thin planar film method,[13] (2) the gas entrapment by a viscous fluid (GEVF) method,[14] and (3) the bulk shell sample method.[4,15] Each of these methods is based on the application of Fick's first law to give a general permeation expression. Because all were used to obtain the data discussed below, a brief review of each method is presented first. The comparability of the values derived from the different methods is also addressed.

The permeability of planar films is measured in a stainless steel permeation cell that supports a 1 in. diameter film on a porous sintered plate. The film is sealed by a flat Teflon® gasket, and a pressure difference is set across the sample thickness. A diaphragm-type pressure transducer measures the pressure increase on the low-pressure side as the permeant gas diffuses through the film into a receiver of known volume.

The GEVF test is a destructive method of measuring the pressure of the gas in individual shells. A shell is immersed in a glycerin bath and its inside diameter is measured. The shell is then broken and the diameter of the released bubble (which expands to equilibrate with the atmospheric pressure) is measured. The pressure of the gas is then calculated according to Boyle's law. To determine a permeability coefficient using this method, a number of shells are filled with gas and the internal pressure is measured immediately (by destroying a sample of the shells). This yields the internal driving pressure at time zero. The internal pressure of other samples is measured after the shells have been allowed to "out-permeate" for designated periods at designated temperatures.

The bulk shell permeation method is a nondestructive method developed to measure the permeation coefficient of a bulk sample of shells. A sample of shells is loaded into a constant-volume chamber, which is then pressurized with gas and held at the fill temperature until a constant fill pressure is assured. Residual gas is then quickly evacuated from the chamber, and the rise in chamber pressure (as gas permeates from the filled shells) is measured at a chosen outgassing temperature at known time intervals. The natural log of the outgassing rate is plotted as a function of time; the permeability coefficient is calculated from the linear slope of this graph. For this method to yield valid

results, the product of inside diameter and wall thickness must fall within a narrow range, since the statistical significance of the slope decreases as the range of this product increases.

Permeation coefficients of similar materials have been measured using combinations of these techniques to verify the consistency of results. Film and bulk shell measurements have been shown to vary as little as 3% for PS samples. Poly(vinyl alcohol) permeation coefficients determined by the GEVF method agreed within about 30% with those calculated from the bulk shell test.

Hydrogen and Deuterium with PVA/PS Composites. The permeability of PVA/PS composites was measured on selected films and shells provided by Lawrence Livermore National Laboratory (LLNL). The PVA coatings on the PS films and shells were examined optically with a microscope. The PVA was doped with green dye to distinguish the coating from the substrate. The coatings appeared to be of high quality, with no apparent defects.

The permeabilities of three LLNL film samples were measured in the planar film permeation cell before and after a heat treatment. These values were compared to permeabilities of two KMSF sample films of pure PVA (measured only after treatment). The results are reported in Table 2-2.

The pre-treatment permeabilities of samples LLNL-1 and LLNL-2 were comparable. The results for LLNL-3 were unexpectedly low; a lower molecular weight is generally associated with a higher permeability,[16] all other parameters being the same.

For heat treatment, sample LLNL-1 was removed from the permeation cell housing and heated for 15 h at 80°C.* When it was returned to the cell housing for post-treatment measurement, the equipment malfunctioned and this measurement could not be obtained. Treatment of samples LLNL-2 and LLNL-3 consisted of in situ heating: The cell was immersed in a constant-temperature bath and maintained at 78°C for 22.5 h (LLNL-2) and 100 h (LLNL-3).

Post-treatment permeability coefficients showed a nominal factor-of-two decrease for LLNL-2 compared to its pre-treatment value. However, its value was higher than the permeability for samples KMSF-1 and KMSF-2. On the other hand, the post-treatment permeability of LLNL-3 is in excellent agreement with the values for samples KMSF-1 and KMSF-2.

*Because PS softens at ~100°C, 80°C was selected as the highest safely achievable temperature. This is considerably below the 180°C heat-treatment temperature normally used for PVA at KMSF; however, it is reasonably close to the lower limit (100°C) of tests performed by Carstens and Ehart.[17] They measured the permeability of PVA films over the temperature range of ~25 to 100°C after heat treatments of 100°C for 24 h, 120°C for 24 h, and 140°C for 2 h. Overall, they report no appreciable difference in permeability as a result of the temperature or duration of the heat treatments. Carstens and Ehart's lowest film heat treatment (100°C) yielded permeabilities lower (by factors ranging from 5 to 28) than any of the PVA or PVA/PS film samples listed in Table 2-2. It must, however, be noted that Carstens and Ehart's films have a higher molecular weight (126,000) than the PVA we have tested (see Table 2-2).

Table 2-2. Room-Temperature Permeation Coefficients of PVA Films and PVA-Coated PS Films

Sample	Coating Material	Substrate Material	Thickness (μm)	Molecular Weight (kg/gmol)	Permeant	PVA Permeation Coefficient (10^{-18} mol·m/m^2·s·Pa) Untreated	Treated
LLNL 1	PVA	PS	7.5	78	H_2	5.0	—
LLNL 2	PVA	PS	7.5	78	H_2	6.7	2.8
LLNL 3	PVA	PS	2.7	25	D_2	1.9	0.54
KMSF 1	PVA	—	51	115	H_2	—	0.47–2.4
KMSF 2	PVA	—	55	115	H_2	—	0.50–2.73

Note: Composite films were heat-treated at 80°C; pure PVA films were heat-treated at 180°C.

The permeability of PVA/PS composite shells was measured by both the bulk shell and GEVF methods. The PVA coating thickness and the nominal shell diameter were reported to be 2.5 to 3.0 μm and 475 μm, respectively.[18] The PVA had a molecular weight of 25,000. There was ~4 μm of PS. As part of our GEVF measurements for these composites, we determined the inside diameters of 17 shells. The average diameter was 487 μm, with somewhat bimodal distribution centered around ~460 and ~514 μm.

The information on total shell wall thickness and PVA coating thickness was supplied by LLNL; we made made no independent measurements of these dimensions. Overall, these diameter and wall thickness distributions are wider than desired for the accurate assessment of permeability using the bulk shell method. Thus, greater care in interpretation is important. These shells were heated for 100 h at 80°C. Sets of these shells were filled with D_2 at 80°C (by pressurizing in three steps) to a fill pressure of 50 psig. Then sets of shells were permitted to outgas at selected temperatures in the range of 41.5 to 83°C. Additionally, a separate determination of permeability was done at room temperature by the GEVF technique. Using data from four of the five composite shells individually evaluated using this method, room-temperature permeation coefficients were calculated that ranged from 2.1 to 2.6 $\times$ 10^{-19} mol·m/m^2·s·Pa. Results for the fifth shell gave a permeation coefficient of 4.4 $\times$ 10^{-19} mol·m/m^2·s·Pa.

The permeation coefficients calculated for the composite shells range from factors of 2.3 to 8.5 higher than the calculated results for the PVA shells. The GEVF results, for which individual shells are measured, have the smaller ratio (2.3). These measurements were also made at the lowest temperature. The permeability ratio increases up to 8.5 as the outgas temperature is increased.

Figure 2-10 shows the permeability results for the PVA/PS shells. For comparison, selected results from Carstens and Ehart[17] and earlier data calculated for two PVA shell batches

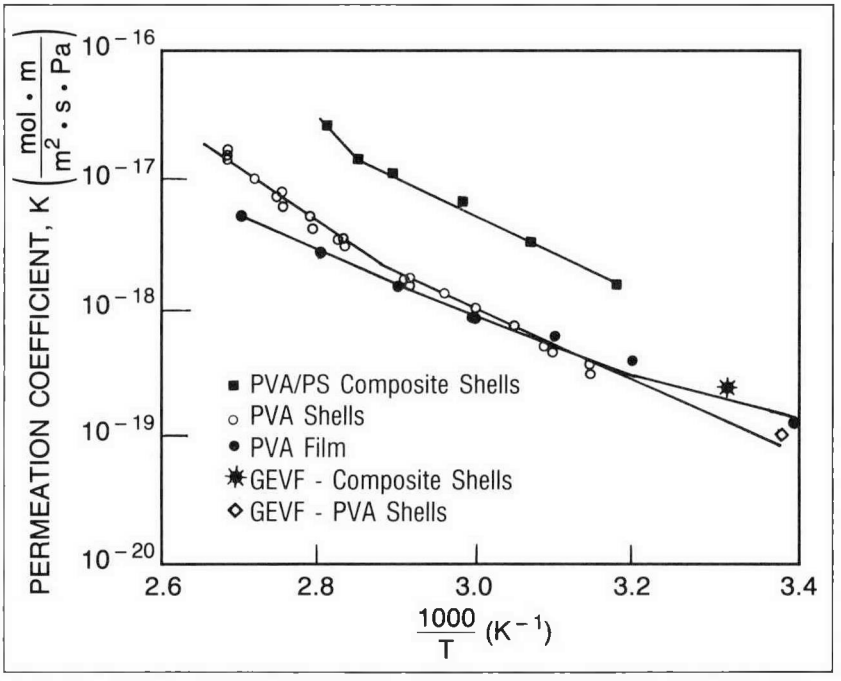

Fig. 2-10. The bulk shell and GEVF techniques were used to measure the permeability to deuterium of PVA layers coated onto PS shells. Data were taken at several temperatures. These values were then compared to those for shells and films of pure PVA. A change of slope is observed in the curve for the PVA coated on the PS shells as well as for the pure PVA. (PVA film data from Ref. 17.)

made at KMSF with our HDG (mean deviation of 1.5% in diameter, molecular weight 115,000, heat-treated at 180°C) are also shown in the figure. These data, coupled with the heat treatment findings reported by Carstens and Ehart, indicate that PVA permeability may be more dependent on molecular weight than temperature for heat treatments greater than 80°C. Overall, however, the current results are not completely consistent and lead to unresolved questions. The agreement between the various results is not what was expected, based on our understanding of the roles of PVA molecular weight, the temperature of the heat treatment, and the duration of the heat treatment. Further work will be needed to resolve these issues. One aspect that will be clearly evaluated is the role of a wide distribution of the product of diameter and wall when the bulk shell method is used. It may well be that a sizeable portion of the disagreement of batch permeation results is directly related to this factor.

Neon Gas with PVA Shells. Because of the possibility of using neon as a diagnostic gas, some work was done to measure the permeability of PVA shells to neon gas. The test batch was produced by the droplet generator and had a narrow range of diameters (158.0 ± 3 μm) and wall thicknesses (3.3 ± 0.2 μm) as determined optically and interferometrically.[19]

Shells were loaded into the bulk shell sample chamber, from which residual air was evacuated. The chamber was then filled

to 50 psig with neon and held at 90°C for at least 8 h. The chamber was again evacuated and its temperature was brought to (and held at) the desired outgassing temperature. Permeation coefficients were determined in this manner for five temperatures, ranging from 61.5 to 100.7°C. The results are shown in Fig. 2-11.

The data show a behavior similar to that for deuterium in PVA: there is an apparent discontinuity in the slope in the range from 70 to 80°C (Ref. 20). This is a temperature range that is associated with a glass transition.[4] The two higher-temperature (90.5 and 100.7°C) data points fit the equation,

$$\ln K = -\frac{10549}{T} - 11.88 \ ,$$

and the lower-temperature (61.5 and 70.5°C) data points fit the equation,

$$\ln K = -\frac{7557.1}{T} - 20.28 \ ,$$

where T is the absolute temperature (degrees Kelvin) and permeability (K) is expressed as $\text{mol}\cdot\text{m}/\text{m}^2\cdot\text{s}\cdot\text{Pa}$. (A fifth data point, at 81.5°C, lay very near the discontinuity and was not used in the calculations.)

The values for the activation energy of permeation, E_a, are 20.9 and 15.0 kcal/mol for the higher and lower temperature ranges, respectively. The lower value is somewhat questionable, since the low permeability at the lower temperatures was close to the detection limits of our apparatus. An attempt to measure permeability at 50°C was unsuccessful; the outgassing could not be detected above the system noise level.

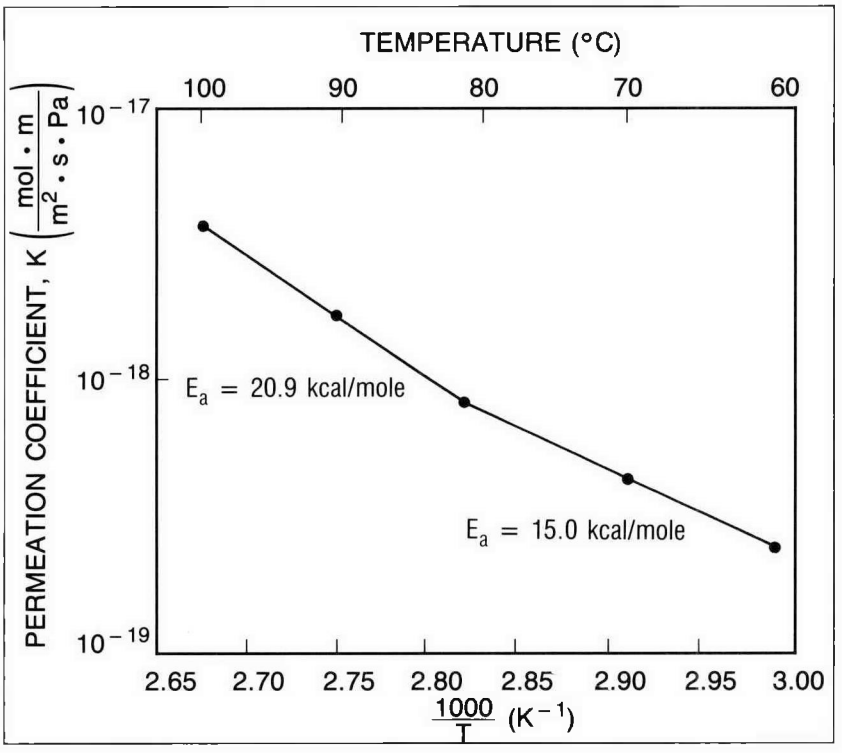

Fig. 2-11. The bulk shell technique was used to measure the permeability of PVA shells to neon at five temperatures. The plot of these data shows two linear regions, similar to those observed with deuterium.[20] The discontinuity is in the range of 70 to 80°C, a temperature range that is associated with a glass transition.

For additional information, please contact Mr. L. A. Scott

SECTION 2.3

Fabrication and Analysis of Glass Shells

The original fuel containers for inertial confinement fusion (ICF) research were made of glass, and glass shells continue to be important to the ICF program. Currently, most of our glass shell fabrication efforts are focused on the production of macrospheres that range from 2 to 10 mm in diameter. It is these larger shells that will be required for commercial energy production.

We are also continuing to expand our basic knowledge of glass shell characteristics. Tensile strength data, while increasingly important, are relatively lacking. This year, we evaluated the factors that affect the tensile strength of large (450 to 750 μm in diameter) glass shells. This resulted in a statistically valid predictive model, which is being used to determine fuel pressure limits for shells of given dimensions.

Fabrication of Macroshell™ Spheres from Vycor® Preforms

The two-step technique that we have developed to produce glass Macroshell™ spheres was described in detail in previous reports.[21,22] Briefly, a glass rod or partially formed shell (the "preform") that contains a nonspherical cavity is heated in a horizontal tube that rotates in a furnace. Ultimately, surface tension forces overcome viscous forces and cause the cavity to become more nearly spherical. Then the rod or shell is cooled and the glass around the cavity is ground and polished into a sphere. A three-point lapping device is used that allows the cavity to be centered within a wall of desired thickness and surface finish. [This latter procedure is currently performed at Los Alamos National Laboratory (LANL).]

We are currently seeking to identify appropriate glass compositions and to identify and control the forces that affect the sphericity of the final cavity. We have worked with several different glasses, including soda-lime[21] and borosilicate[22] glasses. Although early results were promising, both of these glasses have major shortcomings that make them unsuitable for this application.

The best glass would probably be fused silica (SiO_2) because of its permeability and chemical durability. However, it has a very high working temperature (~2000°C). Consequently, this year we chose to use Vycor® (96% SiO_2, 4% B_2O_3), which has a permeability similar to that of fused silica, but an appreciably lower working temperature (<1800°C). This lower working temperature makes it possible to use a furnace that can be operated in ambient air.

Experiments with Vycor® Glass. The Vycor® preforms used in these experiments consisted of core-drilled disks capped at each

end with blank disks. (Sample 19 was the only exception; it was a new type of preform made of two sections, each of which contained a hemispherical cavity.) Before assembly, each disk was cleaned in a chromerge acid solution to remove machining fluids and other contaminants. The Vycor® disk "sandwich" was then loaded into a molybdenum mold, which held the preform during heating.

The molybdenum mold consisted of a tightly fitting molybdenum tube with molybdenum end disks. The end disks were pressed inside the tube, directly against the Vycor® sample; once the preform and end disks were in place in the mold, the end disks were TIG-welded (tungsten inert gas) to the tube in an argon/helium atmosphere. Molybdenum was selected because it withstands the high temperatures needed for Vycor® and does not react with the ceramic processing tube of the furnace. To minimize oxidation of the molybdenum mold, the processing tube of the furnace was flushed with nitrogen throughout the heat treatment.

The furnace used in these experiments has a 10 in. long hot zone; the hot zone contains a horizontally mounted ceramic processing tube (inside diameter = 1 in.) that is surrounded by six lanthanum chromate heating elements. Ceramic radiation shields are located in the processing tube on either side of the sample. A 1/4 in. diameter tube runs along the length of each cylindrical shield (6 × 3/4 in. o.d.) to allow passage of inert flushing gas. The processing tube is driven by a high-torque motor at one end and is mounted on a freely moving tailstock at the other. The tailstock is coupled to the nitrogen line that purges the processing tube throughout the heat treatment cycle. The furnace is linked to a DEC PDP-11/34 computer that controls both temperature and time functions.

Results. Thirty-two Vycor® samples were treated in the high-temperature furnace. Information about the best 19 of these samples is summarized in Table 2-3, which lists treatment conditions, final cavity diameter, and percent noncircularity for orthogonal planar views. Treatment conditions refer to temperature, duration (time), and furnace tube rotation rate (RPM). Samples 1 (which contained two cavities) through 4 were delivered to LANL for processing (lapping) into shells.

Samples 1 through 4 were heated with the radiation shields in place (~2 in. from the molybdenum mold). The extreme temperature cycling degraded the shields after only four treatments. Several subsequent treatments (samples 5 through 13) were performed without radiation shields. The cavities from these treatments showed axial displacement. This was discernible by both the microscopic air bubbles that "trailed" the displaced cavity through the glass and by the actual cavity displacement. Cavity displacement was presumably the result of temperature gradients across the molybdenum mold and within the molten glass that allowed the cavity to migrate. The sphericity induced in a cavity by surface tension cannot compete effectively with bulk flows, such as the cavity movement of samples 5 through 13, especially as cavity volume is increased.

Table 2-3. Characterization Data for Cavities Produced in a Vycor® Matrix

Sample No.	Temperature (°C)	Time (h)	RPM	Tube No.	Diameter (mm)	% Noncircularity Axial	% Noncircularity Radial
1A	1700	4.0	14	NR[a]	2.01	2.17	2.23
1B	1700	4.0	14	NR	1.41	1.42	4.50
2	1700	8.0	14	NR	1.94	0.37	0.89
3	1725	6.0	14	NR	1.92	0.57	3.29
4	1725	2.0	14	NR	2.08	1.42	3.29
5	1725	4.0	14	NR	2.22	3.88	8.60
6	1700	2.0	14	NR	1.82	1.19	0.82
7	1700	8.0	14	1	2.06	0.68	1.61
8	1700	6.0	14	1	1.76	1.12	0.77
9	1700	3.0	14	1	3.78	2.00	5.96
10	1700	1.0	14	1	2.90	0.49	24.40
11	1700	2.0	14	3	3.53	0.83	2.30
12	1700	2.0	4	2	2.71	0.87	1.49
13	1700	9.5	4	2	2.78	0.47	1.13
14	1700	8.0	4	2	6.92	4.05	--
15	1700	2.0	12	2	6.68	0.33	1.99
16	1700	2.0	12	2	6.56	1.31	5.29
17	1700	4.0	4	2	6.44	0.77	1.26
18	1750	1.0	10	3	--	0.64	1.12
19[b]	1750	2.0	10	4	5.89	3.59	3.58

a. Not recorded.

b. Samples 1–18 consisted of core-drilled disks (7/8 × 1/4 in. or 7/8 × 3/8 in., o.d. × thickness) capped at each end with blank disks (7/8 × 1/4 in., o.d. × thickness). Sample 19 was a new, experimental configuration (see text).

We replaced the damaged radiation shields with shields made of high-temperature insulation board. These were used for samples 14 through 19. With these radiation shields in place, cavity movement was not observed. However, the circularity of the orthogonal views was unacceptable and apparently random.

Conclusions and Future Research. Although it is relatively early in this research program, we have reached some preliminary conclusions and identified topics for future research.

1. The temperature of the furnace we use is adequate for work with Vycor®. We plan to determine if this furnace can be used effectively with fused silica.
2. A treatment temperature of ~1700°C seems satisfactory for Vycor® glass. Although, as stated above, the degree of circularity achieved is still poor, the cavities do become more spherical, especially in the radial direction referred to in Table 2-3. Initial optimization will focus upon temperatures in the range of 1650 to 1700°C.

3. The role of gas trapped in the preform volume must be evaluated. At some stage in the heat treatment, the Vycor® disks become sealed, trapping the enclosed gas. If this happens at a relatively low temperature, the gas will be at a higher pressure than the ambient pressure. This has two possible effects: First, a driving pressure will exist for cavity expansion. Second, dissolution of gas in the Vycor® matrix will occur. This latter effect, which can decrease the cavity gas pressure, has been documented by Greene and Gaffney[23] and by Brown and Doremus.[24]

4. The reason that the cavity volume of treated preforms has been smaller than predicted, based upon the volume of the untreated preform, must be investigated. Cavity volume reduction has been as much as 60%, but results have not been repeatable. We have not yet unambiguously identified the cause of this reduction.

   The cause of this reduction is of paramount importance. If it is due to a continuously operating phenomenon, then the associated bulk motion may override the increased sphericity induced by surface tension effects. At worst, this could render this approach useless.

   It may be, however, that the volumetric expansion of Vycor® is greater than that of molybdenum over the temperature range investigated so far. If this is the case, the molybdenum cavity would become overfilled and cause the preform cavity volume to decrease and the molybdenum end caps to bulge. The bulk flow of the glass to fill this cavity would be resisted by the viscosity of the Vycor®. The details and repeatability of the arc welding of the molybdenum end caps and cylinder would affect this reduction in volume. For example, if the end cap is not completely welded shut, an avenue for fluid glass escape would exist and the resistance of the molybdenum to deformation would be compromised.

   On occasions, we have observed bulging of the molybdenum end caps and/or flow of Vycor® out of the molybdenum cavity. This cause will be evaluated and a methodology developed to compensate for the differences in volumetric expansion.

During 1987 we will continue our investigations of both Vycor® and fused silica. The role of relative volumetric expansion and reproducibility of methods of joining the molybdenum parts will be carefully evaluated. Heat-treatment cycle studies will focus on achieving maximum sphericity and effective sealing of the glass disks in a reproducible manner. The reproducibility of the procedures/processes is considered crucial to achieving repeatable production of large spherical cavities and, ultimately, spherical Macroshell™ targets.

For additional information, please contact Mr. L. A. Scott

Evaluation of Tensile Strength in Alkali Silicate Shells

Glass shells used as ICF fuel containers must withstand extreme external and internal pressure. A shell's resistance to external pressure (compressive strength) determines how rapidly it can be filled with fuel by permeation; its resistance to internal pressure (tensile strength) determines how much gaseous fuel it can ultimately hold.

The compressive failure of glass shells has been identified as a buckling failure mode.[25] It is characterized by Young's modulus, which is dependent on composition. The buckling strength of glass shells has been determined for several compositions.[26,27]

Tensile strength data for glass shells are not as plentiful and are incomplete.[28,29] Glass tensile strength is difficult to study because it is a function of the history of the glass and does not have an inherent value. While the theoretical strength of glass is on the order of 1.38×10^{10} to 3.44×10^{10} Pa, the actual (practical) strength of a particular glass object is usually several orders of magnitude lower, and is determined by the condition of its surface. Furthermore, tensile failure can occur in one of two modes: by brittle fracture, caused by stress intensification at the tips of surface flaws and defects, or by crack growth induced by stress corrosion (also known as delayed failure or fatigue). Consequently, since flaws are generally produced in a random manner on the surface of glass objects by handling and exposure to an abrasive or reactive environment, glass fracture is highly random in nature.

These considerations have caused increasing concern in target fabrication, as target sizes have steadily increased and the target specifications have become increasingly stringent; greater target reliability (or predictability) has become increasingly desirable as the failures have become more costly. We have therefore resumed a program to determine the effective tensile strength of glass shells.

The objectives of this program are as follows:

1. To determine the effective tensile strength of glass shells by evaluating the effects of glass composition, glass aging or corrosion, and shell geometry (i.e, wall thickness and diameter). Of particular importance is finding whether the fracture stress (which varies randomly from sample to sample and which depends on the probability of the existence of a fatal flaw) is a function of the surface area or the volume of the glass under stress.
2. To determine the effects of the shell processing conditions on tensile strength. Conditions under investigation include the pressure and temperature used during permeation filling, the composition of the permeant gases, pressure and thermal stress cycling, and exposure of the filled shells to ambient moisture.
3. To determine the effectiveness of several remedial methods in restoring glass strength or retarding weakening.

In this report, we discuss our findings concerning the effects of the permeant gas, geometric characteristics, surface area, and volume.

Experimental Procedure. The shells used in these experiments were alkali silicate glass with a nominal 95 mol% silica composition. Randomly chosen shells were individually characterized for diameter and wall thickness by optical microscopy and interferometry. The diameters of the selected shells varied from 450 to 750 μm, the wall thickness from 1.2 to 8.6 μm, and the aspect ratio from 55 to 590. Between 160 and 250 shells were used in each experiment; the characterized shells were arrayed in aluminum or brass "egg crates" to preserve their identities during the experiment.

To ensure that buckling failure did not occur as the shells were filled with gas (hydrogen or helium) in preparation for the tensile tests and obscure the tensile strength data, the crated shells were subjected to 30 atm buckling pressures prior to permeation. Further, the permeant gas was added in stages (<25 atm) to avoid the development of excessive buckling pressures. These stages generally involved repeated pressure increments of 20 atm at 260 to 360°C, with permeation times between pressure increments long enough to achieve >90% pressure equilibration. (The permeation times were calculated from published glass composition/permeation correlations;[30] glass composition was determined by atomic absorption spectroscopy.)

The tensile strength of the shells was evaluated every 25 atm as the room-temperature pressure in the shells was increased stepwise from 25 to 285 atm (helium) and 25 to 250 atm (hydrogen). As described in the preceding paragraph, the shells were pressurized (in a Parr bomb) at elevated temperatures. The 20 atm pressure increases were repeated as many times as necessary for the room-temperature pressure to increase by 25 atm. Then the Parr bomb was cooled and vented, and failures aurally and visually inventoried.

The actual gas pressure in the shells at each step was verifed only for hydrogen-filled shells because helium permeated from the shells too rapidly at room temperature to yield reliable data. The hydrogen fill pressure was determined by breaking individual shells in an evacuated PVT volume fitted with a Baratron 10 Torr pressure transducer. The sensitivity and resolution of this method are good, especially for large shells with high gas pressures. The method yielded very good gas fill data with a very narrow pressure distribution, generally with a standard deviation of 2%.

The final pressures were limited by the pressure and temperature limits of the Parr pressure apparatus and the permeation rates of the glass; to achieve these high pressures, the final permeation steps had to be conducted at reduced temperatures (<360°C) to remain within the pressure limits of the Parr bomb. The experiments were terminated when 90% (helium) and 86% (hydrogen) of the shells had failed.

Data Analysis. The fracture stress of the failed glass shells

was calculated from the shell diameter, wall thickness, and fill pressure at failure, using the hoop stress equation,

$$\Delta P = \frac{4S}{AR} ,$$

where ΔP is the tensile load on the glass wall, S is the fracture stress, and AR is the aspect ratio (o.d./wall thickness) of the fractured shell. Because of the random nature of failure, these experiments produced failure stress data with very broad distributions.

If the distributions are normal, the characteristic failure stress (tensile strength) for the sample can readily be calculated from histograms, cumulative failure probability curves, or from the slope of a least-squares regression function fitting a scatter plot of the individual shell data (hoop stress format). We elected to use the Weibull statistical treatment, a more versatile method that can accommodate skewed distributions, and that can also be used to predict the probability of failure as a function of the applied stress and the shell geometry.

In the common form of the Weibull expression, failure probability is a function of applied stress and a function of some volume (or surface area) characteristics of the sample,[31,32,33]

$$F = 1 - \exp[-(S/S_0)^m]$$

and

$$F = n/(N + 1) ,$$

where F is the failure probability or the fraction of the sample that failed below the measured sample failure stress, S; m is the Weibull modulus; S_0 is a scaling factor or the characteristic strength;[31] n is the rank of the sample in order of increasing measured failure stress; and N is the total number of tested samples. The Weibull modulus m is an indication of the spread of the distribution. As m approaches zero, the spread of the failure stress distribution increases and the probability of failure at any stress $S < S_0$ increases. As m increases, the spread of the data decreases, indicating greater homogeneity in the sample, and the probability of failure is significant only for $S \approx S_0$ (Ref. 31). In addition, when $m \approx 3$, the sample distribution is considered to be a normal distribution.[32]

In practice, the data are plotted in the double logarithm form of the above equation,

$$\ln[-\ln(1 - F)] = m \ln S - m \ln S_0 .$$

Since the Weibull expression is now a linear function, the Weibull modulus m and scaling factor S_0 can be obtained from the slope and intercept of the least-squares regression fit to the data. The median failure stress S_m can be calculated from the relationship,

$$S_m = S_0(0.693)^{1/m} .$$

The Weibull equation is also useful for predicting the probability of shell failure as a function of fill pressure and aspect ratio of the shells. Using the Weibull expression together with the hoop stress equation gives

$$P = \frac{4S_0}{AR} [-\ln(1 - F)]^{1/m} .$$

Consequently, for known values of S_0 and m, one can plot failure probability, F, contours as a function of fill pressure and shell aspect ratio.

Results and Discussion. We expected to encounter brittle fracture of the stressed shells during the rapid venting of the gas from the Parr bomb (when the shells were exposed only to dry gas). However, in none of the many fill-and-vent cycles could any bursting of shells in the dry gas atmosphere be detected through the walls of the Parr bomb with a stethoscope. Instead, upon opening the Parr bomb to the ambient air (at 75 to 85% relative humidity), there invariably commenced a staccato of bursting shells. Detectable bursting usually ceased within 30 min. The audible count of these bursting shells agreed to within 10% with the subsequent visual inventory; the discrepancy is probably due to the detection error (coincident bursts) in the audible count. Thus these losses must be attributable to failure by stress corrosion by the ambient moisture, rather than to brittle failure in the dry gas environment of the Parr bomb. This conclusion is supported by the fact that the observed delayed failure time, $t_{1/2} \approx 5$ min, is similar to the $t_{1/2}$ fatigue time typical for stressed glass.[33]

The helium experiment was terminated when the cumulative shell failures reached 90% of the original shell population. The distribution of the failure stress data for the sample was broad and nearly normal, ranging from 1.58×10^8 to 2.04×10^9 Pa. The mean and median failure stress of the actual sample data were 8.20×10^8 Pa ($\sigma = 2.82 \times 10^8$ Pa) and 7.99×10^8 Pa, respectively. The Weibull modulus m and the median failure stress S_m were 3.31 (standard error = 0.043) and 8.27×10^8 Pa, respectively. They were calculated from the least-squares fit to the Weibull plot of the sample data, and are shown in Fig. 2-12. The contours for 5% and 50% probability of failure for these shells, calculated as described above, are shown as a function of helium fill pressure and shell aspect ratio in Fig. 2-13.

Milewski and Marsters[28] reported a mean tensile strength of 5.17×10^8 Pa ($\sigma = 3.03 \times 10^8$ Pa), obtained by bursting helium-filled glass microspheres. However, their results pertain to a brittle fracture mode of failure, since in their shell-bursting experiments the shells failed in a dry helium environment during the controlled venting of the pressurization system. Our results, on the other hand, pertain to stress corrosion failure, since 90% of our observed failures occurred upon exposure of the stressed shells to ambient humidity. Thus we would expect the mean and median tensile strength of the shells used in our experiments to be significantly higher in a brittle failure mode.

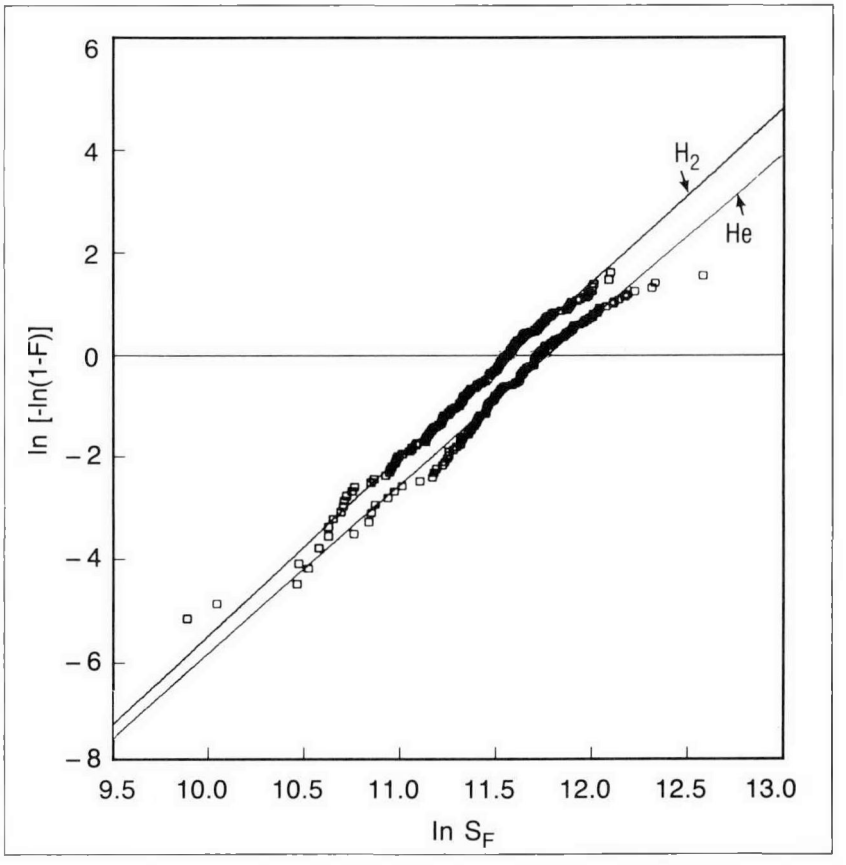

Fig. 2-12. The Weibull distribution of tensile failure stress is shown for helium-filled (lower line) and hydrogen-filled (upper line) glass microspheres. There is only a slight difference in the slope of the two lines, which indicates that the data distributions were similar in shape. However, there is a significant difference in intercept, which indicates a difference in median strength.

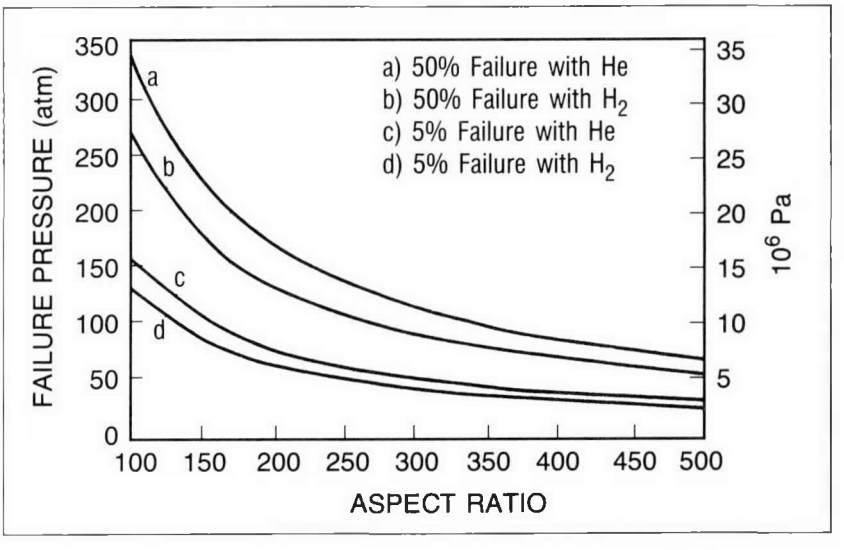

Fig. 2-13. Contours for 5% and 50% probability of failure for hollow glass shells, calculated using Weibull parameters, are shown as a function of fill gas pressure and shell aspect ratio. The 5% failure probability contours for the two fill gases are similar; the difference in the 50% failure probability contours is modest. There is a 95% level of confidence that the means of the two data sets differ by $1.55 \times 10^8 \pm 5.53 \times 10^7$ Pa.

The hydrogen experiment was terminated when the cumulative shell failures reached 86% of the original shell population. The distribution of the failure stress data for hydrogen was broad and normal, similar to that of the helium data, with failure stresses ranging from 1.38×10^8 to 1.23×10^9 Pa. The mean and the median failure stress of the hydrogen sample data were both 6.64×10^8 Pa ($\sigma = 2.09 \times 10^8$ Pa), significantly lower than the helium values.

The comparison of the least-squares regression fits to the Weibull plots of the helium and hydrogen data in Fig. 2-12 shows only a slight difference in slope, indicative of a similarity in the shape of the data distributions, but a significant difference in intercept, indicative of a difference in median strength. The Weibull modulus m and the median failure stress S_m, calculated from the slope and intercept of the regression function, are 3.50 (standard error = 0.02) and 6.82×10^8 Pa, respectively. Nevertheless, the 5% failure probability contour for hydrogen is similar to that for helium; the difference in the 50% failure probability contours is modest, as shown in Fig. 2-13.

As shown in Table 2-4, the mean and median failure stress values for hydrogen sample population were both about 20% lower than the corresponding values of the helium data. The large sigma values for the mean values of these broad data distributions would suggest that the difference is not statistically significant. However, since the confidence intervals at the 95% level for the two means do not overlap, as shown by the data in Table 2-4, the difference between the two mean failure stress values is indeed statistically significant. Furthermore, there is a 95% level of confidence that the means of the two data sets differ by $1.55 \times 10^8 \pm 5.53 \times 10^7$ Pa (see Fig. 2-13).

There are at least two mechanisms that may account for the reduction of glass strength by hydrogen. Hydrogen may react with the glass, reducing the silica to form SiH and SiOH moieties[34,35] in the glass, or hydrogen may react with the residual CO_2 (a blowing gas) in the shell.[36] This reduction reaction could result in the production of as much as 0.2 atm water vapor pressure (at room temperature) in the shell. This water vapor could react with the inner glass surface to cause corrosion-induced flaws to form on the internal surface.

Table 2-4. Failure Stress Values for Gas-Filled Glass Shells

Fill Gas	Failure Stress from Sample Distribution (10^8 Pa) Pressure Median	Mean	σ	95% Confidence Interval	Weibull Characteristics m	S_m (10^8 Pa)
He	7.99	8.20	2.82	7.72–8.68	3.3	8.27
H_2	6.64	6.64	2.08	6.34–6.96	3.5	6.82

Difference between mean (95% confidence interval) = $1.55 \times 10^8 \pm 5.53 \times 10^7$ Pa.

Spectroscopic evidence of the silica reduction reaction has been reported for reaction temperatures greater than 500°C (Refs. 34 and 35). Shelby[34] has also implied that the reaction may proceed at lower temperatures. If this is indeed so, then the extent of reaction and the reaction rate are expected to be highly dependent on the gas pressure, temperature, and cumulative reaction time. Thus one would expect the average failure stress value to decrease steadily as the fill progressed, as a consequence of the increasing hydrogen pressure and reaction (fill) time.

An analysis of the failure data did not reveal such a trend. The failure stress data for hydrogen do not show any relationship to cumulative reaction time or to hydrogen pressure, as shown in the hydrogen scatter plot of Fig. 2-14. This is more readily apparent when only the median failure stress values for each data group at the various pressures are considered, as indicated by the arrows in the figure. The best straight-line fit to these median failure stress values has zero slope, indicating that there is no relationship of failure stress to fill time or hydrogen concentration. (The first three data groups at the lower pressures were not considered in this analysis. These initial data, which comprise only a small fraction of the total, probably include some buckling failures, and represent the lower extreme of the total distribution.)

The present data are more consistent with the residual CO_2 reduction mechanism, which is thermodynamically more favored than the silica reduction. Furthermore, this reaction is expected to have a much higher reaction rate and is expected to go to completion rapidly because of the limited concentration of the residual CO_2. The total reaction time is expected to be considerably less than the cumulative fill times used in these experiments, and the effects of this reaction should manifest themselves early in the fill cycle. However, we have no conclusive evidence to support these speculations. Therefore, the exact mechanism for the reduction of the median tensile strength is still unidentified.

The effects of surface area and glass volume were also evaluated. One consequence of an increase in shell surface area (due to increasing shell diameter) is a probable increase in the number of flaws per shell and an increased probability that a shell will have a fatal flaw. Therefore, one could expect that the observed failure stress will decrease with an increase in shell surface area. However, a detailed analysis of the two sets of failure data has shown no dependence of tensile strength on shell surface area.

There is, however, an apparent relationship between failure stress and glass volume. As shown in Fig. 2-15, plots of failure stress as a function of glass volume show a pattern of decreasing tensile strength with increasing glass volume, both in the hydrogen and the helium data. A portion of this trend may be the result of error in experimental measurements [i.e., error in the method of measurement of shell diameter (o.d. $\pm$ 10 μm), shell wall ($\pm$0.25 μm), and fill pressure at failure ($\pm 6.89 \times 10^5$ to 2.41×10^6 Pa)]. In addition, there is also a strong probability of systematic error, particularly in the measurement of the wall

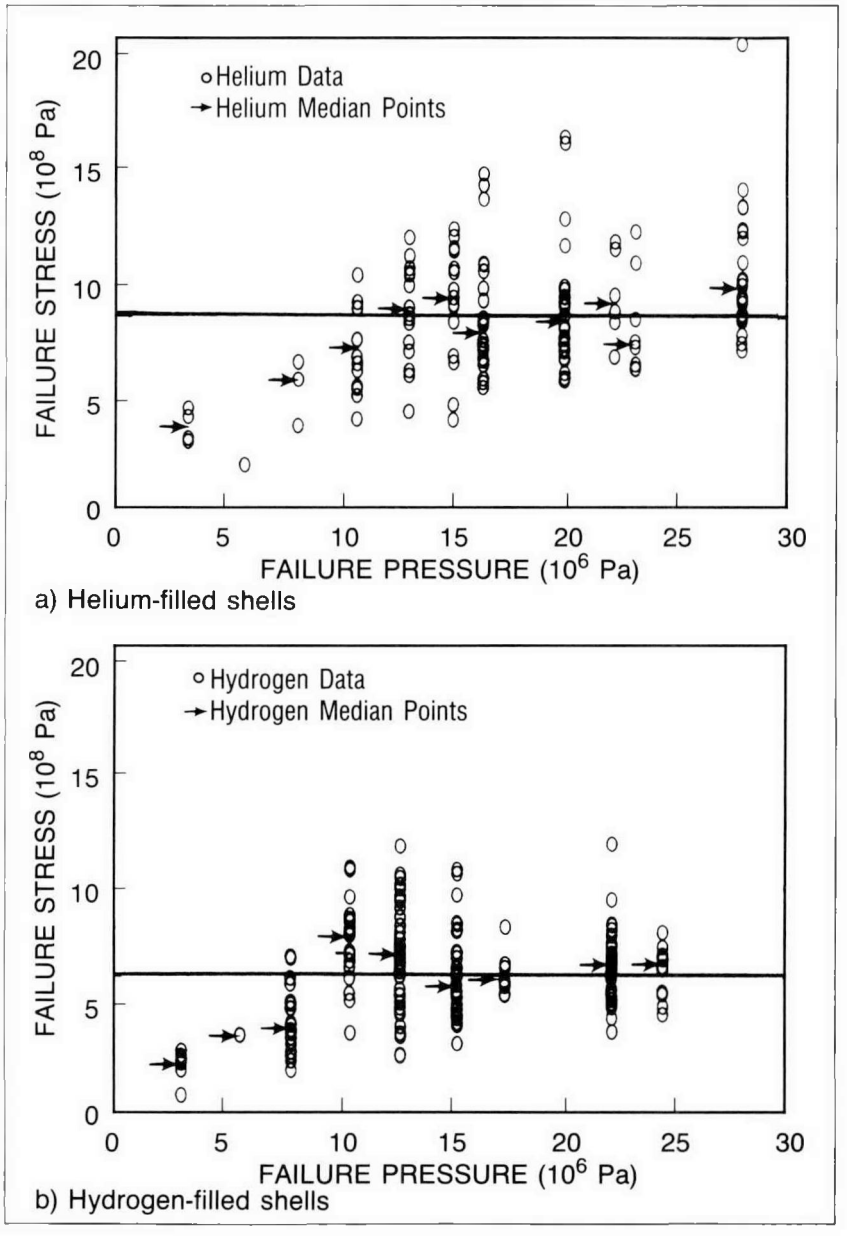

Fig. 2-14. The failure stresses in a population of helium-filled (a) and hydrogen-filled (b) glass shells are shown as a function of the gas concentration (i.e., fill pressure) at failure. Arrows indicate the median failure stress value in each data group. The line, equivalent to the mean failure stress, approximates the best fit to the data (the first three data groups at the lower pressures may have involved buckling failures and were not included in this analysis). The best fit to both data sets can also be approximated with a zero slope function, indicating that the median failure stress is not a function of fill time or gas concentration.

thickness of the shells (e.g., a constant bias of -0.25 μm in the wall thickness determinations) that would have a greater effect on the calculated failure stress values at small values of wall thickness. However, the result of our error analysis reinforces our confidence in the validity of the relationship between glass volume and tensile strength.

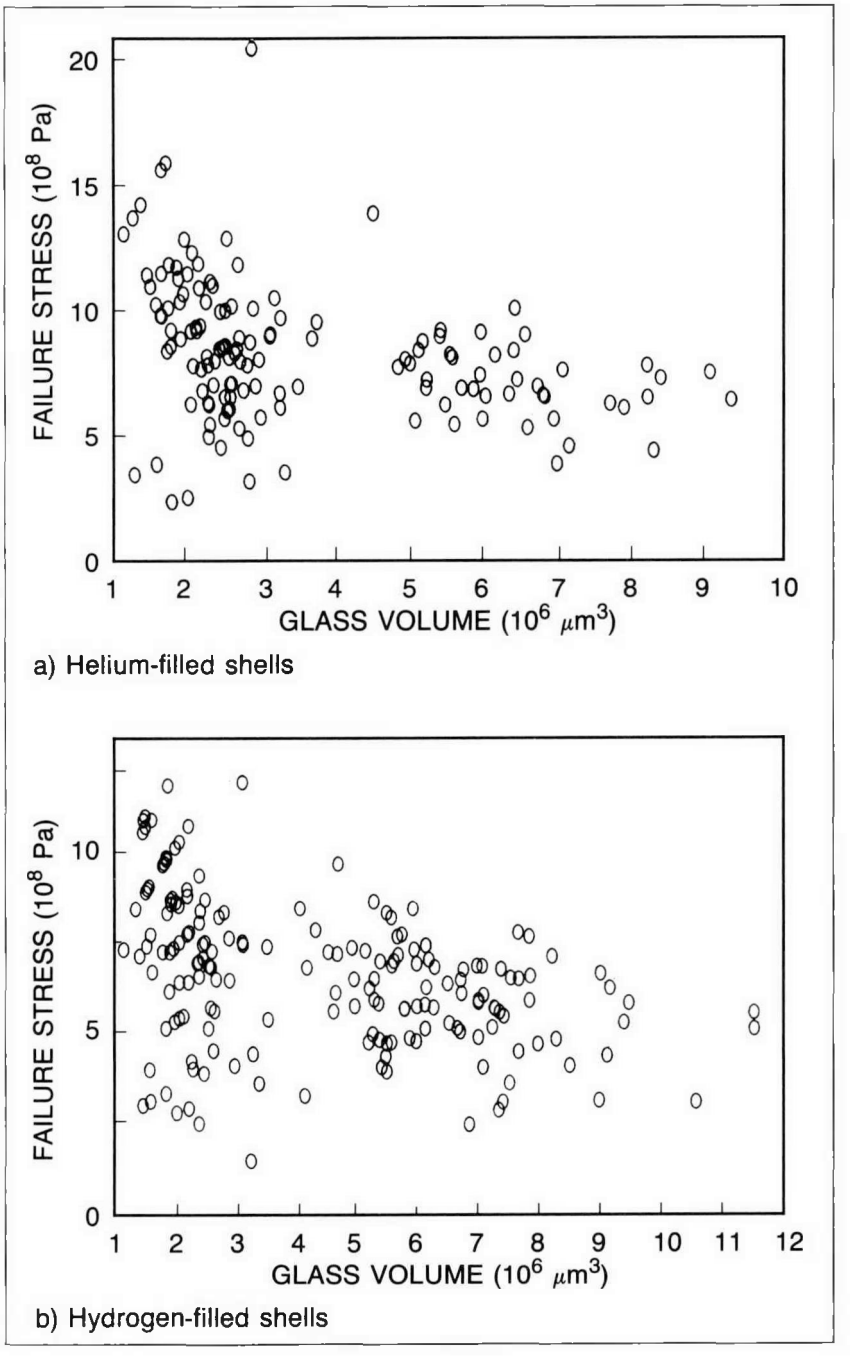

Fig. 2-15. If tensile strength is an intrinsic material property, then the observed failure stress will remain constant, independent of glass volume. Our results, however, suggest that tensile strength decreases with increasing glass volume for both helium-filled (a) and hydrogen-filled (b) glass shells.

In principle, if the tensile strength were truly an intrinsic material property, one would expect the observed failure stress to remain constant, independent of glass volume (i.e., wall thickness and shell diameter). However, the complete Weibull equation, as originally formulated,[37] postulates the relationship of increasing glass volume V to decreasing glass strength,

$$F = 1 - \exp[-V(S/S_0)m] \ .$$

As before, m and S_0 can be obtained from the slope and intercept of the least-squares regression fit. The median failure stress now depends on m, S_0, and V,

$$S_m = S_0(0.693/V)1/m \ .$$

Including the volume term in the Weibull equation results in a much better fit of the calculated probability contours to our data. As shown in Fig. 2-16, excluding the volume term from the Weibull treatment fits our data poorly since the predicted failure stress is independent of the glass volume; including the volume term in the Weibull treatment fits our data well since the predicted failure stress decreases with glass volume.

Further experiments should also test the volume effect. Although the original, complete Weibull model relates increasing glass volume to decreasing failure stress, our data do not show the relationship unambiguously. For the shells tested, the glass volumes are highly correlated to wall thickness and inverse aspect ratio. Further work is needed to clarify that volume, rather than wall thickness or inverse aspect ratio, is causing the decreased failure pressure.

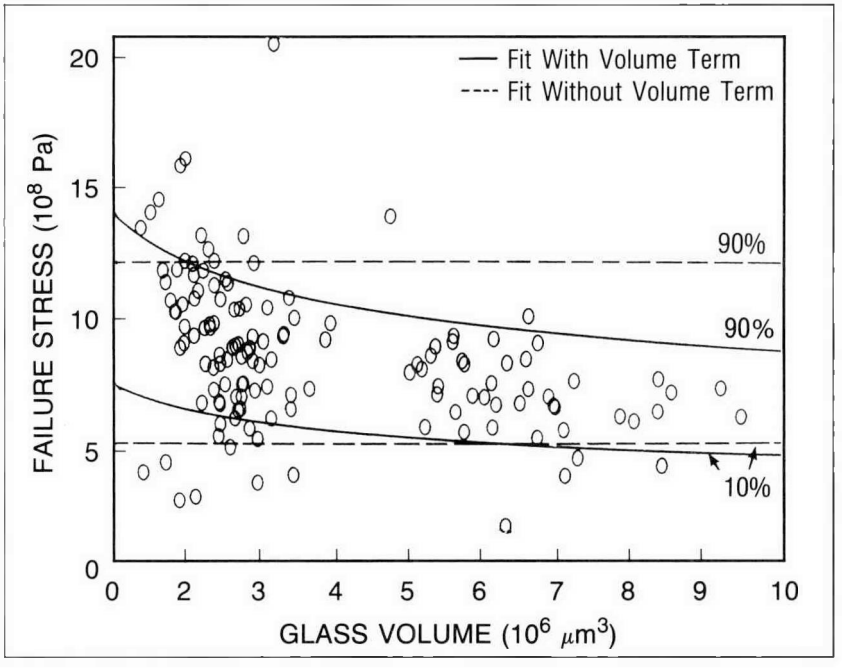

Fig. 2-16. Calculated 10% and 90% failure probability curves are shown superimposed on the data of Fig. 2-15a (failure stress as a function of glass volume for helium-filled shells). The straight lines result from Weibull calculations from which the volume term was excluded. The curved lines represent calculations in which the volume term was included; this results in a much better fit to our data, since the predicted failure stress decreases with glass volume.

For additional information, please contact Mr. M. A. Ebner

SECTION 2.4

Development and Analysis of Shell-Coating Techniques

The variety of targets that we can provide to our own laboratory and to other participants in the national inertial confinement fusion (ICF) program is increased by our ability to apply different types of coatings to targets. We are now able to apply organic and metal coatings to glass and polymer shells. The current needs of the program are for plastic coatings with ultrasmooth surface finishes, and so this year we concentrated on improving our understanding of glow discharge polymerization (GDP) and completing construction of a new parylene coating system that incorporates a plasma-assist capability.

Glow Discharge Polymerization

Glow discharge polymerization is used at KMS Fusion (KMSF) to deposit CH coatings onto shells. In this process, hydrogen and an organic gas are introduced into a plasma tube, where they are maintained at a specified pressure. The tube is surrounded by a radio-frequency (RF) coil, which induces an electric field that ionizes the gases to form a plasma (evidenced by a visible glow). Energetic electrons from the plasma break the organic gas molecules into fragments that attach themselves to the surfaces of shells bouncing in a pan at the bottom of the tube. The fragments then bond to one another through many crosslinks, forming a uniform, polymer-like film on each of the shells.

CH-Coatings on Glass Shells. There are three primary areas of persistent difficulty in the application of GDP-CH coatings to glass shells: (1) reproducibility of the coating rate, (2) achievement of target-quality surface finish, and (3) adhesion of the coating to the target.

Our difficulties in achieving a reproducible coating rate may have been solved by the discovery (and replacement) of a faulty gas flow controller in the GDP system. The faulty system allowed the pressure references to shift slowly during deposition times of many hours. A new flow control system was acquired and will be operational in early 1987.

Improving the surface finish is more difficult. Recent analysis of the coating surfaces suggests that the surface roughness is caused by spherical CH particles, created in the gas phase, that attach themselves to the surface and are subsequently coated. Figure 2-17 shows several phases of particle attachment and overcoating. The simplest way to reduce the formation of these spheres is to reduce the deposition pressure and/or RF power input to the system. However, this also drastically reduces the deposition rate and leads to unacceptably long deposition times.

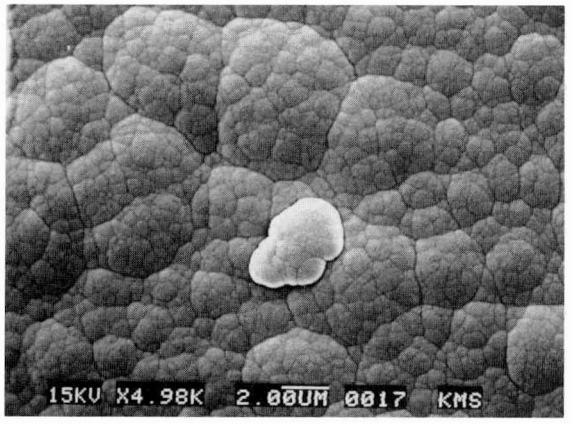

a) Particle formation

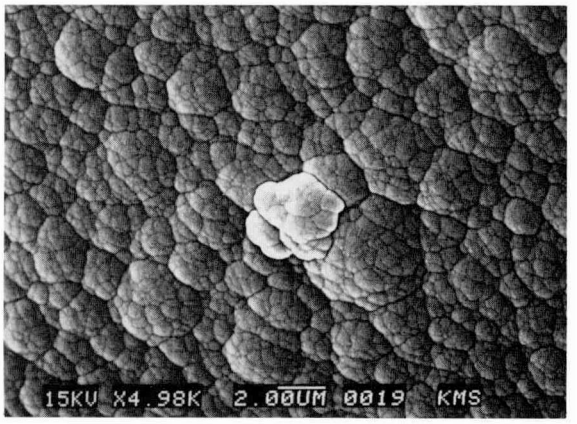

b) Particle attachment

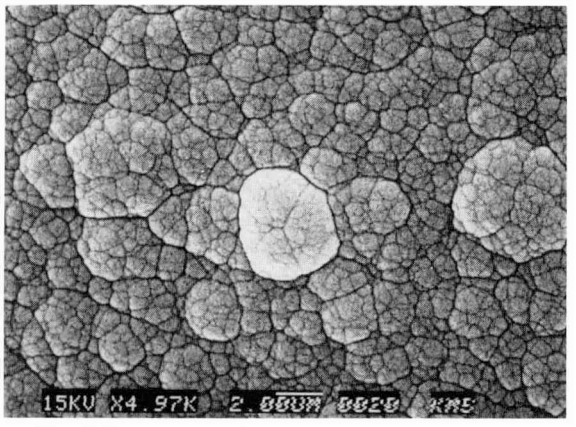

c) Particle overcoating

Fig. 2-17. Some surface roughness in GDP-CH coatings is caused by spherical CH particles that are created in the gas phase, attach themselves to the surface of the shell, and are subsequently coated along with the shell. These photomicrographs of such shells illustrate the steps (a through c) in the incorporation of these particles in the coating.

Minor adjustments to the deposition parameters of pressure and RF power result in only marginal improvements in surface finish. Our goal is to find a power and pressure regime in which (1) formation of these gas-phase particles is eliminated and (2) deposition rates are adequate for the desired coating thicknesses.

Another contributor to surface roughness is deposition onto the shells of debris from the retention screen installed in the shaker cups used to bounce the shells during coating. In our present system the shells must be bounced to a height of about an inch to achieve a good coating rate. To avoid losing the shells, a retaining screen is installed at the mouth of the cup. This screen becomes coated with the same CH that is deposited on the shells, and tiny flakes peel off and fall into the cup. These flakes also become attached to the CH film on the shells and contribute to the surface roughness. To solve this problem, the new parylene coating system (described below) has been modified by the introduction of a shell bouncing system. This

system is being used to develop a more suitable shaker or shell bouncer for the GDP system.

Separation of the coating from the shell surfaces is probably caused by stress in the coatings; consequently, we are trying to solve this problem by eliminating or reducing stress. A preliminary approach to reducing stress has been to increase the flow of hydrogen during CH deposition. Since we began increasing the hydrogen flow by a factor of 10, separation of the coating from the glass shell and fracture of the glass shells during coating has been eliminated. However, only a few such runs have been performed to date; work in this area is continuing.

Improved adhesion of the CH film to the glass shells has also been achieved by changes in the treatment of the glass shells before coating. A major change was to maintain the argon glow discharge, used to sputter-clean the shells, during introduction of the reactive gases to the coating chamber. Previously, the glow discharge was shut off after cleaning and turned back on after introduction of the reactive gases. Based on the limited number of runs so far, these changes seem to have solved the adhesion problem. Although stress is still present in the films, evidenced by the occasional stress-induced fracture of the coated shells, adhesion is so good that no separation of the film from the shells has been observed (see Fig. 2-18).

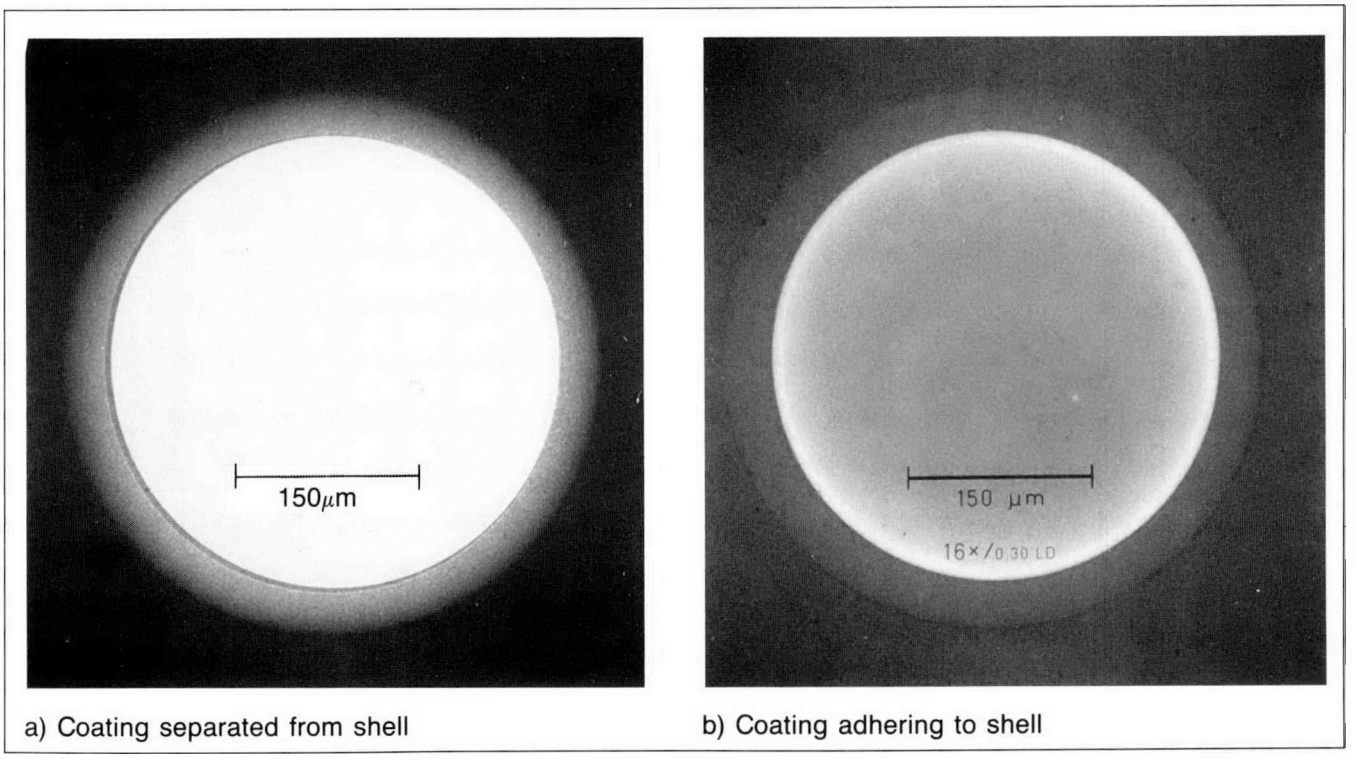

Fig. 2-18. Improved adhesion of the CH film to the glass shells has been achieved by changes in the treatment of the glass shells before coating. A major change was to maintain the argon glow discharge, used to sputter-clean the shells, during introduction of the reactive gases to the coating chamber. Previously, the glow discharge was shut off after cleaning and turned back on after introduction of the reactive gases (a). Although stress is still present in the films, adhesion is so good that no separation of the film from the shells has been observed (b).

As part of this work, we are developing a method to measure stresses in the coatings. We have used a metal strip of known elastic properties as a GDP coating substrate and coated one side with a very thin film of silicone grease while keeping the other side very clean. This ensures that CH will adhere well to the clean side and not at all to the greased side. Due to the stresses induced at the CH/metal interface and the absence of CH stress on the opposite side, the metal strip is bent. The extent of deformation is a measure for the stresses in a deposited film of known thickness.

Preliminary experiments were very encouraging. A significant bending of the metal strip occurred under normal coating conditions, indicating that stress is normally present in the GDP coatings and that this technique should be a sensitive measure of stress. We expect that this approach will enable us to evaluate stresses in situ (using witness foils during deposition) and also allow us to evaluate the influence of gases or moisture on the stresses in CH films after deposition. Environmentally induced post-coating stress development in the films will be investigated by filling the deposition system with selected gases after the deposition is complete.

Effect of Substrate Curvature on Coating Rate. We previously reported that the deposition rate of the GDP coating process showed a dependence on the curvature of the substrate.[38] Substrates with a small radius of curvature (i.e., shells with small diameters) were coated faster than those with a larger radius of curvature (larger diameters) when exposed to identical coating conditions. Since the differences in coating thicknesses were significant, a model was developed to explain this phenomenon, and further experiments were conducted to investigate the phenomenon in greater detail.

The model is based on a spherical dielectric substrate in a plasma. It will assume an electrical charge Q,

$$Q = kT_e \frac{R_0}{2} ,$$

where k is Boltzmann's constant, T_e is the electron temperature, and R_0 is the substrate radius. This charged sphere has an electrical field E,

$$E = \frac{kT_e}{2} R_0 .$$

It is this electrical field that attracts the positive ions formed in the glow discharge to the surface of the sphere, where they collect to form a coating. The rate of ion deposition or coating should therefore be inversely proportional to the radius of the spherical shell substrate.

The rate can be described more quantitatively as follows. We assume that the velocity v of the ions is a product of the ion mobility α in the plasma and the electrical field E of the sphere,

$$v = \alpha E .$$

The rate at which ions arrive at the surface of the sphere is then equal to the number density N of the ions in the plasma times the velocity v. The mass deposition rate per unit area M is given by

$$M = vNm \ ,$$

where m is the mass of the ion. If the resulting density of the deposited film is ρ, then the rate at which the film grows, as a function of the ions in the plasma, is

$$dr = \frac{\alpha k T_e N m}{2\rho (R_0 + r)}$$

where r is coating thickness. It is reasonable, however, to assume that there is also a contribution to the film growth from nonionized but reactive species in the gaseous coating environment that are not attracted by the electrical field.

To account for this contribution, we write a generalized differential equation describing the GDP growth mechanism in the form

$$\frac{dr}{dt} = \frac{a}{R_0 + r} = b \ , \tag{1}$$

where $a = \alpha k T_e N m / 2\rho$ and b is, so far, an unknown constant representing growth from nonionized species and is presumed to be independent of substrate radius. Since a contains the electron temperature and the number density of the ions, it is obvious that it depends on both the RF power used to sustain the plasma and the partial pressure of the starting gas in the system. The nonionic reactive species account for the b portion of the coating rate. They arise either from former ions that recombined with an electron or simply from fragments of the original molecule, possibly in excited states. Either or both species are thus also attributable to the RF power and the partial pressure of the starting gas in the system. Integrating Eq. (1) gives a relationship between R_0, r, and coating time t,

$$-\ln \frac{1 + r}{a + bR_0} = \frac{b(bt - r)}{a} \ . \tag{2}$$

On the basis of these relationships, coating of spherical substrates can be used to gain some insight into the composition of the plasma in a GDP system.

Experiments were conducted to measure the rate of film growth as a function of the substrate radius. In previous measurements, our data were so scattered that we could establish only a qualitative relationship between Eq. (2) and the data. This scatter was, in part, the result of large uncertainties in film thickness measurements on the hollow microsphere substrates. Subsequently, a technique was developed at KMSF that permits

us to measure coating thicknesses on microspheres with an accuracy of about ± 0.2 μm in the range of 1 to ~ 20 μm (Ref. 39).

We also reported previously that there was considerable difference in the deposition rate between different locations inside the deposition system, with the rates changing measurably over distances of a few millimeters.[38] To circumvent this problem, we mounted the glass shells on fibers and arranged them on a carousel that rotated at a speed of 1 rpm; thus, during a run of several hours, the location-dependent differences in deposition rates were averaged.

The measurements reported here were taken from experiments using a 3:2 mixture of trans-2-butene and hydrogen at a total pressure of 13.3 Pa. The RF power input ranged from 1 to 9 W and was held constant throughout any one run. The results of a typical run are shown in Fig. 2-19.

The results of the experiments were curve-fitted with Eq. (2) by choosing the best fitting combinations of a and b. A plot of $\ln(a)$ versus b (Fig. 2-20) produced a linear relationship suggesting that a function of the form

$$a = a_0 \exp(sb)$$

exists, where s is a constant. This expression shows quantitatively the relationship between the contributions of charged and uncharged species to the coating rate in the GDP process. It also confirms the intuitive expectation that the higher the RF power, the smaller the relative contribution to the coating rate by nonionized species.

The ultimate objective of this work is to find a quantitative correlation between the stress conditions in the deposited film

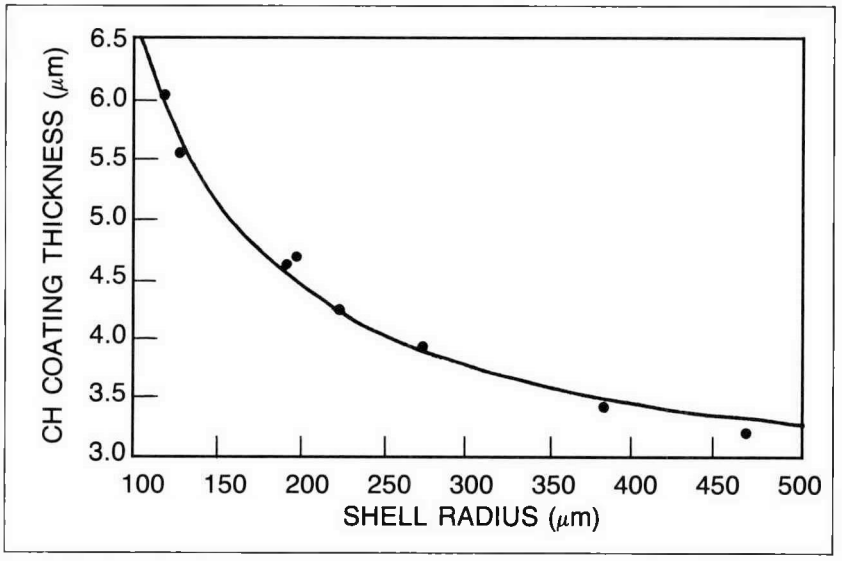

Fig. 2-19. The rate at which GDP coatings are deposited depends on substrate curvature. Here, the variation in CH thickness is shown as a function of shell radius, where feed-gas pressure and RF power are held constant. The results of the experiments (dots) were curve-fitted with Eq. (2) by choosing the best fitting combinations of a (95.64) and b (0.84).

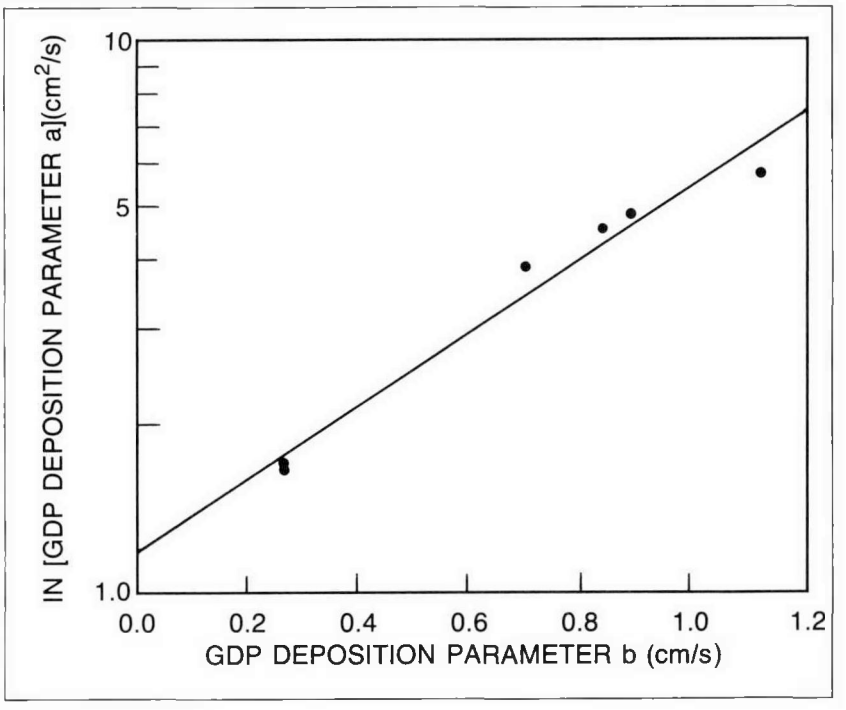

Fig. 2-20. Both the ionized and the nonionized (but reactive) species present in the gaseous GDP environment contribute to the GDP coating. The relative contributions of the two species to the GDP coating rate are given by an equation of the form $a = a_0 \exp(sb)$, where $s \sim 1$, and a and b are deposition parameters that represent the contributions of the ionized and nonionized species, respectively. The higher the RF power, the smaller the relative contribution of the nonionized species.

(indicated in the extreme by fracturing of the films) and the composition of the gases in the glow discharge, as a function of the RF power input and the partial pressures of hydrogen and the precursor gas (in this case trans-2-butene). The analysis is not complete, but the first results show that the model does describe the physics of the GDP process very well. We hope that this research, used together with mass spectrometry, will provide detailed insight into the chemistry of GDP.

Construction of a New Parylene Coating System with Plasma Assist Capability

The coatings produced by GDP are hard, strong, and tough. For applications requiring a soft, elastic coating, parylene is used. In 1986, we constructed a new parylene coating system that is more efficient, easier to operate, and capable of coating larger substrates than our old system. This new system also incorporates a plasma-assist capability. It is shown schematically in Fig. 2-21.

The basic parylene coating system consists of a sublimation furnace, a pyrolization furnace, and a reaction chamber. The parylene dimer, paracyclophane, is transformed from a powder to a gas in the sublimation furnace. The gaseous dimer is then

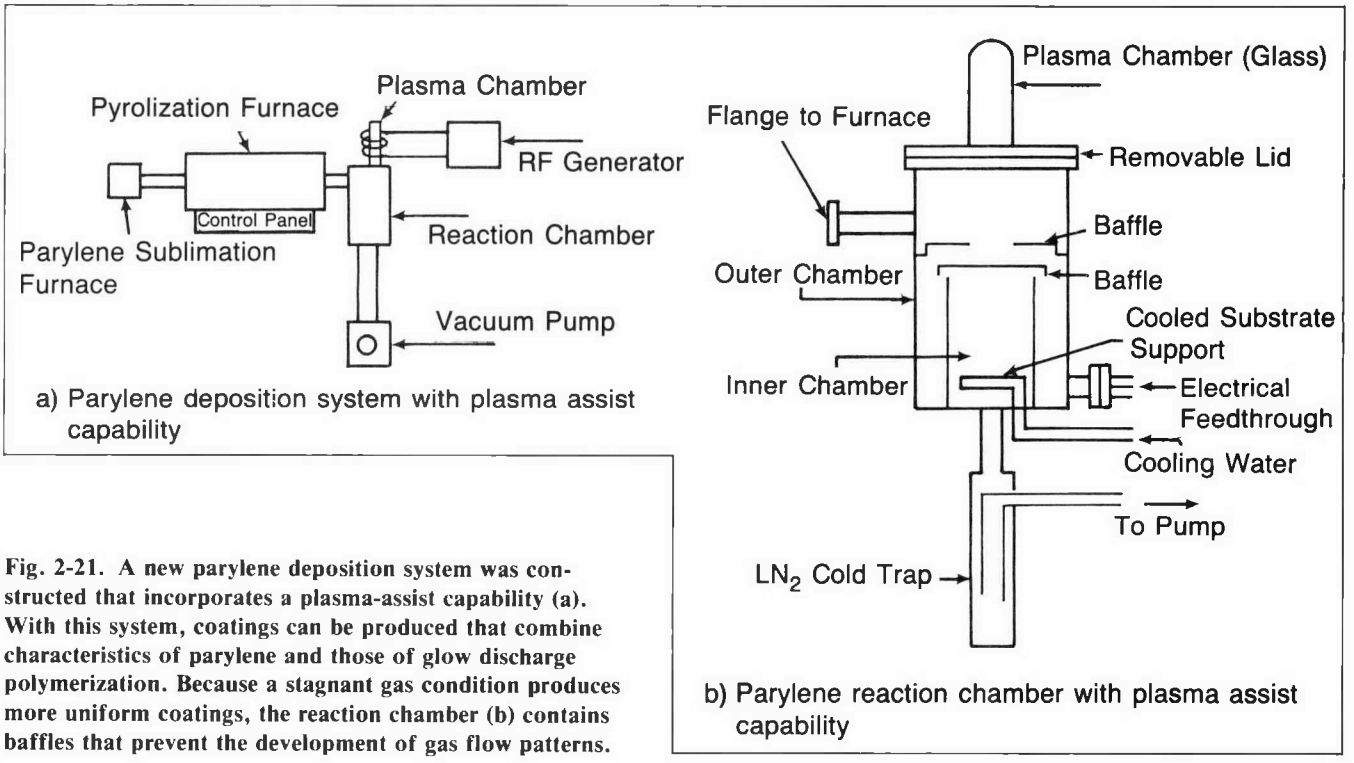

Fig. 2-21. A new parylene deposition system was constructed that incorporates a plasma-assist capability (a). With this system, coatings can be produced that combine characteristics of parylene and those of glow discharge polymerization. Because a stagnant gas condition produces more uniform coatings, the reaction chamber (b) contains baffles that prevent the development of gas flow patterns.

"cracked" into two di-radicals in the pyrolization oven. These organic radicals are then deposited as a partially crystalline polymer film on cold surfaces downstream under reduced pressure.

The new sublimation furnace affords better temperature control, which permits us to use higher parylene dimer sublimation temperatures. Consequently, we can achieve higher coating deposition rates, while still accomplishing efficient pyrolysis of the dimer. The new three-zone pyrolization or tube furnace (which replaces a single-zone furnace) permits increased control over the rate of parylene pyrolysis and thus control over the parylene deposition rate. Replacement of the narrow-bore glass tubing used in the old system with larger-bore metal tubing has increased vacuum pump conductance, simplified cleaning procedures, and minimized the hazards of working with pressure differentials. Substrate size limits have been increased from 35 to 165 mm.

The plasma-assist capability is provided by the plasma chamber and the RF generator. This is a new technique, in which additional molecular excitation (in excess of that achieved by thermal cracking of the parylene dimer), is achieved by RF electromagnetic radiation that is coupled into the system by an inductive coil or capacitive plates. This additional energy produces a plasma, which results in further bond breaking of the parylene monomer radical.

The phenomenon is very similar to GDP. The characteristics of the coatings that are produced are likewise similar to those produced by GDP. By pulsing the signal of the electromagnetic energy source, we hope to produce a composite of soft, elastic

parylene with hard, tough GDP-type films. A harder coating may permit bounce-coating of shells, a technique not possible with pure parylene, since the soft coating tends to promote clumping of the shells when they are bounced.

With this system, we can now produce alternating layers of pure parylene and plasma-assisted, modified parylene, or homogeneous films with various degrees of GDP-like characteristics by operating in a continuous plasma-assist mode. Figure 2-21b shows the details of the components inside the reaction chamber. The baffles are necessary to prevent gas flow patterns, as a stagnant gas condition produces more uniform coatings. Our new system can be run in both the plasma-assisted and conventional modes without any modifications.

Pinhole Experiments. We first used the new system to perform a systematic study of operating conditions to produce pinhole-free conventional parylene films (i.e., without the plasma-assist feature operating). The parameters varied were the parylene sublimation and pyrolysis temperatures, system pressures, substrate temperature, and deposition time. These parameters affected the total flux of radicals through the system (flow rate) and the residence time of the organic species in the critical elements of the system. The films were deposited onto brass disks.

To detect the presence of pinholes, the coated disks were immersed in a copper sulfate solution and a voltage applied across the disks. The presence of pinholes could be detected by observing current passing through the system. The location of pinholes could be observed by the deposition (plating) of copper on and in the pinholes.

The best results were obtained when substrate surfaces were very clean. Variation of pyrolysis temperature between 600 and 740°C had very little effect on the number of pinholes in the films, as long as the flow rate was low enough to permit efficient pyrolysis of the dimer material. (The extent of pyrolysis was empirically checked by optical microscopy of the resulting films. Dimers that pass through the system and condense without being pyrolyzed produce a crystalline appearance in the film.)

Film thickness, which is determined by the deposition time, was the most important parameter affecting the number of pinholes. The thicker the film, the fewer the pinholes. The number of pinholes ranged from 0/in.^{2} to 5/in.^{2}.

Film thickness was also the most important factor affecting the "breakdown" time of the films in the copper plating experiment. (Pinholes can be contorted and convoluted, winding through the coating. In thick films, it can take a long time before electrical contact is established with the brass disk. This sudden electrical contact is called "breakdown.") Breakdown time varied from several seconds to several days, and some films showed no breakdown for test times of up to a week. No breakdown was observed for films thicker than ~6 μm. There was no apparent loss of adhesion of the films after soaking in the copper sulfate solution for several days.

Surface Roughness Experiments. Another set of experiments was conducted to observe the effects of varying the same parameters (parylene sublimation and pyrolysis temperatures, system pressures, substrate temperature, and deposition time) on surface finish. The best coatings, which were optically clear and had the smoothest surfaces, were produced with substrates at room temperature, a parylene sublimation temperature of 120 to 130°C, a pyrolysis temperature of 710 to 730°C, and a deposition rate of 0.5 μm/h. Variation of substrate temperature was found to have a visible effect on the surface roughness of these films: Minor blistering occurred at 140°C; a seemingly crystalline surface was produced at 135°C. The films with very few surface defects were also nearly optically clear. When deposition rates were increased by raising the parylene sublimation temperature, less clear films resulted (milky, but still transparent), which also seem more brittle than films formed at lower deposition rates. We again observed that parylene deposition accentuates imperfections on the substrate surface, a phenomenon also associated with GDP coatings.

Plasma-Assisted Deposition Experiments. We conducted a small number of plasma-assisted parylene depositions. During depositions at high (e.g., 200 mTorr) chamber pressures, relatively large quantities of fine fibrous material, reminiscent of foam, were created. This material seems to be a gas-phase product similar to that seen in GDP. Experiments at pressures lower than 90 mTorr resulted in a surface covered with 2 to 3 μm spheres, a phenomenon also seen in GDP work. We will continue to investigate plasma-assisted deposition in 1987.

For additional information, please contact Mr. H. K. Lintz

SECTION 2.5

Target Characterization Development

Computer Simulation of Interferometric Fringe Patterns

Classical interferometry has historically been the method of choice for determining the wall thickness uniformity of transparent fuel containers[40] and cryogenic fuel layers.[41] Double-pass (Twyman-Green) interferometers are routinely used to determine wall thickness, to analyze wall defects (particularly wall thickness uniformity), and to verify fuel fill. Single-pass interferograms produced by a lateral shearing interferometer are used to evaluate cryogenic (liquid or solid fuel) targets.

During 1986 we extended the capabilities of our three-dimensional ray-trace computer code for the analysis and prediction of classical interferometric fringe patterns for shells. Both single- and double-pass interferograms can be simulated with this code. The code handles transparent hollow spherical fuel containers, either empty or filled with gaseous DT. The ability to model filled shells is important, since interferometric images can change dramatically when fuel is present in a shell. The code can also generate fringe patterns corresponding to single-pass interferograms of shells containing DT layers that are contiguous with the inner surface of the shell.

Two types of defects can be modeled: nonconcentricity defects, in which the centers of the inner and outer surfaces do not coincide, and nonsphericity defects, in which the inner surface of the shell is spheroidal rather than spherical. Nonconcentricity defects can be in any direction, and combinations of nonconcentricity and nonsphericity defects can be modeled, provided that the outer shell surface and the inner surface of the liquid or solid DT layer (if present) are spherical.

The defining equations for nonconcentricity NC and nonsphericity NS are

$$NC = \epsilon / W_{\text{avg}}$$

and

$$NS = 1 - a/b \ ,$$

where ϵ is the offset of the centers of the inner and outer spherical surfaces, W_{avg} is the average wall thickness, and a and b are, respectively, the semi-minor and semi-major axes of the spheroidal surface.

The fringes of the simulated interferograms arise from the calculated differences in optical path lengths between rays that traverse the shell and a reference ray. The code uses the ray along the optical axis of the system, which passes through the center of the shell, as the reference ray. If the path lengths differ by an

integral number of wavelengths, constructive interference (a bright fringe) occurs. The code plots points of destructive interference (dark fringes), which occur when the optical path length difference equals an odd integer multiple of half-wavelengths.

In practice, for a particular application, the code is used to predict the fringe patterns as a function of selected values of shell diameter, average wall thickness, and selected values of *NS* and *NC*. The program also calculates the maximum and minimum wall thicknesses of the shell, along with the wall nonuniformity *NU* which is defined by

$$NU = \frac{W_{max} - W_{min}}{W_{avg}} ,$$

where W_{max} and W_{min} refer to the maximum and minimum wall thicknesses, respectively.

The ability of the code to generate interference fringe patterns, given various values of *NC* and *NS*, provides an extremely valuable visual guideline for establishing the boundaries of shell acceptability in the fuel shell selection process. Figure 2-22 shows computer-generated double-pass interferometric fringe patterns (535 nm light source) for empty 600 μm o.d. glass shells having selected *NC* and *NS* values.

For these representative calculations, the nonconcentricity defect is an offset to the right along the horizontal axis. The patterns are shifted in the direction of the offset. Note that the fringe pattern is quite sensitive to the nonsphericity of the inner surface. For a shell with a 3 μm thick wall and an *NS* value of 0.002, the fringes are highly elliptical; at $NS = 0.005$ they are convoluted. The number of fringes increases as the thickness of the shell wall is increased. As the fringe spacing becomes smaller (due to increasing wall thickness), those fringes nearer the edge of the shell may become indistinguishable from each other. Those near the center of the fringe pattern remain visible, however, and the offset of the center of the fringe pattern, due to nonconcentricity, appears constant as the shell wall thickness is increased from 3 to 7 μm. This is fortunate in view of the effect of nonconcentricity on wall nonuniformity and the maximum wall thickness variation.

For a given shell, a diameter and average wall thickness are determined in a straightforward manner by optics and interferometry. The shell's interferometric fringe pattern is compared with the computed patterns. The normal procedure is to estimate an *NC* value for the shell from the actual pattern first, then to find the set of predicted patterns that bound this pattern. By interpolation, values for *NC* and *NS* are determined. From these values, *NU* is calculated.

If the fringe pattern indicates no asphericity of the shell, then $NU = 2\ NC$. If an elliptical pattern exists, *NU* is a function of both nonconcentricity and nonsphericity defects; use of the code is then essential to provide a single *NU*, or a $(W_{max} - W_{min})$ value, from the determined values of *NC* and *NS*. Either *NU* or $(W_{max} - W_{min})$ is reported for a completely characterized fuel

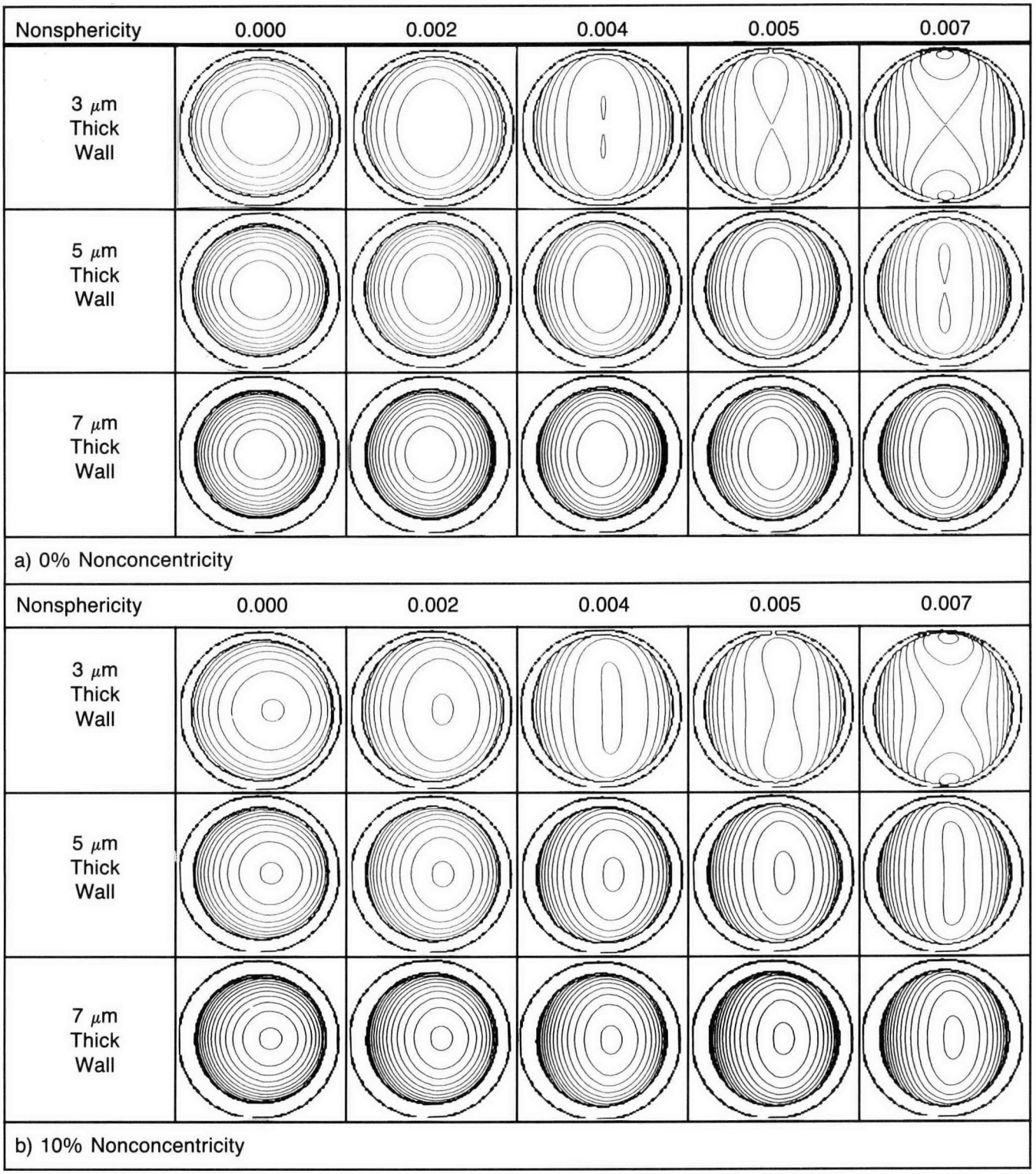

Fig. 2-22. The ability of the computer code to generate interference fringe patterns, given various values of *NC* and *NS*, provides an extremely valuable visual guideline for use in selecting fuel shells. The shell selection technician can choose a shell having a bull's eye pattern no worse than that given by a computer-generated reference pattern. These computer-generated double-pass interferometric fringe patterns represent empty glass (index of refraction $n = 1.475$) shells 600 μm in outside diameter, with the *NC* and *NS* defects indicated. The wavelength of the light used is 535 nm.

shell that will be used in a target shot, depending on the target specifications.

For a requested target set, normally there are limits specified as either a maximum NU or a $(W_{max} - W_{min})$. These specified limits translate to consequent limits on both allowable NC and NS for the target selection process. The maximum NC, NC_{max}, occurs when NS is zero. Similarly, the maximum NS, NS_{max}, occurs when NC is zero. NC_{max} and NS_{max} are expressed as

$$NC_{max} = \frac{NU}{2} = \frac{W_{max} - W_{min}}{2W_{avg}}$$

and

$$NS_{max} = \frac{W_{max} - W_{min}}{R - W_{avg}} = NU \frac{W_{avg}}{R - W_{avg}} .$$

Thus, for targets having both nonsphericity and nonconcentricity defects, $NS \leq NS_{max}$ and $NC \leq NC_{max}$. These bounds for NS and NC are chosen to set the limits for the computations.

For additional information, please contact Mr. A. J. Martin

Image Analysis for Macroshell™ Spheres

The production of spherical cavities in glass preforms, cylinders, or fused hemishells is the first step in one promising method for the production of large (>2 mm diameter) shells[42] (see also Section 2.4). Sphericity requirements for the cavities depend upon the specifications for shell aspect ratio (diameter/wall thickness) and wall thickness uniformity. For example, a shell with an aspect ratio of 100 and a wall nonuniformity of less than 10% requires an inner cavity with a sphericity better than 99.8%. The ability to measure cavity sphericity accurately is therefore essential.

Radiographic[43] and photographic methods have been used to measure cavity sphericity. Since x-ray scattering blurs the radiographic image of the cavity, we have used white-light photography. Sphericity is characterized by photographing the cavity from orthogonal directions and then evaluating the circularity of the two-dimensional cavity images using Fourier analysis.

A dual-aperture system (Fig. 2-23) is used to photograph the sample. One aperture is placed directly over the light source, and a second aperture is placed 11 cm above the light source, just below the sample. This aperture system sharpens the image of the cavity/glass boundary by minimizing the amount of nonparallel light reaching the sample. Orthogonal photographs of the cavity are obtained by immersing the sample in index-matching fluid, photographing it, rotating the cavity so as to view it along an axis orthogonal to the first, and photographing it again. The photographic negatives are formed on glass plates rather than plastic film to eliminate image distortions resulting

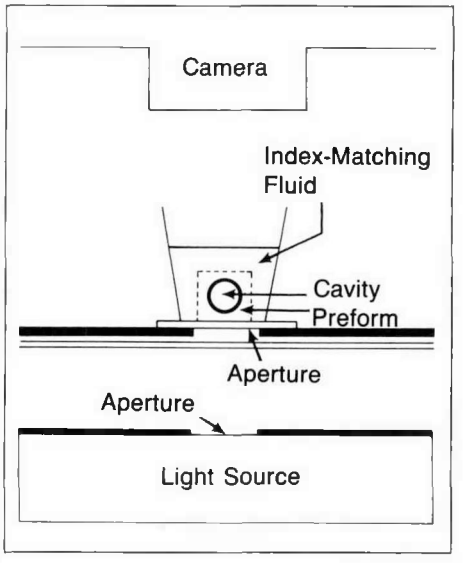

Fig. 2-23. Dual-aperture white-light photography is used to measure cavity sphericity in Macroshell™ targets. The dual apertures sharpen the image of the cavity/glass boundary by minimizing the amount of nonparallel light that reaches the sample. The sample is immersed in index-matching fluid, photographed, rotated so it can be viewed along an axis orthogonal to the first, and photographed again. The circularity of the two two-dimensional cavity images is then evaluated using Fourier analysis.

from shrinkage of the negative. The negative images are enlarged and printed on high-contrast paper to maximize the contrast at the cavity/glass boundary.

The enlarged images are then digitized. For each image, 128 perimeter coordinates are input by means of multiple passes around the image contour using an electronic data tablet.

The image analysis code finds the circle best fit to the coordinates using a least-squares fit analysis. The image is analyzed using a fast Fourier transform (FFT) to yield the types, magnitudes, and positions of the nonuniformities.[44] The code also gives a single figure of merit for the uniformity, the percent noncircularity *NC*, which is calculated using the expression,

$$NC = \frac{2RMS}{\bar{r}} \times 100\%$$

where $\bar{r}$ is the average radius and the *RMS* (root mean square) value is given by

$$RMS = \left[0.5 \sum_{i=2}^{4} (\text{mode amplitude}_i - \text{average noise amplitude})^2\right]^{1/2} .$$

As standards, the image of a high-precision machined steel ball photographed in the same index-matching fluid used for the samples and a compass-drawn circle were digitized using the data tablet, and analyzed. The noncircularity values obtained were less than 0.2% for the steel ball image and less than 0.1% for the circle.

The stringent sphericity requirements for cavities demand greater accuracy in our noncircularity measurements. We plan to design and build an image-analysis system that will digitize the photographic negative directly, thus eliminating errors introduced during image printing and manual data entry.

For additional information, please contact Mr. L. A. Scott

Holography Development for Solid Fuel in Macroshell™ Spheres

Evaluation of the cryogenic fuel layer (liquid or solid) in large or thick-walled targets will require a diagnostic technique that is less sensitive to the effects of the fuel container than is classical interferometry. Results from Lawrence Livermore National Laboratory[45] and the Soviet Union[46] indicate that holographic interferometry is both more accurate and more sensitive than classical interferometry. Development work is underway at KMS Fusion to produce a holographic interferometry system for fuel layer characterization.

Classical interferometry does not work well with thick-walled shells, such as the poly(vinyl alcohol) (PVA) shells used in the Low Preheat Implosion Campaign. Because the thick walls add many fringes to the interferograms, their interpretation is very

difficult. This is illustrated by measurements done on computer-simulated classical interferograms of a cryogenic fuel layer within a perfect, 125 × 5 μm (o.d. × wall) PVA shell.[47] The offset of the center of the interferometric fringe pattern from the center of the shell was only about 3% of the shell image for a fuel layer nonuniformity of 20%. Determination of nonuniformities of less than about 20% is therefore severely hampered by the uncertainty in the location of fringe maxima. In addition, polymer shells tend to be more nonuniform than thin glass shells, making determination of the uniformity of the cryogenic layer much more difficult.

Holographic interferometry significantly lessens this problem by allowing us to observe fringes due to the fuel layer alone. The holographic interferogram of a cryogenic target is formed by making two holograms, one of the target with its fuel in the gas phase, and one of the target containing liquid or solid fuel. These holograms are superimposed to form an interferogram, either by making the two holograms on the same holographic plate, forming a double exposure, or by making them on separate plates and superimposing them upon reconstruction. Only changes in the object (in this case, the cryogenic fuel layer) contribute to fringe formation.

Apparatus and Procedure. The apparatus used in developing our cryogenic holography system is shown schematically in Fig. 2-24. A beam from an argon ion laser is used to form the holograms. Immediately after the beam leaves the laser, 5% is split out to a spectrum analyzer (scanning interferometer). The output of the spectrum analyzer is used to tune an etalon to the desired bandwidth. The beam transmitted by the first beamsplitter then enters a variable beamsplitter, which can vary the ratio of powers of the reference and object beams from 1:1 to about 20:1. The variable beamsplitter is set so that the power of the reference beam is 10 times that of the object beam. The exposure of the holographic plate is controlled by two shutters, one in each beam, which are operated simultaneously by a shutter controller. Both beams pass through spatial filters. The object beam then passes through the target to a focusing lens that images the target on the film plane of the holographic camera. The reference beam goes directly to the holographic camera. The angle between the beams is 24°, the angle required to give optimum resolution with the film used in the holographic camera. Because this film can be reused (up to 300 times) a Polaroid camera is used to photograph the holographic interferogram.

The target is mounted on a post that is attached to a cryostat extension in the target chamber. A heating laser allows us to manipulate the fuel layer within the shell while the cryostat is cold. Since this system employs conduction cooling using one cryostat, only liquid layers have been holographed so far. (A more elaborate cryogenic system is required to produce solid layers.)

A photograph of a holographic interferogram of a liquid layer formed using this system is shown in Fig. 2-25. The shell in the figure is a glass shell with an outside diameter of 680 μm and a

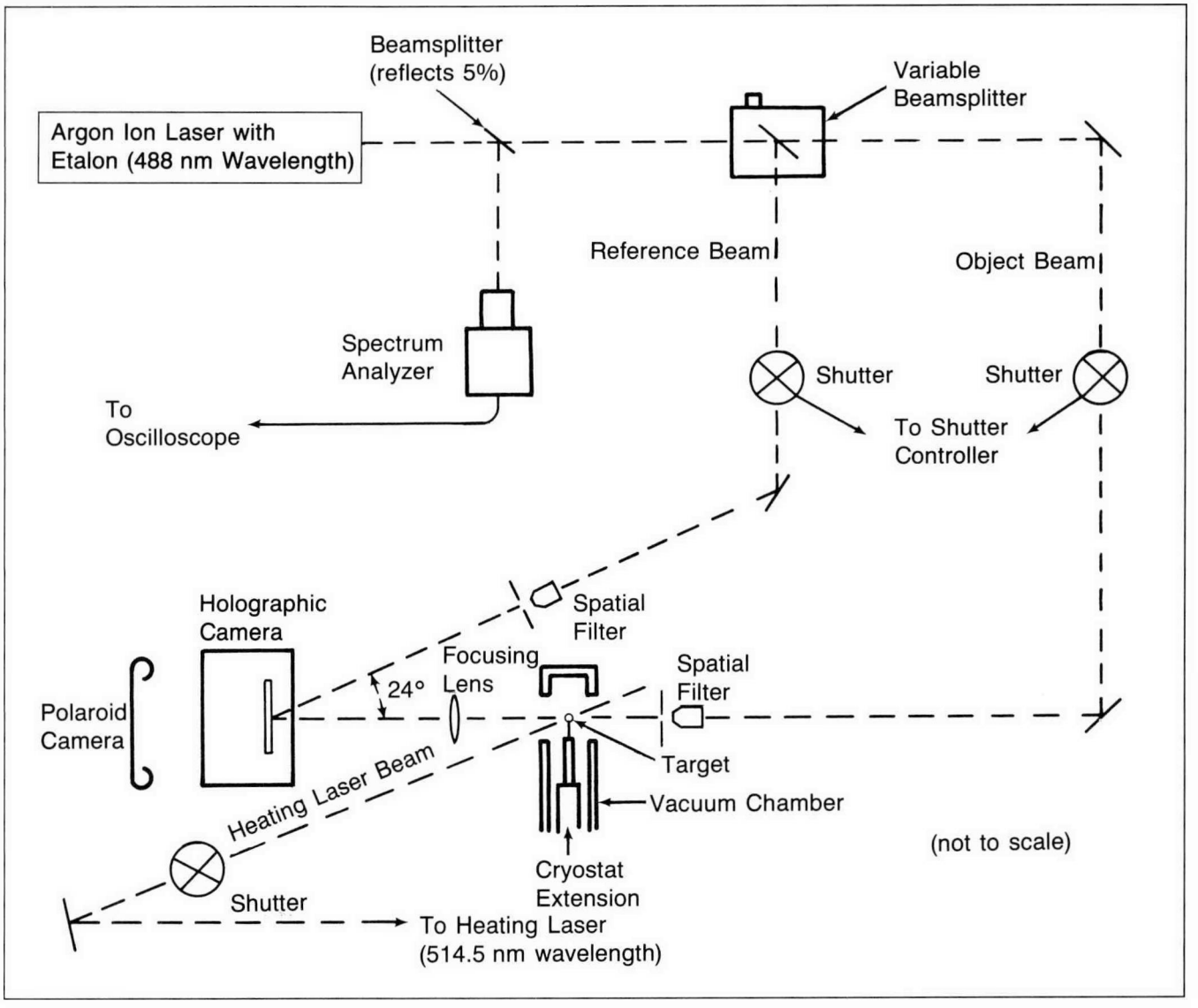

Fig. 2-24. Holographic interferometry is being developed to document fuel layers in cryogenic targets. The target is mounted on a cryostat extension and held in a vacuum chamber; a heating laser makes it possible to manipulate the fuel layer within the shell while the cryostat is cold. A beam from an argon ion laser is used to form the holograms. Five percent of the beam is diverted to a spectrum analyzer to tune an etalon; the remainder is split into reference and object beams. A Polaroid camera creates a permanent record of the holographic interferogram.

wall thickness of about 5 μm. It contains about 50 atm of HD. It has been coated with a colorless transparent polymer to give an additional wall thickness of about 20 μm. The liquid layer (which would be ~6 μm thick if uniform), is thicker at the top of the shell due to the inversion phenomenon, as expected with conduction cooling.[48] The fringes seen are attributable to the fuel layer alone. The only effect of the thick wall of the fuel container is the refraction of light out of the entrance pupil of the viewing optics, which produces the shadows at the edges of the shell image.

There are several technical challenges when using holographic interferometry to document the condensed layers formed in our cryogenic apparatus. The object and reference beams paths must

be equal to within the coherence length of the laser. Vibration, both during and between holographic exposures, must be eliminated. Also, the laser power required to expose a plate may affect the fuel layer within the target. This problem may be most severe when using holographic interferometry to document the fuel layers produced by β-heating (see Section 2.1).

Our efforts to date have addressed the first two of these problem areas. The need for nearly equal path lengths for the reference and object beams was first addressed by making the path lengths equal to within a few millimeters. Later, insertion of an etalon into the cavity of the laser increased the coherence length of the laser from about 2 cm to about 3 m, thus lessening the need for path-length matching considerably. The spectrum analyzer used with the etalon enables us to monitor the stability of the laser output continuously. Vibration of the holographic systems was controlled by mounting the laser, the target chamber, the cryostat, the holographic camera, and all associated optics on a vibration-isolated lab bench (Newport GS-34).

Future Work. The next step in our development program is to mount the system on our simulated target chamber in the cryogenics laboratory. This will enable us to make holographic interferograms of solid layers. We intend to use holographic interferometry to measure the uniformity of layers formed in our planned β-heating experiments. The possibility of disturbance of the fuel layer by the documentation beam may be a problem in this application. We will introduce the beam normal to the direction of the effect that we wish to observe (using a horizontal beam when observing an antigravitational effect) and, if necessary, use pulsed holography. Use of the pulsed mode will not eliminate the effect of the illumination beam on the fuel layer, but it will allow us to form an image of the target before it can respond to heating by the illumination beam.

For additional information, please contact Mr. T. R. Pattinson

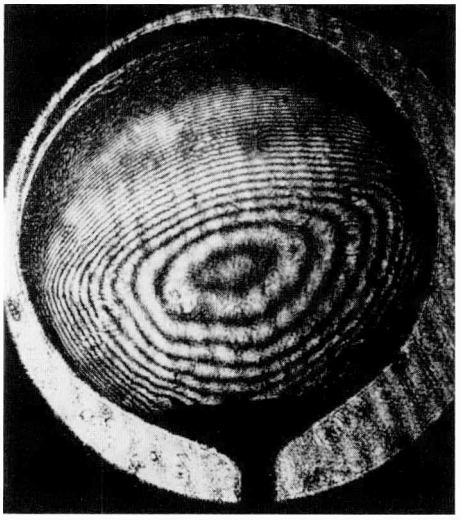

Fig. 2-25. The holographic interferometry system was used to produce this image of an inverted liquid layer within a 680 μm polymer-coated glass shell. The liquid is a 1:1 mixture of hydrogen and deuterium. The fringes are attributable only to the fuel layer. The only effect of the thick wall of the fuel container is the refraction of light out of the entrance pupil of the viewing optics, which produces the shadows at the edges of the shell image.

SECTION 2.6

Cryogenic System and Apparatus for the University of Rochester

In 1984 KMS Fusion (KMSF) agreed to assist the University of Rochester Laboratory for Laser Energetics (LLE) prepare for a series of cryogenic experiments using their Omega laser. Our part of this project consisted of building a simulation chamber (using a vacuum chamber, called Zeta, supplied by LLE), and cryogenic equipment and ancillary hardware that could be used for training and testing on Zeta or for target experiments with the Omega chamber. This year we finished the project, delivering the system in September. Acceptance tests conducted both at KMSF and at LLE verified that the system functioned as intended.

The design of the system is based on the "fast-refreeze" technique[1] for the formation of solid (frozen) fuel layers in gas-filled spherical targets. This technique calls for cooling the targets so rapidly that gravity cannot cause the condensing liquid to sag before it is frozen in place. This results in the formation of a highly uniform frozen fuel layer.

Forming the frozen fuel layer in the target is but one of the tasks that must be accomplished by a cryogenic-experiment apparatus. There are a number of distinct subsystems in the Zeta simulation system that are dedicated to specific functions. Each is discussed individually below; most are shown in Fig. 2-26.

Vacuum Chamber. The vacuum chamber provides the appropriate low-pressure target environment and serves as a mounting site for hardware and diagnostics. Part of this hardware is used to place and hold the target in a precisely specified location to simulate laser irradiation experiments. The Zeta chamber has been modified with flange extensions to mimic the critical dimensions of the Omega system.

Pumping System. The pumping system that maintains vacuum in the chamber comprises a mechanical pump and a diffusion pump. It is a standard configuration and has sufficient interlocks, accessible on the control panel, to make it easy to operate and prevent inadvertent misuse.

Refrigeration System. The Zeta system uses two helium cryostats to cool the target below the triple point (~18K) of the hydrogen isotopes used as fuel. Commercially available cryostats were modified for this application; they are shown in Fig. 2-27. One of the cryostats is part of the target-mounting apparatus; the other, mounted at 180° from the first, is part of the cryogenic shroud that surrounds the target until just before it is irradiated.

The target is mounted on a thin fiber or held in a thin Formvar® tent that is glued to a target post. The post, in turn, is

mounted on the end of a cryostat extension. This configuration ensures that all shrinkage and stress relief of the target mount occurs before the start of the experiment. The target can then be held rigidly at the focal point of the chamber.

The second cryostat is equipped with a helium shroud that is an extension of the cryostat. The shroud carries cold helium gas

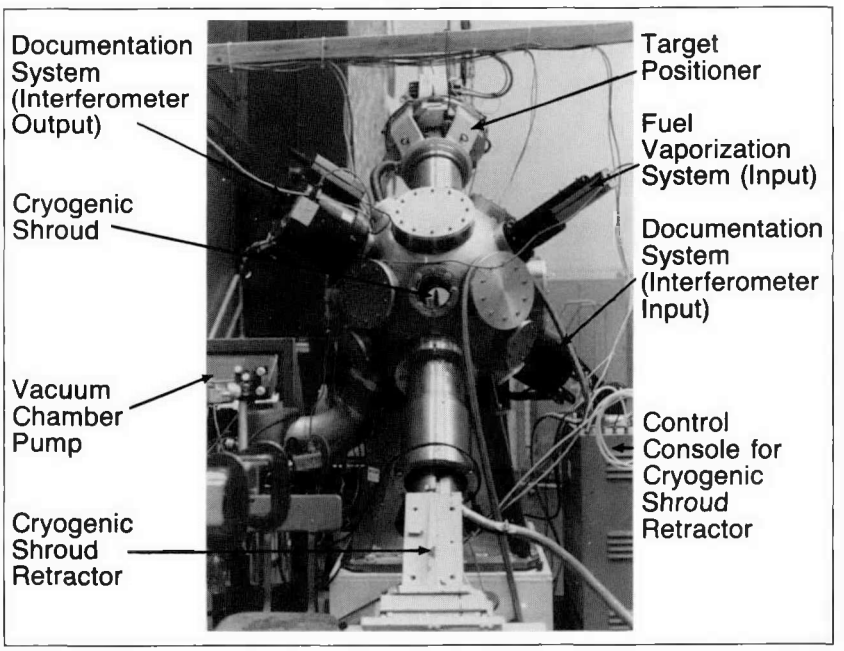

Fig. 2-26. Several separate subsystems are incorporated into the Zeta chamber simulation system. Together these systems produce and document a nearly uniform layer of frozen fuel in a spherical target.

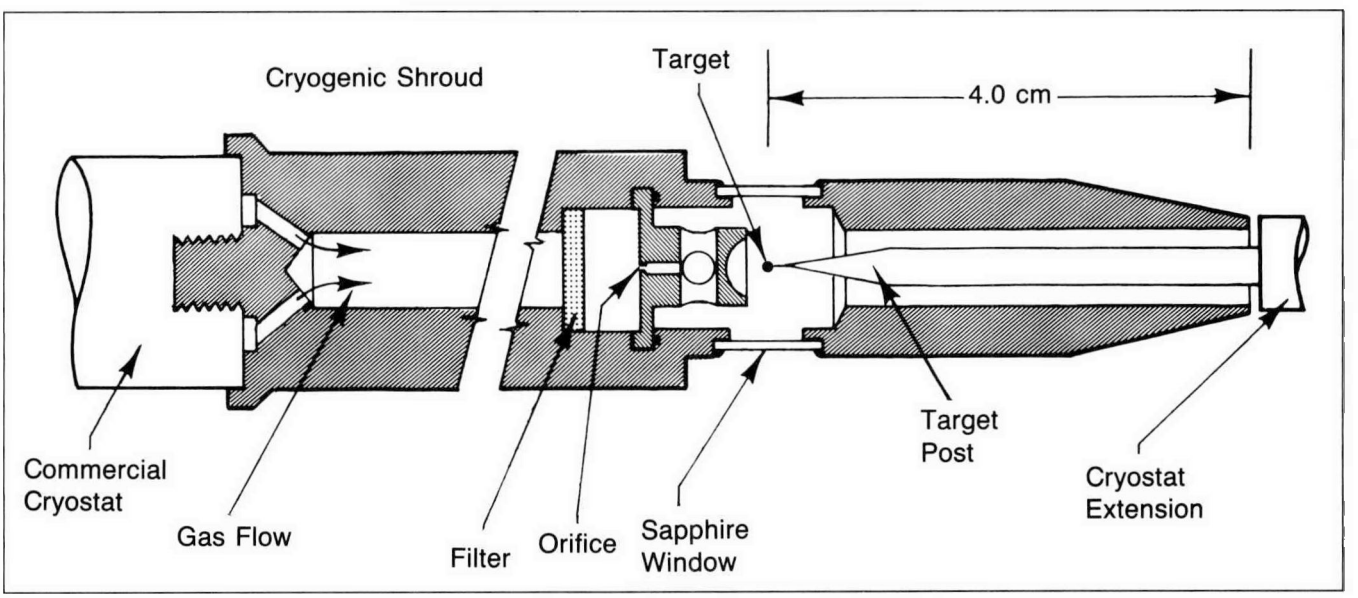

Fig. 2-27. Two helium cryostats are used to cool the cryogenic target below the triple point of the hydrogen isotopes used as fuel. One of these cryostats is part of the target-mounting apparatus; the other, mounted at 180° from the first, is part of the cryogenic shroud.

from the cryostat reservoir through a pinhole orifice into the target region, and then into the vacuum chamber. The size of the pinhole is chosen so that the pressure in the vacuum chamber can be kept below 10^{-4} Torr by the vacuum pumps during the experiment.

Target Positioner System. The target positioner, which holds and positions the target and mounting assembly described above, is bolted directly onto the vacuum chamber. This affords it the rigidity necessary to hold the target in place (the chamber's focal volume is an imaginary sphere with a 5 μm radius) for the extended periods required by cryogenic experiments. The positioner incorporates an airlock, a ball valve, and X, Y, and Z axis positioners.

The target and its mount are moved along three axes via computer-controlled microstepping motors that are controlled from the master control console. Speed controls are available for all three axes. There are adjustable limit switches on each end of travel for all axes to prevent mechanical damage to the target or internal components of the insert.

The positioner incorporates an airlock and ball valve assembly that allows the target to be replaced without disturbing the chamber vacuum. The airlock is the critical component in the achievement of a rapid target-turnover rate. The buffer volume of the airlock can be sealed and pumped to high vacuum or air can be admitted to raise the pressure to atmospheric pressure. The motorized ball valve is controlled by computer command. Interlocks to prevent catastrophic failure modes exist in the control software. The ball valve has limit switches mounted on it to indicate the full-open and full-closed positions. The travel time required to open or close is approximately 90 s.

Cryogenic Shroud and Retractor. The shroud/retractor mechanism is also bolted directly to the vacuum chamber. The shroud performs the dual function of shielding the target from IR radiation and refrigerating the target with a cool stream of helium vapor. In an inertial confinement fusion (ICF) experiment, the retractor removes the shroud from the vicinity of the target (without disturbing the position of the target) just before irradiation by the laser. The extreme sensitivity of cryogenic targets to room-temperature radiation requires millisecond timing and a fast retraction rate.

In addition, the shroud is equipped with four sapphire windows. These provide two orthogonal views of the target for the fuel vaporization system and the target documentation system (both described below) while effectively blocking the 300K room-temperature radiation that can heat the target.

Like the target, the cryogenic shroud must be positioned accurately relative to the focal volume of the chamber. The 4 cm overlap of the shroud and target positioner (refer to Fig. 2-27) and the 2 mm annular spacing between the shroud and the target post are both critical design features. To maintain these parameters, the shroud must maintain stable X and Y coordinates and have long travel on the Z stage.

The shroud cryostat rides in a carriage constructed from a heavy walled tube and cross roller slides. The mounting structure is designed to allow mechanical motion of the shroud along three axes.

The retraction mechanism is operated pneumatically to retract the shroud quickly (as for an ICF experiment) or manually to retract it slowly.

Fuel Vaporization System. An argon laser is used to vaporize the fuel in the target after the helium shroud has been moved into position around the target. The shroud must be moved into position slowly, which causes the target to be exposed to a nonuniform thermal environment. Slow, nonuniform cooling of the target allows the fuel to condense nonuniformly and freeze as a nonuniformly thick layer. This "heating laser" illuminates the target through the sapphire windows in the helium shroud, vaporizing the condensed fuel. Because the helium shroud is now in place around the target, blocking the heating laser beam with a shutter allows the target to refreeze quickly, forming a uniform solid layer.

The heating laser for the Zeta system is an argon ion laser that is normally operated at the 514.5 nm line. The power output at this line can be as high as several watts. Since glass targets absorb visible light very inefficiently at 10K (the temperature to which the target is cooled), this high power output may be necessary for complete vaporization of the fuel within Omega targets.

Figure 2-28 shows the heating laser optical system as installed on the Zeta chamber. The heating laser system is provided with a shadowgraph imaging system to aid in aligning the laser with the target. An image of the target is projected onto a ground-glass screen in front of a closed-circuit television (CCTV) camera. By observing the camera monitor, an operator can quickly align the laser and the target using panel controls for X, Y positioning and focus. The size of the beam and its position relative to the target are controlled by moving the steering lens and may be observed on the shadowgraph of the target on the ground-glass screen. The image on the screen is recorded by the CCTV camera and relayed to a monitor at the control station.

Documentation System. The target-image documentation system incorporates an argon ion laser, a Murty shearing-cube interferometer,[49] a TV camera, and a 35 mm single-lens reflex camera. A beam of visible radiation from the argon ion laser is brought into the chamber at 90° to both the shroud axis and the heating laser axis. The beam passes through the target, is formed into an interferometric image, and is then focused on both photographic film and the CCTV camera. Thus, for actual target shots, an operator can observe the target as the fuel layer is formed and evaluate the uniformity of the final solid layer prior to irradiation with the Omega laser.

The wavelength of the documentation laser is usually the 488 nm line of an argon ion laser because short wavelengths give better resolution than longer wavelengths (e.g., a HeNe laser).

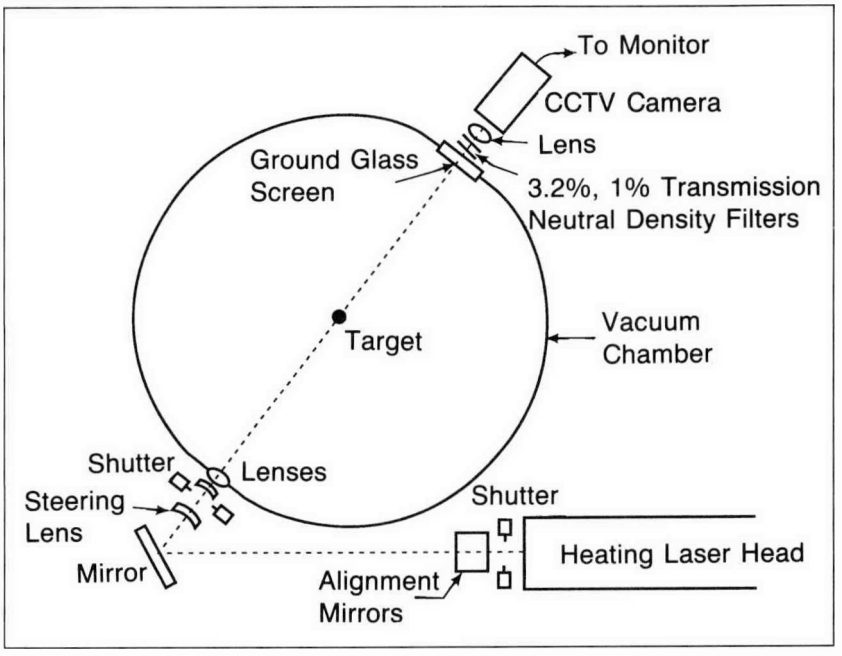

Fig. 2-28. An argon laser is used as a heating laser to vaporize the fuel in the target after the cryogenic shroud is in place. Blocking this laser with a shutter allows the target to refreeze quickly, forming a uniform solid layer. The shadowgraph imaging system (ground-glass screen, CCTV camera, monitor, and associated optics) aids in aligning the laser with the target. The size of the beam and its position relative to the target are controlled by the steering lens and displayed by the imaging system.

Zeta Chamber Control System. All control equipment and functions for the Zeta system are interfaced through CAMAC and CAMAC-compatible circuits. A microcomputer, CAMAC crate controller, and control software were provided with the system. The Zeta system also affords a manual mode of control for all components.

The configuration of the electronic control system is shown in Fig. 2-29. There are three control consoles. The master control console contains the computer and CAMAC controller, an X, Y, Z position control for the target positioner, X, Y, Z motor power and drivers for the shroud retractor, and controls for the heating laser and a 35 mm camera that is part of the documentation system. Separate control consoles were provided for the target positioner and the shroud/retractor mechanism so that the control consoles could be placed close to the hardware. Many of their functions can be activated from the master control console.

The various functional subsystems of the Zeta system are operated by a combination of panel, keyboard, computer, and manual controls.

The target positioner assembly is designed to be controlled entirely by computer command. For the Zeta system, however, X, Y, Z motion of the target positioner is controlled through a separate panel on the master control console. The circuitry of the panel simulates the signals that the computer will provide on the Omega system. All other electronic features on the target

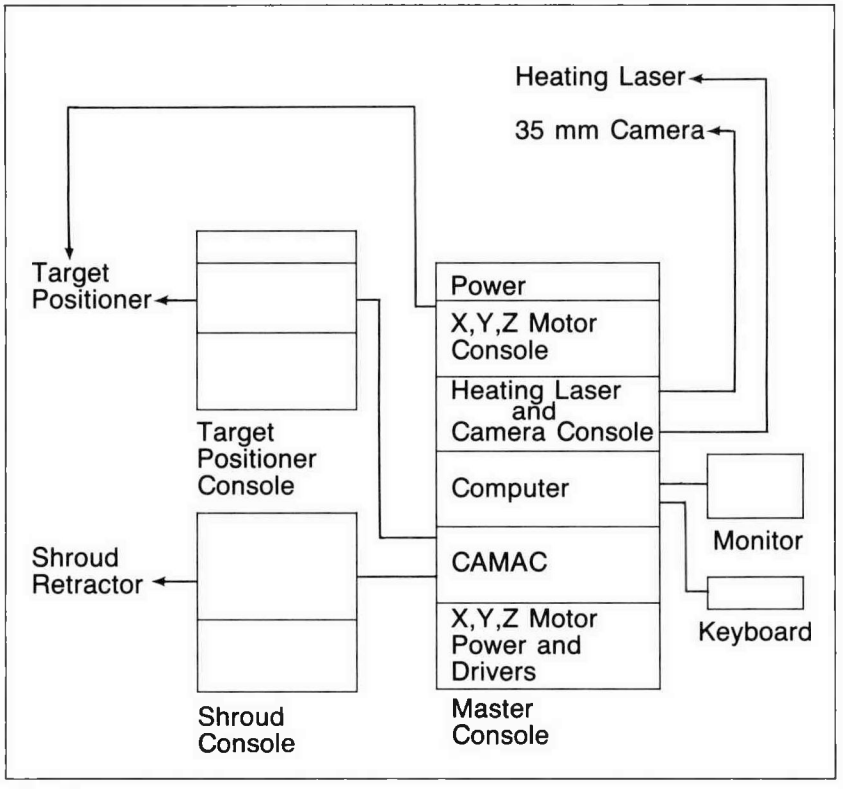

Fig. 2-29. Electronic control on the Omega system will be accomplished entirely by computer. For the Zeta system, panel, keyboard, and computer controls are combined to simulate Omega system functions.

positioner are activated by keyboard commands. These activate the circuitry located in the local control console for the positioner. The target cryostat is operated directly from the local control console.

The shroud retraction assembly is designed with a combination of manual and computer control functions. The X, Y positioning of the retractor is manually controlled. The Z positioning can be controlled either manually or by computer, as determined by a switch on the local control console. Fast retraction of the shroud assembly can only be activated through the computer. The computer keyboard commands activate the circuitry located in the local control panel. The shroud cryostat is operated directly from the shroud control console.

The intensity and X, Y, Z focusing control for the heating laser are designed for computer control. For the Zeta system, however, these are controlled by circuitry in the master control panel. Safety shutters for both the heating laser and the illumination laser are controlled by keyboard commands; a second shutter on the heating laser is controlled remotely.

All of the equipment to control the vacuum environment of the chamber is controlled independently. This equipment is controlled through the pump station console and includes the diffusion and mechanical pumps, all vacuum valves, associated vacuum gauges, and control sensors.

Execution of a Cryogenic Experiment. To prepare for a cryogenic experiment, a fuel-filled target is mounted on a target post, which is then affixed to the end of a target cryostat. This unit is placed in the target positioner system, with the target in the middle of the airlock. The airlock is evacuated and the cryostat cooled (as the target cryostat is cooling, the shroud cryostat can also be cooled). The cryostat extension and target are then moved through the ball valve to the focal volume of the chamber.

When the two cryostats are cold and aligned to the focal volume, the shroud is moved into place over the target post (as depicted in Fig. 2-27). At this point, the interferometer system is adjusted for background phase and phase gradients.

A uniform solid fuel layer is formed in the target by focusing the heating laser onto the target and increasing the intensity until all the fuel is vaporized. (It usually takes only a few heating-laser cycles until a uniform solid fuel layer is formed within the target.) When a satisfactory layer is formed, a 35 mm photograph of the interferometric image is taken.

The cryogenic shroud must then be retracted. To prepare the shroud for its fast retraction cycle, the shroud transfer line must be secured to the central cylinder, foreign objects must be cleared from the path of the central cylinder, and personnel in the area must be alerted. When the area is cleared, computer control of the shroud retraction is activated, and the system is armed. For the Zeta system, the automatic retraction sequence is initiated by an operator through a computer keyboard. For the Omega system, this sequence will be controlled by the main control computer.

For additional information, please contact Dr. D. L. Musinski

SECTION 2.7

Targets Delivered in Support of the National ICF Program

During 1986 we delivered inertial confinement fusion (ICF) targets and target components to Lawrence Livermore National Laboratory (LLNL), Los Alamos National Laboratory (LANL), and the Laboratory for Laser Energetics (LLE) at the University of Rochester. While most requests were for spherical glass shells filled with D_2 or DT at pressures of 5 to 100 atm, other materials, geometries, and fill gases were also requested.

Lawrence Livermore National Laboratory received a total of 13 separate shipments of glass shells. One type of target was 950 to 1050 μm in diameter, with walls between 1 and 3 μm thick, and filled with 14 atm of DT. These targets were used to produce a high neutron yield to aid in the development of new diagnostic equipment for the Nova laser. Another type of target prepared for LLNL was 350 to 390 μm in diameter, with walls 8 to 10 μm thick, and coated with polymeric materials. Because of the nature of the experiments for which these targets were designed, stringent specifications had to be met in their manufacture. Especially for wall thickness uniformity criteria, a major expenditure of effort in fabrication, characterization, and selection was required.

Los Alamos National Laboratory received six shipments of glass shells. For five of these shipments, a variety of diameters and wall thicknesses were required. The shells were filled with argon at pressures ranging from less than 0.5 to 2.1 atm.

Eight shipments of glass shells and one shipment of poly(vinyl alcohol) (PVA) shells were prepared for LLE. Specifications for the glass shells included diameters in the range of ~140 to ~750 μm, walls from ~0.6 to ~5.0 μm, and shell aspect ratios (diameter/wall thickness) from ~28 to ~640. The dimensions of the PVA shells were (nominally) 340 × 3.0 μm (diameter × wall).

From these batches, LLE selected specific shells, which they loaded and sealed in containers (called "eggcrates"). These eggcrates were returned to KMS Fusion (KMSF) to be filled with gaseous fuel. Eighteen such eggcrates were processed. Sixteen were filled with DT at pressures ranging from 10 to 100 atm. Two eggcrates were filled with D_2, one at 20 atm, the other at 50 atm.

We also supplied a variety of targets for KMSF experiments. These included D_2-filled PVA shells and aluminum disks (for x-ray backlighting) for the Low Preheat Implosion Campaign (discussed in detail in Section 1.1), "spot" and "slab" targets of

materials such as magnesium, silicon, aluminum, CaF, etc., for the x-ray spectroscopy series (see Section 1.6), and targets for five different classified experiments. The targets for each of these programs required us to develop new procedures and designs. This resulted in the overall extension of our target-support capabilities.

For additional information, please contact Mr. A. J. Martin

REFERENCES

1. D. L. Musinski, T. M. Henderson, R. J. Simms, and T. R. Pattinson, *J. Appl. Phys.* **51** (1980), p. 1349.
2. *KMS Fusion 1985 Annual Technical Report on Inertial Fusion Research*, Report KMSF-U1728, KMS Fusion, Inc., Ann Arbor, MI, pp. 99–102.
3. R. E. Bank and T. Dupont, "An Optimal Order Process for Solving Finite Element Equations," *Math. Comp.* **36**(153) (January 1981), pp. 35–51.
4. L. A. Scott, R. G. Schneggenburger, and P. R. Anderson, "Deuterium Permeation Properties of Beta-Irradiated and Unirradiated Poly(vinyl alcohol) and Polystyrene Shells," *J. Vac. Sci. Technol. A* **4**(3) (May/June 1986), pp. 1155–59.
5. *KMS Fusion 1985 Annual Technical Report on Inertial Fusion Research*, Report KMSF-U1728, KMS Fusion, Inc., Ann Arbor, MI, pp. 16–21.
6. R. J. Calliger, R. J. Turnbull, and C. D. Hendricks, *Rev. Sci. Instrum.* **48**(7) (July 1977), pp. 846–851.
7. Lord Rayleigh, *Proc. London Math. Soc.* **10** (1978), p. 4.
8. J. G. Pritchard, *Poly(vinyl Alcohol): Basic Properties and Uses* (Gordon and Breach, Publ., New York, 1970), pp. 64–65.
9. J. H. Campbell, J. Z. Grens, J. F. Poco, and B. H. Ives, "Preparation and Properties of Polyvinyl Alcohol Microspheres," Report UCRL-53750, Lawrence Livermore National Laboratory, Livermore, CA, June 1986.
10. R. L. Steinberg and R. E. Treybal, *AIChE Journal* **6** (1960), p. 227.
11. T. B. Drew, *Transcripts of the AIChE* **26** (1931), p. 26.
12. J. V. Milewski, *Rev. Sci. Instrum.* **52**(11) (1981), pp. 1647–1650.
13. C. E. Rogers, J. A. Meyers, V. Stannett, and M. Swarc, "Determination of the Permeability Constant," *TAPPI Monograph Series 23* (Technical Association of the Pulp and Paper Industry, New York, 1962), p. 2.
14. W. B. Rensel, T. M. Henderson, and D. E. Solomon, *Rev. Sci. Instrum.* **46** (1975), p. 787.
15. R. T. Tsugawa, I. Moen, P. E. Roberts, and P. C. Souers, "Permeation of Helium and Hydrogen from Glass-Microsphere Laser Targets," *J. Appl. Phys.* **47**(5) (1976).
16. *KMS Fusion 1977 Annual Technical Report on Inertial Fusion Research*, Report KMSF-U762, KMS Fusion, Inc., Ann Arbor, MI, p. 1–33.
17. D. H. W. Carstens and E. P. Ehart, J. *Appl. Polymer Sci.* **29** (1984), p. 261.
18. Alan Burnham, Lawrence Livermore National Laboratory, Livermore, CA, personal communication.
19. Measurements performed by R. L. Crawley, KMS Fusion, Inc., Ann Arbor, MI, January 9, 1986.
20. *KMS Fusion 1985 Annual Technical Report on Inertial Fusion Research*, Report KMSF-U1728, KMS Fusion, Inc., Ann Arbor, MI, pp. 78–82.
21. *KMS Fusion 1984 Annual Technical Report on Inertial Fusion Research*, Report KMSF-U1574, KMS Fusion, Inc., Ann Arbor, MI, pp. 59–60.
22. *KMS Fusion 1985 Annual Technical Report on Inertial Fusion Research*, Report KMSF-U1728, KMS Fusion, Inc., Ann Arbor, MI, pp. 92–94.
23. C. H. Greene and R. F. Gaffney, "Apparatus for Measuring the Rate of Absorption of a Bubble in Glass," *J. Amer. Ceram. Soc.* **42**(6) (1959), pp. 271–275.
24. R. B. Brown and R. H. Doremus, "Growth and Dissolution of Gas Bubbles in Molten Boric Oxide," *J. Amer. Ceram. Soc.* **59**(11-12) (November/December 1976).
25. R. L. Downs, B. D. Homyk, and R. G. Schneggenburger, *Digest of Topical Meeting on Inertial Confinement Fusion*, paper THB18 (Optical Society of America, Washington, DC, 1980), p. 94.

26. W. J. Miller, R. L. Downs, L. A. Scott, and R. G. Schneggenburger, *J. Vac. Sci. Technol.* **18** (1981), p. 1290.

27. J. V. Milewski, *Rev. Sci. Instrum.* **52** (1981), p. 1647.

28. J. V. Milewski and R. G. Marsters, *J. Vac. Sci. Technol.* **18** (1981), p. 1279.

29. R. G. Schneggenburger, KMS Fusion, Inc., Ann Arbor, MI, unpublished results.

30. R. T. Tsugawa, I. Moen, P. E. Roberts, and P. C. Souers, *J. Appl. Phys.* **47**(1976), p. 1987.

31. W. D. Kingery, H. K. Bowen, and D. R. Uhlmann, *Introduction to Ceramics*, 2nd edition (John Wiley and Sons, Inc., New York, 1976), pp. 787–790.

32. R. H. Doremus, "Fracture and Fatigue of Glass," *Treatise on Materials and Technology* **22**, edited by M. Tomozawa and R. H. Doremus (Academic Press, New York, 1982).

33. B. A. Kschinka, S. Perrella, H. Nguyen, and R. C. Bradt, *J. Amer. Ceram. Soc.* **69** (1986), p. 467.

34. J. E. Shelby, *J. Appl. Phys.* **51** (1980), p. 2589.

35. R. H. Doremus, *Glass Science* (John Wiley and Sons, New York, 1971), pp. 231–232.

36. R. L. Downs, M. A. Ebner, B. D. Homyk, and R. L. Nolen, *J. Vac. Sci. Technol.* **18** (1981), pp. 1272–1275.

37. W. Weibull, *Ing. Vetenskaps Akad. Handl.* No. 151 (Stockholm, 1939).

38. *KMS Fusion 1984 Annual Technical Report on Inertial Fusion Research*, Report KMSF-U1574, KMS Fusion, Inc., Ann Arbor, MI, pp. 76–79.

39. P. C. Alway, "A Spectral/Interferometric Method of Measuring Thin Transparent Films on Spherical Shells," Master's Thesis, Eastern Michigan University, Ypsilanti, MI, June 11, 1987.

40. B. W. Weinstein and C. D. Hendricks, "Interferometric Measurement of Laser Fusion Targets," *Appl. Opt.* **17** (1978), p. 3641.

41. J. A. Tarvin, R. D. Sigler, and Gar. E. Busch, "Wave-front Shearing Interferometer for Cryogenic Laser-fusion Targets," *Appl. Opt.* **18** (1979), p. 2971.

42. *KMS Fusion 1984 Annual Technical Report on Inertial Fusion Research*, Report KMSF-U1574, KMS Fusion, Inc., Ann Arbor, MI, pp. 59–60.

43. *KMS Fusion 1984 Annual Technical Report on Inertial Fusion Research*, Report KMSF-U1574, KMS Fusion, Inc., Ann Arbor, MI, p. 74.

44. S. M. Alexander-True and M. A. True, "Thickness Uniformity Measurements of Plastic-coated Glass Shells by Image Analysis of X-ray Radiographs," *J. Vac. Sci. Technol. A* **3** (1985), p. 1258.

45. T. P. Bernat, D. H. Darling, and J. J. Sanchez, "Applications of Holographic Interferometry to Cryogenic ICF Target Characterization," *J. Vac. Sci. Technol.* **20**(4) (1982), pp. 1362–1365.

46. V. M. Izgorodin, S. B. Kormer, G. P. Nikolaev, and A. V. Pinegin, "Use of Holographic Interferometry in Monitoring the Quality of Cryogenic Laser Fusion Targets," *Sov. J. Quantum Electron.* **16**(1) (1986), pp. 35–37.

47. *KMS Fusion 1985 Annual Technical Report on Inertial Fusion Research*, Report KMSF-U1728, KMS Fusion, Inc., Ann Arbor, MI, p. 21.

48. *KMS Fusion 1984 Annual Technical Report on Inertial Fusion Research*, Report KMSF-U1574, KMS Fusion, Inc., Ann Arbor, MI, pp. 63–64.

49. M. V. Murty, *Appl. Opt.* **9** (1970), p. 1146.

LASER DEVELOPMENT

SECTION THREE

Scientific Editor, Dr. N. K. Moncur

Introduction

KMS Fusion (KMSF) has been active for 15 years in developing lasers and laser components for inertial confinement fusion (ICF) research. In addition to operating the Nd:glass laser, Chroma, for our ICF experiments, we are participating in the search for an efficient, high-energy laser driver. Other participants in the national ICF program have devoted many years of research and development to high-power, electrically driven glass lasers and gas lasers. We are currently completing a series of measurements on a type of chemically driven laser, the chemical oxygen-iodine laser (COIL). The COIL has the potential to meet many of the requirements for an ICF driver: It is an efficient, high energy-storage-density laser; it is capable of a high pulse rate; and its output can be converted into visible light.

The conditions required for operating the COIL as a pulsed fusion driver differ significantly from the conditions required for continuous-wave operation of COILs studied previously.[1] To study the kinetics of the COIL under these different conditions, a laboratory was constructed that includes a peroxide/chlorine singlet-oxygen generator and a fast-flow gas-handling system for mixing iodine vapor with flowing singlet oxygen. A variety of diagnostic instruments have been developed and assembled, and the kinetics of chemical reactions under varied conditions are being examined. Our work on the COIL for 1986 is reported in Section 3.1.

The results of laser-driven ICF experiments indicate that the wavelength of a fusion driver will most likely be in the visible or near-ultraviolet region. Consequently, if high-power solid-state lasers are to be used as drivers, their output will have to be converted to shorter wavelengths. This can be done by placing crystals in the beam path that double or triple the frequency of the laser output. Currently, harmonic frequency-conversion methods require high laser powers with low beam divergence to achieve high efficiency. A new approach has been developed at KMSF that uses multiple crystals with the optic "Z" axes reversed. Called the alternately reversed crystal axis (ARCA) technique, this approach, which is described in Section 3.2, significantly reduces the stringent requirements on laser power and beam divergence for efficient conversion. Although this technique was developed for laser pulses on the order of microseconds in duration, it may be possible to extend it to the nanosecond regime.

SECTION 3.1

Chemical Oxygen-Iodine Laser Project

During 1986, the chemical oxygen-iodine laser (COIL) experimental facility became fully operational, and several notable milestones were achieved. We produced continuous-wave lasing in the chemical laser amplifier, implemented computer control of the chemical reagent delivery and data-acquisition systems, and demonstrated highly reproducible pulsed singlet-oxygen generation. Reaching those milestones required us to assemble the iodine vapor injection system, code the process control logic, calibrate the optical detection elements, and develop the data-reduction software.

A remarkable amount of information on the operation of our oxygen-iodine laser has been collected and analyzed. Such laser system parameters as pressure, temperature, flow, and status conditions are all digitized directly from the analog transducer signals, then stored in an IBM® PC-AT (AT). Nonspatially resolved spectral data are first captured in a digitizing storage oscilloscope (DSO) and then transferred to a magnetic disk in the AT. Spatially resolved data are acquired via video camera and stored on magnetic tape for later digitization and image processing.

System Operation

The COIL at KMS Fusion (KMSF) is based on the standard basic hydrogen peroxide (BHP)/chlorine reaction to produce the excited oxygen,

$$H_2O_2 + 2KOH + Cl_2 \rightarrow 2KCl + 2H_2O + O_2(^1\Delta) \ . \qquad (1)$$

This reaction produces the highly metastable $O_2(^1\Delta)$ from chlorine and an aqueous mixture of base (KOH) and hydrogen peroxide (H_2O_2). The mixture of H_2O_2 and KOH must be maintained at sub-zero temperatures to remain stable to catastrophic spontaneous decomposition of the BHP. In our COIL system (shown in Fig. 3-1), this is accomplished by cooling the solution via evaporation of water, which is then recondensed in the liquid-nitrogen-cooled facility cold trap. Further, for the solution to be stable against spontaneous decomposition, the molar ratio of H_2O_2 to KOH must always be greater than about 2 to 1.

To ensure the correct molar ratios, the liquid reagent delivery system first delivers a metered amount of 50 wt. % H_2O_2 in aqueous solution to the singlet-oxygen generator vessel. The generator is a borosilicate glass vessel fitted with ports for reagent delivery and with pressure and temperature sensors. The computer monitors the temperature of this solution until it drops

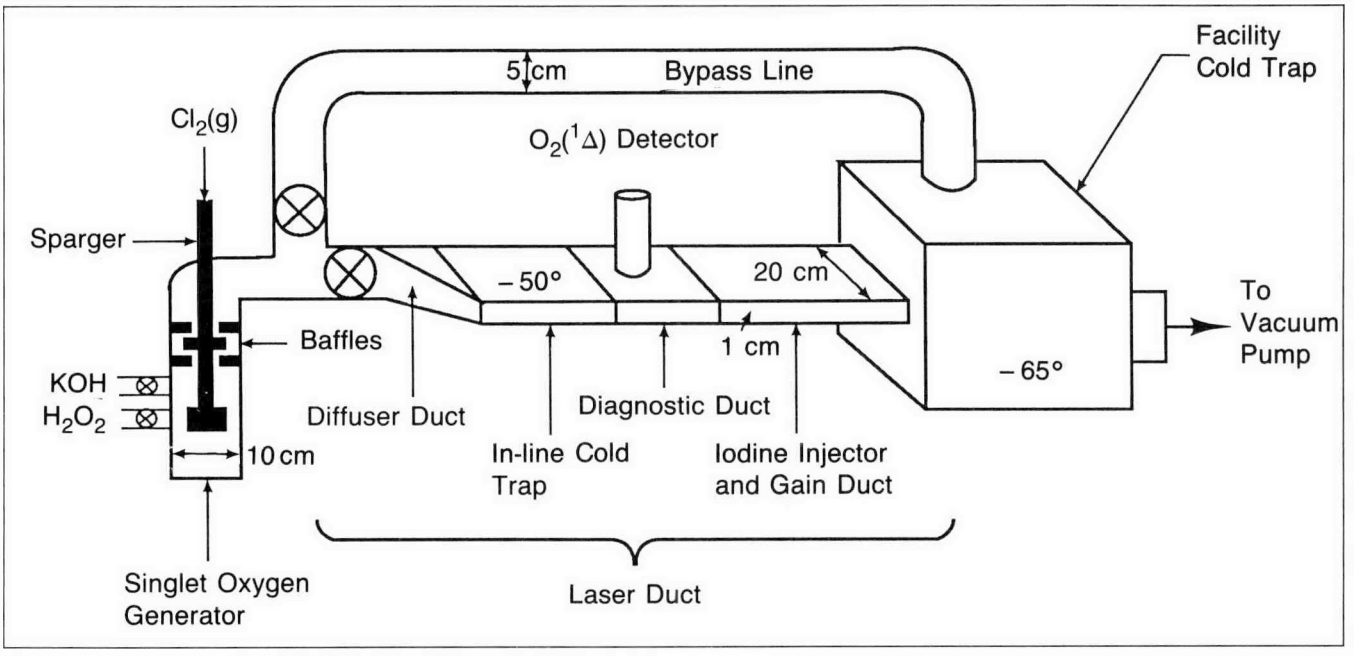

Fig. 3-1. In the KMSF COIL system, singlet oxygen is generated from the reaction of basic hydrogen peroxide (BHP) and chlorine. The BHP solution is cooled by the evaporation of water, which is recondensed in the facility cold trap. Because the reaction produces a great deal of heat, which decreases system efficiency, an in-line cold trap has been built in the laser duct. The trap consists of twenty 1-cm^2 channels. After the oxygen leaves the cold trap, it passes through a diagnostic duct that measures the amount and species of the excited oxygen produced, and then into the iodine injector and gain duct, where iodine vapor is transversely injected into the oxygen flow.

to less than −10°C and then begins adding 100 ml increments of 45 wt. % KOH in aqueous solution. After each addition, the computer waits until the solution temperature has again dropped below −10°C before it adds more KOH. The computer continues to add KOH until the predetermined amount of solution has been accumulated in the generator vessel. For most of the experiments, the total amount of BHP loaded was 2.5 l, with final molar ratios of about 1:2:6 of KOH:H_2O_2:H_2O. Using only evaporative cooling at a few Torr absolute pressure, the entire addition sequence takes about 1 h to complete. Supplementary cooling, coupled with active mixing of the solution, could significantly reduce this time. For our experiments, however, this is not critical, since various other routine tasks can proceed in parallel with the reagent loading. A typical load of BHP represents about 1 MJ of energy available for conversion to the energy of chemical excitation.

Once the full load of BHP has been added and cooled sufficiently, chlorine may be safely added to produce singlet oxygen. The chlorine is introduced into the BHP through a polytetrafluoroethylene sparger immersed into the liquid. This sparger finely disperses the gaseous chlorine throughout a region just below the gas/liquid interface in the singlet-oxygen generator. Bubbles of chlorine form and react with the BHP as they rise to the surface. The chlorine is thought to diffuse into the liquid layer surrounding the bubble and the singlet oxygen produced therein diffuses back out into the BHP solution. Under typical

BHP operating conditions near the maximum stable concentration, this reaction layer is on the order of only a few hundred micrometers thick.

The distance that the gas bubbles must travel through the BHP strongly affects the fraction of singlet oxygen that is delivered to the flow stream, since $O_2(^1\Delta)$ is strongly quenched while it is in the liquid. Thus, the depth at which the sparger is operated affects the $O_2(^1\Delta)$ yield. It is, in fact, difficult to define the sparger depth or the distance that the bubbles must travel in the BHP precisely, as the surface layer of the solution is chaotic and frothy when the reaction is taking place.

When they reach the surface, the oxygen and any unreacted chlorine are removed from the generator along with H_2O and H_2O_2 at their equilibrium vapor pressures by pumping them through the vacuum system. Splashing liquid at the surface has caused problems related to the entrainment of droplets in the gas as it flows away from the BHP surface. This has been minimized by the use of baffling above the liquid level and before the output of the generator. However, the baffles result in higher pressures in the generator, with associated greater loss of $O_2(^1\Delta)$ due to the so-called "pooling" reaction,

$$O_2(^1\Delta) + O_2(^1\Delta) \rightarrow O_2(^3\Sigma) + O_2(^1\Sigma) \ . \qquad (2)$$

Although it has been shown fairly conclusively that the $O_2(^1\Sigma)$ quenches rapidly back to $O_2(^1\Delta)$, Eq. (2) is nevertheless the main loss mechanism for $O_2(^1\Delta)$. Since the rate for Eq. (2) increases as the square of the $O_2(^1\Delta)$ density, the time that the laser gas is at high pressure should be kept to a minimum for maximum $O_2(^1\Delta)$ lifetime.

The reaction in Eq. (1) produces a copious amount of heat. In fact, the amount of heat released to the liquid in this reaction is about equal to the amount available in the singlet oxygen. Thus, at 100 mmole/s flow of $O_2(^1\Delta)$, about 10 kW of energy is present in the singlet oxygen and a like amount is released directly to the BHP. Any quenching of oxygen in the liquid will increase the heat input to the liquid, thereby increasing its temperature and the partial pressure of each of the solution components (including water vapor). Although water vapor is not a strong quencher of $O_2(^1\Delta)$, it is a strong quencher of I^* and $O_2(^1\Sigma)$. If the water vapor is not removed before the iodine is introduced, it will reduce the amount of I^* available. Any diminution of I^* directly affects the gain of the laser, and as $O_2(^1\Sigma)$ is implicated in at least an initiator role in molecular iodine dissociation, its decrease adversely affects the injection kinetics.

To alleviate the water vapor problem, an in-line cold trap (ICT) has been placed between the singlet-oxygen generator and the iodine injection duct. (The details of the trap design were fully discussed in our 1985 Annual Technical Report.[2]) When the oxygen leaves the generator, it is steered by a valve tree either to bypass the laser duct and flow directly to the facility cold trap (FCT) or to flow into the laser duct and thence to the

FCT. The laser duct consists of a diffuser duct, the ICT, a diagnostic duct, and the iodine injector and gain duct. Because the singlet-oxygen generator is a round tube and the ICT is a rectangle, the diffuser duct effects a transition between them. This duct begins as a 5 cm round section and quickly becomes a 1×20 cm rectangular section. The rectangular section is followed immediately by the ICT, which consists of twenty 1-cm^2 channels. Our experience shows that the ICT becomes severely blocked after 15 min of flow through it. A set of capacitance manometers, one upstream of the cold trap in the diffuser duct and one downstream in the diagnostic duct, monitors the pressure drop across the trap. When it has been determined that the trap is blocked, a warm-up cycle is initiated that raises the trap temperature from that of normal operation (−50°C) to 25°C. The ice that was condensed in the ICT is vaporized and transported to the FCT, where it remains until the experiment is completed. The entire warm-up, transfer, and recooling of the ICT takes about 60 min. The loading of the ICT is ameliorated by the pulsed singlet-oxygen flow mode (discussed in more detail below), because the gas flows through the laser duct only when data are being acquired.

When the gas leaves the ICT, it flows through a short diagnostic duct where its composition is evaluated. In this region, the flow is monitored with a 634 nm interference-filtered photomultiplier tube (PMT) calibrated for the oxygen a-state "dimol" emission,

$$2O_2(a^1\Delta) \rightarrow 2O_2(X^3\Sigma) + h\nu\ (634\ \text{nm})\ . \qquad (3)$$

From time to time, a liquid-nitrogen-cooled 1.27 μm interference-filtered germanium detector is used to compare the "primary" $O_2(^1\Delta)$ emission to that of the "dimol" in the diagnostic duct,

$$O_2(a^1\Delta) \rightarrow O_2(X^3\Sigma) + h\nu\ (1.27\ \mu\text{m})\ . \qquad (4)$$

While the primary emission is generally considered more reliable for $O_2(^1\Delta)$ density measurement, it suffers from a combination of drawbacks that have forced us to use the dimol emission in our experiments. The lower sensitivity and considerably longer time constant of cryogenic germanium, compared to a PMT, has required the use of the latter for measurement of $O_2(^1\Delta)$ when the system is operated in pulsed mode. Pulsed mode operation is used for most experiments since we want to minimize heating of the BHP and fouling of the ICT. We also monitor the oxygen b-state emission, as the ratio of its intensity to that of the a-state is a measure of the water vapor density,

$$O_2(b^1\Sigma) \rightarrow O_2(X^3\Sigma) + h\nu\ (762\ \text{nm})\ . \qquad (5)$$

The oxygen next flows from the diagnostic duct into the iodine injection zone of the gain duct. At the top and bottom of the gain duct are ceramic plates into which four rows of sonic nozzles have been drilled. Iodine vapor is transversely injected into

the oxygen flow as a set of plumes formed by the sonic nozzles. Before the iodine is injected, it is vaporized, mixed with a carrier gas, and distributed at high pressure to the injector plates by the iodine delivery system (depicted schematically in Fig. 3-2). The entire system is contained in an oven maintained at 120°C.

A two-part vaporization system maintains a constant iodine vapor pressure during fluctuations in iodine demand. This is accomplished as follows: Iodine crystals are distributed over the surface of a brass vessel that is coated with fluoroethylene polymer and plated with nickel. The vapor pressure of the iodine crystals is controlled by the temperature of water flowing through the vessel. When iodine injection begins and the demand for iodine increases, a 4 kW infrared (IR) radiation source directed at the crystals is switched on to provide the additional heat of sublimation required for the increased flow. The desired iodine number density is regulated by an iodine densitometer that drives a feedback control system to modulate the vessel water temperature and the IR lamp power. The densitometer uses a green HeNe laser operating at 541 nm in an absorption band of molecular iodine.*

Numerous diagnostic devices were brought on line during 1986 in support of the COIL project. Generally, as a new instrument is integrated into the data acquisition system (Fig. 3-3), it is incorporated as a standard feature for subsequent experiments. Most of the kinetic measurements were made in the gain duct region using optical diagnostic instruments. The typical experimental configuration is shown schematically in Fig. 3-4: Spatially resolved excited species fluorescence is recorded with an IR camera, high-resolution optical spectroscopy is provided by a 0.6 m Czerny-Turner spectrograph and an intensified diode array, and iodine densitometry is accomplished with a green HeNe laser.

As noted above, the singlet-oxygen generator is operated in the pulsed mode. This is made possible, in part, by minimizing gas dead-volumes in the generator and chlorine delivery system and maximizing the chlorine valve switching speed. It has been especially valuable from an experimental standpoint, as heating of the BHP and choking of the ICT have been minimized. The rapid approach to peak generator output and the maintenance of steady-state $O_2(^1\Delta)$ levels during the chlorine pulse are evident in Fig. 3-5. For this shot, the actual timed pulse to the chlorine valve was 100 ms, which can be seen to result in a 150 ms full width at half-maximum (FWHM) singlet-oxygen pulse. The valve pulse-time is currently limited by a choice of computer-control system-interrupt rate of 10 Hz. Improvements

*Because the available literature values for the extinction coefficient were obtained with relatively low-resolution spectrophotometers compared to the spectral width of the HeNe laser, we measured the extinction and accounted for the molecular iodine fine structure at the wavelength and bandwidth of the HeNe laser, using a temperature-controlled cell. A similar densitometer measures the iodine density in the gain duct.

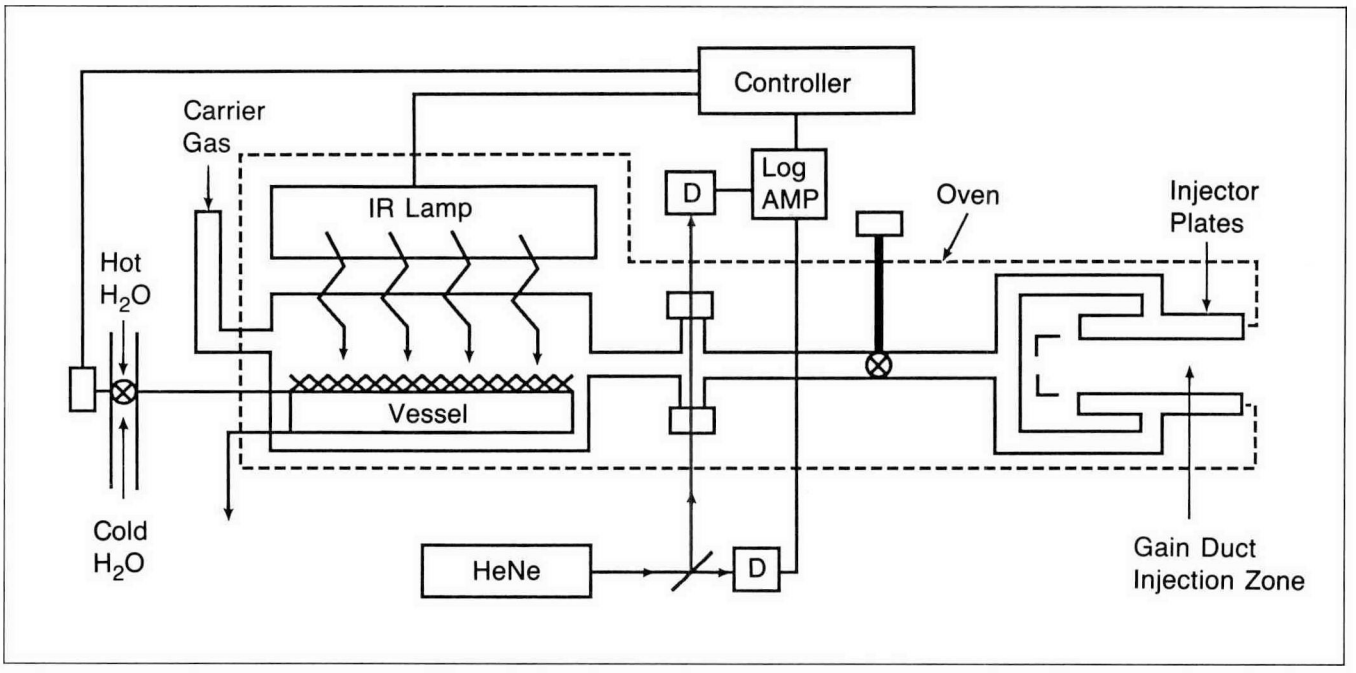

Fig. 3-2. The iodine delivery system prepares iodine for injection into the oxygen flow. Iodine crystals are distributed over the surface of a bronze vessel; the temperature of water that flows through the vessel is manipulated so as to maintain the crystals in equilibrium at a desired vapor pressure. When iodine injection begins, an IR lamp above the vessel is used to provide additional heat of sublimation and maintain vapor pressure. An iodine densitometer that uses a HeNe laser drives a feedback control system to modulate the vessel water temperature and IR lamp power. The vaporized iodine is mixed with a carrier gas and distributed at high pressure to the injection plates. The entire system is contained in a 120°C oven. Abbreviations in the figure are D, detector; log AMP, logarithmic amplifier.

in chlorine valve placement and actuation time, and redesign of the flow system to minimize turbulent mixing, should result in attainable pulse lengths of the order of 50 ms. Thus, efficient production of $O_2(^1\Delta)$ pulses at a rate of 10 Hz would appear to be within the realm of engineering feasibility.

Although the COIL system was designed to operate principally as a kinetics experiment and, as a result, has marginal net gain per pass, it has been set up in an oscillator configuration and has achieved lasing. Typical COILs now in operation use mirrors mounted inside the vacuum system to minimize losses and thermal effects that would occur in intracavity optical elements. Because this system was not intended as an oscillator, vacuum windows were mounted directly on the gain duct to facilitate spectroscopic measurements. Continuous-wave lasing was obtained with high-reflectance mirrors and a stable optical cavity that yielded multi-transverse-mode oscillation.

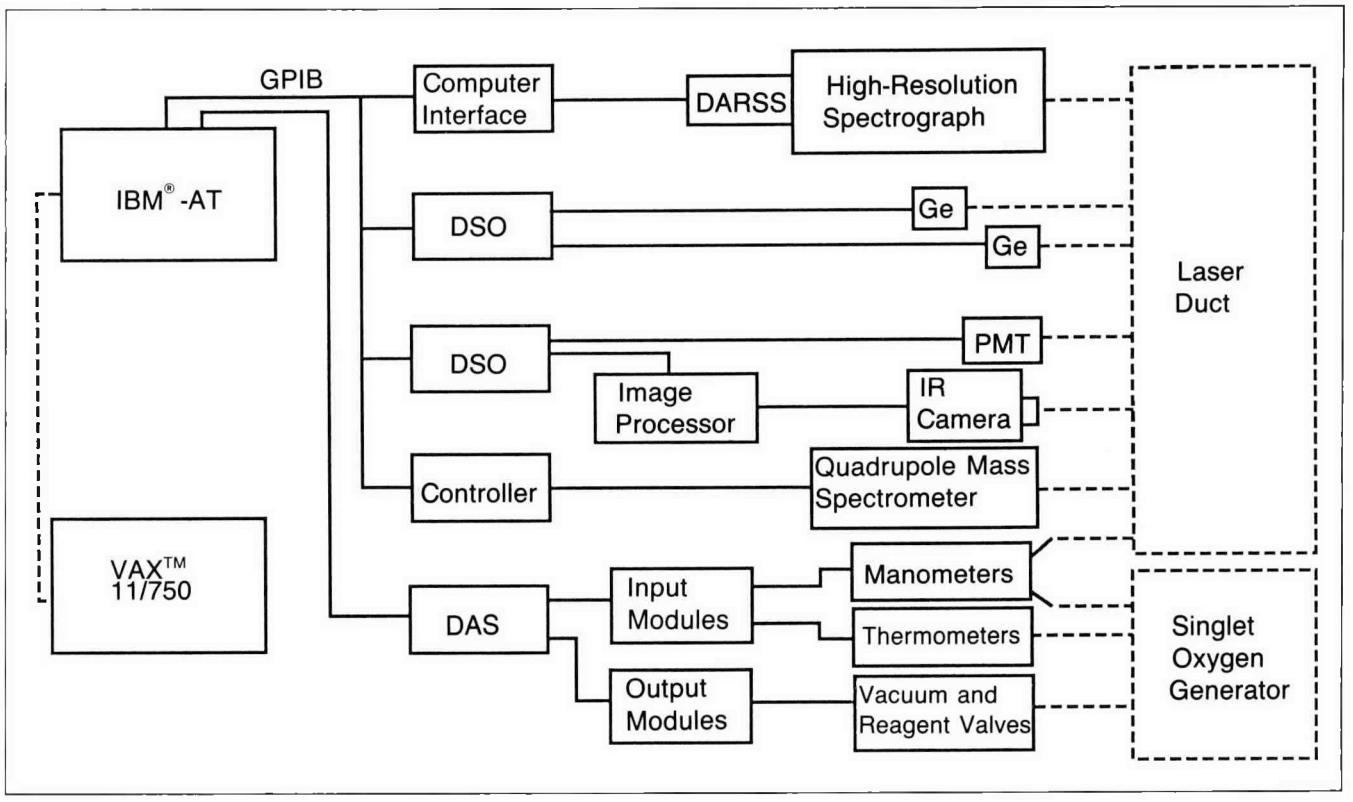

Fig. 3-3. Data are acquired from both the singlet-oxygen generator and the laser duct via many diagnostic instruments. Laser system parameters such as pressure, temperature, flow, and status conditions are digitized directly from the analog transducer signals and stored in an IBM® PC-AT. Nonspatially resolved spectral data are captured in a digitizing storage oscilloscope (DSO) and then transferred to a magnetic disk in the AT. Most of the kinetic measurements are made in the gain duct region using optical diagnostic instruments. The functions of the various diagnostics are discussed in the text; abbreviations in the figure are Ge, germanium; DAS, data acquisition system; DARSS, diode array rapid scan spectrometer; GPIB, general purpose interface bus; PMT, photomultiplier tube.

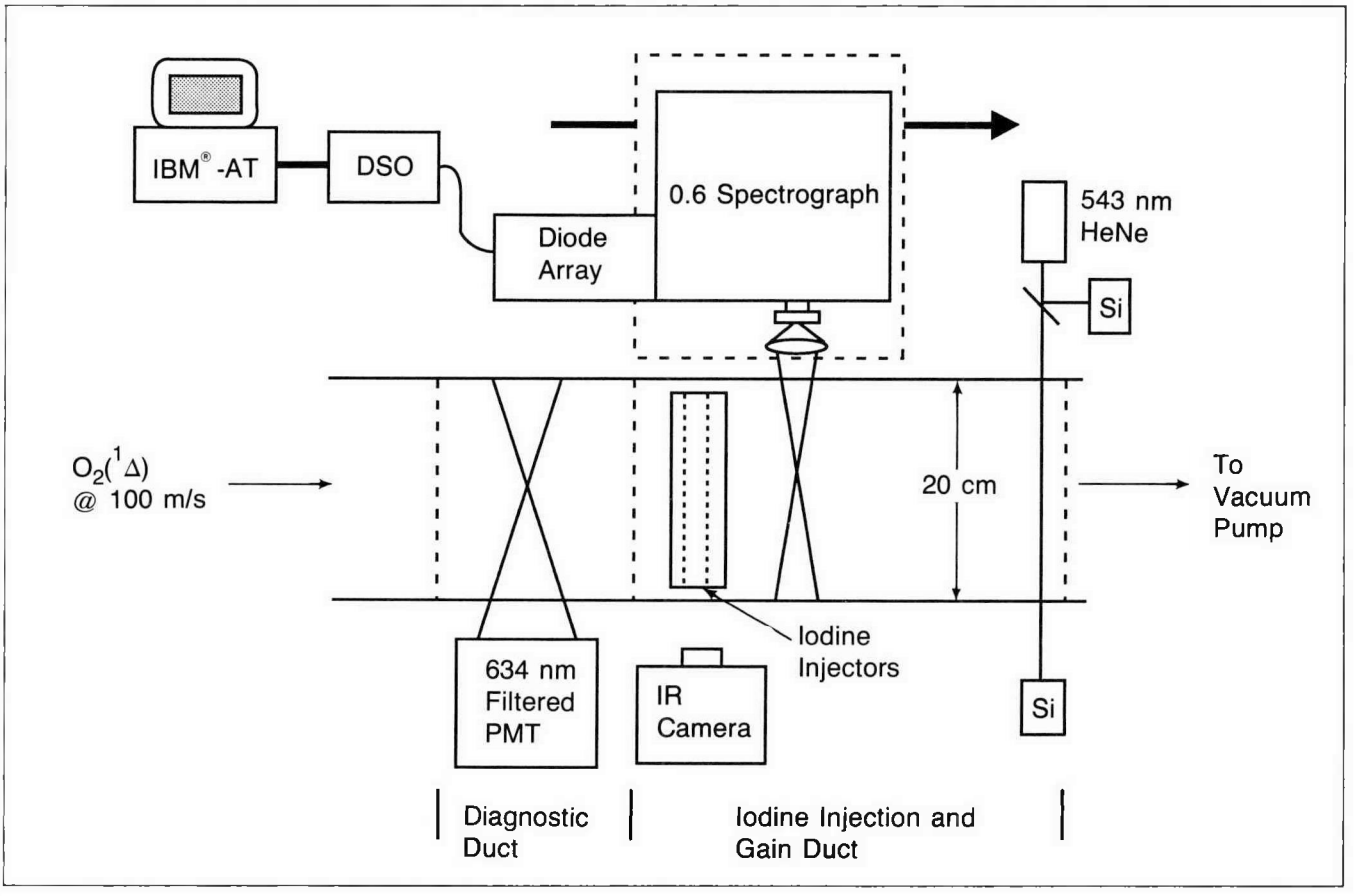

Fig. 3-4. The location of diagnostic instruments relative to the diagnostic and iodine-injection-and-gain ducts is shown for a typical experiment. The IR camera is used for observation of spatially resolved excited species fluorescence; the 0.6 m Czerny-Turner spectrograph and intensified diode array are used for high-resolution optical spectroscopy; and the green (543 nm) HeNe laser is used for iodine densitometry. The 634 nm filtered PMT monitors the oxygen a-state "dimol" emission.

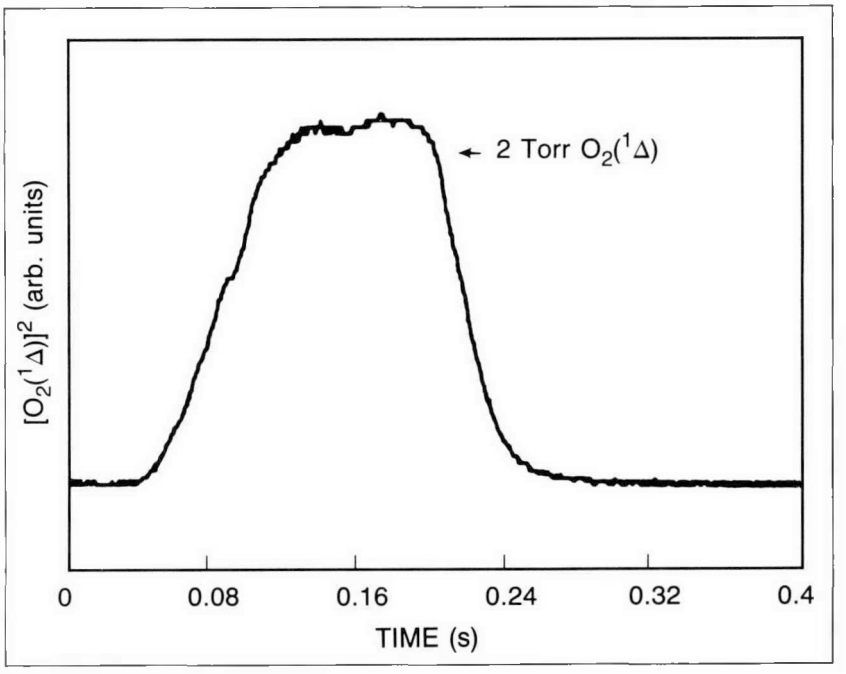

Fig. 3-5. Operation of the singlet-oxygen generator in the pulsed mode has minimized heating of the BHP and choking of the ICT. To achieve the pulsed mode operation, we have minimized gas dead volumes in the generator and chlorine delivery system and maximized the chlorine valve switching speed. The rapid approach to peak generator output and maintenance of steady-state $O_2(^1\Delta)$ levels during the chlorine pulse is evident in this temporal profile of pulsed $O_2(^1\Delta)$ production. Conditions: 634 nm PMT into diagnostic ducts; P_{total} = 5 Torr; $O_2(^1\Delta)$ yield = 40%; FWHM = 150 ms. The timed pulse to the chlorine valve was 100 ms FWHM.

Chemical Kinetics Experiments

An understanding of the chemical kinetics of the various energy-transfer processes that occur in a COIL is crucial to the design of an efficient laser. When molecular iodine is injected in singlet-oxygen [in this sense, singlet oxygen means both the $O_2(^1\Delta)$ and $O_2(^1\Sigma)$ species], the I_2 is dissociated and the resulting atomic iodine is excited by energy transfer from $O_2(^1\Delta)$. The dissociation mechanism is not yet fully understood, but it is probably tied to autocatalytic processes initiated by $O_2(^1\Sigma)$,

$$I_2 + \text{singlet oxygen} \rightarrow 2I \text{ [or } I^* + O_2(^3\Sigma)] \ .$$

Vibrationally and electronically excited molecular iodine intermediates are definitely present in the injection zone and are thought to play a role in dissociation. Once atomic iodine is present, energy transfer from the oxygen proceeds at the gas collisional rate,

$$O_2(^1\Delta) + I(^2P_{3/2}) \rightarrow O_2(^3\Sigma) + I^*(^2P_{1/2}) \ .$$

Measurements of fluorescence spatial profiles of the various iodine and oxygen species in the injection zone of the gain duct

have been made and are related to the temporal evolution of those species. The experiment uses a PbO/PbS Vis/IR camera coupled with the appropriate bandpass filters to record such profiles. In addition to the oxygen emissions represented in Eqs. (3), (4), and (5), we have observed the following for molecular and atomic iodine:

$$I_2(B^3\pi_0) \rightarrow I_2(X^1\Sigma) + h\nu \text{ (500 to 700 nm)} , \quad (6)$$

$$I^*I^*(^2P_{1/2}) \rightarrow I(^2P_{3/2}) + h\nu \text{ (1.315 } \mu\text{m)} . \quad (7)$$

Equation (6) represents the yellow-green molecular emission from iodine that is seen immediately upon injection, and Eq. (7) is the fluorescence that corresponds to the atomic iodine laser transition of interest.

Figure 3-6a shows the relationship between the emission of the $I_2(B)$ state given by Eq. (6) and that of I^* given by Eq. (7), where the horizontal scale measures the distance downstream from the extreme upstream row of injectors. From this, and data at other iodine densities, it appears that the $I_2(B)$ state emission is a maximum near the maximum net rate of I^* production. Whether or not $I_2(B)$ is an intermediary to I_2 dissociation and thus I^* production, or merely a side reaction, is yet unclear; however, it is definitely an indicator of dissociation. Further investigation into the infrared bands of the $I_2(A)$, $I_2(A')$, and vibrationally excited ground state, $I_2(X)$, is required before a definitive answer will exist.

Figure 3-6b demonstrates the correlation between I^* and $O_2(^1\Sigma)$ on the same horizontal scale as Fig. 3-6a. The link between I^* and $O_2(^1\Sigma)$ comes through a pooling reaction similar to that of Eq. (2),

$$I^* + I^* + O_2(^1\Delta) \rightarrow I + O_2(^1\Sigma) . \quad (8)$$

As long as the $O_2(^1\Delta)$ density remains approximately constant, the $O_2(^1\Sigma)$ will track the I^*. A full understanding of the role of the initiator effects resulting from an increase in $O_2(^1\Sigma)$ upon injection of iodine, due to an excursion away from the equilibrium density established by Eq. (2) and the establishment of a new equilibrium based on Eq. (8), awaits a detailed, high-resolution study of the high-density regions at the boundary of the iodine injection plume.

The comparison in Fig. 3-6c illustrates the change in kinetics between low and high iodine densities at equivalent $O_2(^1\Delta)$ flows. The low density profile represents the upper end of the operating regime typical of a continuous-wave laser, whereas the high density profile is near the lower limit, at which short pulse extraction is considered practicable. The much later rise of the I^* emission, and thus its density, in the latter case suggests initiator effects in an autocatalytic process.

The most novel experiments performed on this COIL during 1986 were spectroscopic measurements of the rotational temperature of $O_2(^1\Sigma)$ in the injection zone of the laser. The spectral

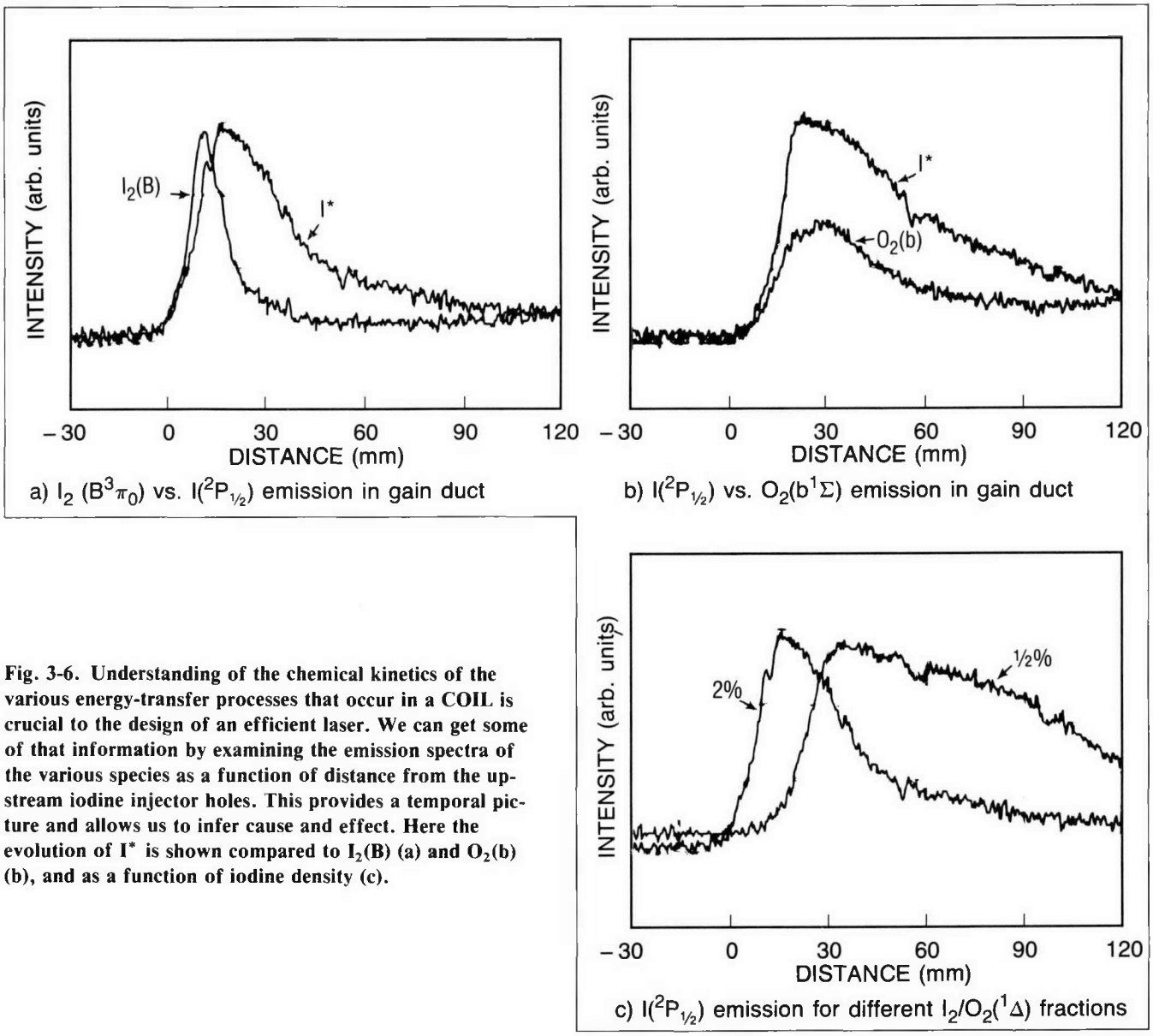

Fig. 3-6. Understanding of the chemical kinetics of the various energy-transfer processes that occur in a COIL is crucial to the design of an efficient laser. We can get some of that information by examining the emission spectra of the various species as a function of distance from the upstream iodine injector holes. This provides a temporal picture and allows us to infer cause and effect. Here the evolution of I^* is shown compared to $I_2(B)$ (a) and $O_2(b)$ (b), and as a function of iodine density (c).

data are collected by an intensified diode array with 1024 channels positioned at the output focal plane of a 0.64 m Czerny-Turner spectrometer operated near 762 nm in second order. The data are recorded by a DSO and then transferred to the AT. The spectrograph and diode array are positioned on a large translation stage so that they may be scanned along the direction of flow of the laser gases. Iodine is transversely injected at two different molar flow rates (i.e., densities) into the 100 m/s oxygen flow and a spectrum is recorded for various positions of the spectrograph.

In typical oxygen-iodine systems, most of the energy in the system is carried by the oxygen, which is highly metastable, but consequently is unavailable for short-pulse extraction via stimulated emission from the iodine. The extractable energy of the system is distributed between the oxygen and iodine according to

the equilibrium reaction given originally in Eq. (8) but rewritten here to include the energy defect ΔE,

$$O_2(^1\Delta) + I \rightleftarrows O_2(^3\Sigma) + I^* + \Delta E \ , \qquad (9)$$

where

$$\Delta E = 279 \text{ cm}^{-1} \ .$$

The equilibrium constant K_E for Eq. (9) is given by

$$K_E = \frac{[O_2(^3\Sigma)]\,[I^*(^2P_{1/2})]}{[O_2\,(^1\Delta)]\,[I(^2P_{3/2})]} = \frac{g(^3\Sigma)g(I^*)}{g(^1\Delta)}\, e^{(\Delta E/kT)} \ , \qquad (10)$$

where [ ] signifies concentration, g is the electronic degeneracy of the parenthetical state, the other symbols have their customary meanings, and rotational partition function differences between the two oxygen states are insignificant and ignored. The degeneracies involved in Eq. (10) are $^1\Delta:^3\Sigma:I^*:I = 2:3:2:4$. Thus, $K_E = 0.75\, e^{(\Delta E/kT)} = 2.89$ at 298K but decreases to 1.46 at 600K. This implies that, for a given fraction of singlet oxygen, $O_2(^1\Delta)/O_2(^3\Sigma)$, there is only about half as much energy available in the iodine at 600K as at 298K.

Modeling of the COIL has suffered from the lack of temperature-dependent rate coefficients. To begin to correct this problem, we have developed a method whereby the temperature of the laser gases can be measured nonintrusively with a spectroscopic technique. Specifically, we have recorded a portion of the ^{P}P rotational branch of the $O_2(^1\Sigma) \rightarrow O_2(^3\Sigma)$ electronic transition at various positions and iodine densities in the laser injection region and fit the spectra to a temperature model. Major advantages of the spectroscopic method versus an intrusive probe are that the laser gas is unperturbed and that there exists no preferential deactivation of excited-state laser gases on the probe that would heat its surface and yield erroneous temperature values.

The intensity, $S(J \rightarrow J')$, of a ^{P}P-branch rotation line from an upper state, J, to a lower state, J', of the $O_2(^1\Sigma) \rightarrow O_2(^3\Sigma)$ transition is given by

$$S(J \rightarrow J') \cong C(H_J)e^{[-J(J+1)B+(2\lambda-\gamma)]hc/kT} \ , \qquad (11)$$

where C is a constant of the optical system, $H_J = (J + 1)/2$ is the Hohl-London factor, B is the rotational constant for the molecule, λ and γ are spin-coupling constants to the internuclear and rotational axes, respectively, and the other terms have the usual meanings. Equation (11) can be rearranged to give the temperature of a rotational spectrum in terms of the intensity of the lines, the angular momentum J of the upper state, and the molecular constants. This rearrangement is given as

$$(-T)^{-1} = \frac{\ln(S/H_J)}{E/k} \ ,$$

where

$$E = [J(J+1)B + (2\lambda - \gamma)]hc,$$
$$B = 1.43777 \text{ cm}^{-1},$$
$$\lambda = 1.984 \text{ cm}^{-1},$$
$$\gamma = -0.0084 \text{ cm}^{-1},$$

and S corresponds to the appropriate $J \rightarrow J'$ transition. Thus the slope of a plot of $\ln(S/H_J)$ versus E/k for a set of rotational transitions is proportional to $-1/T$. It is by this means that the rotational temperature of $O_2(^1\Sigma)$ will be determined.

A P-branch rotational line spectrum of the $O_2(^1\Sigma) \rightarrow O_2(^3\Sigma)$ electronic transition and its associated temperature plot is shown in Fig. 3-7. The ^{P}P-branch lines of the spectrum that are used for the temperature determination are denoted by the asterisks. A least-squares method was used to find the line of best fit and, from its slope, the temperature $T = 335$K and the standard deviation of 6K were calculated. Figure 3-8 plots the results of calculations of temperature versus position at two different iodine densities. The increase in temperature as a function of position

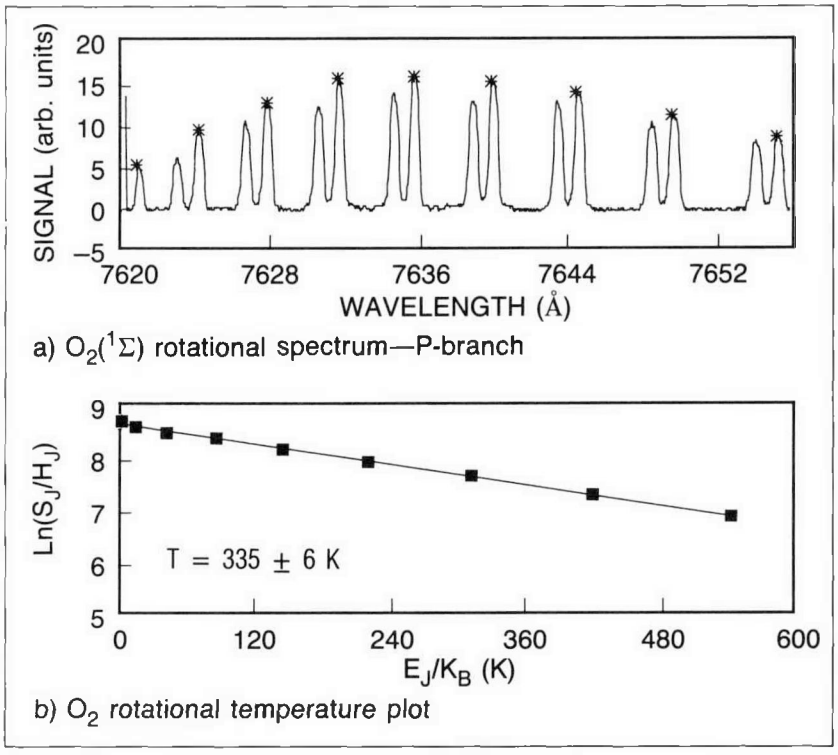

Fig. 3-7. Experiments were performed in which the rotational temperature of $O_2(^1\Sigma)$ was measured spectroscopically in the injection zone of the laser. Iodine was transversely injected at two different molar flow rates (densities) into the 100 m/s oxygen flow and a spectrum recorded for various positions of the spectrograph. A P-branch rotational line spectrum of the $O_2(^1\Sigma) \rightarrow O_2(^3\Sigma)$ electronic transition (a) and its associated temperature plot (b) are shown here. The ^{P}P-branch lines of the spectrum that are used for the temperature determination are denoted by the asterisks. A least-squares method was used to find the line of best fit and, from its slope, the temperature and standard deviation were calculated.

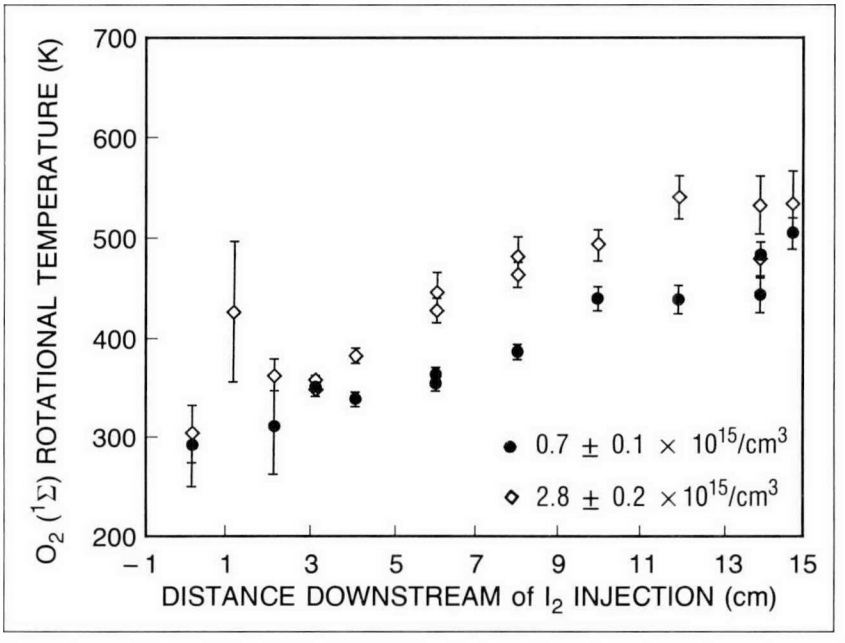

Fig. 3-8. The rotational temperature of $O_2(^1\Sigma)$ was calculated as a function of distance downstream from iodine injection for two different iodine densities (0.7×10^{15}/cm^2 and 2.8×10^{15}/cm^3). The temperature increases with distance downstream from the iodine injectors for both densities, but increases more rapidly for the higher iodine density.

downstream of the iodine injectors and the greater rate of the increase at higher iodine density is evident from this plot.

After the injection of the iodine, the energy content of the $O_2(^1\Delta)$ is eventually converted to heat unless it is extracted as laser light. The pathways for this heat evolution surely include direct quenching of excited species, as well as the energy defect of the various energy-pooling, energy-transfer, and iodine dissociation processes. Over the time-scale that the heat is released from the excited species, the effect of thermal conduction to the walls of the system is negligible. It is during this same time-scale of energy transfer and quenching that the energy must be extracted if high efficiency is to be attained. The increase in temperature will adversely affect the energy partition and equilibrium between the oxygen and iodine. This technique can be applied as a diagnostic for kinetic studies of the temperature-dependent rate coefficients needed to model the COIL adequately. Future investigations will address the effect of adding high-heat-capacity buffer gas to the flow streams to reduce the temperature rise.

Conclusion

Chemical kinetic experiments on oxygen-iodine systems have been performed in the KMSF COIL laboratory. Our COIL facility is unique in its ability to provide pulses of singlet oxygen on demand at tens of millimoles per second for hours on end. The instrumentation and microcomputer control systems allow for nearly turn-key operation of the oxygen generator and reagent

delivery systems. Measurements in the injection zone of time-resolved fluorescence of the various excited species have begun to reveal the relationships between them. The novel, nonintrusive measurements of rotational temperature by high-resolution spectroscopy has provided new information on the evolution of stored energy in the laser system.

Much more remains to be learned before the full potential of this laser is known. Understanding of the iodine dissociation process is of major importance to full utilization of the energy of the system, and thus high efficiency. Closer study of the electronically and vibrationally excited molecular iodine states in the near IR is indicated. Ultimately, short-pulse gain measurements at saturation fluences should be performed and the energy transfer recovery kinetics from oxygen to iodine determined. For accurate modeling of fusion driver-class COILs, the temperature-dependent rate constants for each reaction listed herein, and more, must be determined.

For additional information, please contact Dr. Geo. E. Busch

SECTION 3.2

High-Efficiency Frequency Tripler Using the ARCA Technique*

Highly efficient frequency doubling and tripling of infrared laser beams has been achieved at high peak powers[3,4,5] in inertial confinement fusion (ICF) laser systems. Power densities on the order of 1 GW/cm^2 and beam divergences of 0.1 mrad or less permit conversion efficiencies of 80% or more at a wavelength of 1.053 μm with nonlinear single crystals like potassium dihydrogen phosphate (KDP). For high-average-power lasers or long-pulse lasers, however, power densities are limited by energy-dependent damage levels, and beam divergences are set by laser design. The crystal lengths required for high conversion are thus long and the permissible beam divergence is then very low.

A multiple-crystal technique, called the alternately reversed crystal axis (ARCA) technique, has been developed at KMS Fusion (KMSF) that significantly reduces the requirements on laser power and beam divergence for efficient conversion of long laser pulses. In a series of tests performed with the KMSF Chroma laser in 1986, a tripling efficiency of 24% and a doubling efficiency of 35% were demonstrated. For these tests, the laser was operated at 1.053 μm with a pulse length of 1 μs. Optical damage to bare and Sol-Gel-coated KD*P crystals for 1 μs pulses appeared at a level of about 300 J/cm^2. Damage to the UV mirrors, however, occurred at about 5 J/cm^2.

Theory

Frequency-doubling efficiency for perfect phase-matching is given by

$$Eff = \tanh^2(K1\, E_p^{\omega} L) \ ,$$

where

$$K1 = [\pi/(n\lambda^{\omega})]\,(d_{\text{eff}}/e_0) \ ,$$

λ^{ω} is the wavelength in m, n is the refractive index of the crystal, d_{eff}/e_0 is the effective nonlinear coefficient in V^{-1}, E_p^{ω} is the electric field intensity of input optical beam in V/m, and L is the crystal length in m.

For a conversion efficiency of >58%,

$$K1\, E_p^{\omega} L > 1.0 \ . \qquad (12)$$

*Work performed under TRW contract AB2775-DS6S, "Raman-Shifted Excimer Laser Enhancement."

The effect of phase mismatch (at low conversion efficiencies) is given by

$$Eff = [\sin(dk\,L/2)/(dk\,L/2)]^2 \ ,$$

where dk is the phase mismatch for the nonlinear crystal in rad/m. The half-power phase mismatch (i.e., the point at which the second harmonic power and the efficiency drop by a factor of 2) occurs at

$$dk\,L = 2.78 \text{ rad} \ ,$$

where

$$dk = \Delta\theta\, dk/d\theta \ .$$

If the half-power phase mismatch defined above is taken as the maximum tolerable phase mismatch, the crystal length and the deviation from the exact phase-matching angle are limited to

$$\Delta\theta\, L = 2.78/DK \ ,$$

where $\Delta\theta$ is deviation from the phase-matching angle θ_m in mrad and DK is phase-matching angle sensitivity $dk/d\theta$ in rad/(m·mrad). The crystal length is then limited to

$$L = 2.78/(\Delta\theta\, DK) \ .$$

If the crystal length L is replaced in Eq. (12), the condition for high conversion efficiencies becomes

$$[2.78\,K1/DK]^2[E_p^{\omega}/\Delta\theta]^2 > 1.0 \ .$$

Let

$[2.78\,K1/DK]$ be the nonlinear crystal parameter K_{eff}, and

$[E_p^{\omega}/\Delta\theta]^2$ be the laser beam parameter P_{eff}, or

$P_d/\Delta\theta$ be the alternate laser beam parameter P_{eff_a} .

The laser beam parameter could be considered a figure of merit for frequency doubling. It is proportional to the power density divided by the beam divergence squared. Note that reducing the beam diameter increases the power density but increases the beam divergence squared by the same factor; hence, the laser beam parameter is not a function of the beam diameter. The nonlinear crystal parameter is a function of the basic crystal characteristics and is a constant for a particular type of crystal doubler and a given wavelength; the values for some common crystal doublers are given in Table 3-1. Thus, for a given laser beam, the efficiency of a single crystal doubler is determined by the doubler material, and not much can be done to increase conversion efficiency.

Table 3-1. Crystal Merit Factor K_{eff} for Several Nonlinear Crystal Doublers and Triplers

Crystal Parameters at 1.053 μm					
Crystal	KDP	KDP	KDP	KDP	LiO_3
Type of Phase-Matching	Type I Doubler	Type II Doubler	Type I Tripler	Type II Tripler	Type I Doubler
Nonlinear Coefficient, d/e (pm/V)	0.39	0.39	0.39	0.39	4.7
Refractive Index at Phase-Match Angle	1.5	1.5	1.5	1.5	1.8
Phase-Match Angle, Internal (degrees)	41.2	59.2	47.7	59.1	28.5
d_{eff}/e (pm/V)	0.51	0.69	0.58	0.69	4.4
$K1 = P1/n\ (d_{eff}/e)$ (1/V)	1.02×10^{-6}	1.37×10^{-6}	1.15×10^{-6}	1.37×10^{-6}	7.4×10^{-6}
Phase-Match Angle Sensitivity, DK (rad/cm·mrad)					
Internal	−5	−2.56	−8.07	−5.26	−16.1
External	−3.38	−1.73	−5.45	−3.51	−8.5
$K_{eff} = 2.78\ K1$ (ext) (cm·mrad/V·rad)	8.39×10^{-7}	2.20×10^{-6}	5.87×10^{-7}	1.09×10^{-6}	2.49×10^{-6}

The ARCA technique described here avoids this limitation by using multiple crystals. The optic "Z" axes of the crystals are reversed so that the phase-matching angles are of opposite sign. The phase mismatch angles and the mismatch in propagation vector amplitude will be of opposite sign in successive crystals. The magnitude of the phase mismatch due to beam divergence (in the sensitive direction) will then oscillate but never reach an amplitude that will limit the conversion efficiency.

Figure 3-9a shows the basic configuration using four crystals. The directions of the optical "Z" axis and the electric field vectors for the first and second harmonic are shown for a Type I KDP crystal. Figure 3-9b shows the phase-matching angles for the center two crystals. The angle between the propagation vector k^{ω} and the crystal "Z" axis determines the phase-matching. The crystals are initially aligned so the central ray of the input laser beam (k^{ω}) makes an angle of θ_m with the "Z" axis. Then a ray that is divergent by $\Delta\theta$ will incur a phase-match angle of $\theta_m + \Delta\theta$ in the left crystal and a phase-match angle of $\theta_m - \Delta_m$ in the right crystal. These alternately signed phase mismatches tend to cancel if they are less than $\pi/2$ rad. Crystal orientation is important since the sign of the effective nonlinear coefficient can be reversed if the proper orientation is not chosen.

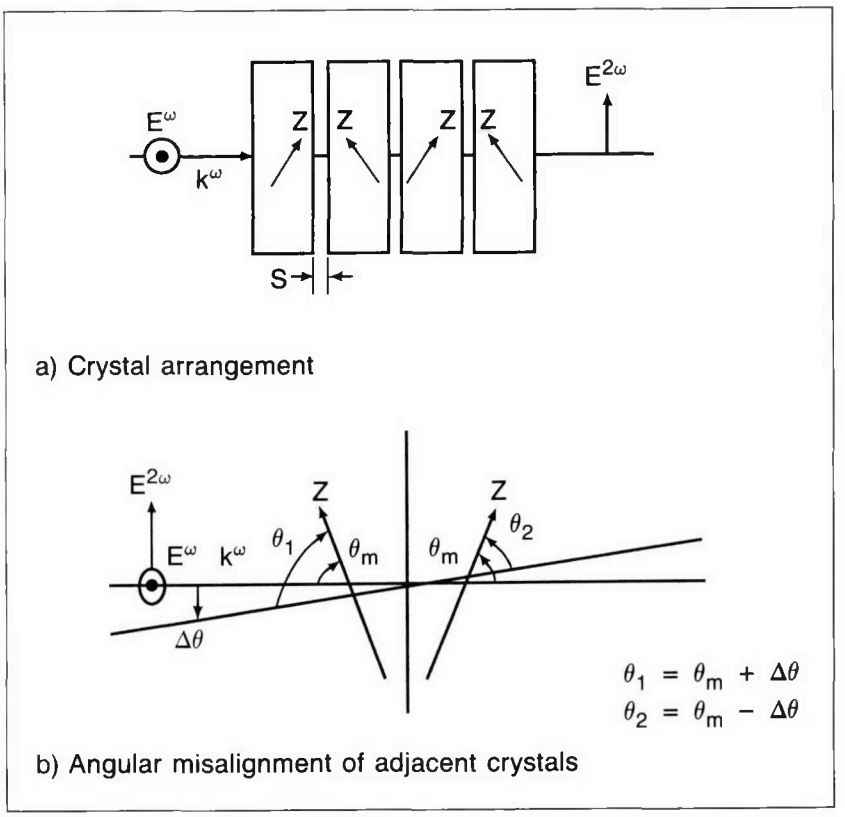

Fig. 3-9. The ARCA technique employs multiple crystals with the optic "Z" axes reversed so that the phase-matching angles are of opposite polarity. The basic configuration using four crystals is shown in (a). The directions of the optical "Z" axis and the electric field vectors for the first and second harmonic, E^{ω} and $E^{2\omega}$, are shown for a Type I KDP crystal (k^{ω} is the propagation vector and S is spacing between crystals). The phase-matching angles θ_m and the effect of angular misalignment for the two center crystals are shown in (b). Phase-matching is determined by the angle $\Delta\theta$ between k^{ω} and Z.

This technique is applicable to Type II crystals, too; however, for Type II KDP, for example, it is not possible to orient the "Z" axes alternately as shown in Fig. 3-9 with crystals from the same "cut" without changing the effective sign of the nonlinear coefficient. This change in the sign of the nonlinear coefficient will produce second-harmonic light in the second crystal that is opposite in sign from that in the first, thus reconverting the second harmonic back into the fundamental. To avoid this effect, the dispersion of the air between the crystals is used to change the phase of the second harmonic with respect to the fundamental by 180°.

More precisely, the phase-matching condition between the crystals is

$$(k^{2\omega} - 2k^{\omega})S = \pi \ ,$$

where

$$S = (\lambda^{2\omega}/2)/(n^{2\omega} - n^{\omega})$$

and S is the spacing of air (or other gas) between crystals; $k^{2\omega}$ and k^{ω} are propagation constants for the second harmonic and the fundamental, respectively; $\lambda^{2\omega}$ is the wavelength of the second harmonic; and $n^{2\omega}$ and n^{ω} are the refractive indices of the gas for the second harmonic and the fundamental, respectively.

For a Type II KDP mixer crystal, the phase-matching condition for the material between crystals is

$$(k^{3\omega} - k^{2\omega} - k^{\omega})S = \pi \ .$$

where

$$S = (\lambda^{\omega}/2)(3n^{3\omega} - 2n^{2\omega} - n^{\omega}) \ ,$$

$n^{3\omega}$ is the refractive index of the gas for the third harmonic, and λ^{ω} is the wavelength of the fundamental.

The effect of reducing the phase mismatch by the ARCA technique is dramatically demonstrated in Fig. 3-10a for a 20 cm length of KDP in a Type II doubling configuration with a uniform power density from 0 to 10 MW/cm^2. The top curve shows the theoretical conversion efficiency with no phase mismatch (i.e., the phase-matching angle is exact for the whole laser beam and there is no beam divergence), and the other curves assume no reflection losses at the crystal surfaces. For an error in the phase-matching angle of 0.2 mrad, a single 20-cm long crystal would give a conversion efficiency of less than 3%. If that

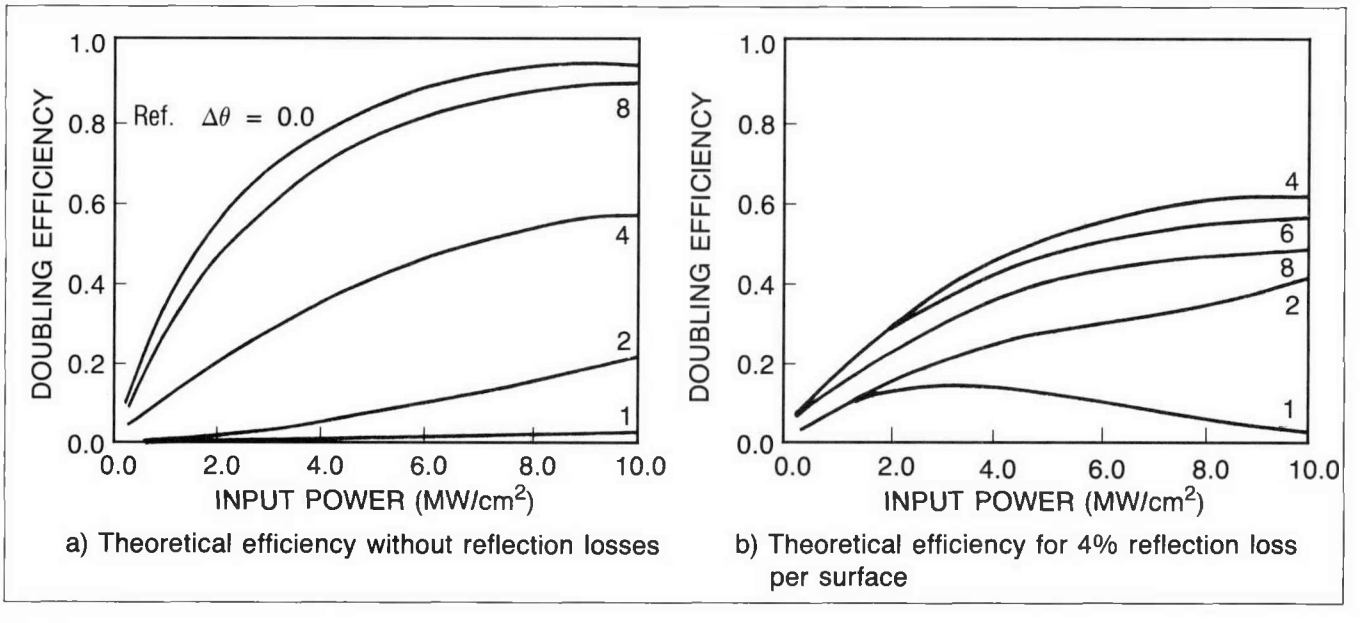

Fig. 3-10. The doubling efficiency of a 20 cm length of KDP in a Type II doubling crystal with uniform power density is increased by the ARCA technique. The curves in (a) assume no reflection losses: The top curve shows the theoretical conversion efficiency of a single crystal with no phase mismatch; the other curves show the effect of a phase mismatch of 0.2 mr for one, two, four, and eight crystals. For one crystal, the efficiency is only 3%; for two, four, or eight crystals in the ARCA configuration, the efficiency increases until it approaches the theoretical limit. When the doubler design is optimized for 4% reflection loss per surface, the conversion efficiencies (for the same phase mismatch) are as shown in (b). In this case, the maximum conversion efficiency is obtained with four crystals.

same crystal is cut into two crystals in the ARCA configuration, the efficiency goes up to about 20%, while four crystals give >50%; eight crystals reduce the effect of angular phase mismatch nearly to zero and approach the theoretical limit for conversion efficiency.

The number of crystals can be chosen to reduce the effective phase mismatch to an arbitrarily small amount for any amount of angular mismatch. However, the losses introduced by surface reflections must be accounted for in optimizing the doubler design. Anti-reflection (AR) coatings are becoming available that can reduce the surface losses to 1% or less at both wavelengths. An example of this optimization for no AR coatings (i.e., a loss of 4% per surface) using a computer model is shown in Fig. 3-10b; the maximum effective conversion efficiency is obtained with four crystals. Low loss, dual-wavelength AR coatings will bring the conversion efficiency up significantly. This technique can also be used for tripling and quadrupling laser light where any other processes require angular phase-matching.

This multiple crystal technique is probably the only technique that would simultaneously provide for the wide acceptance angles and heat removal required for high-average-power doublers and triplers. The acceptance angle becomes very low for low-peak-power laser beams where the nonlinear crystals must be very long, and consequently the heat absorption is high in long crystals. The basic configuration for a high-average-power doubler is shown in Fig. 3-11. Helium gas would be a very desirable coolant, since it has a very low dispersion and a high thermal conductivity.

Experiment

To demonstrate generation of a third harmonic light in a 1 μs pulse with the Chroma laser (operating at 1.053 μm), the ARCA technique was tested with a three-crystal Type II KD*P doubler and a four-crystal Type II KD*P mixer. The laser beam from the rod amplifier of Chroma was reduced to 1.5 cm in diameter, passed through a vacuum spatial filter (to place the image plane of the laser at the position of the KD*P crystals), and into the harmonic conversion crystals. Figure 3-12 shows the basic test configuration. Photodiodes monitored pulse shapes, and calorimeters monitored the IR and UV laser energies. The polarization at the input to the doubler was set with a half-wave plate to 35° from the ordinary direction in the doubler, as shown in Fig. 3-13. Etalons were used to obtain density versus log (exposure) curves for the film and to provide a range of exposures for the far-field patterns. Ultraviolet mirrors (M1 and M2 in Fig. 3-12) were used to separate the UV output from the green and IR light. Appropriate colored glass filters were used to pass only the desired wavelength into the calorimeters and photodiodes and to control the exposure of the near-field and the far-field photographs.

The hygroscopic KD*P crystals were placed in acrylic covers that were purged with dry nitrogen to protect them from mois-

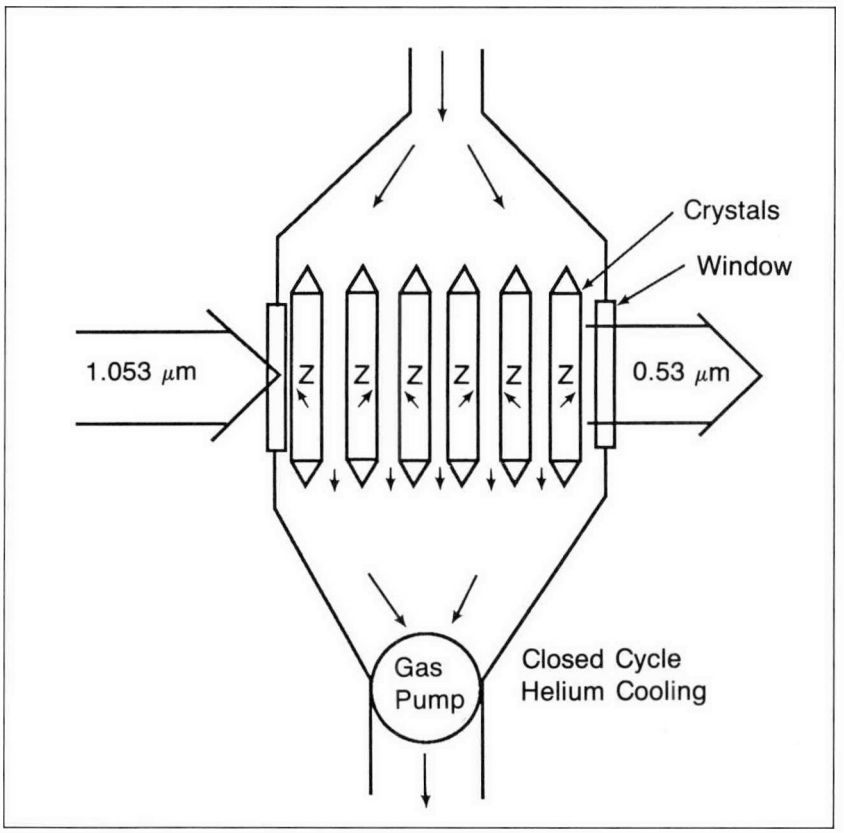

Fig. 3-11. The multiple crystal technique simultaneously accommodates wide acceptance angles and heat removal, which is required for high-average-power doublers and triplers. The basic configuration for a high-average-power doubler is shown here; helium gas would be a very desirable coolant, since it has a very low dispersion and a high thermal conductivity.

ture and dirt. Since these crystals were Type II KD*P all of the same "cut," the dispersion of the nitrogen had to be used to introduce the 180° phase reversal to cancel the phase reversal caused by reversing alternate crystals. The dispersion length was measured by mounting one of the crystals on a precision slide and moving it with respect to another crystal until a null in the nonlinear output was obtained. This length represented a phase shift of 360°. One-half of this length was then used as the correct dispersion distance. For the doubler, the calculated dispersion distance in air was 6.07 cm and the measured dispersion distance in nitrogen was 6 ± 0.2 cm. For the mixer, the same measurement technique gave a half-wave dispersion distance in nitrogen of 2.3 ± 0.3 cm, compared with a calculated value of 1.9 cm for air.

Before performing the frequency conversion tests, we measured the damage level on two 1 × 1 × 1.2 cm KD*P test samples. One of the samples was a bare crystal and the other was coated by Lawrence Livermore National Laboratory with Sol-Gel AR coating. Neither sample was damaged by the 1.5 cm diameter beam at 40 J/cm^2. The samples were then tested in the converging beam of a 50 cm focal length lens at a beam diameter of 0.75 cm. At this diameter, some damage began to appear

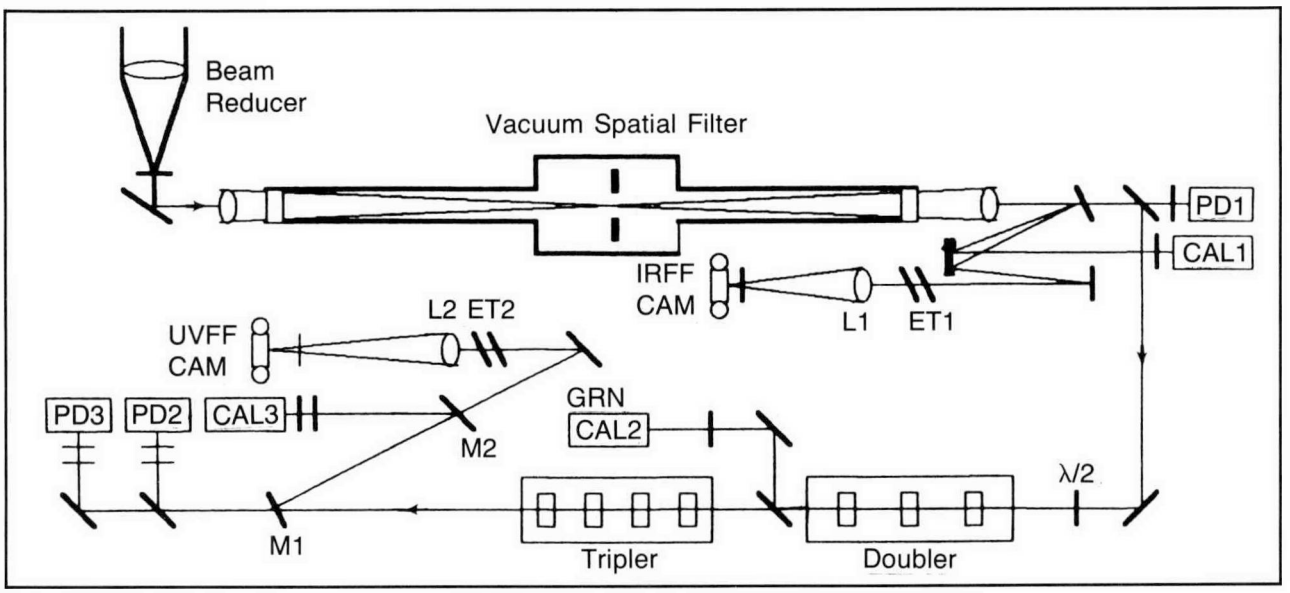

a) Configuration of optics used to test the ARCA technique

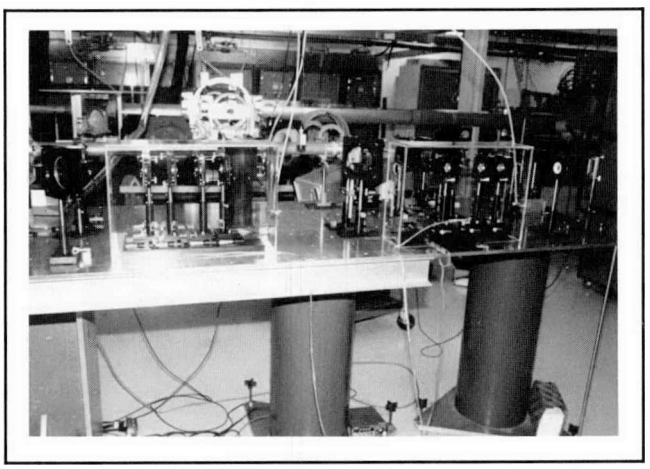

b) Three-crystal Type II doubler and four-crystal Type II tripler

Fig. 3-12. The ARCA technique was tested on the Chroma laser with a three-crystal Type II KD*P doubler and a four-crystal Type II KD*P mixer to demonstrate generation of third harmonic light in a 1 μs pulse. The laboratory configuration is shown schematically in (a); a close-up photograph of the doubler and tripler is shown in (b).

Key to abbreviations:

IRFF, UVFF CAM: infrared and ultraviolet far-field cameras
L1,2: lenses
ET1,2: etalons used to obtain density vs. log (exposure) curves for the film and to provide a range of exposures for the far-field patterns
PD1,2,3: photodiodes used to monitor pulse shapes
CAL1,2,3: calorimeters used to monitor IR and UV energies
M1,2: UV mirrors used to separate the UV output from the green and IR light
GRN: green
λ/2: half-wave plate used to establish polarization at input to doubler

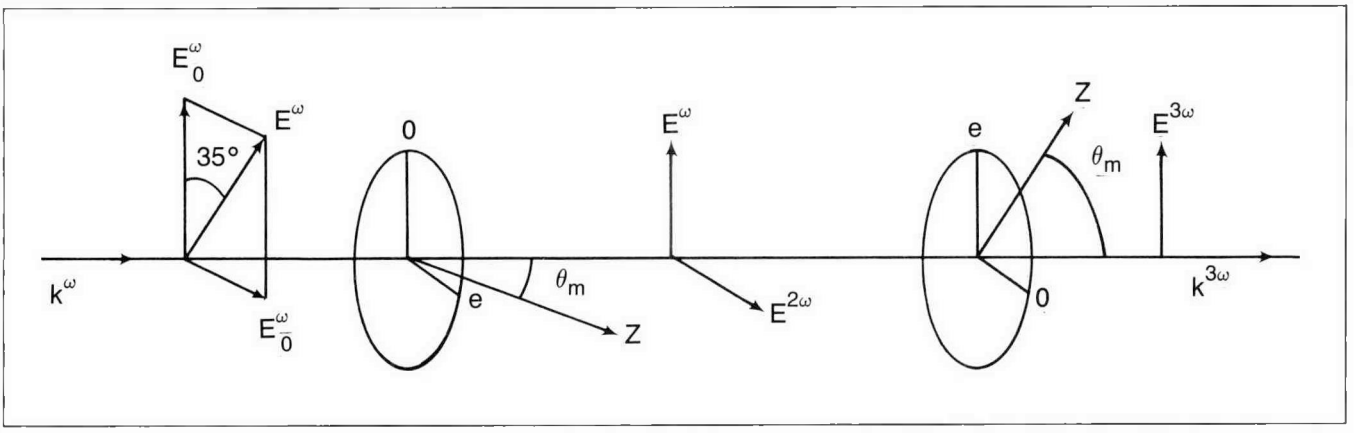

Fig. 3-13. The phase-matching configuration of Type II doubling and Type II tripling in the KD*P crystals is shown schematically. The polarization at the input to the doubler was set with a half-wave plate to 35° from the ordinary direction in the doubler. The symbols are as defined in the text.

at an average energy density of 100 J/cm^2. However, the beam intensity pattern at this position was a "bull's eye" with a peak energy density of about 300 J/cm^2. Both the uncoated and the Sol-Gel coated crystals showed about the same damage threshold. Photographs of this crystal surface damage are shown in Fig. 3-14. These crystal samples were not perfectly clean prior to irradiation, and it appeared that the small amount of damage that did appear occurred at dust particle locations.

The theoretical conversion efficiency for a three-crystal doubler and a four-crystal mixer with reflection losses included is shown in Fig. 3-15. The experimental efficiencies that we observed in our brief tests covered the range of power densities from 12 to 65 MW/cm^2. Conversion efficiencies reached 24% for real conversion with uncoated crystals. We expected to achieve higher conversion efficiency, but alignment of the individual crystals to the precise phase-matching angle was not possible with the fixture used. However, the ARCA technique worked as expected, and the highest conversion efficiencies were demonstrated with well characterized calorimeters that were used to measure both the input IR and the output UV.

The doubling efficiency of the three-crystal doubler is shown in Fig. 3-16. A conversion efficiency of 35% was measured. With better alignment, higher conversion efficiencies would be achieved. The lower values of conversion efficiency for both the doubling and tripling were attributable to misalignment resulting from vibration, air currents, and the inability to align each crystal to the required accuracy. Early in the experiment, axial mode beating caused large fluctuations in the oscillator output. After the oscillator was mode-locked to stabilize it, the accuracy of crystal alignment was still insufficient to obtain optimum conversion efficiencies. Also, the polarization angle nominally set at 35° was not optimized.

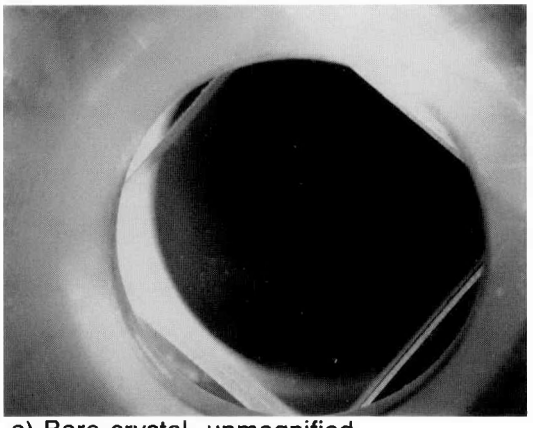

a) Bare crystal, unmagnified

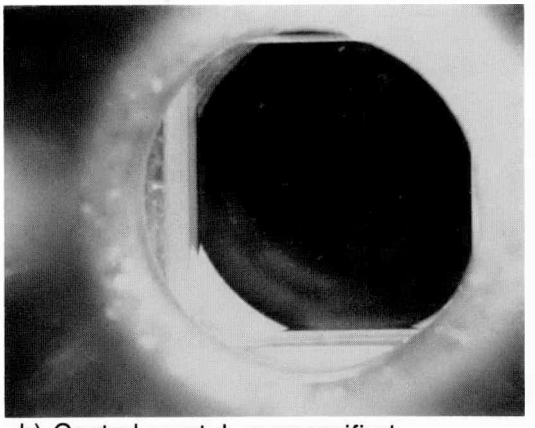

b) Coated crystal, unmagnified

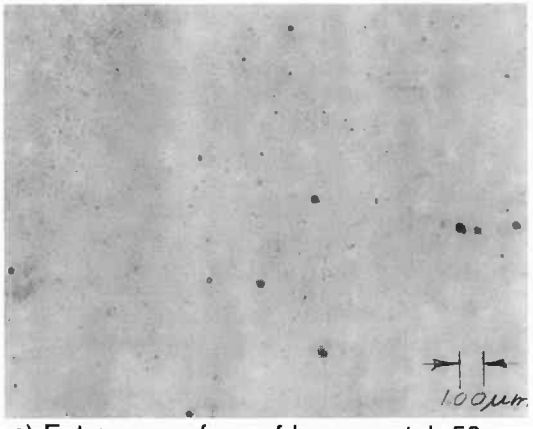

c) Entrance surface of bare crystal, 50x

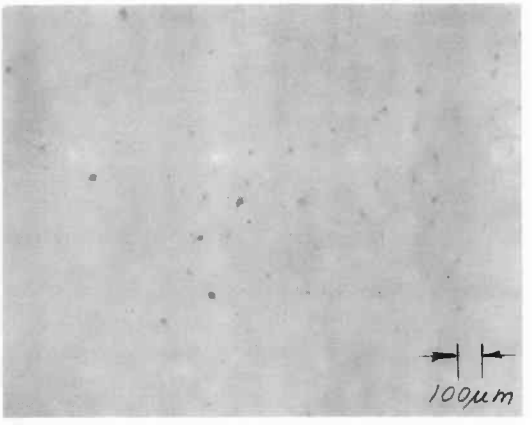

d) Entrance surface of coated crystal, 50x

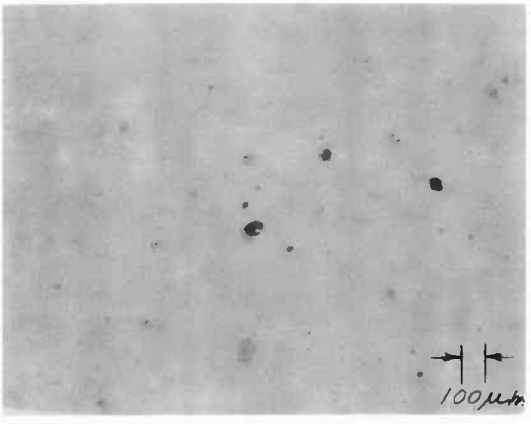

e) Exit surface of bare crystal, 50x

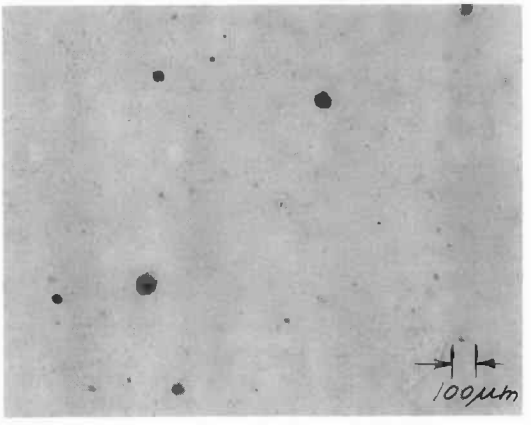

f) Exit surface of coated crystal, 50x

Fig. 3-14. The damage level on two KD*P test samples was measured before the frequency conversion tests. A bare crystal (a) and a crystal coated with Sol-Gel anti-reflection coating (b) were tested in the converging beam of a 50 cm focal length lens at a beam diameter of 0.75 cm. Some damage began to appear at an average energy density of 100 J/cm^2 (the peak energy density was ~300 J/cm^2) in 1-μs pulses. Both uncoated and coated crystals showed about the same damage threshold, and the damage appeared to occur at dust particle locations. The entrance surfaces are shown at 50× for the bare (c) and the coated (d) crystals; the exit surfaces are shown at 50× for the bare (e) and the coated (f) crystals.

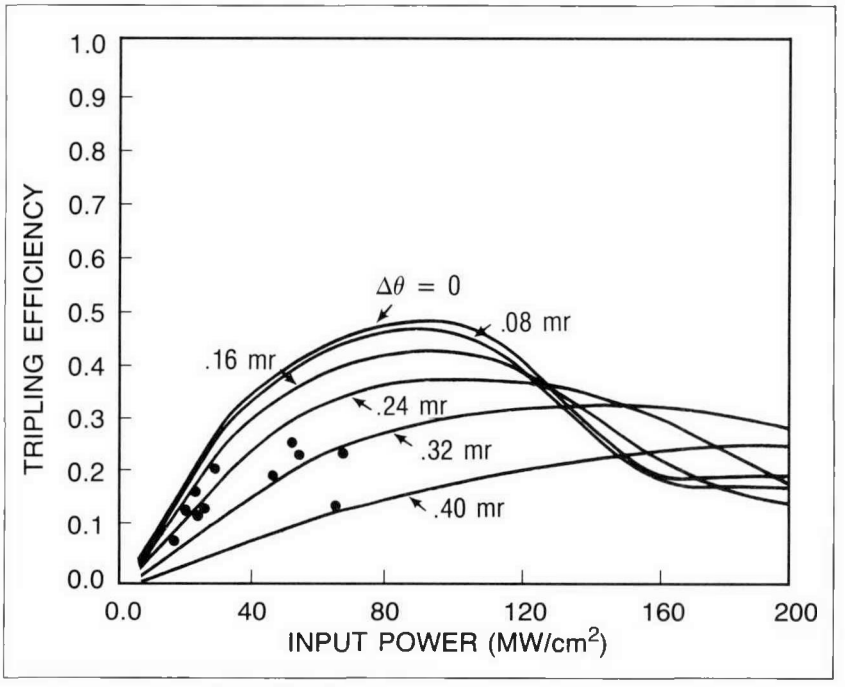

Fig. 3-15. Theoretical conversion efficiency (curves) with reflection losses included is shown for a three-crystal doubler and a four-crystal mixer. The experimental efficiencies (circles) observed in our tests are shown for power densities from 12 to 65 MW/cm^2. The total length of KD*P crystal was 6 cm in the doubler and 6 cm in the mixer. Conversion efficiencies reached 24% for real conversion with uncoated crystals.

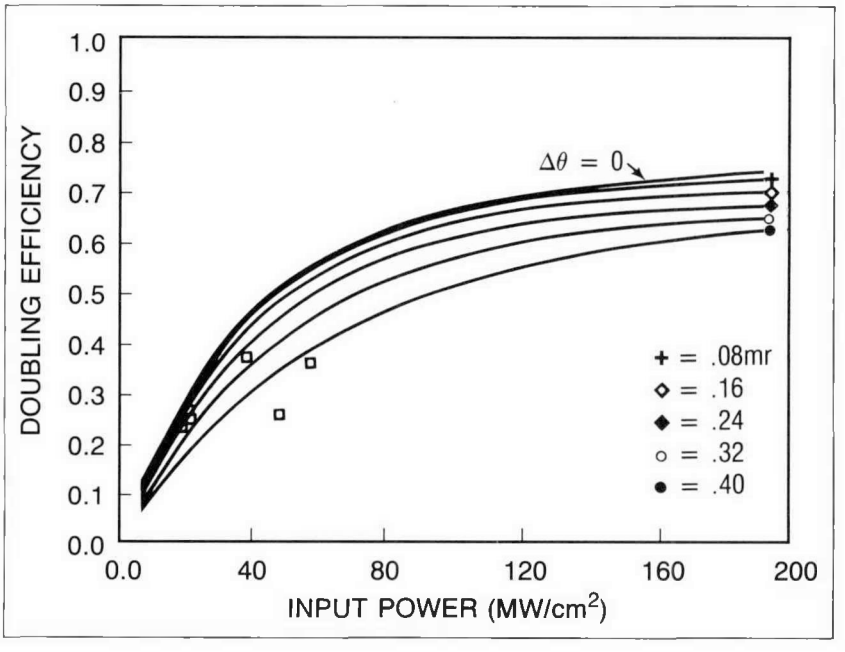

Fig. 3-16. The experimental conversion efficiency of the three-crystal doubler (squares) is compared to the theoretical efficiency (curves). The measured conversion efficiency was 35%; however, the accuracy of crystal alignment was not sufficient to obtain optimum conversion efficiencies. Significantly higher conversion efficiencies should be possible with more careful alignment.

Near- and far-field photographs from one experiment are shown in Fig. 3-17. The input IR near-field shows some diffraction rings and three opaque spots that were due to damage spots on the turning mirror just before the vacuum spatial filter. The UV near field shows these same characteristics with additional spatial noise probably resulting from the interference of the reflections from the seven uncoated surfaces of the KD*P crystals. Etalon effects between the parallel surfaces of the crystals can make the reflections from these surfaces quite large (15% vs. 4%). This noise could be significantly reduced by applying an AR coating to the crystals. The full-angle beam divergence

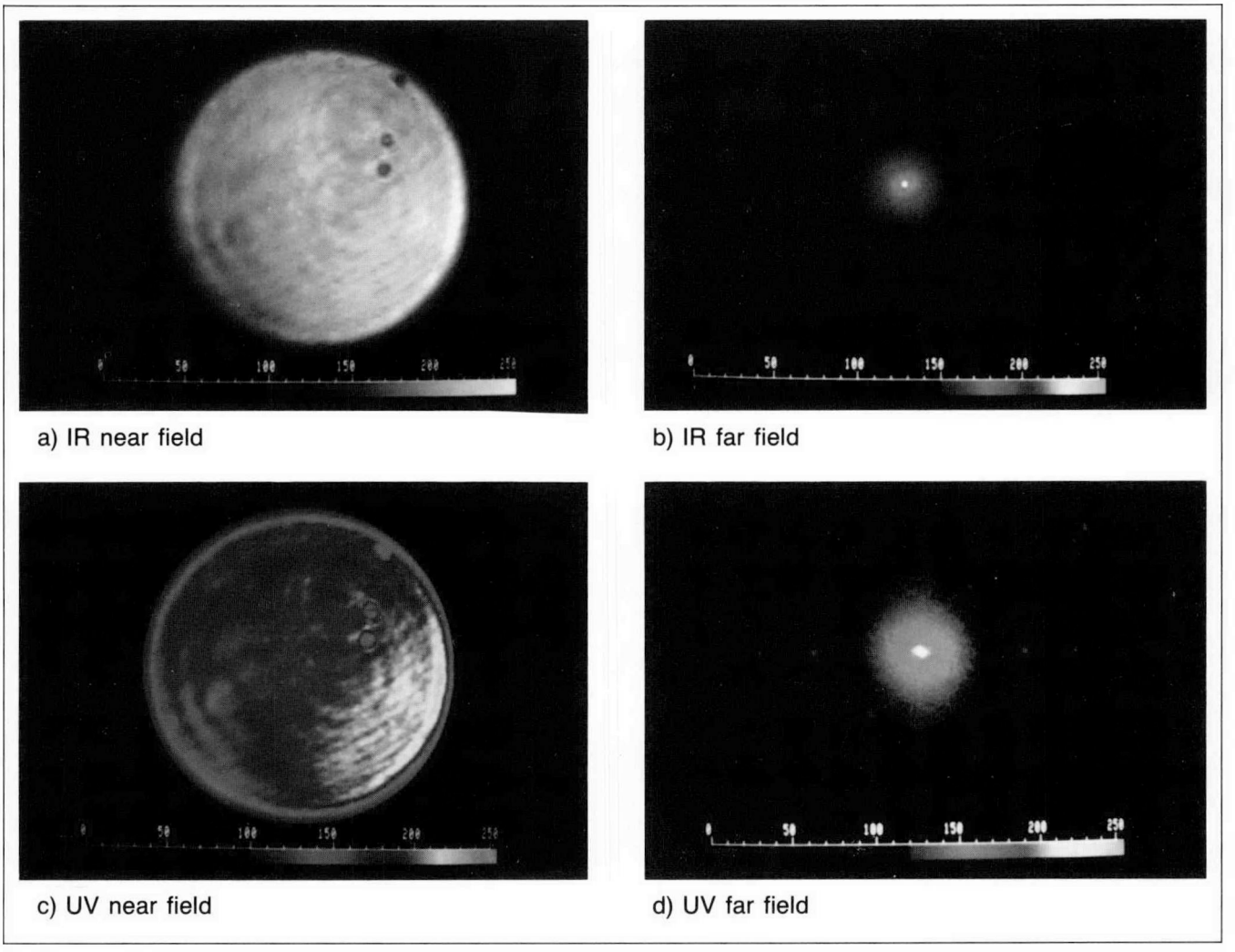

Fig. 3-17. Near-field and far-field photographs of the input IR and output UV from the multiple-crystal ARCA tripler were used to document the laser beam quality. The input IR near-field (a) shows some diffraction rings and three opaque spots, which were caused by damage spots on the turning mirror just before the vacuum spatial filter. The small-scale variations in intensity were only about ±10%. The UV near-field (c) shows these same characteristics, with additional spatial noise (±~30%), probably caused by interference of the reflections from the seven uncoated surfaces of the KD*P crystals. The etalon effects between the parallel surfaces of the crystals can make the reflections from these surfaces quite large (15% vs. 4%).

inferred from the far-field photographs was 60 μrad for the IR beam and 80 μrad for the UV beam. Hence, the beam spread was not increased significantly even with the degraded near-field.

We conclude that the multiple-crystal ARCA technique does work as expected, but good broadband AR coatings and alignment techniques are required to optimize efficiency and beam quality.

For additional information, please contact Mr. L. D. Siebert

REFERENCES

1. W. E. McDermott, N. R. Pchelkin, D. J. Benard, and R. R. Bousek, *Appl. Phys. Lett.* **32** (1978), p. 429.

2. *KMS Fusion 1985 Annual Technical Report on Inertial Fusion Research*, Report KMSF-U1728, KMS Fusion, Inc., Ann Arbor, MI, pp. 112–114.

3. *KMS Fusion Annual Technical Report on Inertial Fusion Research*, 1977 (KMSF-U762), 1978 (KMSF-U884), 1979 (KMSF-U1046), 1980 (KMSF-U1110), and 1981 (KMSF-U1198); KMS Fusion, Inc., Ann Arbor, MI.

4. W. Seka, S. D. Jacobs, J. E. Rizzo, R. Boni, and R. S. Craxton, *Opt. Commun.* **34** (1980), p. 469.

5. *Laser Program Annual Report*, 1979, 1980, 1981, 1982, 1983, and 1984; Lawrence Livermore National Laboratory, Livermore, CA.

PRESENTATIONS AND PUBLICATIONS

SECTION FOUR

Introduction

Communicating our results to the scientific community is an integral part of our research effort. In addition to preparing reports such as this Annual Technical Report, KMS Fusion scientists also present papers at conferences and publish articles in technical and scientific journals. In this section are listed our 1986 presentations and publications relating to inertial confinement fusion research.

SECTION 4.1

Presentations

J. S. Ankney and Gar. E. Busch, "A Dual-Purpose Cryogenic Target Documentation System," *5th Target Fabrication Specialists Meeting*, Las Vegas, NV, March 24–27, 1986. KMSF-U1686ab.

J. S. Ankney and Gar. E. Busch, "Classical and Holographic Interferometry Systems Combined to Document Inertial Fusion Experiments," *1986 Optical Society of America Annual Meeting*, Seattle, WA, October 19–24, 1986. KMSF-U1758ab.

R. L. Berger, Gar. E. Busch, E. F. Gabl, R. J. Schroeder, C. L. Shepard, and J. A. Tarvin, "Stimulated Raman Scattering Theory and Interpretation of Recent Experiments," *7th International Workshop on Laser Interaction and Related Plasma Phenomena*, Monterey, CA, October 28–November 1, 1986. KMSF-U1671ab.

G. Charatis, Gar. E. Busch, C. L. Shepard, and M. D. Rosen (LLNL), "Hydrodynamic Aspects of Selenium X-ray Laser Targets," *International Colloquium on X-ray Lasers*, Aussois, France, April 14–22, 1986. KMSF-U1739ab.

G. Charatis, Gar. E. Busch, C. L. Shepard, and M. D. Rosen (LLNL), "Hydrodynamic Aspects of X-ray Laser Targets," *7th International Workshop on Laser Interaction and Related Plasma Phenomena*, Monterey, CA, October 28–November 1, 1986. KMSF-1670ab.

G. Charatis, Gar. E. Busch, B. K. F. Young (LLNL), and R. E. Stewart (LLNL), "Spectroscopic Characterization of Laser Irradiated Spot Targets: I. Scope," *28th Annual Meeting of the Division of Plasma Physics of the American Physical Society*, Baltimore, MD, November 3–7, 1986. KMSF-U1814ab.

P. D. Dao, L. A. Good, and A. J. Twarowski, "Luminescence Quenching-Dye Molecules Absorbed on Solid Supports by Gas Phase Oxygen," *American Chemical Society Symposium*, Anaheim, CA, September 9–12, 1986. KMSF-U1750ab.

R. D. Day (LLNL), D. D. Stewart (LLNL), L. A. Scott, and S. Murrell, "Hollow Glass Spheres Lapping and Characterization," *5th Target Fabrication Specialists Meeting*, Las Vegas, NV, March 24–27, 1986.

J. G. Downward, "Just a Modest VMS Proposal," *Spring DECUS Symposium*, Dallas, TX, May 1986.

J. G. Downward, "VAX Migration," *Spring DECUS Symposium*, Dallas, TX, May 1986.

J. G. Downward, "The VAXintosh Working Group," *Spring DECUS Symposium*, Dallas, TX, May 1986.

D. J. Drake, "A View Factor Code for Solving Three-Dimensional Radiation Transport Problems Involving Fixed Surfaces with Intervening, Participating Media," *28th Annual Meeting of the Division of Plasma Physics of the American Physical Society*, Baltimore, MD, November 3–7, 1986. KMSF-U1775ab.

D. J. Drake, "Recent Advances in View Factor Code Development at KMSF," *11th Topical Conference on the Physics of Radiatively Driven ICF Targets*, Albuquerque, NM, December 8–11, 1986. KMSF-U1802ab.

M. J. Dunning, F. J. Mayer, S. B. Wineberg, and T. Kamash (University of Michigan), "Evaporation of a Cold, Dense Hydrogen Sphere in a Hot Plasma: The Evolution to Steady State," *16th Annual Anomalous Absorption Conference*, Lake Luzerne, NY, July 13–18, 1986. KMSF-U1807ab.

M. A. Ebner and J. L. Evans, "Millimeter-Sized Hollow Glass Spheres from Aqueous Silicate Preforms," *5th Target Fabrication Specialists Meeting*, Las Vegas, NV, March 24–27, 1986. KMSF-U1689ab.

B. H. Failor, J. R. Brundage, G. Charatis, E. F. Gabl, R. R. Johnson, L. V. Powers, P. D. Rockett, and D. Sullivan, "Time-Resolved X-ray Radiography of Low Preheat Implosions at KMSF," *28th Annual Meeting of the Division of Plasma Physics of the American Physical Society*, Baltimore, MD, November 3–7, 1986. KMSF-U1778ab.

B. H. Failor, C. L. Shepard, E. F. Gabl, and G. Charatis, "An Examination of Experimentally Measured Plasma Density Distributions Produced between Two Exploding Foils," *16th Annual Anomalous Absorption Conference*, Lake Luzerne, NY, July 13–18, 1986. KMSF-U1743ab.

W. J. Felmlee, J. S. Ankney, M. T. Mruzek, D. L. Musinski, and T. R. Pattinson, "A Polymer Cryogenic Target Campaign from an Operations Point of View," *5th Target Fabrication Specialists Meeting*, Las Vegas, NV, March 24–27, 1986. KMSF-U1688ab.

E. F. Gabl, P. M. Campbell, B. H. Failor, R. R. Johnson, J. T. Larsen, and L. V. Powers, "Modeling of the KMSF Low Preheat Implosion Experiments," *28th Annual Meeting of the Division of Plasma Physics of the American Physical Society*, Baltimore, MD, November 3–7, 1986. KMSF-U1780ab.

A. J. Glass, "The Status of Inertial Confinement Research," *European Conference on Optics and Optical System Applications,* Florence, Italy, October 2, 1986. KMSF-U1804ab.

C. J. Hailey, Gar. E. Busch, R. P. Johnson, Z. M. Koenig, J. H. Lupton, R. J. Schroeder, D. Sullivan, and W. Goldstein (LLNL), "Time-Dependent X-ray Reflectivity of a Germanium Crystal Heated with 25 ps, 1.06 μm Laser Light," *19th Symposium of the Society of Photo-Optical Instrumentation Engineers* (SPIE), San Diego, CA, August 17–22, 1986. KMSF-U1726ab.

R. R. Johnson, Gar. E. Busch, J. S. Ankney, J. R. Brundage, B. H. Failor, G. J. Fomin, E. F. Gabl, J. T. Larsen, M. T. Mruzek, D. L. Musinski, L. V. Powers, P. D. Rockett, R. J. Schroeder, C. L. Shepard, J. D. Simpson, J. M. Stiegman, and D. Sullivan, "Spherical Implosion Experiments with Cryogenic PVA Targets at 0.53 μm Laser Wavelength," *16th Annual Anomalous Absorption Conference*, Lake Luzerne, NY, July 13–18, 1986. KMSF-U1746ab.

R. R. Johnson, Gar. E. Busch, J. S. Ankney, B. H. Failor, E. F. Gabl, J. T. Larsen, M. T. Mruzek, L. V. Powers, P. D. Rockett, R. J. Schroeder, C. L. Shepard, and D. Sullivan, "Low Preheat Implosion Experiments with Cryogenic PVA Targets at 0.53 μm Laser Wavelength," *28th Annual Meeting of the Division of Plasma Physics of the American Physical Society*, Baltimore, MD, November 3–7, 1986. KMSF-U1777ab.

J. T. Larsen, "The KMSF Low Preheat Implosion Experiments," *1986 Optical Society of America Annual Meeting*, Seattle, WA, October 19–24, 1986. KMSF-U1760ab.

A. J. Martin, R. J. Simms, and R. B. Jacobs (R. B. Jacobs Associates), "Beta Energy-Driven Uniform DT-Ice Layers/Part II," *5th Target Fabrication Specialists Meeting*, Las Vegas, NV, March 24–27, 1986. KMSF-U1694ab.

F. J. Mayer, W. B. Fechner, and M. R. Wixom, "Dynamic High Pressure Materials Processing in Spherical Geometry," *Spring Meeting of the American Physical Society*, April 1986.

W. J. Miller and R. P. Belanger, "Optimum Alkali Ratios in Glass Shells," *5th Target Fabrication Specialists Meeting*, Las Vegas, NV, March 24–27, 1986. KMSF-U1685ab.

M. T. Mruzek and W. J. Felmlee, "Experimental Details and Results Pertaining to Inversion in Liquid Layers," *5th Target Fabrication Specialists Meeting*, Las Vegas, NV, March 24–27, 1986. KMSF-U1690ab.

D. L. Musinski, J. S. Ankney, D. N. Decker, W. J. Felmlee, R. E. Frazier, W. A. Groves, and M. T. Mruzek, "Cryogenic ICF Target Technology at the Omega Facility, University of Rochester," *33rd National Symposium of the American Vacuum Society*, Baltimore, MD, October 27–31, 1986. KMSF-U1754ab.

D. L. Musinski, W. J. Felmlee, D. L. Melmoth, and M. T. Mruzek, "Cryogenic Target Technology at the Omega Facility, University of Rochester," *5th Target Fabrication Specialists Meeting*, Las Vegas, NV, March 24–27, 1986. KMSF-U1684ab.

L. V. Powers, "Two-Plasmon Decay Eigenmodes in a Two-Dimensional Bounded Plasma," *28th Annual Meeting of the Division of Plasma Physics of the American Physical Society*, Baltimore, MD, November 3–7, 1986. KMSF-U1772ab.

L. V. Powers and R. L. Berger, "Nonlinear Competition between Two-Plasmon Decay and Stimulated Raman Scattering," *16th Annual Anomalous Absorption Conference*, Lake Luzerne, NY, July 13–18, 1986. KMSF-U1748ab.

R. G. Schneggenburger, "Radiation Damage to ICF Shells of Poly(vinyl alcohol)," *5th Target Fabrication Specialists Meeting*, Las Vegas, NV, March 24–27, 1986. KMSF-U1693ab.

R. J. Schroeder, Gar. E. Busch, B. H. Failor, E. F. Gabl, R. R. Johnson, L. V. Powers, C. L. Shepard, and T. Speziale, "Coronal Plasma Conditions in KMSF Low-Preheat High Compression Experiments," *28th Annual Meeting of the Division of Plasma Physics of the American Physical Society*, Baltimore, MD, November 3–7, 1986. KMSF-U1779ab.

L. A. Scott and A. J. Martin, "Formation and Characterization of Large Cavities for Fuel Shells," *5th Target Fabrication Specialists Meeting*, Las Vegas, NV, March 24–27, 1986. KMSF-U1695ab.

J. P. Sheerin, "Intense Electromagnetic Wave Interactions in Very Large Scale Plasmas," *16th Annual Anomalous Absorption Conference*, Lake Luzerne, NY, July 13–18, 1986. KMSF-U1751ab.

C. L. Shepard, R. R. Johnson, G. Charatis, B. H. Failor, E. F. Gabl, J. T. Larsen, L. V. Powers, P. D. Rockett, and P. Hammerling (LaJolla), "Compression Measurements from X-ray Backlighting of Cryogenic Implosion Experiments," *16th Annual Anomalous Absorption Conference*, Lake Luzerne, NY, July 13–18, 1986. KMSF-U1749ab.

C. L. Shepard, Gar. E. Busch, E. F. Gabl, B. H. Failor, and R. J. Schroeder, "Lateral Thermal Transport Smoothing of Laser Intensity Nonuniformities in 0.53 μm Laser Irradiated Disks," *28th Annual*

Meeting of the Division of Plasma Physics of the American Physical Society, Baltimore, MD, November 3–7, 1986. KMSF-U1776ab.

T. Speziale and C. L. Shepard, "Diffusive Mixing Across an Interface in a Multicomponent Plasma," *28th Annual Meeting of the Division of Plasma Physics of the American Physical Society*, Baltimore, MD, November 3–7, 1986. KMSF-U1774ab.

D. A. Steinman, "A Simple Method for Shell Wall Uniformity Analysis," *5th Target Fabrication Specialists Meeting*, Las Vegas, NV, March 24–27, 1986. KMSF-U1691ab.

O. E. Ulrich, Geo. E. Busch, K. G. Cuneo, M. B. Knickelbein, K. L. Marsh, R. D. Mehler, and O. P. Ohar, "Temperature Measurements to Characterize Reactive Flows in a Chemical Oxygen-Iodine Laser," *Lasers '86*, Orlando, FL, November 3–7, 1986. KMSF-U1812ab.

O. E. Ulrich, Geo. E. Busch, K. L. Marsh, J. P. Sercel, J. D. Simpson, and A. J. Twarowski, "The Short-Pulse Chemically-Pumped Oxygen-Iodine Laser at KMSF," *14th International Quantum Electronics Conference/6th Conference on Lasers and Electro-optics*, San Francisco, CA, June 9–13, 1986. KMSF-U1719ab.

S. A. Von Laven and L. M. Liebrock (Michigan Technological University), "Free Electron Laser Simulations on the MPP," *Massive Parallel Processor Symposium*, Greensbelt, MD, September 24–25, 1986. KMSF-U1773ab.

S. B. Wineberg, E. F. Gabl, L. R. Scott, and J. F. McGrath, "Spectral Methods for the Numerical Solution of the Kadomtsev-Petviashvili (K-P) Equations of Wave Propagation," *28th Annual Meeting of the Division of Plasma Physics of the American Physical Society*, Baltimore, MD, November 3–7, 1986. KMSF-U1783ab.

B. K. F. Young (LLNL), R. E. Stewart (LLNL), G. Charatis, and Gar. E. Busch, "Spectroscopic Characterization of Laser-Irradiated Dot Targets: II. Results," *28th Annual Meeting of the Division of Plasma Physics of the American Physical Society*, Baltimore, MD, November 3–7, 1986.

SECTION 4.2

Publications

J. S. Ankney, M. T. Mruzek, and W. J. Felmlee, "The Use of Poly(vinyl alcohol) Shells as Fuel Containers for Inertial Fusion Experiments," *J. Vac. Sci. Technol. A* **4**(3) (May/June 1986), pp. 1124–25. KMSF-U1610.

R. L. Berger, Gar. E. Busch, E. F. Gabl, R. J. Schroeder, C. L. Shepard, and J. A. Tarvin, "Stimulated Raman Scattering: Comparison of Theory and Experiment," *Laser Interaction and Related Plasma Phenomena* Vol. 7, edited by H. Hora and G. Miley (Plenum Publishing Corporation, 1986), p. 371. KMSF-U1671.

Gar. E. Busch, "Twenty Picosecond Pulsed UV Holographic Interferometry of Laser-induced Plasmas," *NATO-ASI Series E—Applied Sciences* **2** (1986), p. 789. KMSF-U1506.

Geo. E. Busch, K. L. Marsh, J. P. Sercel, J. D. Simpson, A. J. Twarowski, and O. E. Ulrich, "Short-Pulse Energy Extraction from a Chemically-Pumped Oxygen-Iodine Laser," *Digest of Technical Papers, Conference on Lasers and Electro-Optics* (San Francisco, CA, June 9–13, 1986), p. 254.

Geo. E. Busch, M. B. Knickelbein, and O. E. Ulrich, "RedSOX: A Chemically Pumped Red Singlet Oxygen Laser," *Digest of Technical Papers, XIV International Conference on Quantum Electronics* (San Francisco, CA, June 9–13, 1986), p. 74. KMSF-U1721ab.

P. M. Campbell, "Transport Effects of Interacting Hot and Cold Electrons in Laser-Heated Plasmas," *Fusion Technology* **9** (May 1986), pp. 391–400. KMSF-U1503.

G. Charatis, Gar. E. Busch, C. L. Shepard, and M. D. Rosen (LLNL), "Hydrodynamic Aspects of X-ray Laser Targets," *Journal de Physique* **47** C6(10), edited by H. Hora and G. Miley (Plenum Publishing Corp., New York, 1986), pp. C689–C698. KMSF-U1739.

R. L. Crawley, "A Hollow Droplet Generator for Polymer Shell Production," *J. Vac. Sci. Technol. A* **4**(3) (May/June 1986), pp. 1138–1141. KMSF-U1674.

P. D. Dao and A. J. Twarowski, "The Photophysics of Gas Phase Europium Chelates. I. Temperature Dependence of Luminescence," *J. Chem. Phys.* **85**(12) (15 December 1986), pp. 6823–6827. KMSF-U1770.

J. G. Downward, "Customizing EDT V3.0 for DCL Windows," *The DEC Professional* **5**(2) (February 1986), pp. 74–80. KMSF-U1502.

E. F. Gabl, "Requirements for Three-Dimensional Resonant Interaction of Ion-Acoustic Solitons," *Phys. Fluids* **29**(5) (May 1986), pp. 1737–1738. KMSF-U1596.

A. J. Glass, "An Historic Overview of Inertial Confinement Fusion: What Have We Learned?" *J. Vac. Sci. Technol.* A **4**(3) (May/June 1986), pp. 1098–1105. KMSF-U1680.

Y. S. Kuo, R. F. Bunshah (LLNL), and D. Okrent (LLNL), "Hot Hollow Cathode and its Applications in Vacuum Coating: A Concise Review," *J. Vac. Sci. Technol.* A **4**(3) (1986), pp. 397–402. KMSF-U1806.

J. T. Larsen, "Computations in Fusion Physics," *Appl. Math. Comp.* **20**(1&2), edited by D. F. Lockhart and D. L. Hicks (North-Holland Publishing Co., Sept. 1986), pp. 111–142. KMSF-U1657.

J. T. Larsen and R. R. Johnson, "The KMSF Low Preheat Implosion Experiments," *Digest of Technical Papers, XIV International Quantum Electronics Conference* (San Francisco, CA, June 9–13, 1986), p. 320. KMSF-U1725ab.

A. J. Martin and R. J. Simms, "Details of the Response of a Kodak High Resolution Plate to X-irradiation for the Characterization of Inertial Confinement Fusion Targets and Components," *J. Vac. Sci. Technol.* A **4**(3) (May/June 1986), p. 1160–1162. KMSF-U1616.

F. J. Mayer, R. L. Maynard, D. L. Musinski, N. W. Schmerberg, M. R. Wixom, and R. F. Benjamin (LLNL), "Recent Developments in Microshell®-Tipped Optical Fibers as High-Pressure Shock Detectors," *Shock Waves in Condensed Matter*, edited by Y. M. Gupta (Plenum Publ. Co., New York, Sept. 1986), pp. 547–551. KMSF-U1586.

F. J. Mayer, W. B. Fechner, and M. R. Wixom, "Laser-Initiated Spherically Symmetric High-Explosive Detonation for High-Pressure Materials Processing," *Digest of Technical Papers, XIV International Quantum Electronics Conference* (San Francisco, CA, June 9–13, 1986), p. 118. KMSF-U1731ab.

J. F. McGrath, D. L. Hicks, and L. M. Liebrock, "Parallel Algorithms for Computational Continuum Dynamics," *Appl. Math. Comp.* **20**(1&2), edited by D. F. Lockhart and D. L. Hicks (North-Holland Publishing Corp., New York, Sept. 1986), pp. 145–173. KMSF-U1663.

M. T. Mruzek, D. L. Musinski, and R. B. Jacobs (R. B. Jacobs Associates), "Observations of Mass Transport Phenomena in Multicomponent Liquid Mixtures," *J. Vac. Sci. Technol.* A **4**(3) (May/June 1986), pp. 1125–1127. KMSF-U1678.

L. V. Powers and R. L. Berger, "A Real Space Calculation of Absolutely Unstable Modes for Two-Plasmon Decay in Inhomogeneous Plasma," *Plasma Physics and Controlled Nuclear Fusion Research* **28**(10) (May 1986), pp. 1575–1587. KMSF-U1489.

P. D. Rockett, C. R. Bird, and C. J. Hailey, "Crystal R_c Calibrations with an Uncollimated Point X-ray Source," *X-ray Calibration Techniques, Sources, and Detectors*, edited by P. D. Rockett and P. Lee, Proc. SPIE 689 (1986), p. 114.

M. D. Rosen, P. L. Hagelstein, D. L. Matthews, E. M. Campbell, A. U. Hazi, B. L. Whitten, B. MacGowan, R. E. Turner, R. W. Lee (all LLNL), G. Charatis, Gar. E. Busch, C. L. Shepard, P. D. Rockett, and R. R. Johnson, "Exploding Foil Technique for Achieving a Soft X-ray Laser," *Phys. Rev. Lett.* **54**(2) (1986). KMSF-U1647.

L. A. Scott, R. G. Schneggenburger, and P. R. Anderson, "Deuterium Permeation Properties of Beta-Irradiated and Unirradiated Poly(vinyl alcohol) and Polystyrene Shells," *J. Vac. Sci. Technol. A* **4**(3) (May/June 1986), pp. 1155–1159. KMSF-U1620.

S. B. Segall, M. S. Curtin, and S. A. Von Laven, "Key Issues in the Design of a Two-Stage FEL," *Nuclear Instrum. Methods* A **250** (1986), p. 376.

C. L. Shepard, J. A. Tarvin, R. L. Berger, Gar. E. Busch, R. R. Johnson, and R. J. Schroeder, "Raman Scattering in Experiments with Planar Au Targets Irradiated with 0.53 μm Laser Light," *Phys. Fluids* **29**(2) (February 1986), pp. 583–593. KMSF-U1562.

J. D. Simpson, D. J. Drake, and T. Speziale, "Light-Integrating Cylinder for Inertial Confinement Fusion Light Balance Measurements in Mirror Illumination Systems," *Rev. Sci. Instrum.* **57**(12) (December 1986), pp. 2951–2956. KMSF-U1717.

T. Speziale, "Use of the Beat-Wave Acceleration Concept to Improve the Range of Charged Particle Beams," *Digest of Technical Papers, XIV International Quantum Electronics Conference* (San Francisco, CA, June 9–13, 1986), p. 166. KMSF-U1718ab.

J. A. Tarvin, Gar. E. Busch, E. F. Gabl, R. J. Schroeder, and C. L. Shepard, "Laser and Plasma Conditions at the Onset of Raman Scattering in an Underdense Plasma," *Laser and Particle Beams* **4**, Parts 3 and 4 (February 1986), pp. 461–471. KMSF-U1676.

M. A. True and S. M. Alexander True, "Thickness Uniformity Measurements of Plastic Coated Glass Shells by Image Analysis of X-ray Radiographs," *J. Vac. Sci. Technol. A* **3**(3) (1986), pp. 1258–1261. KMSF-U1509.

J. F. Ward (University of Michigan), S. A. Von Laven, and S. B. Segall, "Annular Reflectors for an FEL Resonator," *Nuclear Instrum. Methods* A **250** (1986), p. 304.

REPORT DISTRIBUTION LIST
CONTRACT NO. DE-AC08-82DP40152

Lawrence Livermore National Laboratory
P. O. Box 808
Livermore, CA 94550
L. P. Altbaum, L488
T. P. Bernat, L-482
E. M. Campbell, L-473
L. W. Coleman, L-481
K. G. Estabrook, L-472
A. J. Glass, L-1
J. F. Holzrichter, L-295
R. L. Kauffman, L-473
W. L. Kruer, L-472
W. F. Krupke, L-488
B. F. Lasinski, L-472
J. D. Lindl, L-477
D. L. Matthews, L-473
G. H. Miller, L-20
J. H. Nuckolls, L-1
R. L. Pond, L-302
E. K. Storm, L-481

University of California
Lawrence Livermore National Laboratory
P. O. Box 808
Livermore, CA 94550
Laser Program Library

Department of Energy
Inertial Fusion Division
Code DP-243
Washington, DC 20545
D. Bixler, DP-243
G. D'Alessio, DP- 243
C. B. Hilland, DP-243
S. L. Kahalas, DP-243
T. G. Owen, DP-243

Naval Research Laboratory
Washington, DC 20375
S. Bodner
T. Coffey

U.S. Department of Energy
Attn: Grace Plummer
Information Management Div.
Nevada Operations Office
P. O. Box 14100
Las Vegas, NV 89114-4100
(3 copies)

U. S. Department of Energy
Office of Scientific and Technical Information
Technical Information Center
P. O. Box 62
Oak Ridge, TN 37831

Sandia National Laboratory
Organization 1260
P.O. Box 5880
Attn: Pace Van Devender
Albuquerque, NM 87185
(4 copies)

Los Alamos National Laboratory
Attn: David C. Cartwright
Code E-527
P.O. Box 1663
Los Alamos, NM 87545
(4 copies)

University of Rochester
Laboratory for Laser Energetics
250 East River Road
Rochester, NY 14627
R. McCrory
J. Soures

U. S. Department of Energy
San Francisco Operations Office
Attn: Dennis Neely (WDD)
1333 Broadway
Oakland, CA 94612

DO NOT MICROFILM
THIS PAGE